TECHNISCHE UNIVERSITÄT MÜNCHEN

TUM School of Engineering and Design

Performance Optimisation of a Coupled Cone and Dog Clutch for Automotive Application

Marco Mileti

Vollständiger Abdruck der von der TUM School of Engineering and Design der Technischen Universität München zur Erlangung eines

Doktors der Ingenieurwissenschaften

genehmigten Dissertation.

Vorsitz:		Prof. Dr. Markus Zimmermann
Prüfer der Dissertation:	1.	Prof. Dr.-Ing. Karsten Stahl
	2.	Prof. Dr.-Ing. Giampiero Mastinu

Die Dissertation wurde am 07.12.2022 bei der Technischen Universität München eingereicht und durch die TUM School of Engineering and Design am 14.03.2023 angenommen.

Preface

The present doctoral thesis bases largely on the results of the research project “Alternative Shifting Elements for Automatic Transmissions”, founded by the Bavarian Research Association (BFS), which I conducted during my time as a research associate at the Gear Research Centre (FZG) of the Technical University of Munich (TUM).

I want to thank all persons who have made this achievement possible. In particular, I would like to mention:

Prof. Dr.-Ing. Karsten Stahl, for being my doctoral supervisor at FZG,

Prof. Dr-Ing. Gianpiero Mastinu, for accepting to be my second examiner and for all the worthy input and the discussions,

Prof. Dr-Ing. Markus Zimmermann for accepting to be the chairperson of the evaluating committee,

Dr.-Ing. Hermann Pflaum, for being my mentor and guide during my time as research associate, for the many technical discussions, the trust and the invariably friendly working atmosphere,

To all former colleagues from laboratory, workshop, secretary and administration for the support, help and good working atmosphere,

To my students, who have contributed to the finalization of my project through their work and theses; and especially to Lukas and Patrick, who decided to follow my path at FZG and remain until today good friends I can always rely on,

To the Speed4E team: Bernd Morhard, Daniel Schweigert and Lukas Pointner-Gabriel, for your hard work and all the fun we had,

To all my former colleagues at FZG, and in particular Michael Hein, Maximilian Strebel, Patrick Fischer, Christopher Illenberger, Jakob Winkler, Dominik Kratzer, Daniel Fuchs, Nadine Sagraloff, Christian Weber, Benedikt Siewerin and Stefan Reitschuster for the always positive working environment and the friendships that last until today,

To all my friends from Milan and especially to Pietro for the many sailing adventures and Luca, for being a friend indeed – one I could always count on, even during my darkest times,

To my Italian and German families, to Antonella, Antonio, Donato, Toni, Monika, Gabi,

To my brother Stefan, who is younger, yet has so often been an example to me,

To my parents, Renate and Lucio, who have made all this possible in the first place, who have supported and motivated me, and whom I can always count on.

And finally to my wife Valentina, who has been on my side during the last years, who is my adventures companion, my lighthouse when the sea gets stormy and who (almost always) stands me when I am frustrated the world is not ruled by engineers.

Munich, July 2023

Abstract

Aim of this work is to define a method for determination and optimisation of thermomechanical resistance to hotspots of cone clutch and dynamic engagement behaviour of dog clutches. The described method is developed and applied to a novel and highly efficient shifting element, namely CCDC, which combines qualities of cone and dog clutches, while at the same time compensating their drawbacks with respect to multiple-disc wet clutches. Experiments show improved efficiency by at least 50 %, with a consequent reduction of CO_2 emissions of about 2.5 g_{CO_2}/km in the WLTP cycle.

Thermomechanical stability and operating boundaries of the cone clutches under high and extreme loads are determined simulatively. For good robustness of the model, material parameters and results are validated through extensive experimental testing. In a second step, results obtained form thermomechanical simulations are utilised to train a neural network. Once trained to an adequate level of preciseness and robustness, the neural network is capable of calculating thermomechanical loads for any combination of working conditions extremely fast. This allows to produce accurate maps, where the critical sliding speeds responsible for hotspot initiation, are easily identified.

Dynamic engagement performance of dog clutches subjected to constant torque load is determined through multibody simulation. Also in this case, the simulation model is extensively validated through experimental data. From simulation results, an analytical approach is developed, which is capable of showing operational limits of different dog clutch variants and compare them to each other. Such approach enhances design optimisation without the need of experimental proof.

The method is applied for CCDC development and for proof of concept at vehicle level, where comfort and thermal stability ratings are shown.

Contents

Nomenclature

Symbol	Unit	Description
α	rad	Cone angle
β	rad	Half-angle of blocker teeth
$\beta_{1,4}$	m	Shape function coefficients
$\beta_{2,3,5,6}$	-	Shape function coefficients
γ_f	rad	Tooth flank angle
γ_{zr}	-	Shear strain
$\Delta\omega$	rad/s	Angular velocity difference
Δn_{ICE}	rpm	ICE overshoot
ΔT	Nm	Dog clutch engagement torque step
ϵ	rad	Relative engagement angle
ϵ_θ	-	Circumferential strain
ϵ_{lim}	rad	Limite engagement relative angle
ϵ_r	-	Radial strain
ϵ_z	-	Axial strain
ζ	Nm/ms	Engagement jolt
η	-	Efficiency
η_l	Pa$\cdot s$	Dynamic lubricant viscosity
ϑ	K	Temperature
ϑ_{crit}	K	Thermomechanically critical temperature
ϑ_{lim}	K	Threshold temperature for hotspot formation
$\vartheta_{max,nn,i,k}$	K	Max. temperature of NN k, validation load i
$\vartheta_{max,sim,i}$	K	Max. simulated temperature of validation load i
ϑ_{max}	K	Maximum temperature
ϑ_{oil}	K	Oil Temperature
ϑ_0	K	Initial or mass temperature
κ	-	Mass markup factor
μ	-	Coefficient of friction
μ_{avg}	-	Average coefficient of friction
$\mu_{min,Grad}$	0	Negative gradient of minimum coefficient of friction
μ_{steel}	-	Coefficient of friction of steel
μ_z	-	Coefficient of friction of blocking teeth
ν	-	Poisson's coefficient
ξ	°	Dog clutch rotation angle
ω	rad/s	Angular velocity
$A_{f,tot}$	mm^2	Total friction surface

Symbol	Unit	Description
A_f	m^2	Friction area
b	m	Elastic layer thickness
c_γ	N/(mm·μm)	Mean mesh stiffness per unit face
c_l	N/m^3	Elastic layer stiffness per unit area
D_i	mm	Inner diameter
D_o	mm	Outer diameter
E	N/m^2	Young's modulus
$e_{avg,abs}$	-	Absolute value of relative averaged error
E_{kin}	J	Kinetik energy
F	N	Force
$F_{ax,s,d,i}$	N	Friction force between splines of carrier and inner dog clutch body
$F_{ax,s,d,o}$	N	Friction force between splines of carrier and outer dog clutch body
$F_{ax,s,d,t}$	N	Friction force between tooth flanks of dog clutch
$F_{ax,s,f,o}$	N	Friction force between splines of carrier and outer friction cone(s)
F_{spring}	N	Reaction force of wave spring
F_a	N	Axial force
F_D	N	Actuation force at Clutch D (K81)
F_a	N/s	Actuation force gradient
F_D	N/ms	force gradient at clutch D (K81)
h	m	Clearance between friction surfaces
h_{el}	m	Element size
h_{max}	m	Geometric axial tooth overlap
h_g	m	Pad axial separation
h_p	m	Groove axial separation
i_{FD}	-	Final drive transmission ratio
i_{xy}	-	Transmission ratio between x and y
J_{red}	kgm^2	Rotational inertia
K	N/m^2	Elastic layer module
k_{AS}	Nm/rad	Torsional stiffness of axle shafts
k_{CS}	Nm/rad	Torsional stiffness of cardan shaft
k_{FD}	Nm/rad	Torsional stiffness of final drive
m_V	kg	Vehicle mass
$MSE_{\vartheta,avg}$	-	Averaged MSE
n	rpm	Rotational speed
n_{ICE}	rpm	Rotational speed of ICE
n_{nn}	-	Number of performed NN trainings
n_{sim}	-	Number of validation simulations
n_0	rpm	Initial speed difference

Symbol	Unit	Description
n_g	-	Number of disc grooves
p	N/m^2	Contact pressure
P''	W/m^2	Friction power per unit area
p_{avg}	N/m^2	Average contact pressure
$p_{e,j}$	N/m^2	Average pressure at element, time increment j
q	J/m^2	Specific friction loss
Q	J	Heat
$q_{e,j}$	J/m^2	Heat per element area, time increment j
q_D	J/mm^2	Specific friction loss at clutch D (K81)
q_j	J/m^2	Heat per unit area transferred during time increment j
$\dot{q}_0$	W/m^2	Initial specific friction loss
$\dot{q}$	W/m^2	Specific friction power
$\dot{q}_D$	W/mm^2	Specific friction power at clutch D (K81)
$\bar{\dot{q}}_{e,j}$	W/m^2	Heat flux per element area, time increment j
Q_{oil}	l/min	Oil flow rate
r	m	Radial coordinate
r_{dyn}	m	Dynamic rolling radius
$r_{m,e}$	m	Average radius of element
r_f	m	Tooth face convexity radius
r_i	m	Inner friction radius
r_I	m	Indexing diameter
r_m	m	Mean friction radius
r_o	m	Outer friction radius
r_w	mm	Wear induced tooth radius
s	mm	Sleeve position
$S_{V,opt}$	rad	Optimal backlash of dog clutch
S_V	rad	Backlash of dog clutch
$\widehat{S_V}$	rad	Circular backlash
T''	Nm	Friction torque per unit area
t	s	Time
T	Nm	Torque
T_{CCDC}	Nm	Torque at CCDC
T_{st}	Nm	Static load torque
T_D	Nm	Drag torque
T_f	Nm	Friction torque
t_s	s	Sliding time
$\vec{u}$	m/s	Circumferential clutch speed

Symbol	Unit	Description
u_x	m	Radial displacement
$v_{g,0}$	m/s	Initial sliding velocity
v_0	m/s	Initial velocity
v_f	mm/s	Piston velocity
v_s	m/s	Sliding speed
v_z	m/s	Axial velocity of damper
$\bar{v}_{s,e,j}$	m/s	Average sliding speed at element e, time increment j
$\vec{v}$	m/s	Axial piston velocity
$\vec{w}$	m/s	Dog clutch relative velcity
w	m	Axial displacement
z	m	Axial coordinate
z	-	Number of friction surfaces
z_1	-	Number of teeth of sun gear
z_2	-	Number of teeth of ring gear
z_p	-	Number of teeth of planet

Abbreviations

AI	Artificial Intelligence
AMT	Automated Manual Transmission
AT	Automatic Transmission
CAE	Computer Aided Engineering
CCDC	Coupled Cone and Dog Clutch
CoF	Coefficient of Friction
COG	Centre of Gravity
DCT	Dual Clutch Transmission
DHT	Dedicated Hybrid Transmission
DOF	Degree of freedom
ECU	Engine Control Unit
ECU	Engine Control Unit
EOM	Equation of motion
EV	Electric Vehicle
FD	Final Drive
FEM	Finite Element Model
FVA	Research Association for Power Transmission Engineering
FZG	Gear Research Centre
HAMT	Hybridised Automated Manual Transmission
ICE	Internal Combustion Engine
MSE	Mean Squared Error
MT	Manual Transmission
NN	Neural Network
PHEV	Plug-in Electric Vehicle
RTF	Real Time Factor
SPHEV	Series-Parralel Hybrid Electric Vehicle
TC	Torque Converter
TCU	Transmission Control Unit
NEDC	New European Driving Cycle
WLTP	Worldwide harmonized Light vehicles Test Procedure

1 Introduction

Restrictions in terms of local CO_2 emissions are forcing automotive manufacturers and suppliers to come up with innovative solutions to increase the efficiency of vehicles. In particular, the European legislation dictates that only 95 g CO_2/km average fleet emissions will be acceptable by the year 2021 with further reductions to be achieved by end of 2024 [Eur19]. Through electrification of the drivetrain, these ambitious objectives can be adhered to. However, as full electric vehicles (BEV) are still limited by high costs - especially of batteries - and maximum ranges, hybridisation and optimisation of existing dirvetrains are valid alternatives to reach the foreseen objectives on a short to medium term. [Son19]
If the objectives in terms of emissions will not be reached, penalty payments shall be due. Should this be the case, a reduction of 1 g_{CO_2}/km average fleet emissions would already lead to considerable savings.

1.1 Initial situation and motivation

Even though efficiency of modern drivetrain components is already very high, some systems still offer potential for optimisation. For example, in automatic transmissions, a major amount of losses is generated by drag torque between disengaged multiple-disc wet clutches. Additionally, once the clutches are engaged, the torque is transmitted via friction-fit. Thus, an axial force directly proportional to the required torque is to be applied to the clutch. The axial force, in turn, has to be continuously held and is generated by a hydraulic actuator, causing further losses. Conversely, shiftable dog clutches do neither generate noteworthy drag losses, nor have to be actuated with high axial forces. However, as the latter can neither shift under load - which is a basic requirement for automatic transmissions-, nor synchronise masses and are characterised by relatively high discomfort during the engagement process, they are rarely found in traditional automotive series applications.

On the other hand, several automotive applications of dog clutches can be found in electrified vehicles. In particular, vehicles with parallel hybrid drivetrains often come with the functionality of disengaging one of the electric motors, in order not to drag it while not operating. The motor is then reconnected to the drivetrain when a boost or additional power is required. As most state-of-the-art electric and hybrid vehicles are driven by permanent-magnet synchronous motors, which generate high drag torque, such a disconnect function can become highly desirable. This function is mainly overtaken by a dog clutch, as electric motors are capable of synchronising speed very precisely. However, due to the usually high transmission ratios that intercur between electric motor and clutch, even small speed differences can possibly lead to perceptible jolts.

Since the utilisation of dog clutches in shiftable gearboxes is highly desirable to reduce losses, a solution that unites the qualities of form-fit and friction clutches is developed. As an alter-

native shifting element, substituting multiple-disc clutches in automotive transmission or mere dog clutches in hybrid and electrified transmissions, the Coupled Cone and Dog Clutch (short CCDC) is designed to successfully find a compromise between efficiency, comfort and controllability. The joint research project "Alternative Shifting Elements for ATs" between FZG and HOERBIGER Antriebstechnik Holding GmbH is a consistent part of the development and design of the CCDC.

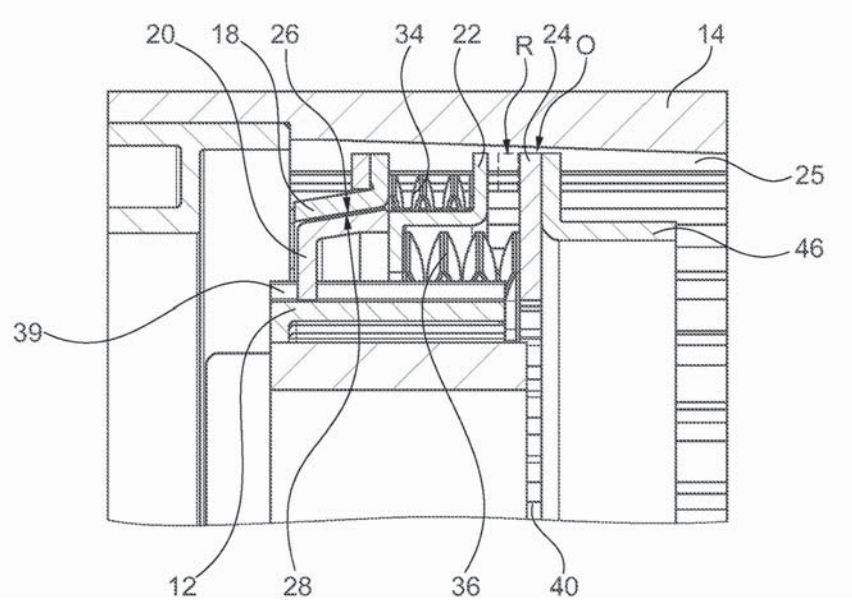

Figure 1.1: Cross section of the second design of CCDC from patent [Dem18]

1.2 Research objective and approach

The working principle of the CCDC bases on a cone clutch for synchronizing masses and a dog clutch to transmit static torque. A similar working principle can be found in sychronizers of manual transmissions. However, CCDC has to be additionally capable of performing powershifts, transmitting very high torque and guarantee a successful and comfortable shift in every load condition. In order to be able to comply with all of these stringent requirements, clutch performance has to be assessed. Research is mainly focused on individuating the capabilities of a cone clutch and asses its performance and thermal stability. Parallely, the dynamic behaviour of the dog clutch was thoroughly analysed and optimised, to design an innovative and efficient shifting element that does not affect package or comfort. In fact, especially those applications are affected by major changes with respect to existing series applications.

As an approach to solve the above mentioned problem, a combination and integration between simulations and experiments is chosen. In Chapter 3, the general aim and focus of both simulations and experiments is shown. In particular, the design parameters the present research is concentrated on will be explained and a motivation for their choice be given. In Chapter 4, the method developed for performance optimisation is explained into detail. After motivating why a functional distinction between cone and dog clutch is performed, both simulative and experi-

mental set-ups are shown for both sub-systems. Based on simulative results, it will be shown how their performance and limits can be assessed and the functionality optimised. In Chapter 5, the developed method will be applied to CCDC and its validity proven. The results will be discussed and design recommendations given. Finally, in Chapter 6, tests of the optimised design of CCDC by means of a transmission and vehicle simulation model will be described. Indeed, in such a way, the effectiveness of CCDC can be proved by performing gearshift simulations in reference and extreme conditions.

2 State of the art

2.1 Automotive transmissions

The necessity to employ transmissions in vehicles is determined by different speed-torque characteristics of driving motors. As the characteristic curves of internal combustion engines (ICE) do not approximate properly the traction force hyperbola for a reasonable range of speeds, the latter are generally combined to multispeed transmissions. On the other hand, while electric motors are well capable of approximating the traction force hyperbola, at least a fixed ratio transmission remains necessary to effectively increase torque at the wheels, thus reducing the dimensions of the motors and connected costs. Evolution of transmission systems for ICE-driven passenger vehicles has led to the affirmation of five types of multispeed transmissions. Their diffusion is strongly dependent on the considered vehicle segment and market. So, while manual transmission systems (MT) are widely diffused in Europe and Asia, automatic transmissions (AT) possess the highest share in the US market. The CVT application can be found almost only in the Chinese and Japanese markets. Over the last decade, also the dual clutch transmission (short DCT) has gained in importance, especially in the European market. Noteworthy is also the automated manual transmission (AMT), which is however still a niche product, due to its incapability of performing powershifts. [Xu18]

Even though ICE-driven passenger vehicles are supposed to maintain the greater share of sold vehicles for at least the next decade, many studies show that electrified and fully electric vehicles will take over more and more.

As the designed and tested coupled cone and dog clutch for automotive application is aimed to improve efficiency of automatic transmissions and electrified drivetrains, the next section will focus especially onto these very systems.

2.1.1 Automatic transmissions

Known as automatic transmission, this system is essentially a combination of one or more planetary gear sets, whose degrees of freedom are constrained and defined by couplings, clutches or brakes. Automatic transmissions were developed in the early 30s and first introduced in series by General Motors in 1940 under the name of Hydra-Matic [Pos39]. Automatic transmissions are nowadays widely spread across Northern America and the European market in the premium segment. The design of a modern transmission system, characterized by up to 10 speeds, is very complex and the transmission's exact topology depends strongly on it. For instance, Kahraman et al. [Kah04] describe a novel methodology for effectively designing gear trains and their connections to be used in automatic transmissions. They point out the difficulty to automatically eliminate solutions that are not feasible or possible to assemble. Indeed, the developer can choose between many degrees of freedom, that generate an almost infinite

number of possible design variants.

Generally, all modern automatic transmission systems are composed of the following elements [Fis15]:

- As a start-up element, the Trilok torque converter (TC) has been used since the first automatic transmission because of its high comfort and capability of increasing the torque at high speed difference between input and output shaft. In modern ATs, the TC can be bypassed by a lockup clutch operated in slip mode for vibration damping.
- The planetary gear sets, usually disposed in series, whose shafts are connected either to other shafts, to shifting elements or to the input or output shaft. Their transmission ratio is the key to a convenient gear ratio stepping.
- The shifting elements, which are mainly multiple-disc wet clutches and brakes. Modern automatic transmissions usually do not exceed 6 shifting elements.
- The hydraulic system, that enhances actuation of the shifting element
- The TCU (namely, Transmission Control Unit), which controls automatically the power-shifts by considering many factors in real time and translating them into an objective function (e.g. fuel saving, sporty driving).

Understanding of the kinematics of an automatic transmission is indispensable to determine torques and velocities that insist on each shifting element and will be described in detail in the following section.

2.1.1.1 Kinematic analysis

As every automatic transmission system has its own peculiar kinematics, the analysis will be performed on the example of the 9G-Tronic automatic transmission by Daimler, which is utilised as reference system and presented in more detail in Chapter 6. A schematic view of the transmission is shown in 6.1. Core elements of such a system are the planetary gear sets. Through engaging and disengaging clutches and brakes, the power flow is forced to follow precise paths, hence generating new overall transmission ratios. Planetary gearboxes are the transmission systems with the highest power density. A standard planetary gear set is generally composed of a sun (1), a ring gear (2), a number of planets (p) and their carrier (s). The first written documentation of a planetary gearbox is probably to attribute to Leonardo da Vinci [Sta07].

The kinematics of a single planetary gear set can be solved by defining the fixed carrier ratio

$$i_{12} = -\frac{z_p}{z_1} \cdot -\frac{z_2}{z_p} = \frac{z_2}{z_1} \tag{2.1}$$

and combining it with the Willis equation [Wil70]:

$$n_1 - i_{12} \cdot n_2 - (1 - i_{12}) \cdot n_s = 0 \tag{2.2}$$

The Kutzbachplan, developed by Kutzbach in 1927 [Kut27], enhances a graphical representation of the velocity vectors within the planetary gear set. For a detailed description of the method, refer to VDI guideline 2157 [VDI12].

In order to solve the kinematics of planetary gear set, Wolf [Wol58] introduces a symbolic method to graphically simplify a system of coupled planetary gear sets. The planetary gear set is represented as a circle, whereas the three degrees of freedom are represented as lines. In particular, the carrier shaft is represented as a line entering the gear set while sun and carrier stop at the circumference. Moreover, the shaft the total power is merged to or split from, i.e. the shaft with the highest power, is represented by two parallel lines. The method is described in detail in Klein [Kle62] and Müller [Mül98].

In his PhD Thesis, Stangl [Sta07] develops a novel system to determine speeds and torque of all shafts of an epicyclic-gearbox based transmission. For the calculation of the automatic transmission 9G-Tronic, a simplified version of this method is employed. Indeed, speed and torque are calculated using an efficiency of $\eta = 1$. While efficiency does not have any effect on the calculated speeds, torque at the shifting elements and at the output is higher than in reality. This has however a positive effect on the design of the CCDC, as it increases its safety factor. For each transmission, the fixed-carrier ratios of the planetary gear sets, a topology matrix and a shifting scheme have to be provided.

All transmission elements, i.e. planetary gear sets, shifting elements and shafts, are numbered. This way, an automated routine can compile the Jacobian matrix of the velocities. The latter has to have as many rows as the shafts in the system. In particular, it includes the Willis equations for every planetary gear set, the couplings between shafts and the actuated shifting elements for each transmission ratio. Eventually, the linear system can be solved and the velocities of all shafts found. All velocities are related to the input speed, which is set conventionally to 1. For instance, speed calculation of all shafts in the first speed is shown detailedly in Appendix A.1. For the solution procedure of torque on all shafts refer to [Sta07]. Through extensive simulation of the main automatic transmissions on the market, Brake C of Daimler's 9G-Tronic is set as reference for the design of CCDC, as it offers the main advantages in terms of kinematics and efficiency. The results in terms of speed and torque insisting on Brake C are represented in Figure 2.1. For a detailed analysis of Daimler's 9G-Tronic automatic transmission

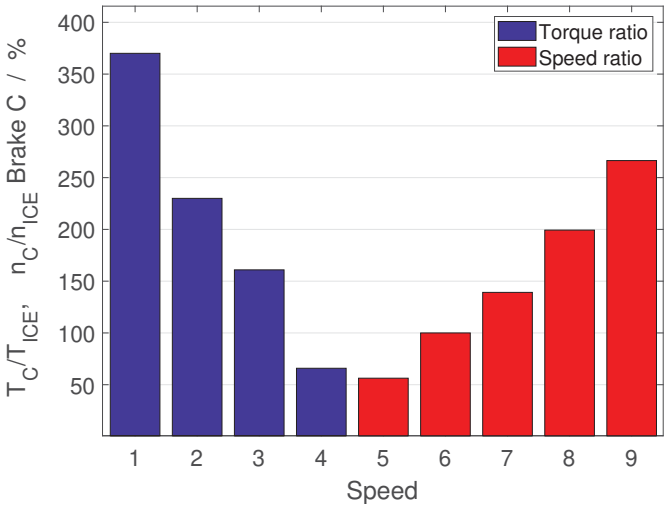

Figure 2.1: Speed and torque at clutch C (B06) of AT 9G-Tronic referenced to transmission input speed and torque, respectively [Ech17]

refer to Appendix A.1.

2.1.2 Hybrid and electric transmissions

The increasing pressure on automobile manufacturers to reduce their average fleet CO_2 emissions has led especially over the last decade to an enormous effort to develop efficient and cost-effective electrified vehicles. When united with a sustainable electric energy mix, these vehicles may dramatically contribute to lower emissions, at least locally. For instance, the latter can generally be divided in hybrid and fully electric vehicles. Hybrid vehicles can in turn be subdivided in categories basing on the position of the e-drivetrain, on the installed capacity and power, if the e-drivetrain is serially or parallelly installed with reference to to the internal combustion engine. Also, the partial recovery of braking energy can alone lead to a fuel consumption reduction of up to 10 % [Son19].

Even though transmissions of electrified and fully electric vehicles are nowadays generally characterized by a fixed transmission ratio, many efforts are being put in the development of multistage gearboxes. Consequently, a highly efficient and performant shifting element is needed to enhance the gearchanges.

2.1.2.1 Transmissions for electric vehicles

In [Fis17], Fischer et al. state that even though fully electric vehicles will have an increasingly dominant role in the future, mechanical transmissions will continue to be employed in drivetrains. A drivetrain composed of a combination of electric motor and transmission will lead to higher efficiency and reduced costs.

While generally no more than 3 speeds are needed for electric transmissions, a fixed ratio usually leads to a bigger electric motor in order to achieve same acceleration and maximum speed. In [Zhu15], Zhu et al. explain that in order to achieve comparable performance in electric vehicles with reference to ICE-driven vehicles, multispeed transmissions will be necessary for future BEVs.

Liebold et al. [Lie18] and Walker et al. [Wal15] identify the same opportunities in multispeed transmissions for electric vehicles. In particular, they state the overall efficiency of the drivetrain can be increased by effectively decoupling acceleration and maximum velocity and thus increasing the motor's efficiency. However, in their proposed solution for a multispeed transmission, they propose a multiple-disc clutch based DCT for powershift implementation. In fact, they pose very strict requirements in terms of acceptable longitudinal jolt ($\zeta < 5m/s^3$) and shifting time.

König states in [Kön12] and [Kön14] that a 2-speed transmission for electric vehicles with a dog clutch as shifting element could help reduce the energy consumption by up to 6 %, resulting in a sensible increase of the vehicle's range. In order to achieve acceptable shifting performance and comfort with a dog clutch, in his model he proposes a robust anti-jolt control for clutch

actuation.

In the Project Speed2E, Sedlmair et al. [Sed17] show the advantages of a multispeed transmission for electric vehicles in combination with a double-electric architecture. Efficiency and weight reduction are experimentally proven. They adopt an interlocking clutch ss shifting element and lay the foundation for the drivetrain developed within the project Speed4E.

The joint project speed4E bases on the same concept described in Speed2E, as explained by Mileti et al. [Mil18a, Mil19a]. Additionally, however, a focus is set on the shifting element, as it can enhance a noteworthy increase in efficiency. Indeed, an intelligent operating of the shifting strategy contributes to let the electric motors operate at an optimal regime [Sch19c]. Schöneberger et al. [Sch19b] state that in order to guarantee a comfortable and seamless shift with a mere dog clutch, a highly dynamic actuation and control of the system is necessary. In order to reduce inertia of the actuation system and improve its response time, they develop a linear actuator for the dog clutch combined with an angle-exact synchronisation for direct engagement.

Also Peng et al. underline in [Pen19] that the shifting schedule strategy in AMT for pure electric vehicles is of great significance and develop a shifting strategy based on fuzzy control of the actuator of the splined clutches. This way, they are able to show an increase in drivetrain's efficiency and comfort.

2.1.2.2 Transmissions for hybrid vehicles

Generally, hybrid vehicles can be subdivided in serial, parallel and mixed depending on the interaction between electric motor and internal combustion engine. The transmission of serial hybrid vehicles can be linked to the ones used for fully electric vehicles, as the driving torque is generated only by one or more electric motors. On the other hand, a parallel hybrid vehicle is driven both or separately by the internal combustion engine and one or more electric motors, being the driving torque added (refer, e.g., to Klement [Kle17])

Chopra underlines in [Cho14] that the development of efficient drivetrains is even more important when considering electrified vehicles. He thus develops a dog clutch coupled with an electromechanical actuation in order to substitute standard multiple-disc clutches for reducing drag losses of hybrid transmissions.

As often these hybrid solutions are employed for boosting and recuperation, a shifting element can possibly increase efficiency by decoupling the electric motor from the drivetrain when it is not needed. This holds especially for P3 and P4 hybrid drivetrains, as the torque to be delivered is generally higher, and thus either a high-torque electric motor or a transmission with a relatively high transmission ratio has to be employed. In [Cav19], Cavallino et al. present a P3/P4 hybrid 2-speed rear axle module. Being the module installed after conventional transmission in the traction power flow, its boost function is improved by the fact that the delivered torque is not proportional to ICE velocity, but to the vehicle's speed. Also in this case, gearshifts are taken

over by a dog clutch to reduce drag losses. To guarantee an optimal engagement, however, shifting control has to be highly precise and becomes rather complex to develop.

Smejkal and Wirth [Sme18] present an innovative transmission and show that the electric motor of a P2 hybrid configuration coupled with an AT can possibly lead to a partial replacement of standard shifting elements by more efficient dog clutches. This can be achieved by using the electric motor for speed synchronization, with however a great effort in controlling properly the powershift and still the need of three multiple disc clutches.

In [Vac18], Vacca et al. present an innovative HAMT (hybridised automated manual transmission) concept. The electric motor can here be disconnected from the drivetrain by using a coupled cone and dog clutch instead of a multiple-disc wet clutch, thus reducing coasting losses and increasing efficiency of the transmission by 5 % to 13 %.

Efficient and innovative shifting elements can also be employed in DHT (dedicated hybrid transmissions). The first DHT designated as such was introduced in the market by Toyota in 1997. Since its introduction, many OEMs and suppliers have developed own DHT concepts. A distribution of the yearly DHT sales in the USA starting from the year 1999, shown in Figure 2.2, shows how such technology has gained an important role over the both last decades.

In his article, Goppelt [Gop16] describes the AVL 7-Mode and the Chevrolet Voltec DHTs, both composed of planetary gearboxes and multiple-disc wet clutches, with the drawback of considerable drag losses. According to the topology of the dedicated hybrid transmissions, a substitution of such clutches with an interlocking clutch appears to be realisable without major changes or loss in performance. In fact, electric motors can support synchronisation and reduce necessary friction torque.

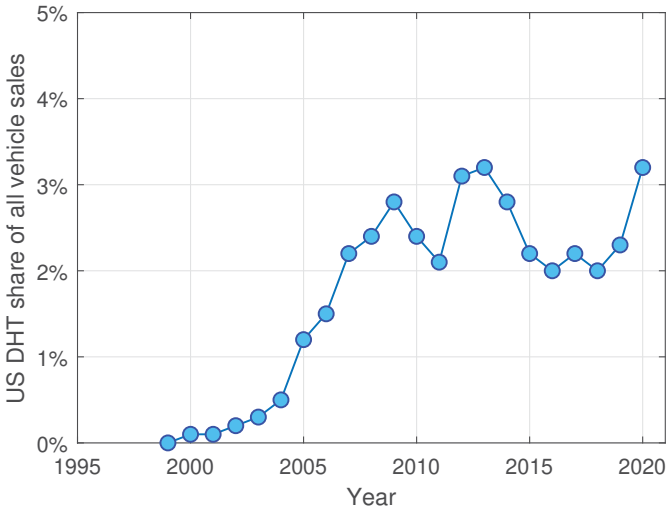

Figure 2.2: DHT sales share in the US market of all light vehicles in years between 1999 and 2020. Data from the US department of energy [Dav21]

Yang et al. present in [Yan19] dual mode power split hybrid module and analyse the shifting control under dynamic conditions. Here, the shifting elements of the transmission cannot be designed as mere dog clutches without compromising the powershift capabilities. Thus, interposing a friction element between electric motor and a dog clutch appears the only solution if an efficiency increase of the shifting unit is pursued.

Wishart et al. [Wis08] present a series of multi-regime hybrid drivetrains and analyse their ge-

ometry and control. They point out that a friction clutch is often present as a shifting element in planetary gearbox-based DHTs for seamless gearchanges or as a disconnect element. In particular, they analyse the designs by GM and their 2-mode hybrid transmission [Gre07] and the E-CVT design by Renault [Vil04]. Additionally, they analyse some E-CVT concepts by Timken and Silvatech, realised by controlling the torque of brakes, clutches and electric motors on the shafts of planetary gearboxes [Ai05, Dyc04]. Finally they show a multi-mode hybrid designed at the university of Michigan and presented in [Zha05], where the electric motor can be disconnected by a standard synchronizer. In all shown concepts, a substitution of pure friction clutches with positive clutches for efficiency increase is deemed at least challenging if powershifting capabilities are to be maintained.

Chen et al. [Che11] show the concept of an SPHEV (series-parallel hybrid electric vehicle) and analyses its transmission, composed of a combination of two planetary gearsets and four clutches. Despite the majority of the transmission losses is mainly derived by the introduction of friction elements, an efficiency increase of up to 5.62 % in the NEDC can be achieved. Gupta [Gup15] presents a similar concept of a DHT, composed of two planetary gearsets in the Simpson configuration and four electromagnetic clutches. The latter have however to be continuously actuated in order to generate the required friction torque.

Also disengaging the electric motor from its transmission while coasting could lead to reduced drag loss and thus increased efficiency. Camilleri [Cam13] proves experimentally that disengaging the transmission while coasting can lead to a reduction of coast losses by up to 35%. This especially holds for permanent-magnet electric motor based hybrid and fully electric drivetrains [Zir17].

From the proposed examples, it is clear that especially hybrid transmissions are characterised by a number of shifting elements. Due to powershifting requirements, such shifting elements are generally designed as mere friction clutches. The latter do, however, generate a consistent amount of drag losses (see Section 2.3), which reduce overall efficiency of the transmission. Further, especially in DHTs, electric motors can partly support mass synchronisation, which further reduces the need of friction clutches.

2.2 Shifting elements

Multispeed transmissions allow the internal combustion engine to better adapt to the torque requirements at the wheels and, generally, to the traction force hyperbola [Bre08]. Selecting a different transmission ratio, however, is always connected to a change in rotational speed of definite shafts and flywheels within the transmission itself. Speed synchronisation of these components, that can be generally simplified to just one flywheel with a reduced inertia, and the subsequent transmission of torque in the steady state is taken over by shifting elements.

Depending on the transmission type, requirements to the shifting elements change considerably.

Indeed, in MTs, the motor can be decoupled with the dry clutch, making it possible to use compact synchronizers for the gearshift itself. Also in DCTs, synchronizers are used for speed selection, while a generally-wet dual clutch replaces the dry clutch, enhancing powershifts. In ATs, speed synchronisation and torque transmission is taken over by multiple-disc wet clutches, guaranteeing high comfort and controllability of the powershifts [Nau07]. In the following section, shifting elements which can be found in the most common automotive applications will be shortly presented and described.

2.2.1 Multiple-disc wet clutches

Multiple-disc wet clutches are frictional shifting elements used i.a. in automotive transmissions to connect and disconnect two shafts. Like all frictional shifting elements, they are capable of transferring but not transforming torque [Mas14]. A multiple-disc wet clutch is generally composed of a number of lamellae, which are connected to their inner and outer carrier, respectively. Lamellae are connected to their carriers via form-fit, are however free to move axially. [Fre14]

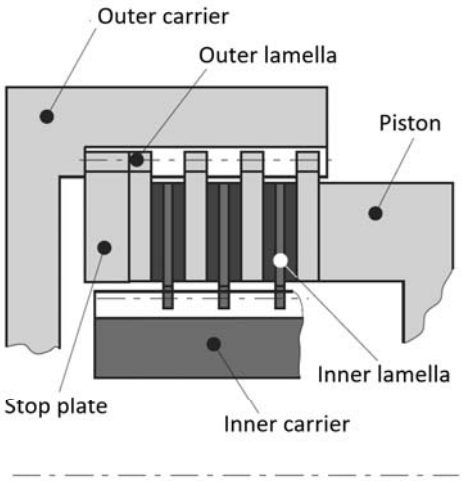

Figure 2.3: Schematic representation of an engaged multiple-disc wet clutch based on [Str17]

A schematic representation of a multiple-disc wet clutch is exemplarily shown in Figure 2.3. When the clutch is disengaged, the lamellae of a multiple-disc wet clutch are separated by a gap, through which lubricant can flow. To engage the clutch, an axial force is applied to the piston and a frictional force is generated on the contact surfaces [Hen14, Str17]. The friction force generates in turn a friction torque, as expressed in Equation 2.3.

$$T_f(t) = F_a(t) \cdot \mu \cdot z_f \cdot r_m \tag{2.3}$$

$T_f(t)$	Nm	Friction torque	$F_a(t)$	N	Axial force
μ	-	Coefficient of friction	z_f	-	Number of friction surfaces
r_m	m	Mean friction radius	–		

The mean friction radius is calculated as:

$$r_m = \frac{2(r_o^3 - r_i^3)}{3(r_o^2 - r_i^2)} \tag{2.4}$$

r_i	m	Inner friction radius	r_o	m	Outer friction radius

The specific friction power transmitted during synchronisation of a multiple-disc clutch is thus determined as:

$$\dot{q}(t) = \frac{T_f(t) \cdot \Delta\omega(t)}{A_f} \tag{2.5}$$

$\dot{q}(t)$	W/m^2	Specific friction power at instant t	$\Delta\omega(t)$	rad/s	Speed difference at instant t
A_f	m^2	Friction surface	–		

Finally, the specific friction loss can be calculated as follows:

$$q = \int_0^{t_r} \dot{q}(t)dt = \int_0^{t_s} \frac{T_f \cdot \Delta\omega(t)}{A_f} dt \tag{2.6}$$

q	J/m^2	Specific friction loss	t_s	s	Sliding time

These equations can be found i.a. also in Strebel and Winkelmann and Harmuth [Str17, Win85].

Multiple-disc wet clutches can be employed either as powershifting elements, as they enhance a seamless shifting without traction interruption (e.g. in ATs and DCTs) [Mas14], or in permanent slip operation (e.g. in differentials or as torque converter lockup clutches) [Abu].

As a complex friction system, the coefficient of friction and its stability are strongly dependent on a number of factors. Layher [Lay11] and Stockinger et al. [Sto18] describe in detail the effects of i.a. lubricant, friction material pairing, geometry, porosity and dimensions on the friction behaviour of multiple-disc wet clutches. In particular, the effect of lubricant - i.e. its chemical composition, its additives, viscosity and state of ageing - are of high relevance. [Ash93]. Also the choice of the friction lining as a part of the friction material pairing has a major impact on the friction behaviour of the clutch. Considerable efforts are being put into developing highly performant friction materials that can comply with the growing requirements of modern transmissions in terms of thermomechanical stability and torque capacity (refer to Merkel [Mer19]).

Also static friction stability is an important factor for clutch performance assessment. Meingaßner describes in [Mei17] the friction behaviour of multiple-disc wet clutches under slow speed and micro-slip conditions, extensively analysing and investigating the tribological system under said conditions. In his work, he identifies complex connections in the friction system in the interface area between static and dynamic friction.

2.2.2 Positive (interlocking) clutches

Positive (a.k.a. dog) clutches are shifting elements that transfer torque between two shafts via form-fit, that is, interference. Unlike friction clutches, the contact surface between both clutch bodies is generally normal to the force to be transmitted [Toc68].

Habermeier [Hab96] splits mechanically actuated positive clutches into dog clutches and splined clutches. Standard claw clutches are the most common dog clutches used in automotive trans-

missions and drivelines generally. However, the Hildebrandt clutch, where the claws are on a sliding sleeve, and the Maybach clutch, which can only engage under defined speed differences of the shafts, are listed as noteworthy in modern drivelines. Also splined clutches are widely diffused in modern transmissions, exemplarily as part of synchronizers. They are the most compact clutches in radial direction for what concerns torque transferability. [Ben72, Hab96].

As no friction torque can be generated, positive clutches are not capable of synchronizing speeds of the according flywheels. Hence, if a synchronization is required, other components must be present to perform this task. Though an interlocking clutch is only shiftable under limited speed differences, it can be disengaged under load torque. However, this results in poor shifting comfort, as sensible jolt is generated when load torque is completely converted into acceleration [Die05]. When an interlocking clutch is present in a powershiftable transmission system, the shifting process during engagement and disengagement is most likely handled by the transmission control unit (TCU). In such a case, shifting comfort, while being a function of the controller's quality, is however also strongly dependent on the topology of the positive clutch itself, as is confirmed by Kuncz [Kun17].

In [Poi19], Pointner et al. identify the tooth gap, the number of teeth, their geometry - i.a. in terms of tooth-tip shape, positive/negative backlash and edge roundness - as the main parameters influencing the shifting quality of dog clutches.

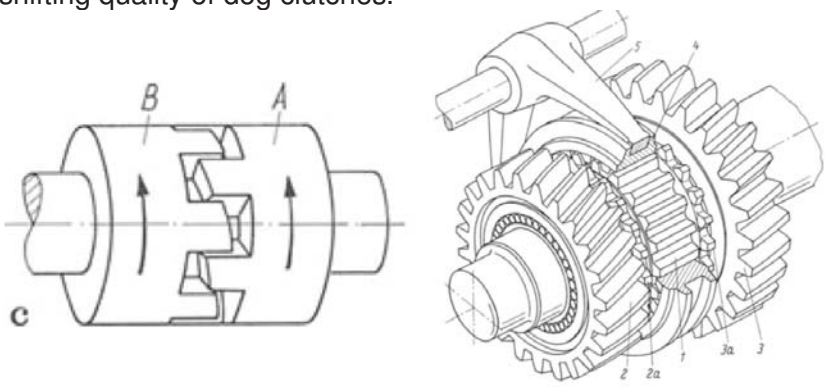

Figure 2.4: Schematic representation of a Maybach dog clutch (left) and of a splined clutch (right) [Hab96]

2.2.3 Synchronizers

Synchronizers are shifting elements employed in modern manual, automated manual and dual clutch transmissions (MT, AMT and DCT, respectively). Their main task is to enhance smooth gearshifts by matching the speed of the input shaft and all its connected masses to the velocity of the gear to be selected (idler gear). While the synchronization process is carried out by a friction cone clutch, the torque is transmitted through a positive (splined) clutch [Soc68]. To increase performance and torque capabilities of the cone clutch, synchronizers can be implemented with two or three friction surfaces [Sta14].

Amongst others, Stahl et al. [Sta14], M'Ewen [MEw49] and Mastinu et al. [Mas06] divide the

synchronization process for a BorgWarner type synchronizer generally into three main phases. For a more detailed description of the process, refer to the aforementioned literature.

- Pre-synchro phase: The sliding sleeve is moved from neutral position towards the gear to engage. The struts, located in grooves in the synchronizer hub, are pulled towards the blocker ring, generating a relatively small axial force. The latter generates, in turn, a friction torque and hence a rotation of the blocker ring, disposing it in the final blocking position.
- Synchronization phase: The full axial force is transmitted to the blocker ring through the blocker teeth, generating the synchronizing friction torque. As long as a friction torque persists on the blocker ring, no unlocking is possible (in correct working conditions).
- Shifting-through: Once masses are synchronized, the friction torque drops and the locking condition is no longer satisfied. The sleeve slips past the blocker ring and the splined clutch can engage.

During the synchronization phase, the locking condition is to be always met in order to avoid premature shifting through and, consequently, clashing. Essentially, the blocking release torque (or indexing torque), which would lead to a relative rotation of the blocker ring, shall not be greater than the friction torque. The locking condition can be rearranged as expressed in Equation 2.7.

$$\frac{\mu}{sin(\alpha)} \geq \frac{r_I}{r_m} \cdot \frac{cos(\beta) - \mu_Z sin(\beta)}{sin(\beta) + \mu_Z cos(\beta)} \tag{2.7}$$

μ	-	CoF of conical friction surface	α	rad	Cone angle of cone clutch
r_I	m	Indexing radius	r_m	m	Cone clutch mean firction radius
μ_Z	-	CoF of blocking teeth	β	rad	Half-angle of blocker teeth

The friction torque for a cone clutch is generally determined as:

$$T_f = \frac{F_a \cdot \mu \cdot z_f \cdot r_m}{sin(\alpha)} \tag{2.8}$$

Both specific friction loss and power can be calculated according to Equations 2.5 and 2.6.

During the shifting-through phase most of the comfort-relevant issues are originated. In [Pin92], Pinnekamp gives a detailed overview of typical phenomena that lead to a diminution of shifting comfort. Especially upshift scratching is analysed, which originates from drag torque in the transmission during the shifting-trough phase. Indeed, no friction torque can be transmitted during this phase, which makes the development of speed differences possible. Consequently, BorgWarner type synchronizers are not capable of performing powershifts.

2.3 Drag losses

In [Klu99], Kluger et al. analyse the efficiency of various automotive transmissions and point out that drag torque of disengaged clutches causes a major share of losses in automatic transmissions (see Figure 2.5).

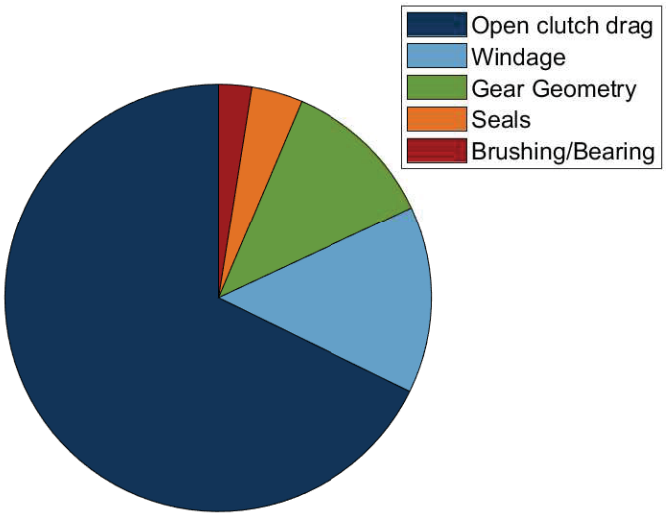

Figure 2.5: Breakdown of losses in an automatic transmission based on [Klu99]

Lubricant flowing through disengaged multiple-disc wet clutches and synchronizers generally generates drag torque. When two friction surfaces are located close enough and the lubricant supply at their inner diameter is sufficient, whilst said surfaces have a speed difference, viscous shear stresses in the fluid generate a torque on both surfaces. While Strebel et al. [Str14] describe drag torque of synchronizers in manual and dual clutch transmissions and put in evidence that the oil flow rate has the major effect on losses, the majority of research on drag losses concentrates on multiple-disc wet clutches. Indeed, drag torque strongly depends on the amount and extension of friction surfaces.

As is confirmed by Dräxl [Drä16] et al. and Kitabayashi et al. [Kit03], drag torque behaviour that occurs between disengaged friction surfaces related to the speed difference can be divided into three regions. Generally drag torque follows the law of viscosity at low speed range, as the gap between friction surfaces is completely filled with lubricant. With increasing speed difference, the centrifugal pumping effect of the plates overcomes the oil supply, so that air is sucked within the gap. The average viscosity of the oil-air mixture drops and so do drag losses. Drag torque stabilises on a plateau until sufficiently high speed differences are reached to cause mechanical instability, which denotes the third region. Mechanical instability is not of interest in this work, as it occurs at speed differences generally well above working limits.

For the first region, Kitabayashi et al. [Kit03], assuming fully laminar flow of the lubricant, develop a simplified analytical model describing the drag torque:

$$T_D = z_f \cdot r_m \cdot \eta_L \cdot \pi \cdot \frac{(r_o^2 - r_i^2) \cdot \omega \cdot r_m^2}{h} \tag{2.9}$$

T_D	Nm	Drag torque	z_f	-	No. of friction surfaces
r_m	m	Average (effective) radius	η_L	Pas	Dynamic viscosity of lubricant
r_o	m	Outer radius	r_i	m	Inner radius
ω	rad/s	Angular velocity	h	m	Clearance between surfaces

This formula shows a very good correlation with experimental results, is however validated up

to speed differences of 800 rpm only.

Leighton et al. develop in [Lei19] an experimentally validated numerical study of drag losses in wet brake packs, considering different temperatures. They attribute the drag torque breakdown at operating conditions with growing speed to cavitation onset. Due to cavitation, a coherent film of the lubricant between disengaged friction surfaces cannot be maintained.

In [Mor19], Morris et al. provide an analytical model, which is validated with extensive experimental results and takes grooves into account. They assume the Couette flow in tangential direction to generate the parasitic drag losses between the inner radius of the friction plates and the free boundary. Neglecting shear from any Poiseuille tangential flow, the Couette-flow-caused shear generates a drag torque of:

$$T_D = \omega \cdot \eta \cdot \left(\frac{\pi}{2h_p}(r_o^4 - r_i^4) + \frac{n_g \cdot w_g \cdot (r_o^3 - r_i^3) \cdot (h_p - h_g)}{3h_p \cdot h_g} \right) \tag{2.10}$$

w_g	m	Disc groove width	n_g	-	Number of disc grooves
h_p	m	Groove axial separation	h_g	m	Pad axial separation

Aphale et al. [Aph06] define an analytical model basing on an asymptotic analysis of the Navier-Stokes equations. Here, steady state and axisymmetric flow distribution between plates are assumed, so that all derivative with respect to time and angle equal zero. They additionally simulate the pressure distribution through a CFD analysis utilizing the software Fluent and perform corresponding experiments on a test-rig. A very good accordance is found between analytical, simulated and experimental results.

Basing on these results, Aphale et al. [Aph10] develop a two-dimensional, multiphase-flow CFD model. This way, also the torque breakdown can be modelled appropriately, taking into account air entering the clearance.

Neupert and Bartel [Neu19] and Grötsch et al. [Grö20] propose similar CFD models to calculate drag torque in multiple-disc wet clutch sets, including multiphase simulation of the lubricant - and thus torque breakdown - and cavitation. Both achieve excellent accordance between simulative and experimental results. They point out that the simulation of drag losses, while being relatively time-consuming, can however possibly reduce experimental expenses. Through their research, they are able to demonstrate that drag losses represent a major share of the overall losses of powershifting transmissions, even after a clutch design optimisation is performed.

2.4 Alternative shifting elements for automotive transmissions

In this section, state-of-the-art alternative shifting elements for automotive transmissions are presented. A particular focus is set onto powershiftable transmissions. As a result of a thorough literature and patent search, the lack of a compact, effective and drag-loss-saving shifting element for powershiftable transmissions is identified. Being a suitable gap-filler, the CCDC

(acronym for Coupled Cone and Dog Clutch) is presented as part of the current research. In particular, the motivation and the design process that led to the second variant of the shifting element are shown.

2.4.1 Introduction and motivation

As can be appreciated in Figure 2.5, drag losses generated by disengaged shifting elements in automatic transmissions are responsible for a considerable share of efficiency decrease. Especially modern automatic transmissions are affected by drag losses, as a growing number of speeds requires at least two to three disengaged multiple-disc wet clutches. Minimising said losses can hence lead to a noteworthy increase in efficiency and, consequently, reduction of vehicle CO_2 emissions.

One of the simplest ways to reduce drag torque of a shifting element is to reduce its overall friction surface. Back et al. [Bac16] describe how efforts are made in automatic transmission design to reduce parasitic losses of engaged and disengaged shifting elements, including minimising the number of open clutches and support disc opening through elastic elements. They show the advantages of combining friction-fit and form-fit and how this can help to drastically reduce drag torque and at the same time allows high torque transfer with limited actuation force.

State of the art patents by ZF, GM and Scania confirm, for instance, how many development efforts are made especially to replace multiple-disc with cone clutches. Boss et al. (ZF) [Bos11] develop and patent a cone clutch system for automatic transmissions capable of performing powershifts. Samie et al. (GM) [Sam12] patent a shifting element for electro-mechanical transmissions consisting of a mere cone clutch. Both these systems transmit load torque via friction fit. Slapak [Sla14] substitutes a multiple-disc wet clutch with a synchronizer as shifting element for the ring gear of a planetary gearbox, in order to reduce drag losses.

Merkel [Mer19] describes a novel shifting element that decouples the function of synchronization and static torque transmission. Since torque required for synchronization is lower than the static one, the friction surfaces of the multiple-disc clutch of the High Torque Low Drag (short, HTLD) system can be reduced. The transmission of static torque is taken over by a dog clutch after synchronisation is completed. Yet, at least four drag loss generating friction surfaces are present in the final design of HTLD.

Zabala [Zab13] describes an innovative transmission system composed of a cone and a dog clutch actuated sequentially with different and independent actuators. Powershifts are performed by actuating a cone clutch. Once the synchronization process has terminated, a second actuator, which is connected to the same shaft of the first one, engages a positive-fit clutch.

Gaertner and Ebenhoch [Gae13] present the new 9-speed automatic transmission by ZF. Here, two multiple disc clutches are substituted by dog clutches without any friction elements. The lack of synchronizing capability is taken over by the engine and an intelligent operation of the

remaining friction clutches. A slight diminution of shifting comfort together with an in increase of shifting time is however to be expected in this case.

Shiotsu et al. [Shi19] analyse the performance of a novel shifting element that replaces a multiple-disc brake in an automatic transmission. A sole dog clutch with a one-way mechanism can be utilised thanks to the topology of the analysed transmission. Helix splines use the torque acting on the dog clutch to keep it engaged. A piston is still present to overcome regions of little or reverse torque. The drag losses of the clutch could be reduced by up to 60 %, while the necessary actuator force could be halved.

Tonius et al. [Ton15] develop a dog clutch as an innovative shifting element to be implemented in automatic transmissions. They point out that generally shifting elements that enegage in a downshift are suitable to be implemented as positive fit clutches. This is possible because the synchronisation process can be taken over and/or supported by another friction clutch. They show that by substituting a multiple-disc wet clutch with a dog clutch, a drag torque reduction of up to 10 % can be achieved. They further analyse different possible geometries and eventually propose an optimised dog clutch concept, characterised by rotationally elastic teeth on one dog ring. This way, a considerable reduction of jerks can be achieved.

Echtler et al. present the CCDC in [Ech17]. They show through extensive measurements that considerable reductions in parasitic losses, and especially drag losses, are possible when combining friction and form-fit in an new shifting element. Through the reduction of friction surfaces by employing a cone clutch, the measured reduction of drag torque is noteworthy. Indeed, for typical revving regimes of ICE-driven passenger vehicles, they compare drag torque of a reference multiple-disc design and of CCDC. They evaluate the efficiency increase under varying conditions and show experimental values of up to 90 %. These values correspond to 2.5 g_{CO_2}/km in the WLTP.

2.4.2 Working principle

The main idea behind the CCDC is to decouple the functions of speed synchronisation and static torque transmission, which in ATs are both taken over by multiple-disc clutches. A torque transmission interruption during the so-called free-flight phase (i.e. during shifting through, refer to Section 2.2.3) is not permissible. Accordingly, the friction torque needed for synchronisation is delivered by a cone clutch. The latter, characterised by an angle α, is capable of considerably increasing the normal contact pressure (see Equation 2.8), equalling friction torque of standard multiple-disc clutches. After synchronisation is successfully completed, the dog clutch engages, providing extreme torque-transferring capabilities through form-fit, independently of axial force. The engagement process can be subdivided in 4 main phases, which are described in the following and can be appreciated in Figure 2.6.

- Neutral position (1): The shifting element is completely disengaged, defined positions and

clearance are provided by release springs. Oil flowing between the friction surfaces of the cone clutch generates moderate drag torque.

- Pre-synchronisation (2): In this phase, as the shifting has to begin, the valve controlled by the TCU opens and the chamber behind the piston starts to fill with hydraulic oil.
- Synchronisation (3): The hydraulic oil pressure is increased to the value required for synchronisation and friction torque is generated at the cone clutch. Oil pressure is modulated by the TCU, in order to generate a friction torque sufficient to equal the sum of load torque from ICE and a dynamic component resulting from reduced inertia and required deceleration. During this phase the piston cannot move, as the reset-spring is mounted with a definite preload, which is higher than the actuator force.
- Shifting-through (4): As soon as the inner carrier is synchronous with the outer carrier, axial force at the piston is increased, exceeding the spring preload. The axially-movable body of the dog clutch can now travel and eventually engage to generate form-fit.

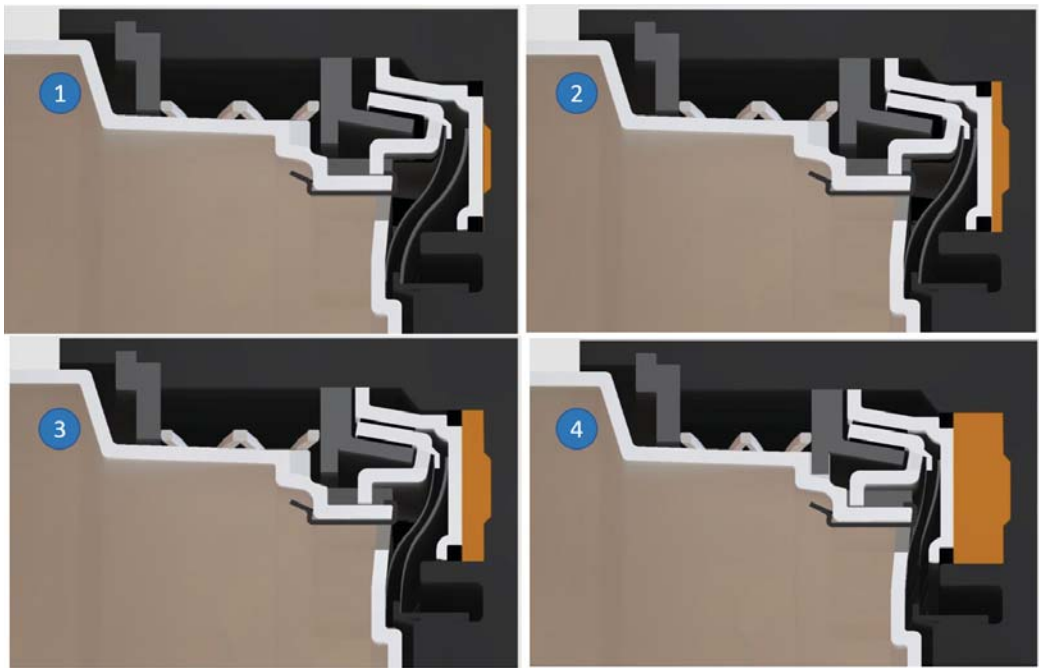

Figure 2.6: Representation of the phases of a gearshift with CCDC based on [Bac16]: (1) neutral position, (2) pre-synchronisation, (3) synchronisation, (4) shifting-through

2.4.3 Design CCDC 1

The first design of CCDC is developed to match the capabilities of existing multiple-disc wet clutches. A cross section is represented in Figure A.4 in the Appendix. It is characterised by a cone clutch with two friction surfaces and a dog clutch connected serially. The inner and outer steel cones are connected to the outer carrier, while the intermediate cone is rotationally connected to the inner carrier. Two carbon friction linings of the type HC310 are glued on both sides of the intermediate cone. The dog clutch is composed of an axially movable body, rotationally

connected to the housing, and a fixed body, connected to the inner carrier. Six dog clutch geometries are designed (V1 to V6), manufactured and tested (V1 to V5). An overview of the most important characteristics of the CCDC in its first design can be found in Table 2.1.

Cone Clutch						
Outer mean friction diameter					mm	176.7
Inner mean friction diameter					mm	169.7
Friction surface width					mm	10.5
Cone angle					°	10.0
Prestress wave spring					N	3500
Metal sheet thickness of cones					mm	2.0
Friction Lining					Carbon, HC310	
Dog clutch						
Mean tooth diameter					mm	166.0
Tooth radial height					mm	5.0
Toot axial length					mm	2.5
Tooth geometry	**V1**	**V2**	**V3**	**V4**	**V5**	**V6**
No. of teeth	18	36	36	36	36	36
Angular backlash (fully engaged)	12°	1°	2°	1°	0°	0°
Tooth circumf. angle	4°	5°	4°	5°	5.4°	5.4°
Tooth flank angle	0°	0°	0°	0°	14°	14°
Tooth tip shape	flat	flat	flat	convex	convex	flat

Table 2.1: Main characteristics of CCDC in its first design variant

2.4.4 Design CCDC 2

Based on the knowledge gained with extensive testing and simulating of CCDC, an improved design is developed by HOERBIGER Antriebstechnik Holding GmbH. Thermomechanical stability of CCDC could be improved, while an optimised dog clutch geometry is designed. According to powershift simulations performed with a coupled transmission-vehicle 1D model, it can be shown that even in the worst-case scenario, one friction surface is sufficient to generate enough torque to perform the powershift. Demfle et al. [Dem19] show that in this improved variant the CCDC, while further increasing its efficiency, does not show any peculiar aggravation in thermomechanical properties or higher discomfort when compared to the reference multiple-disc clutch.

A cross section of the second design can be appreciated in Figure A.5 in the Appendix.

With reference to the first design variant, positions of dog and cone clutch are switched in axial direction. Hence, the dog clutch is the first element in the force flow, reducing the axial force necessary for form fit generation. The dog clutch geometry is improved and integrated in the

inner carrier. Dog teeth are designed axially staggered to improve engagement behaviour and virtually increase axial wear gap in disengaged position. Friction surfaces of the cone clutch are reduced to one, while its wall thickness is increased by 50 %, to improve thermomechanical stability. The wave spring is substituted with a disc spring pack and positioned between dog and cone clutch. The spring characteristic (see Figure 4.6) allows to reach the desired prestress during synchronisation and, to reduce the necessary axial force during dog clutch engagement, as the force-displacement curve flattens with increasing spring compression. The most important characteristics of CCDC variant 2 are listed in Table 2.2.

Cone Clutch		
Mean friction diameter	mm	163.0
Friction surface width	mm	8.0
Cone angle	°	10.0
Prestress disc spring pack	N	1900
Metal sheet thickness of cones	mm	3.0
Friction Lining		Carbon, HC310
Dog clutch		
Mean tooth diameter	mm	140.6
Tooth radial height	mm	7
Toot axial length	mm	3.0
No. of theeth		40
Angular backlash (fully engaged)	°	1.4
Tooth circumf. angle	°	6.1
Tooth flank angle	°	0
Tooth tip shape		flat

Table 2.2: Main characteristics of CCDC in its second design variant

2.5 Applied methods for performance evaluation of clutches

As discussed above, the design of CCDC is a combination of friction and form fit. As the actuation of the shifting element consists of these two independent phases, they will be considered separately in the following. Beside long term damages, Acuner et al. [Acu16], Meingaßner et al. [Mei17], Schneider et al. [Sch19a] and Takezaki and Kubota [Tak92] confirm, amongst others, that the key factor determining performance for friction clutches is the maximum temperature reachable on the friction surface during synchronisation. This holds both for multiple-disc and cone clutches, being heat directly dependent on the friction loss of the shifting process. Since the CCDC is designed to be integrated in automatic transmissions, where gearshifts are performed without torque interruption and hence increased friction power, its thermomechanical stability is of primary importance. Long-term friction stability of CCDC's friction clutch has been extensively tested, yet results will not be presented in this work. For detailed results refer to

Mileti et al. [Mil18b]. On the other hand, a dog clutch introduces a novel dynamic component to the engagement, due to its dichotomic state - i.e. either engaged or disengaged. Independently of load conditions and dog geometry, the form-fit generation has to be always carried out correctly. In order to assess engagement performance of the designed dog clutch, its dynamic behaviour is to be methodically analysed. In the present section, state of the art methods for evaluation and assessment of thermomechanical stability of friction clutches and dynamic engagement behaviour of interlocking clutches are presented and discussed.

2.5.1 Thermomechanical stability of friction clutches

As the name suggests, thermomechanical damaging of friction clutches relates to a deterioration triggered by temperature which turns into a mechanical failure of a component. this phenomenon is referred to as spontaneous damaging. Spontaneous damages of friction clutches are usually linked to a short-term deterioration of the friction surface due to too high temperature.

According to Strebel et al. [Str17], spontaneous damages of clutches can be further divided, depending on the friction pairing. They essentially identify *hotspots* when the friction pairing is organic vs. steel. On the other hand, metal vs. steel friction pairings tend to show adhesive wear / scuffing (also refer to [Dum77]). As carbon counts to the organic friction linings, only hotspots will be considered as relevant damaging mechanism in the following. Generally, hotspots are discolourings on one or both friction surfaces, which usually occur when a friction clutch is operated beyond its thermomechanical stability region. Hotspots can lead to a rapid deterioration of both friction and dynamic (NVH issues) behaviour of the clutch. Further, mechanical strength of the clutch may be affected too. Indeed, according to Rossmanith et al. [Ros06], thermomechanical induced fatigue cracks can occur due to high temperature gradients and propagate rapidly on the friction surface.

In literature, many hotspot classifications can be found.

Strebel [Str17], Graf and Ostermayer [Gra12], Mann et al. [Man21] and Panier et al. [Pan04] discern between hotspots and hot bands. Albeit designations are often used indistinctly in literature, hot bands refer to a nonhomogeneous temperature distribution with respect to the radial direction. In fact, hot bands are recognisable as one (or more) ring occurring on a circumference with a definite radius. On the contrary, hotspots occur due to a highly distorted temperature field in circumferential direction. In particular, hotspots are the maxima of the temperature field and can be easily identified as single dark discolourings.

Anderson and Knapp [And90] propose a hotspot classification and categorisation basing their studies on automotive brakes. In particular they distinguish between critical and non-critical (cosmetic) hotspots. Critical hotspots are characterised by plastic deformation, cracks on the surface and residual martensite. Based on the latter fact, they state a temperature of at least 750 ^{o}C is necessary for critical hotspot development. Conversely, cosmetic hotspots only reach

temperatures of about 300 °C. They additionally identify focal hotspots as typical for automotive systems.

Similar to the work of Anderson and Knapp [And90], Panier et al. [Pan04] identify five classes of hotspots, based on width, temperature and time. Asperity induced hotspots are caused by friction at high pressure for a very limited amount of time and comprehend very limited areas on the friction surface (Fig. 2.7a). Gradients on hot bands are hotspots appearing on one or more circumferences on the friction surface (Fig. 2.7b). Hot bands (Fig. 2.7c) are macroscopic yet reduced areas of the total friction surface. Macroscopic hotspots (Fig 2.7d) are large discolorings on the surface associated with a buckling pattern of the disc. Regional hotspots (Fig 2.7e) originate from non uniform cooling of the surface. Gradients on hot bands are among the most damaging hotspots and are of particular interest for CCDC.

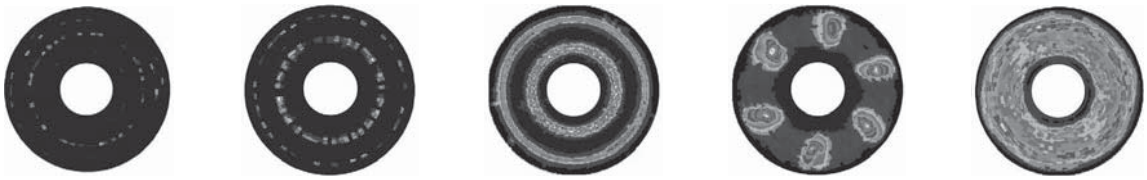

(a) Asperities **(b)** Gradients on hot bands **(c)** Hot bands **(d)** Macroscopic hotspots **(e)** Regional hotspots

Figure 2.7: Hotspot classification according to Panier et al. [Pan04]

Mann et al. [Man21] perform a thermomechanical characterisation of hotspots and hot bands in brakes for high-speed trains. As braking times are much longer than automotive applications and dimensions allow, they experimentally individuate and analyse formation and evolution of hotspots and hot bands through infrared thermography. They identify hotspots over the whole circumference of the friction surface. Hotspots, however, also concentrate radially on two hot bands, characterised by different diameters. After having identified the formation process of focal hotspots, they build a 3D finite element simulation model and optimise the brake geometry.

Fairbank et al. [Fai01] distinguish between cosmetic and severe hotspots, leaning on the classification by Anderson and Knapp [And90]. Cosmetic hotspots manifest themselves as black stains on the steel surface, yet they do not affect performance of the clutch. Severe hotspots are characterised by sort of smearing of the metal in the concerned region, which can be ascribed to plastic yielding of the material. The effect of plastic deformation is also clearly recognisable in the measured signals, as it causes an evident friction torque disruption in a relatively early phase of synchronisation.

A similar hotspot classification can be found in Hirano et al. [Hir07], who also divide hotspots into cosmetic and severe, the first being mere discolourings on the friction surface, the seconds being caused by plastic deformation of steel. Accordingly, they attribute cosmetic hotspots to thermoelastic deformation, while thermoplastic deformation is claimed to be the generation mechanism for severe hotspots. They state that thermoplastic instabilities involve temperatures at the steel friction surface higher than 900 °C, as residual martensite is generally detected by

microscopy.

Beside the aforementioned research on hotspots, for instance also Jang et al. [Jan02] and Krempatzky et al. [Kre08] agree on the hotspot generation mechanism being thermoelastic instability (TEI). A categorisation of the phenomenon is first described by Barber in 1967 [Bar67]. Barber starts his studies indeed with analysing hotspots. Here, he attributes hotspot generation to a thermal distortion of the friction surface. He however indicates that description of the heat generation phenomenon is uncertain. In [Bar69] he eventually introduces the concept of thermoelastic instability. Due to roughness-induced higher pressures on certain regions of the friction surface, friction power is locally increased, accordingly. The thermal expansion of one friction partner causes the local pressure to once again increase even further. TEI represents hence a self-reinforcing instability which increases continuously, unless it is externally damped (e.g. through wear). According to Barber, TEI is mainly a function of sliding velocity and contact pressure. It can be partly avoided by choosing different and more suitable friction partners characterised by smaller thermal expansion coefficients or a ratio between thermal conductivities closer to 1.

A few years later, Dow and Burton [Dow72] postulate that, as TEI is to be considered an unstable physical process, there must be a threshold that triggers the phenomenon. For their analysis they base on a simple setup composed of a blade sliding on a semi-infinite rigid body in absence of wear. Their analytical approximation, which describes a time-dependent evolution of the temperature field on the friction surface, is used to identify such threshold. Burton et al. [Bur73] further develop the analytical model focusing on seal-like contacts. For their analysis, they consider two thin tubes contacting at each end and rubbing under definite conditions in absence of wear. They model the excitation of the system by considering roughness wave length and sliding velocity and derive the threshold for TEI insurgence. Of particular interest is the analytical solution for two limit cases, i.e. when the friction partners are equal or when one friction partner acts as a perfect insulator. Furthermore, they show how the latter case approximates very well the situation where one friction partner is a poor conductor, as is the case with organic friction linings. In [Dow73], Dow and Burton expand their original pin-on-disc model and add the effect of wear, whose main effect is to damp thermoelastic instability. In fact, worn particles present on the friction surface absorb heat and enhance its dissipation. As wear is generally undesired, in [Dow78] they propose design modifications to reduce or avoid insurgence of TEI, such as specific coatings or sacrificial parts. Wear generated by the latter shall damp TEI while protecting the friction partners at the same time.

Lebeck [Leb76] states TEI is triggered both by point of operation (i.e. contact pressure and sliding velocity) and waviness of friction surfaces. Based on the stability theory by Timoshenko (refer to [Tim61]), he develops an analytical model for TEI description, similar to the one by Dow and Burton [Dow72]. The model is able to discriminate between stable and unstable operation depending on a critical velocity.

Lee and Barber [Lee93] further elaborate the equations proposed by Barber. They however move from an ideal, semi-infinite geometry to automotive disc brakes. In fact, geometry is one of the most important factors to consider when analysing hotspots. Especially clutches and brakes are usually disc-shaped, their thickness being usually the order of some millimetres. Analogously to what done in [Bar69], they trigger the instability through a distorted temperature field moving over the still standing surface. They sum disturbances deriving from both symmetric and antisymmetric components by effect superimposition. If thermomechanical instability occurs, the exponentially growing term will dominate all other effects. They too identify where thermomechanical behaviour is stable or unstable. The regions are delimited by a critical velocity, which in turn depends also on asperity frequency. Their experiments are however carried out with constant axial force, meaning influence of contact pressure is not considered.

Zelentzov and Mitrin [Zel19] present an approach for analytically solving a quasi-static coupled thermoelasticity problem. They also divide friction sliding in stable and unstable regions and concentrate on design parameters such as plate coating and thickness, which they identify as critical. While being valid only for simple geometries, their analytical model allows to find an exact solution to the problem.

Decuzzi et al. [Dec01] propose a bidimensional analytical model with finite thickness for analysing the frictionally excited TEI in friction clutches. They analyse the thicknesses ratio between the two friction partners and its effect on critical speed, focusing on a ratio of about 1, typical of multiple disc clutches. They point out that Lee and Barber's model, which considers an infinitely thick plate, overestimates noteworthy the critical speed. As friction partners with thickness ratio around 1 are especially susceptible to hotspotting, they suggest either increasing thickness of the friction lining or decreasing thickness of the steel plate.

Also Jang and Khonsari [Jan02, Jan03] analyse hotspot formation on wet clutch systems, developing an analytical model, which serves for TEI characterisation in presence of a lubricant. Similarly to Lee and Barber, they consider both symmetric and antisymmetric modes. They identify a critical speed which represents the threshold to hotspotting on the steel surface and select five independent parameters the critical speed depends on, amongst which thickness and roughness of the conducting body are noteworthy. They show how TEI tends to being triggered at much lower speed for *rough* rather than *smooth* bodies. Their approach allows also an estimation of the amount of hotspots.

Further analytical TEI-based approaches have been pursued for solving generic hotspot-related problems. For instance, Graf and Ostermeyer [Gra12, Ost13] and Abdullah and Schlattmann [Abd16] develop models for thermal behaviour analysis of clutches and brakes considering the effect of wear, solving the problem numerically. They too identify wear as a key element for mitigation of TEI-induced temperature maxima. Notwithstanding, in literature finite element analysis is generally preferred when assessing thermomechanical performance of automotive clutches

and brakes, usually characterised by more complex geometries.

Kinugasa et al. [Kin99] develop a FE-based thermal analysis of Borg-Warner synchronizers. While their axisymmetric model is fairly simple, it allows to estimate temperatures arising on the friction surface and to subsequently optimise the friction lining basing on the results.

Poll and Spreckels [Pol03] develop a time-dependent, axisymmetric finite element thermomechanical simulation model for temperature characterisation in synchronizers with molybdenum-steel friction pairings. They compute friction power according to local contact pressure and assume it completely converts in heat flux. They however lack to validate the simulation model with temperature measurements, allowing only qualitative assessments.

Zagrodzky and Truncone [Zag03, Zag08] discuss pro and contra of a two and three dimensional finite element model. Though maximum temperatures may be slightly underestimated, the computational effort of choosing an axisymmetric model is significantly reduced. They hence opt for a bidimensional model considering only focal hotspots. They identify critical velocities as a function of the wavelengths of the considered modes. They also choose to evaluate the growth rate, which, if positive, indicates an unstable behaviour of the system and thus hotspot formation.

On the contrary, Bao et al. [Bao16] develop a three dimensional finite element model. They calculate pressure distribution on the friction surface through a static analysis and in a second step perform the thermal analysis. They trigger TEI through pressure disturbance, which occurs in their system e.g. when one of the return springs fails. Of the distorted pressure signal they perform a Fourier transform and solve the associated problem.

Abbasi et al. [Abb14] develop a thermomechanical finite element simulation model for railway brakes. They calibrate their model using experimental results, setting thermal contact resistance and convective cooling. They also model wear. They suggest their model may be used for determination of heat partitioning factors between friction partners. Temperatures predicted with the simulation model correlate well with measurements. It is however to note that railway braking occurs within a time up to 2 orders of magnitude higher than synchronisation time in automotive transmissions. Yet, their work helps to individuate appropriate simulation approaches for modelling TEI.

Häggström et al. [Häg18b] develop a one-dimensional thermal model of molybdenum-coated synchronizers for heavy trucks. They consider a wide range of load points and identify focal temperature increase on the friction surface as more adequate than energy and power for failure prediction. They additionally identify a temperature threshold which determines whether the synchronizer fails after just few cycles or not. Häggström et al. [Häg15, Häg18a] also develop a bidimensional finite element thermomechanical simulation model which enhances development of Mo- and CPRF-coated heavy duty truck synchronizers. They use a similar approach to the one presented in Mileti et al. [Mil18c] and Chapter 4. In fact, they assume all the initial kinetic energy is transformed in friction heat and dissipated on the friction surface. Heat flux is however

modulated by a heat partitioning factor calculated a priori. They iteratively perform multiple simulations until the whole kinetic energy is transformed into heat, i.e. the speed difference equals zero. They validate their model by measuring surface temperature of the latch cone with a pyrometer and bulk temperature with thermocouples. Using the validated simulation model, in [Häg18c], they analyse the effect of manufacturing deviations on synchronizers. They focus on cone angle difference, latch cone roundness and tolerances and their effect on maximum focal temperature. Especially roundness deviations at the latch cone may significantly decrease synchronizer performance with respect to thermomechanical stability.

Stockinger et al. [Sto20] analyse the thermomechanical behaviour of single and multi cone synchronizers with a thermomechanical simulation model based on Acuner [Acu16] and Mileti et al. [Mil18c]. Supported by numerous experiments at the test-rig SSP-180, they point out that localised maximum temperature deriving from unsteady pressure distribution on the friction surface has a major influence on friction behaviour and endurance of synchronizers with carbon friction linings.

In the approaches shown above, either analytical equations are derived starting from physical considerations, or a simulation model is developed and validated experimentally. Albers et al. [Alb18] propose a measurement setup with fibre optic sensing technology for temperature measurement of the friction surface of dry clutches. They tune and validate fibre measurements with thermocouples, which are located at different depths with respect to the friction surface. With this method, they are able to obtain a high spacial resolution and identify experimentally temperature concentrations during sliding. However, this method requires significant investments in terms of time and has to be repeated for every geometry, making sensitivity analyses *de facto* impossible.

Strebel [Str17] and Schneider et al. [Sch19a] also propose an experimental method for thermomechanical stability assessment of multiple disc wet clutches. They first define hotspots according to their appearance and to friction behaviour of the clutch. After having performed several experiments with variation of specific friction loss and power, they identify sliding time as critical for hotspot generation. Sliding time is directly proportional to friction loss and inversely proportional to friction power, as can be obtained by integrating Equation 2.6. They find thermomechanical performance is generally linear in a friction loss vs. sliding time graph and determine through a regression analysis the linear coefficients for a number of different clutch geometries and friction layer types. They generally determine two lines in the aforementioned graph for average contact pressure lower than 0.5 MPa and higher than 1 MPa, respectively. Notwithstanding, they only perform very few experiments with contact pressure higher than 2 MPa, not considering sliding times approaching zero. Their experimental results will be used to prove validity of the proposed method in Chapter 5.

2.5.2 Dynamic behaviour of positive clutches

The dynamic study of gearchanges is of primary importance when considering vehicle and, in particular, shifting comfort. As is widely confirmed in literature, the key parameter for comfort characterisation is jolt, which is the time derivative of acceleration. In particular, shifting-induced jolt is perceived by the driver as a sudden change in longitudinal acceleration, which depends in turn on the value of angular jolt at the shifting element. The latter is, accordingly, the time derivative of angular acceleration.

Depending on stiffness and damping of the whole drivetrain, a defined value of angular jolt propagates to the driving wheels and eventually causes longitudinal jolt. For instance, Huang and Wang [Hua04] discuss the effect of jolt deriving from gearshifts in transmissions of passenger vehicles. They propose numerous models for evaluating the shifting comfort evaluation basing both on literature and experimental data. They set their focus on the physiological experience of jolt on the driver. They classify jolt into transient and durative and propose a method for quantifying comfort through jolt magnitude and its root mean square.

Characterisation of the dynamic behaviour of positive clutches is of primary importance when considering the comfort of automotive transmissions, as they directly affect the whole shifting process. In fact, as positive clutches have to engage under a minimum speed mismatch, an abrupt halt of the clutch body connected to the shaft with the lower inertial moment translates in a jolt through the complete drivetrain.

Laird et al. [Lai90] present how more robust form-fit shifting elements can be a valid alternative and replacement for traditional friction clutches in all kinds of automotive transmissions. They extensively analyse the effect of dog clutches on gearbox dynamics and conclude that, while these clutches are widely employed in military and commercial vehicles, where rapid gearshifts are essential, they do not find application in passenger vehicles. Indeed, though dog clutches can improve efficiency, the engagement dynamics during powershifts lead to jolts that are not accepted by consumers.

Nezhadali and Eriksson [Nez15] develop a simulation model of an automatic transmission. They analyse the dynamic behaviour of clutches during powershifts by utilising an analytically derived state-space simulation model. They focus especially on jolts and propose a dynamic optimisation of the transmission by iteratively minimising the shifting jolt itself. By utilising these results, an optimisation of the shifting control can be implemented especially during the inertia phase of a powershift. Such optimisation can also be applied to shifts performed with mere interlocking clutches.

Irfan et al. [Irf18] develop a dynamic performance assessment and optimisation method for synchronisers through a Pareto front optimisation. They model the form-fit generation process analytically with a lumped parameter approach. They then solve the derived equations of motion numerically. By computing the Pareto front for different parameters they identify and evaluate

the variation of the corresponding objective functions.

Lin et al. [Lin19] develop a method to improve shifting quality of a synchronizer actuated by an electromagnetic actuator. In their work, they focus on the form-fit generation process with the splined clutch. Once design and geometry of the splined clutch are fixed, they show how to perform successful engagements basing on an optimised active disturbance rejection control. Beside shifting speed, they utilise jolt in order to characterise between shifts with different actuation control strategies.

Lovas et al. [Lov06] develop a complex simulation model of a synchromesh mechanism considering all phases of the gearshift independently. They perform for every phase iterative simulations and summarise all results in a multiphysics model. In their simulation, they analyse thoroughly the first and second bump phenomena, as they cause torsional jolt, affecting shifting comfort. The second bump, caused when splines of the sliding sleeve engage the ones of the clutch body, are caused by a speed mismatch, which is in turn dependent of the splines' chamfer angle. In their work, Lovas et al. show the effect of such speed mismatch on comfort and propose reduction of mean axial force (i.e. reduction of speed mismatch between splines of sliding sleeve and clutch body) as an effective way of minimising second-bump-induced jolt without changing synchromesh geometry.

Achnetova et al. [Ach14] present a shifting mechanism for passenger vehicles that bases on a dog clutch relying an external synchronisation. A Maybach-type clutch is designed and its engagement smoothness assessed. Indeed, they measure acceleration on different positions of the gearbox to determine jolts. They perform several shifts under relatively high speed difference and compare acceleration results with tests with standard synchronizers. They identify wear in form of chamfering of the tooth edges of the clutch as a parameter determining shifting smoothness and hence comfort. In [Ach18] they present an improved geometry of the dog clutch with flat claw faces and tapered sides. Analogously to V5 of the CCDC, they develop a zero circular backlash variant. Tests on the dog clutch reveal that even under speed mismatches of up to 5,000 rpm, the dynamic behaviour remains comparable to the one of synchronizers. They however do not consider powershifts, as the dog clutch is integrated in an MT. Additionally, they identify the dog flank angle as a decisive geometric parameter to define the working region of correct engagement.

Bóka et al. [Bók10, Bók11] analyse the engagement capabilities of dog clutches and develop an optimisation method for increasing their performance. They build a dynamic analytical model of the dog clutch by isolating two engaging teeth. They point out that the relative initial position of the clutch bodies, which is aleatory, has an influence on successful or unsuccessful engagement of the positive clutch. Probability of achieving a correct engagement is hence analytically elaborated as a function of, i.a., geometry and speed difference. They derive, ceteris paribus, an optimal speed difference for engagement. According to these results, they develop engage-

ment probability maps, which in turn depend on the speed difference of the clutch bodies and the piston pressure (i.e. the actuating force).

König et al. [Kön12] design and model a positive-fit clutch for a two-speed transmission for electrified vehicles. They study the dynamic behaviour of the dog clutch by deriving the equations of motion (EOM) of the two clutch bodies through a lumped parameter approach and solve them numerically. Beside contact stiffness and damping, they also introduce a term for stick-slip condition of the tooth roofs. Additionally, in [Kön14], they optimise the designed clutch variant by parallelly implementing an optimal control with an electromechanical actuator. This way, they are able to demonstrate that the developed shifting element can engage avoiding jolt in any working condition.

König et al. [Kön16] investigate the gearshifts of a dog clutch used in a research parallel-series hybrid powertrain. They analyse different dog clutch geometries and point out how - also according to Buchberger [Buc13] - different geometries offer various benefits but generally lead to some drawbacks. The considered dog clutch has teeth with pointed roofs increasing noteworthy the engagement probability. They model the powertrain with lumped parameters and extend it with a dog clutch sub-model, which is implemented in SimulationX. For simulations they consider an axial speed of the clutch body of 80 mm/s. They further analyse the effect of speed difference on longitudinal acceleration deriving from torsional oscillation. They point out how the shifting time and oscillation amplitude generated by shocks during engagement of the dog clutch are indeed dependent on the speed difference between clutch bodies and have to be controlled attentively in order to achieve high comfort.

Duan [Dua14] develops an analytical model of a dog clutch in automatic transmissions by considering the teeth as rigid bodies and calibrating fictitious lumped springs and dampers on the middle of the contact surface. He validates the model with experimentally determined dynamometric data, observing good correlation between simulation and measurement. He therefore suggests this approach for dynamic behaviour analysis of dog clutches subjected to powershifts.

Goetz et al. [Goe03] propose a multibody simulation model for dynamic analysis of synchronizers. Here, they focus especially on the dynamic engagement of the positive clutch at the end of the synchronisation process. Simulated self-excited torsional vibration is observed and an optimal control of the actuation is developed accordingly, in order to solve this issue.

For dynamic analysis of the CCDC, Dempfle et al. [Dem19] propose a multibody simulation system basing on the lumped parameter approach and integrate it within the reference automatic transmission. They identify i.a. the number of teeth as an important parameter to improve shifting comfort, while no description of the influence of circular backlash and no validation of the dog clutch engagement is shown. For dynamic and comfort assessment of the shifting process, nine parameters are identified and confronted with the ones of analogous powershifts

with multiple-disc clutches. The parameters include i.a. positive and negative jolts, acceleration smoothness, flare of the ICE, shifting time and discomfort. The latter is determined basing on the equation proposed by Kahlbau in [Kah13a]. They point out that no appreciable difference exists between a shift with a series multiple-disc clutch and a combined friction and form-fit shifting element.

A similar approach is developed by Mileti et al. and Pointner et al. in [Mil19b, Mil21, Poi19] and will presented into more detail in the following chapter.

2.6 Summary

After an overview of state of the art solutions to replace conventional shifting elements with highly efficient systems, the Coupled Cone and Dog Clutch (CCDC) is presented in its two variants and their functionality shown. According to the presented literature and patents, three macro categories of alternative shifting elements can be individuated, which serve as alternatives for comfortable yet drag-loss-affected multiple-disc wet clutches.

- Mere interlocking clutches: These systems represent the most advantageous solution in terms of efficiency, yet synchronisation is to be taken over by another drivetrain component (e.g. the ICE). Shifting time and comfort may be affected with respect to traditional systems.
- Friction and interlocking clutches - non powershiftable: These systems are analogous to BorgWarner type synchronizers, as speed synchronisation is taken over by a cone clutch and torque transmission is yielded to an interlocking clutch. Due to the presence of a free flight phase, such systems are mainly found in DHTs (e.g. as a disconnecting element for an electric motor) and applications where traction interruption is acceptable.
- Friction and interlocking clutches - powershiftable: Those systems rely on friction and interlocking clutches, yet they are powershiftable. Generally, multiple-disc wet clutches serve as friction elements. Those solutions are adopted for friction surface and consequent drag loss reduction. The transmittable friction torque is however reduced accordingly.

CCDC is affine to the latter category. Yet, the novelty of CCDC resides in the employment of a cone clutch for powershifts, for maximum drag loss reduction. Dempfle et al. [Dem19] show and quantify the efficiency increase that can be achieved by substituting conventional multiple-disc clutches with CCDC not only in automatic transmissions, but also in hybrid transmissions (DHT and conventional P3 and P4 hybrids).

Since friction power and friction loss arising in powershifts are significantly higher than in gearshifts with traction interruption, appropriate methods for the study and subsequent design of the shifting element are investigated. In Section 2.5.1, state of the art methods are identified, which

provide calculation methods for determining thermomechanical stability of friction clutches subjected to high loads. In Section 2.5.2, existing methods for the analysis of dynamic behaviour of dog clutch engagement are proposed and discussed.

3 Aim and focus

The working principle of the innovative shifting element for automatic, hybrid and electric transmissions CCDC is described in Section 2.4.

In Section 2.3, an overview on drag losses arising in disengaged automotive clutches is presented and approaches for their determination are discussed. In particular, it is shown that drag losses of disengaged clutches significantly contribute to reduce the overall efficiency of automotive transmissions. Diminution of oil flow rate through e.g. dry sump and on-demand lubrication of the clutch represents one possible approach to reduce drag losses, yet it requires major changes in the overall design of transmissions. Beside flow rate diminution, a valid approach for drag loss reduction is to decrease the overall friction surface. The latter is pursued in the development process of CCDC and does not require relevant transmission modifications. Echtler et al. [Ech17] show the potential of such approach by comparing measured drag losses of CCDC and a reference multiple disc clutch (see Figure 3.1). Drag torque is reduced by up to 95 %.

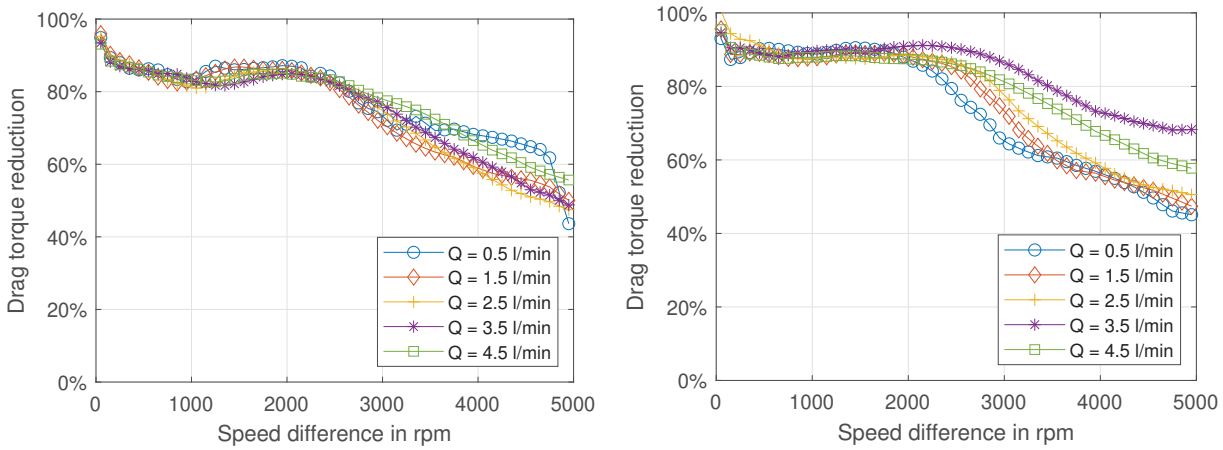

(a) ϑ_{oil} = 60 °C **(b)** ϑ_{oil} = 85 °C

Figure 3.1: Drag torque difference between reference multiple disc clutch and CCDC for typical operating conditions of an automotive transmission [Ech17]

The innovative shifting element for powershiftable automotive transmissions is characterised by a cone and a dog clutch disposed in series, resembling the functionality of Borg-Warner type synchronizers (see Section 2.2.3). However, the high load torque and the consequently high amount of energy dissipated during a powershift represent a challenge in the development process in terms of thermal stability and shifting comfort. In fact, generally, synchronizers are not designed for synchronising masses under high static torque and dog clutches are not designed for engaging under too high speed mismatches. Many validated design and optimisation methods can be found in literature for development of friction and dog clutches singularly and with different requirements. Yet, the employment of combined cone and dog clutches in form of synchronizers in MT, AMT and DCT is linked to relatively low synchronisation power, due to the

limited friction loss and power, as the driving engine can be disconnected via a dry or double clutch. Conversely, wet multiple-disc clutches, which are widely employed as shifting elements for powershifts, are characterised by a greater friction surface and can therefore bear accordingly higher friction power and energy. In general, no design optimisation method is available to effectively design cone and dog clutches capable of performing powershifts (cf. Section 2.5). Hence, a design optimisation method is proposed, with the aim of filling such research gap.

The design optimisation method presented in the following chapter chronologically follows the shifting process of CCDC. Indeed, the two phases of synchronisation and form-fit generation will be considered separately. For what concerns the synchronisation process, the focus will be set onto the thermomechanical stability of the cone clutch. Hence, a method to determine the operation limits of the friction clutch and its ability to withstand high specific energy powershifts will be developed and utilised. Long-term stability of the considered friction pairing is experimentally tested and assessed in different clutch applications and will not be treated here (for instance, refer to Acuner et al. [Acu14]). After synchronisation is completed, according to the description of CCDC shown in Section 2.4, the engagement process of the dog clutch becomes relevant. Here, all forces and torques acting in the system have an effect on performance and shifting comfort. Thus, a dog clutch performance assessment method is developed, capable of identifying the working conditions where a successful engagement is always guaranteeable. Thanks to this method, a dynamic shifting optimisation can be performed in order to guarantee a smooth engagement without any comfort drawbacks of the innovative shifting element in comparison to state of the art multiple-disc wet clutches. The mechanical design process is not treated here, as it relies on state of the art development methods typical for these components, such as standards and finite element analyses.

4 Development of a method for CCDC performance optimisation

4.1 Introduction

In this Chapter, a method will be presented to individuate the performance of the CCDC and its functional limits. Influencing parameters, which determine a correct and successful shifting process will be identified. These parameters will be used as design variables to obtain an optimal design of a coupled cone and dog clutch for automotive application. As mentioned afore, the design process is kept divided for the friction and the dog clutch.

4.2 Thermomechanical cone clutch performance

During the design process of a novel friction clutch, many parameters have to be taken into account. Both macro-categories of short and long term damages have to be avoided and the clutch designed accordingly. The short-term damages, also referred to as spontaneous damages are of thermomechanical nature and usually appear when extreme conditions - e.g. misuse shifts - occur. Thermal and thermomechanical stability are hence to be guaranteed in every working condition. While calculating the mere thermal stability of clutches is relatively straightforward, as it considers steady and uniform conditions, the thermomechanical stability unites two separate phenomena and can be a self-reinforcing mechanism. It is therefore of primary importance to determine the minimum load, from which such an effect begins manifesting. The proposed method bases on a finite element thermomechanical simulation. As many physical properties are of difficult determination and the thermal contact model is complex, an experimental validation of the simulative results is necessary. Temperature is chosen as the main validation parameter, as both literature and experiments indicate it as the trigger to thermoelastic instability, i.e. hotspot generation. Once the simulation model is successfully validated, extensive simulations can be performed to individuate critical operational loads that determine the performance limits of the friction clutch. The simulation program and input parameter variation can be either planned analogously to a design of experiments (DOE) or performed on a fully factorial plan, depending on the needed results. In the present work, simulations are employed as a link between experimental validation and extensive results. The latter are obtained by training an artificial intelligence algorithm with simulated data. Due to the black-box nature of the chosen algorithm, knowledge of the analytical correlation between load parameters and thermomechanical stability is not given. This makes an aleatory choice of input load parameters for simulations much more effective than the design of a complex simulation plan.

4.2.1 Simulative setup

In a first step, the simulation model of the cone clutch is built. It is important that all possible parameters are free to chose. Indeed a parametric and easily parametrisable model can be

effectively used for sensitivity analyses and automated simulations, which do not require continuous user input. For the thermomechanical simulations, the software ANSYS APDL (ANSYS Parametric Design Language) is used.

Except for some very simple cases, a finite element analysis is not able to deliver an exact solution of displacements and stresses. Indeed, a finite element analysis is a piecewise polynomial interpolation - that is, field quantities are approximated over nodes with simple functions. However, it can deliver a good approximation of reality, provided that the element size is correctly chosen and the problem is well posed. It is hence necessary to perform a convergence analysis to confirm the validity of simulations. For the study of the cone clutch, an axisymmetric model is used. The advantage of such a formulation is that it sensibly increases calculation performance with negligible loss of accuracy. Axisymmetric elements are very close to plane elements, but for the presence of circumferential strain ε_θ. For instance, considering a generic triangular element, the displacement field can be written as [Coo90]:

$$u = \beta_1 + \beta_2 r + \beta_3 z \tag{4.1}$$

$$w = \beta_4 + \beta_5 r + \beta_6 z \tag{4.2}$$

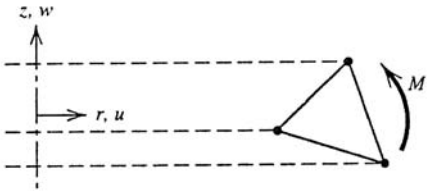

Figure 4.1: Displacement field on the example of a triangular axisymmetric element [Coo90]

Finally, adding four more equation to the linear system, the finite element problem can be rewritten in matricial form as:

$$\begin{cases} \varepsilon_r = \beta_2 \\ \varepsilon_\theta = \frac{\beta_1}{r} + \beta_2 + \beta_3 \frac{z}{r} \\ \varepsilon_z = \beta_2 \\ \gamma_{zr} = \beta_5 + \beta_3 \end{cases} \qquad \begin{Bmatrix} \varepsilon_r \\ \varepsilon_\theta \\ \varepsilon_z \\ \gamma_{zr} \end{Bmatrix} = \begin{bmatrix} \frac{\partial}{\partial r} & 0 \\ \frac{1}{r} & 0 \\ 0 & \frac{\partial}{\partial z} \\ \frac{\partial}{\partial z} & \frac{\partial}{\partial r} \end{bmatrix} \begin{Bmatrix} u \\ w \end{Bmatrix} \tag{4.3}$$

u	m	Radial displacement	w	m	Axial displacement
r	m	Radial coordinate	z	m	Axial coordinate
$\beta_{1,4}$	m	Coefficients of shape functions	$\beta_{2,3,5,6}$	-	Coefficients of shape functions
ε_r	-	Radial strain	ε_θ	-	Circumferential strain
ε_z	-	Axial strain	γ_{zr}	-	Shear strain

The generation of a 2-dimensional geometry is kept as easily parametrisable as possible. All geometric quantities are defined by keypoints that are united by lines. The keypoints are generated by calculating their position in the plane starting from geometric inputs, such as, e.g., inner and outer cone diameter, cone angle, clutch width, etc. Lines closing an area are subsequently turned into surfaces and an automatic meshing of the friction surface takes place.

Here it is important to determine sufficiently small elements, in order to achieve feasible results. However, as a too refined mesh has noteworthy drawbacks in terms of computational effort, a convergence analysis is performed. Additionally, as high stresses and strains, both mechanical and thermal, arise in proximity of the friction surface, a refinement of the mesh in that very region is sensible. The chosen elements differ depending on the performed analysis. For the mechanical finite element analysis, PLANE182 elements are used. For the thermal analysis, PLANE55 elements are used. For the contact surface, CONTA171 elements are used, having the same geometric characteristic as the plane element it is connected to. A contact between the friction surfaces occurs when the element surface penetrates one of the target segment elements on a specified target, which is defined by TARGE169 elements. Due to the relatively simple 2-dimensional geometry, a structured mesh with rectangular elements is used. Being the geometry mostly defined by perpendicular lines, an element distortion can be avoided, while the element size can be controlled by just one parameter h_{el}, which represents the average length of each element's sides. Additionally, rectangular elements do not tend to overestimate the general stiffness, as can happen with triangular elements. Basing on a convergence analysis and considering that acceptable computational times are required for the FEM solution, an average element size of h_{el} = 50 μm is chosen. For convergence analysis, the maximum temperature arising on the friction surface is chosen as control parameter. Results of the analysis can be appreciated in Figure A.7. Another important parameter to be set is the time increment, which is to be assumed constant during synchronisation. Indeed, the unsteady synchronisation process is approximated by time steps. During each time increment, linear mechanical and thermal finite element problems are solved. Convergence analysis shows a minor influence of time increment on maximum temperature, hence the time increment has to be chosen small enough not to misestimate the energy input. Here, a time increment of Δt = 1 ms is chosen. For a detailed description of the performed convergence analysis refer to Section A.3 in the Appendix.

4.2.1.1 Boundary conditions

Once geometry and mesh are fixed, the Dirichlet and Neumann boundary conditions have to be set. These comprehend both mechanical and thermal boundary conditions.

The mechanical boundary conditions represent external forces and reactions acting on the system. The axial force is applied to the surface the piston is acting on. The value of the force is divided by the number of nodes on said surface. The reduced force values are eventually applied to those very nodes in order to reduce the risk of mechanical instabilities in that region. Rigid motion, and hence lability of the system, is to be avoided by constraining appropriate nodes. Theoretically, in the axisymmetric formulation, it is sufficient to block only one degree of freedom in axial direction. However, analogously to what is done for axial force to avoid instabilities, displacement of all nodes lying on the constrained surface is locked in order to split the total reaction force.

The thermal boundary conditions are set in likewise manner. Friction heat is introduced on the friction surface. The heat is modulated by the contact pressure and set to the nodes. The boundary conditions are applied to all boundary regions of the system. For thermomechanical analyses of the synchronisation process, which in most cases last less than one second, all boundary regions can be reasonably considered as adiabatic. Indeed, this allows to keep the model simple. No heat transfer by convection or irradiation has to be implemented. Amongst others, Acuner [Acu16], Strebel [Str17] and Häggström [Häg18a] confirm that said cooling effects are negligible when considering the sole friction phase and not the cooling phase. An exemplary figure representing mechanical boundary conditions is shown in Figure A.6.

Once the simulation model is set, an iterative solution process is started. The aforementioned time increment determines, together with the sliding time, the number of steps necessary to complete a simulation, i.e. the computational effort. During each iteration a mechanical and a thermal finite element analysis are performed sequentially. After each analysis results are saved and partially used as starting conditions for the following iteration. In the following, a brief overview of the solution process is given.

4.2.1.2 Solution process

As mentioned above, the solution process consists of a number of iterations depending on the discrete time increment and sliding time. Within each iteration, a mechanical and then a thermal finite element analysis is performed. The thermal analysis is further divided into 10 sub-steps, as temperature gradients are the predominant phenomenon during synchronisation. The first step of each iteration is a mechanical FE analysis. Nodal stresses and strains are computed and saved. Once this step is concluded, the calculated deformation field is used as initial condition for the following thermal analysis. The most important parameter for the thermal simulation is, though, the contact pressure between clutch cones on the friction surface. The latter can be easily determined using the selected contact elements. Indeed, albeit the nominal average contact pressure remains constant over the whole synchronisation process, its distribution may not. Some areas characterised by hotspot formation may accordingly show extremely high pressure, while other regions may even show zero pressure, i.e. detachment. A continuous control for contact or detachment at the surface elements is performed automatically. The coefficient of friction, while being determined experimentally, is kept constant. The assumed value corresponds to the average coefficient of friction of a shift μ_{avg}. Determination of μ_{avg} from experimental data is done according to the procedure described e.g. by Hensel in [Hen14]. For determining the local heat flux entering the surface elements, its distribution has to be determined. Assuming that all parameters are independent of time during one simulation step, the local friction torque per unit area arising on the contact surface is just a function of the radial coordinate r. Also the axial coordinate can be expressed as a function of the radius, as the friction surface is defined by a line. Its direction is tangential to the friction surface and its

absolute value is computed in Equation 4.4.

$$T''(r) = \mu \cdot p(r) \cdot r \tag{4.4}$$

T''	Nm/m^2	Friction torque per unit area	p	Pa	Contact pressure
r	m	Radius	$-$		

Accordingly, the local friction power associated to the torque is computed in Equation 4.5 by utilising Equation 4.4.

$$P''(r) = T''(r) \cdot \Delta\omega = \mu \cdot p(r) \cdot r \cdot \Delta\omega = \mu \cdot p(r) \cdot r \cdot \frac{v_S(r)}{r} = \mu \cdot p(r) \cdot v_S(r) \tag{4.5}$$

P''	W/m^2	Friction power per unit area	$\Delta\omega$	rad/s	Speed difference
μ	-	Coefficient of friction	v_S	m/s	Sliding speed

In order to compute the total friction power, equation 4.5 can be integrated over the conical friction surface. The coupling between mechanical and thermal model consists in the assumption that all the mechanical friction energy is converted into heat. The validity of this assumption is supported and confirmed, amongst others, by Häggström [Häg15] and Neudörfer [Neu08].

For this 2-dimensional finite element simulation, the friction power per unit area is converted in values per element area. It appears clear, that a small enough element length is important in order to effectively represent local effects. Based on the assumption that all mechanical energy is converted into heat, the average heat flux per element area at time increment j $\bar{\dot{q}}_{e,j}$ can be expressed as in Equation 4.6.

$$\bar{\dot{q}}_{e,j} = \mu \cdot \bar{p}_{e,j} \cdot \bar{v}_{s,e,j} \tag{4.6}$$

$\bar{\dot{q}}_{e,j}$	W/m^2	Avg. heat flux per element area, time increment j	$\bar{p}_{e,j}$	N/m^2	Avg. pressure at element, time increment j
$\bar{v}_{s,e,j}$	m/s	Avg. sliding speed at element, time increment j	$-$		

The heat flux per element length is then applied to each surface element on one of the friction partners according to Equation 4.6. The heat flux per element area can be integrated within the j-th time increment Δt in order to obtain the transferred energy. The summary of the energy input of each element results, hence, in the total energy transferred during said time interval. The results are summarised in Equation 4.7.

$$q_{e,j} = \bar{\dot{q}}_{e,j} \cdot \Delta t \qquad \Rightarrow \quad q_j = \sum_{e=1}^{n_{el,f}} q_{e,j} \tag{4.7}$$

$q_{e,j}$	J/m^2	Heat per element area, time increment j	$\bar{\dot{q}}_{e,j}$	W/m^2	Avg. heat flux per element area, time increment j
Δt	s	Time increment	$n_{el,f}$	-	No. of elements on frict. surface

Since heat is applied to only one friction partner, a sufficiently high thermal contact transmittance coefficient $\alpha_{cont} = 10^9$ W/m^{2}K is chosen, which allows almost immediate temperature equilibrium between contact and according target elements.

In order to couple mechanical and thermal energy, an overall energy balance is computed at the end of every iteration j (see Equation 4.8). This is necessary to determine the mechanical energy reduction in order to recompute the speed difference of the next time increment.

$$E_{kin,0} + Q_0 = E_{kin,j} + Q_j \tag{4.8}$$

$E_{kin,0}$	J	Initial kinetic energy	$E_{kin,j}$	J	Kinetik energy at iteration j
Q_0	J	Initial heat	Q_j	J	Heat transmitted until iteration j

All terms of Equation 4.8 can be rearranged in order to obtain the speed difference between clutch bodies at the end of the j-th increment. Indeed, the reduction of kinetic energy corresponds to the increase of thermal energy in the system. Equation 4.9 is obtained.

$$\frac{1}{2} \cdot J_{red} \cdot \Delta\omega_0^2 + 0 = \frac{1}{2} \cdot \ J_{red} \cdot \Delta\omega_j^2 + \sum_{k=0}^{j} \sum_{e=1}^{n_{el,c}} (2\pi \cdot r_{m,e} \cdot h_{el}) \cdot \bar{\dot{q}}_{e,k} \cdot \Delta t \tag{4.9}$$

J_{red}	kgm^2	Inertia	$\Delta\omega_0$	rad/s	Initial speed difference
$\Delta\omega_j$	rad/s	Speed difference at iteration j	Δt	s	Time increments
$r_{m,e}$	m	Average radius of element	h_{el}	m	Element length
$\bar{\dot{q}}_{e,k}$	W/m^2	Average heat flux at element i, time increment k	$-$		

The only unknown in Equation 4.9 is the speed difference at the end of the time increment $\Delta\omega_j$, which will be used to calculate the friction power for iteration j+1. $\Delta\omega_j$ is explicitised in Equation 4.10.

$$\Delta\omega_j = \sqrt{\Delta\omega_0^2 - \frac{2 \cdot \sum_{k=0}^{k=j} \sum_{e}^{n_{el,c}} A_e \cdot \bar{\dot{q}}_{e,k} \cdot \Delta t}{J_{red}}} \tag{4.10}$$

At the end of each iteration, all results are saved for postprocessing. The solution process is interrupted if the value of $\Delta\omega_j$ is equal or less than zero.

4.2.2 Experimental setup

Experiments are necessary in order to validate the results obtained with simulations. Once the simulation model is validated, performance and optimisation of the friction clutch can be

performed through extensive simulation. In general, validation tests should be performed at a synchronisation test-rig with the possibility to set the same load parameters as in the simulative setup. In particular, the inertia J_{red}, the initial speed difference $\Delta\omega_0$, and the axial piston force F_{ax} should be selectable within reasonable limits. From these parameters, friction loss and power can be derived. The tested shifting element together with its adapters to the test-rig is shown in a cross section in Figures A.4 and A.5 in the Appendix. Through measurement of torque and axial force, the coefficient of friction can be evaluated for every cycle. Additionally, as the thermomechanical simulation model is to be validated, temperature measurements shall be performed. With the aforementioned test setup, wired temperature measurement can be performed during braking cycles. For instance, measured signals of a synchronisation cycle can be appreciated in Figure 5.5. Description of results and according statistical considerations on their validity can be found in Section 5.1.2.2. All experiments are carried out at the test-rig ZF/FZG KLP-260. For a detailed description of the test-rig refer to the Appendix A.4

4.2.3 Model validation

One important step before proceeding to the performance assessment of CCDC is the validation of the simulation model. Indeed, even though the model bases on empirical data, some effects are neglected in the simulation. For instance, material non-linearities are neglected in order to guarantee improved comparability of the final results. Additionally, no variations in micro-geometry of the friction surface are considered, as this would sensibly increase the computational effort without tangible benefits in the results. Further, the simulation system has no degrees of freedom other than axial, so that no tilting of the clutch bodies can be represented. Moreover, a simulation model with adiabatic system borders is able to represent the synchronisation process with sufficient preciseness, yet some heat loss mechanisms are neglected. Hence, in order to verify the assumptions that simplify the simulation model and to assure its robustness and affability while quantifying the loss of information, a validation of the simulation model appears to be necessary every time a radically different geometry is considered.

As the focus of the optimisation method is set onto the assessment of the thermomechanical stability of the cone clutch, the validation of the simulation model bases both on measured data and visual analysis.

4.2.3.1 Experimental plan

Experimental data is generated according to a testing plan. For the purpose of validation, it is decided not to choose a partially factorial setup basing on design of experiments (DOE) techniques. Indeed, the aim of performed experiments is to prove validity of the designed simulation model. Experiments are in this very phase not intended to show correlations between load parameters and respective results. It is however necessary to define the regions within which the simulation model will work, i.e. the minimum and maximum load conditions of the shifting element. In order to determine real working conditions of the shifting element, a simple

multibody simulation model is built with Simulink's tool SimDriveline. In particular, Daimler's automatic transmission 9G-Tronic is modelled and load parameters at the reference shifting element computed. For a detailed description of the automatic transmission refer to both Sections 6.1 and A.1. As input values, inertias are esteemed through component measurement and are employed along with maximum speed and torque delivered by the internal combustion engine. Even though maximum torque occurs slightly before maximum speed is reached, these values are assumed for worst-case scenario calculations. All powershift-calculations are performed without ICE-support, in order not to underestimate loads. For maximum simulated parameters refer to Figure 5.4 for the reference shifting element. Basing on these values, the experimental plan is set up. Out of these values, appropriate load conditions shall be defined. During experimentation, the correct sequence of load conditions is essential. Indeed, misuse tests are performed purposely and thermal stress on the clutch could lead to deterioration of the surface and of the sensor itself. It is hence preferred, after a running-in procedure, to perform tests with limited friction power and loss first.

4.2.3.2 Data-based validation

The data-based validation relies on the comparison between measured and simulated signals of temperature. It is hence important to make these datasets of different origins comparable. As temperature measurements can suffer from stochastic deviations during the experiment, each synchronisation cycle is repeated 10 times. Number of repetitions is computed according to Bland [Bla96] by setting the 95% confidence interval as 50% of the estimate of the standard deviation. The temperature values of each cycle are linked to each other by the corresponding value of instantaneous specific friction power. This way, all curves can be normalised by means of the sole differential speed, as axial force is kept constant and even limited fluctuations in friction torque - that is, in turn, coefficient of friction - do not influence the final result. Once the measured temperatures are normalised, an average temperature curve is built, as is exemplarily shown in Figure 5.5.

In order to confirm validity of measured data, the 95 % confidence intervals are plotted for the temperature curves. As generally 10 measurements are performed for each load condition, a t-student distribution of measured signals is assumed instead of the Gaussian for confidence interval computation. Additionally, every 100 ms, scatter bars are plotted to identify possible dispersion of data and hence inaccurate results.

For the data-based validation, maximum temperature during synchronisation and temperature gradient at the begin of sliding process - i.e. when the friction power is highest - are chosen as representative of the thermomechanical behaviour of the friction clutch. Basing on the aforementioned assumptions for the simulation model (i.e. no heat transport other than conduction and adiabatic boundaries), the simulated temperature is expected to be generally higher than the measured one.

As the synchronisation temperature is measured on the outer surface of the steel ring, maximum temperature at the friction surface can be estimated only through simulated values. It becomes hence evident that a perfectly validated model is necessary in order to obtain an accurate esteem of temperature distribution on the friction surface. Ceteris paribus, average and maximum temperatures are to increase linearly with increasing friction loss in a simple adiabatic model. This assumption is a good approximation for low temperatures, whereas increasing thermal expansions sensibly affect stresses and stains, and, in turn, thermal behaviour. On the other hand, experiments are characterised by heat transfer to adjacent components and lubricant which are generally negligible, yet increase with increasing temperature difference between components and ambient. Basing on these considerations, a difference in maximum - and average - temperature during synchronisation is acceptable, it is however to remain constant and within a narrow bandwidth. Important differences are index of strongly non-linear phenomena and generally occur when thermomechanical performance limits are exceeded.

The temperature gradient during synchronisation also gives information on the performance of the simulation model. Also in this case, a correct application of thermocouples is assumed. Generally, however, due to the limited, yet inevitable, increase in heat resistance between clutch body and sensor, simulated temperature gradients will tend to be higher than measured ones. Time range to evaluate the temperature gradient is determined to be between 0 and 30 % of the total sliding time. In such a way, only the linear temperature increase is considered. Hence, while maximum temperature gives information on how good the simulation model works with increasing friction loss, with its gradient the validity in relation to friction power can be rated.

4.2.3.3 Visual validation

Also a visual validation of the simulation model is indispensable for assessing the goodness of the simulation model. This holds especially for load conditions that cause permanent damage on the friction surface, that is, hotspots. During experiments with extreme load conditions - comparable to misuse shifts in transmissions - extreme temperatures close to the friction surface cause the micro-structure of the steel cone to change. Macroscopically, typical hotspot-signs appear on the surface. As the simulation model is able to reproduce this effect, their position in axial direction is to be compared. Additionally, alterations in microstructure and their depth can help to estimate the maximum temperatures that arose during simulation process. Microstructure analysis at the microscope is however invasive, meaning only the effects of the highest load condition, which is performed last, can be assessed. In figure 4.2, a hotspot can be appreciated macroscopically and microscopically.

4.2.4 Identification of performance limits

Once the simulation model is successfully validated, the performance limits of a given geometry can be identified by analysing the influence of load conditions on the thermomechanical behaviour. Indeed, if results from the simulation model prove to be correct, the boundaries

(a) Photograph of a hotspot on the friction surface of the steel cone

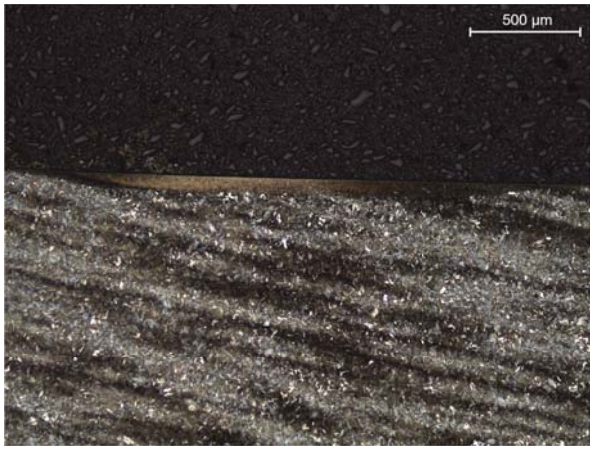

(b) Microscopic image of the cross section of the hotspot. Thermally altered region is clearly visible

Figure 4.2: Visual validation of a hotspot on the steel cone friction surface: macroscopic (a) and microscopic (b) image

defining performance limits of the cone clutch can be exactly identified. However, before being able to determine those values, it is necessary to define valid criteria that determine failure of the clutch. State of the art investigations presented in Chapter 2 show that generally a threshold temperature is responsible for triggering thermoelastic instabilities, i.e. hotspots.

It is hence of primary importance to determine a temperature value, after which the thermomechanical stability of the system cannot be given further. The identification of such a value from experimental data is made possible by the performed temperature measurements. Indeed, thermomechanical instabilities are characterised by highly non-linear processes. In the hotspot region, a high energy concentration can be found in comparison to adjacent regions on the clutch body. As a result, given the radial distance from the heat generation zone, the measured temperature at the outer surface of the steel cone is sensibly lower that the one that would be measured if a uniform heat distribution would take place. Conversely, being the simulation model and the material parameters strictly independent of temperature, a linear maximum temperature evolution will be expected when increasing friction loss and power, respectively. It can be hence assumed that as soon as the gradient of measured temperature versus friction loss - or power - changes and diminishes noteworthy, non-linear phenomena are occurring at the friction surface. The critical temperature not to be exceeded can be correspondingly determined as the maximum one arising when such change in gradient occurs. In literature, threshold temperatures between 360 °C and 600 °C can be generally found, depending on the considered clutch and friction partners. For CCDC such value is set to be ϑ_{crit} = 400 °C, as from such temperature simulated and measured temperature curves begin to diverge.

Once the threshold temperature is identified, the influence of load parameters on maximum temperature at the friction surface is to be determined. Specific friction loss and power are suitable as load parameters to describe maximum temperature, yet they are not independent

of each other. It is hence decided to utilise average contact pressure p_{avg}, maximum tangential velocity $v_{g,0}$ and reduced moment of inertia J_{red} as load parameters. In order to define their correlation with maximum temperature, several simulations may be run and results processed with regression analyses. However, given the intrinsic non-linearity of the thermomechanical sliding process, such regressions may be valid for very limited regions and differ with varying geometries of the clutch. Differently from dynamic engagement performance, an analytic equation correlating loads and performance is not given. For instance, in Figure 4.3, simulated values of maximum temperature arising on the friction surface are shown for selected loads versus specific friction loss and power. As mentioned above, the simulation model does not take into account melting temperature or plastic deformation. The value of reduced inertia is constant for all simulations and equals J_{red} = 0.25 kgm^2. Four average contact pressure levels are chosen, and, in turn, each level consists of ascending speed steps. It is clear that maximum temperature is indeed affected by both specific friction loss and power. However, as can be appreciated especially in Figure 4.3a, contact pressure changes the exponent of the curve, which varies from less to more than 1. In fact, in the simulation model, contact pressure not only affects friction power distribution (and thus temperature), but also the purely mechanical deformation of the system. The effect of contact pressure on maximum temperature is of difficult analytical determination and varies depending on both sliding speed and inertia.

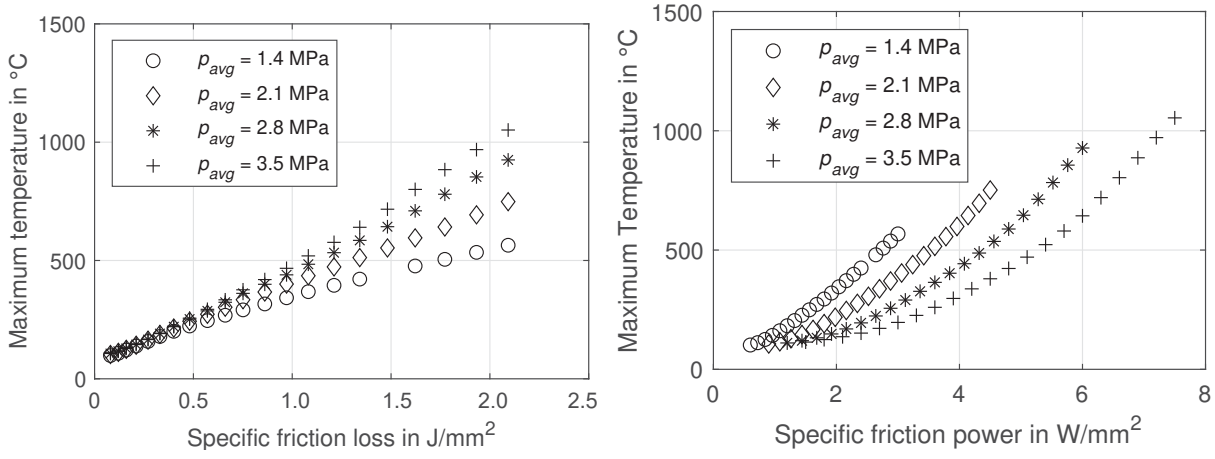

(a) Maximum Temperature vs. specific friction loss **(b)** Maximum Temperature vs. specific friction power

Figure 4.3: Simulated maximum temperature at friction surface arising during synchronisation vs. specific friction loss (a) and power (b). Starting temperature ϑ_0 = 80 °C, inertia J_{red} = 0.25 kgm^2. CCDC variant 2, for geometrical data refer to Table 2.2

In order to obviate this lack of information, alternative tools can be used. In case of CCDC, as inputs and outputs are limited, artificial intelligence (AI) algorithms can be used, which do not require extreme computational effort. For determining performance limits of CCDC, a neural network (NN) is used. Neural networks offer numerous advantages compared to many other algorithms in terms of time-efficiency. Once a network is well trained, it can extrapolate maximum temperature for virtually any combination of load parameters. Input parameters shall however be within the training limits of the network. It is so possible to determine when max-

imum temperature exceeds the selected threshold for a fully factorial plan of input parameters with extremely refined meshing. However, neural networks work as black boxes, not allowing to establish analytical correlations between inputs and outputs. Furthermore, they deliver slightly different results each time the network is newly trained. Such variation depends on robustness of the network. Training data for the neural network is generated by aleatorily creating load combinations within the 3-dimensional input space, which is characterised by the independent variables p_{avg}, $v_{g,0}$ and J_{red}. Thermomechanical simulations are performed accordingly, the maximum temperature at the friction surface being evaluated in the post-processing. Simulated maximum temperature is used as output for the network training.

Net architecture is kept as simple as possible, as the problem is characterised by only three variables. Yet, its robustness and efficacy are to be assessed and proved before results can be generated. In particular, sensitivity analyses for determination of effects of hidden layer size and number of training epochs shall be the decisional basis for topology determination. Sufficient and randomised training data is also necessary in order to avoid overfitting issues. Satisfying results are obtained when training the algorithm with at least 100 simulation points. An increase of datapoints for training improves precision of the extrapolation, accordingly. Training is performed with Bayesian regularisation. Contrary to back-propagation training algorithms, Bayesian regularisation can noteworthy increase robustness and eliminate cross-validation. For a more detailed description of said training algorithm, refer for instance to Neal [Nea95] or Burden and Winkler [Bur08]. Once training is completed, performance plots and regression curves of both trained and tested data are to be analysed carefully. Further, the error between approximation and real data is to be computed for all available datapoints and its Gaussian distribution around zero proved.

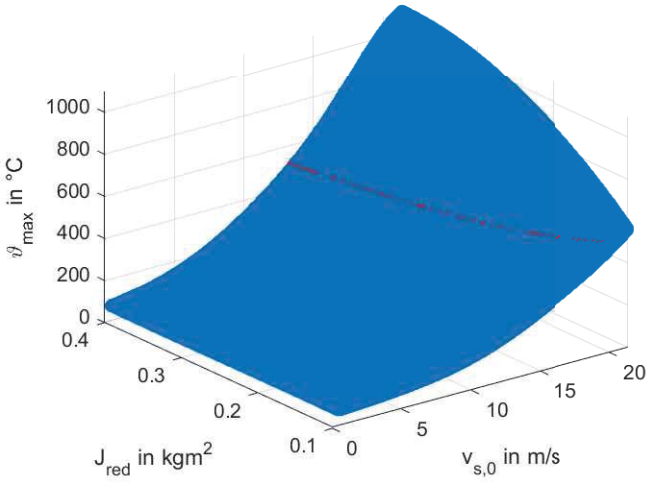

Figure 4.4: Maximum temperature evaluated with the trained neural network vs. sliding speed and inertia. Average contact pressure of p_{avg} = 3 N/mm^2. In red, the datapoints are highlighted, whose temperature equals ϑ_{lim}

Once statistical correctness of the trained network is ensured and sufficient preciseness reached, the net can be utilised to predict maximum temperature at the friction surface for shifts with any combination of input load parameters. However, input parameters p_{avg}, $v_{s,0}$ and J_{red} shall not exceed training boundary values by more than 10 % of the training range, in order to avoid incorrect extrapolation of results. Given the computational efficiency of neural networks, out-

puts corresponding to a fully factorial plane of input parameters are effortlessly evaluated in a very limited time. As the posed problem consists of three independent inputs and one output, a 4-dimensional space has to be considered for results post-processing. However, in order to simplify results interpretation, one dimension is kept constant while maximum friction surface temperature is evaluated for the remaining two. Average contact pressure p_{avg} is selected as constant parameter, as this facilitates individuation of its influence on both thermal and mechanical behaviour of the clutch. Maximum friction surface temperature is evaluated for all input load combinations. Of the latter, those are evaluated, which would lead the friction surface to overheat above the threshold temperature ϑ_{lim}. To do so, the temperature surface plot is cut at the ϑ_{lim}, as is visually explained in Figure 4.4. The union of individuated points generates a performance limit curve. Such curve is valid only for the considered average contact pressure p_{avg}. Once this step is concluded, the fixed input parameter can be increased stepwise. The aim of such procedure is eventually met when all performance-limit curves can be displayed in a sole plot. For immediate understandability of performance of the considered design, performance curves are plotted in a friction-power vs. friction-loss plane. This way, the influence of contact pressure on performance can be easily recognised and taken into account for possible improvements. Also, results can be displayed on a J_{red} vs. $v_{s,0}$ plane to identify the limit sliding speed identified in literature.

4.2.5 Thermomechanical optimisation

A validated simulation model which allows to find performance limits of the cone clutch can be employed in a further step to improve its stability. Ceteris paribus, this is obtained by changing geometric parameters of interest. In order to improve the thermomechanical stability of the clutch during synchronisation, it is necessary to reduce the temperature peaks on the surface and within the clutch body. According to both geometry and material properties of the friction lining, the following modifications should be taken into account:

- Sheet thickness in radial direction: According to the relatively low thermal conductivity and high specific capacity of organic friction linings with reference to metal, a very high share of heat generated during synchronisation flows into its steel counterpart. Consequently, relevantly high temperature arise within the steel cone and especially on regions on or very close to the friction surface. It is hence important to avoid any heat accumulation in the steel cone. Such overheating can for instance occur when the sheet thickness is too low. Thus, thermal capacity of the steel cone should be in any condition sufficient to avoid hotspot generation (refer to Acuner [Acu16]).
- Clutch stiffness/elasticity: While an increase in sheet thickness can help improve thermal stability of the clutch, it increases also its stiffness. A reduced elasticity of the clutch may however lead to non-uniform pressure distributions on the friction surface, as the bodies are less capable of adapting to their counterparts. Manufacturing tolerances and rotation around axes different from symmetry axis caused by axial force generate small angle

differences between friction partners which need to be compensated.

- Cone angle: Depending on the force-induced deformation and tilting of both cones - i.e. depending on the system's stiffness - an angle difference between inner and outer cone can lead to a more advantageous pressure and, in turn, temperature distribution.
- Friction surface: If feasible within package boundaries, enlargement of the friction surface can possibly lead to lower temperatures within the clutch, as specific loads lessen. If analyses show that performance limits of the clutch are well above the actual loads, also considering a diminution of the friction surface can be an option. This allows a stiffer design or, for instance, a reduction of the number of friction surfaces.

Once the effects of geometric modifications to be analysed are fixed, simulations can be performed accordingly. The effect of changing those parameters can be subsequently identified by analysing the corresponding maximal temperatures on the friction surface. For this purpose, it is important to create an easily parametrisable simulation model. This allows, amongst others, to create geometry modifications through automatic compilers. In such a way, many configuration setups can be quickly implemented and simulated. Improved geometry setups can be eventually identified through sensitivity analyses of simulation results. This way, optimisation recommendations can be derived and utilised for improved designs of the cone clutch.

4.3 Dynamic dog clutch performance

The functional distinction between friction and positive clutch are treated in Chapter 3. After having discussed the thermomechanical stability of the cone clutch in the previous section, the dynamic behaviour of the dog clutch during its engagement will be extensively treated in the following. Analogously to what is done for the thermomechanical stability analysis of the friction clutch, the dynamic behaviour of the dog clutch will be identified and assessed through a simulation setup thoroughly validated by means of numerous experiments. First, both simulation model and corresponding experimental setup are shown. The main parameters that influence the dynamic behaviour and performance of the dog clutch are then analysed to eventually proceed with showing operational and comfort optimisation criteria.

The positive fit generation takes place after masses are synchronised by the friction clutch. However, in order to guarantee an engagement in most conditions, a speed difference between the two dog-clutch bodies is necessary. In fact, probability that the teeth of one clutch body meet the corresponding gap on the counterpart is dependent on the rotational tooth gap, and can be very low. The form-fit generation process can be divided into 3 main phases:

1. Closing: the axially movable clutch body is actuated by the piston with determined axial speed and force. The piston force equals the sum of reset spring force and inertia. The latter is characterised by the axial acceleration of the clutch body and its mass. This term can however be neglected, as the mass is very low. If a torque transmitting element is located in between, the axial friction force between splines and inner/outer carrier has to

be added. Additionally, a damping force has to be considered, as the piston is actuated hydraulically and is hence influenced by the dynamics of pumps and control (see Equation 4.13).

2. Kiss point: Analogously to friction clutches, the kiss point for the dog clutch is here defined as the position where the axial position of the tooth tips of both dog-clutch bodies is coincident. In most cases, as mentioned before, this position corresponds to a tooth-vs-tooth contact.
3. Engagement: Through relative rotation of the two clutch bodies, a toot-vs-gap position is reached and the claws can engage. As soon as the tooth flanks are in contact, the full torque can be transmitted through the dog clutch.

The description of those phases, and in particular phase 3, is essential to assess the dynamic behaviour of the clutch.

4.3.1 Simulative setup

In order to analyse the system's dynamics, a multibody simulation model is set up using the software SIMPACK. The choice of a comprehensive software is necessary to reliably represent the complex contact models. The chosen contact models are to stably work also with impacts, i.e. very high deceleration rates / jolts. Additionally, the complex geometries of teeth and splines have to be correctly modelled. The complex contact models do not allow the system to be solved with a simple lumped parameter approach, as the rigid bodies' properties cannot be reduced at their centre of gravity (COG). A multibody simulation model solves a set of differential equations of motion (EOM), which depend on the degrees of freedom of the system. It consists of a set of rigid bodies connected to each others by a series of joints, springs and dampers. Generally, in space every rigid body has 6 degrees of freedom (DOF) - three translational and three rotational. All displacements and rotations have to be described with reference to an inertial reference system. To simplify calculations, usually motion is referred to local reference systems, which in turn are referenced to other relative references or to the inertial reference through transformation matrices. For more detailed information about the theory of multibody system dynamics refer for instance to Cheli and Diana [Che15], Bauchau [Bau11] or Shabana [Sha20].

The simulation model is used to determine and optimise behaviour and performance of the dog clutch. As is done for the thermomechanical model, a validation through experiments is however necessary. Thus, in a first step, the multibody simulation model of the dog clutch has to reflect the test-rig as accurately as possible. Only in this way the validity of the model can be assured. To achieve this, two distinct simulation models are implemented: one, replicating the test rig, for validation, and performance assessment and optimisation and another to be integrated in a transmission model, which will be dealt with in Chapter 6. The cone clutch has an influence on the system's dynamics with i.a. its mass, elasticity and friction forces between spline-flanks. It is thus necessary to include these components in the model, though their behaviour is not further

analysed. Components of the test-rig simulation model are described in the following.

The cone clutch is modelled as an union of gearing and conical geometry. For this purpose, the geometry elements 'Gear Wheel' and 'Rotational Body' are used. The body geometries can be imported from any CAE system. The very same holds for the dog clutch. Here, 'Gear Wheel' elements are used to build the splines geometry. Preliminary simulations with the dog teeth modelled as flexible bodies and simulated by coupling the multibody model with a FEM simulation have shown no increase in precision. Neither, could any effects be observed, which would influence or affect engagement dynamics. Hence, due to the noteworthy increase in computational effort deriving from the real time coupling of the simulation models, it is eventually chosen to model the dog clutch as rigid body, neglecting local deformations. Inner and outer carrier are modelled accordingly: the splines with 'Gear Wheel' elements and the massive parts as 'Rotational Bodies'. Between all steel-on-steel surfaces, a coefficient of friction of $\mu = 0.05$ is assumed based on experimental data. 'Spline Coupling' force elements are used to connect inner and outer carrier with inner and outer cone dog clutch bodies, respectively.

The axial force of the piston $F_A(t)$ is modelled as a time-dependent load element which works along the axial coordinate. Force is led through the piston into the shifting element. A spring, which in turn is fixed on one end to the housing, absorbs the piston force. The piston is free to move only in axial direction (z direction). Additionally to the time-dependent force, a linear damper with damping constant d is added in order to represent dynamics of the hydraulic system at the test-rig. The damper element is only proportional to axial speed. Moreover, thanks to the damper, a constant axial velocity of the piston can be generated and analytically determined as expressed in Equation 4.11.

$$v_z = \frac{F_A(t)}{d} \tag{4.11}$$

The damping coefficient d is tuned basing on the real piston velocity values measured at the test-rig. A schematic representation of piston, force and damper is shown in 4.5.

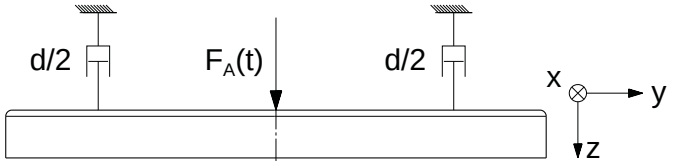

Figure 4.5: Schematic representation of the piston, with applied force and damper

The preloaded spring is modelled as a standard spring element with stiffness k. Depending on the type of spring, the stiffness k is set either as constant or as the derivative of the corresponding force vs. displacement curve. Characteristic curves are determined experimentally and can be appreciated in Figure 4.6 for the reset springs of Variants 1 and 2 of CCDC.

Inner and outer carrier are modelled according to the test-rig configuration. The inner carrier is connected to a slip clutch, which limits the maximum transferable torque to a predefined value.

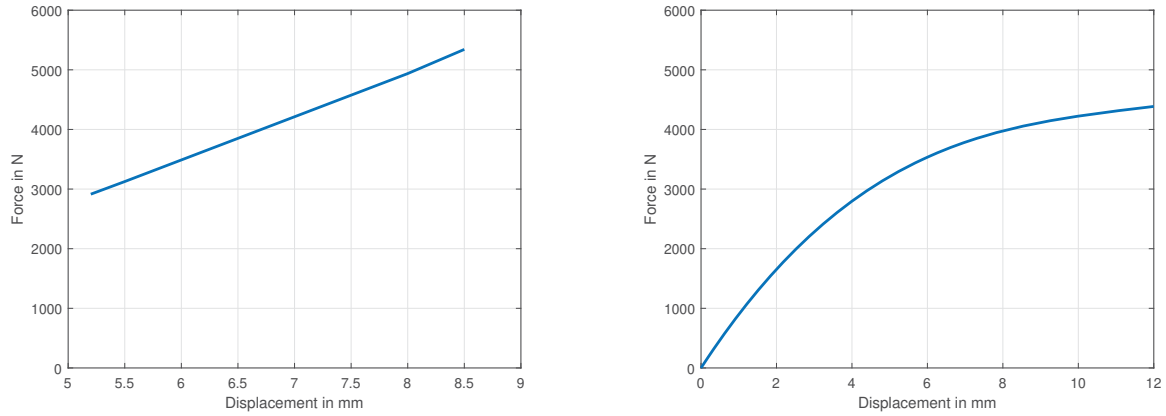

(a) Wave spring

(b) Plate spring

Figure 4.6: Measured force vs. displacement curves for wave spring of CCDC1 (a) and disc spring of CCDC2 (b)

The outer carrier can also rotate about its axis, is however connected to a torsional spring with high stiffness. Said spring is fixed on the other end, where reaction force is evaluated, representing at the test-rig the load cell for torque measurement.

Contact surfaces of friction and dog clutches and of splines at inner and outer carrier are modelled through a polygonal contact model (PCM), leaning on the model developed by Hippmann [Hip04b]. The model bases in turn on an elastic-layer-model, which defines the contact process by exclusively considering the bodies' contact surfaces. Needed input parameters to the model are Young's modulus, Poisson's coefficient and the elastic layer thickness. Additionally, the contact surfaces are to be discretised in a sufficient number of elements. Contact properties for steel vs. steel as contact partners are known from literature. Values for contact partners steel vs. friction lining are to be investigated experimentally, as organic friction materials are characterised by a wide range of values of Young's modulus and Poisson's coefficient. For determination of the elastic layer thickness, a force vs. displacement curve is obtained experimentally by compressing a friction lining of 6 mm diameter with a steel piston. Stiffness is determined as the derivative of the curve. The elastic layer thickness of each partner is determined according to Equation 4.12. For both contact partners, a linear-elastic boundary layer is assumed. The elastic layer stiffness is comparable to a series of parallel springs originating from the discretisation points.

$$c_l = \frac{K}{b} = \frac{1-\nu}{(1+\nu)(1-2\nu)} \cdot \frac{E}{b} \tag{4.12}$$

c_l	N/m^3	Elastic layer stiffness per unit area	K	N/m^2	Elastic layer module
b	m	Elastic layer thickness	ν	-	Poisson's Coefficient
E	N/m^2	Young's modulus	–	-	-

Determination of the elastic boundary layer of the steel cone is complex. Hence, as also suggested by Hippmann [Hip04a], validated empirical data is utilised. Table 4.1 summarises material parameters used for steel cones and friction lining.

Parameter	Symbol	Unit	Steel	Carbon HC 310
Density	ρ	kg/m^3	7850	1200
Young's modulus	E	N/m^2	210·10^9	0.8·10^9
Poisson's coefficient	ν	-	0.30	0.25
Elastic layer thickness	b	mm	1.0	0.7

Table 4.1: Contact parameters and material properties

As mentioned above, also discretisation of the contact surfaces has a sensible influence on computational performance and results accuracy. For CCDC geometry, the discretisation optimum is identified at 140 and 200 polygons for steel cones and friction lining, respectively. Calculation of friction is performed with the classic Coulomb approach.

Discretisation of the dog clutch is more complex, due to the surface shape of teeth tips and flanks. It is hence performed in an intermediate step with a commercial CAE software. The polygonised surface is then imported in the multibody simulation environment. Determination of the elastic layer thickness is performed according to what is done for the friction cone. Coefficient of friction for steel vs. steel tooth contact is set to μ = 0.05, according to experimental results. A representation of the discretisation can be appreciated in Figure 4.7.

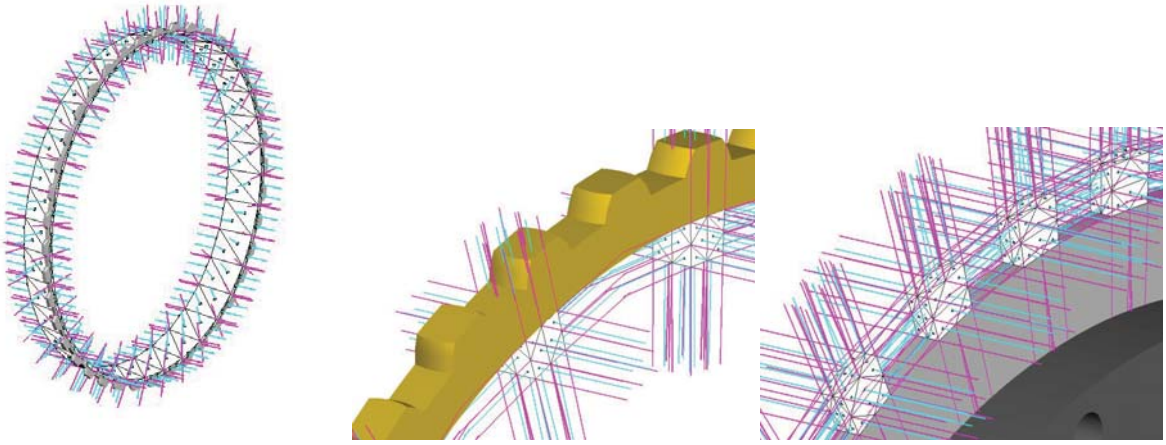

(a) Steel cone **(b)** Outer dog clutch body **(c)** Inner dog clutch body

Figure 4.7: Representation of discretisation for steel cone (a), outer (b) and inner (c) dog clutch bodies

4.3.2 Experimental setup

The test-rig ZF/FZG KLP-260 can be operated with a creep drive, capable - thanks to a transmission with a high transmission ratio - of delivering high torque at the shaft (refer to Appendix A.4). The driving motor is speed-controlled, yet, during engagement, the speed difference between clutch bodies varies from the predefined value to zero. An element, which decouples

speeds of clutch and driving motor while continuing to deliver torque is hence necessary. For this reason, a slipping clutch is designed, whose slipping torque can be adjusted depending on the needed load (refer to Figure A.4 in the Appendix). The slipping torque represents the load torque the dog clutch has to transmit after engagement is complete. It can be adjusted by varying the clamping force of the slip clutch. Such axial force defines the slipping torque and is absorbed by a plate spring, in order to allow a precise setting. The same friction lining as in the cone clutch is used.

On the other hand, the outer carrier is stationary. It is however rotably mounted, the torque being measured by a load cell with known lever arm. Experiments are performed by manually mounting the desired dog clutch geometry and slipping torque. Once the test-rig is ready to operate, speed, axial force and piston speed are set. In order to obtain acceptable reproducibility, each experiment shall be repeated at least ten times.

4.3.3 Model validation

Some simplifications and assumptions are made to the simulation model to reduce computational effort. These assumptions are considered to be valid and do not contribute to significant loss in accuracy. They can be divided into model-dependent and model-independent. Model-independent assumptions comprehend:

- Classic multibody simulations describe mechanic behaviour of a system of rigid bodies. No deformations are hence considered.

Model-dependent assumptions are i.a.:

- For contact modelling, all coefficients of friction are assumed constant. For instance, no influence of sliding speed or contact pressure on friction is considered. Friction-induced vibrations, originated from negative CoF gradients with respect to sliding speed, cannot be represented. This is acceptable, as the focus of simulations is laid on dog clutch engagement.
- Control of the actuation piston is not modelled as such. It is instead substituted with a damping element validated a posteriori.

Because of assumptions and simplifications, the simulation model is to be validated. Only so, reliable results can be generated. After validation, the simulation model can be used as a robust alternative to experimental testing. However, before introducing validation methods, it is necessary to define an engagement process. In particular, three possible outcomes for a shift are identified and described in the following.

Successful engagement. A successful engagement is defined as such when the teeth of the axially movable dog clutch body are able to travel to the full depth of their counterpart's gaps and torque is transmitted through tooth flanks. An exemplary cycle is described by the following phases:

- Begin of shifting and closing of the axial gap of the cone clutch. No torque is transferred during this phase.
- Friction phase: Axial force is increased, the piston comes to a halt. Force is absorbed by the prestressed spring. Friction torque is proportional to the axial force.
- When synchronisation is completed, axial force is increased and becomes higher than the spring preload. The piston can move forward together with the axially movable dog clutch body only if its force is higher than the sum of spring preload and friction between splines of the cone clutch. The gap between dog clutch bodies is reduced.
- Kiss point: Depending on the relative position of dog teeth with respect to each other, tooth vs. gap or toot vs. tooth position can occur. Should the latter be the case, the piston cannot travel further and force is increased to its maximum value, as it is not absorbed by the spring anymore. The piston can proceed when the next possible tooth vs. gap position is met due to relative rotation, provided load torque is higher than friction torque.
- Shifting-through: Once teeth meet the gaps of their counterpart, the axially movable dog clutch body travels further. The piston works again against the prestressed spring and the friction between splines of the cone clutch. The full load torque can be transmitted through tooth flanks after shifting through.

Tooth rejection. Toot rejection is an unsuccessful engagement. It occurs when a combination of geometry and load parameters are above the maximum allowable. For instance, given a geometry with defined angular tooth gap, too high rotational speed difference or too low axial piston velocity can cause tooth rejection. On the other hand, if the load parameters are well defined, decreasing circular backlash can reduce engagement performance of the dog clutch. Tooth rejection can be assimilated to clashing of synchronizers. However, due to the additional load torque, dog clutch tooth rejection usually leads to serious tooth damage within a very short time. In general, it can be stated that tooth rejection occurs when a too small tooth flank area comes into contact, due to the extremely high pressure being generated on such surface. In the following, an analytical method for identifying the minimum tooth flank overlap necessary to avoid tooth rejection is developed. A shifting characterised by tooth rejection is generally described by the following phases:

- Friction phase: No differences to successful engagement.
- Tooth vs. tooth position: Depending on the relative position of dog teeth with respect ot each other, tooth vs. gap or toot vs. tooth position can occur. In both cases, also due to axial inertia and damping, the advancing dog clutch body has not time to advance sufficiently within the gap of its counterpart. In fact, the following tooth approaches too fast and rejects its counterpart. This phenomenon is caused by a too high pressure on the contact area of the flanks.
- Rejection: The above described phenomenon repeats each time a tooth meets the subsequent gap.

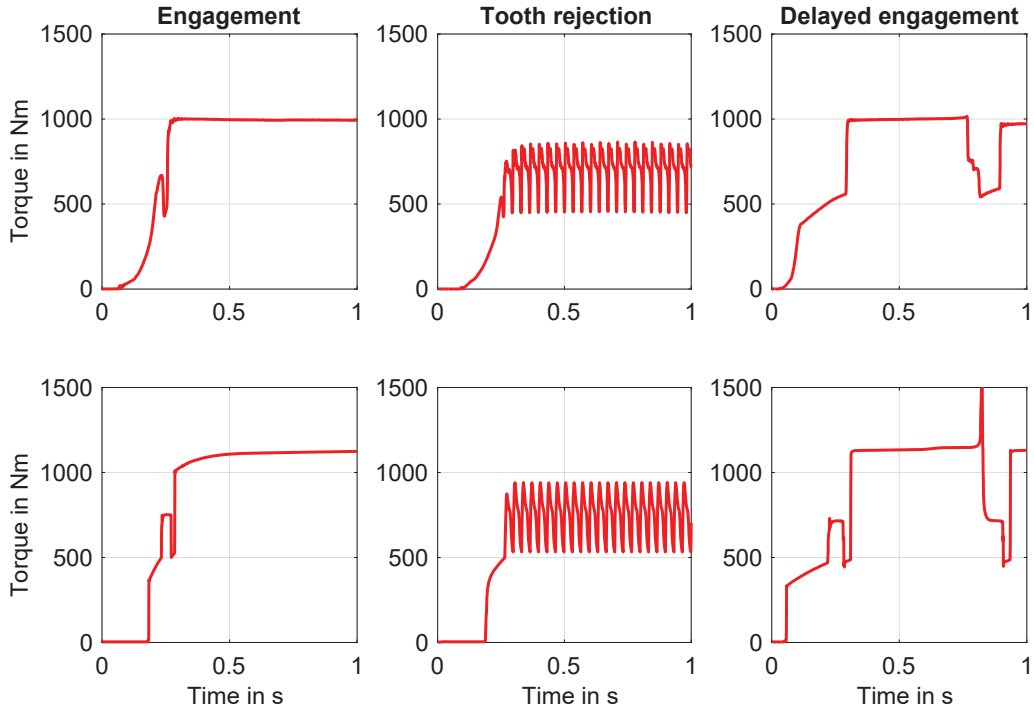

Figure 4.8: Possible outcomes of CCDC actuation: Successful engagement (left), tooth rejection (middle) and delayed engagement (right). The upper row shows experimental data, whilst the lower the corresponding simulations

Delayed engagement. As a combination of the two aforementioned phenomena, a delayed engagement begins as a positive engagement. However, due to too high speed or small piston velocity, the clutch does not have time to fully engage. Therefore, torque is transmitted for a short time through a limited contact surface of the tooth flanks, which generates in turn high contact pressure. Due to manufacturing imperfections and wear of the edge between tooth flanks and faces, the axially movable dog clutch body can slip out and engage in the subsequent gap. This phenomenon is not representable by the simulation model when considering perfect tooth shapes and edges. In this case, the engagement is unsuccessful, as also the following teeth are rejected. Vibrations and not modelled elasticities determine the eventual engagement of the clutch during experiments. Nonetheless, through adaption of tooth edges, the phenomenon can be reproduced also in simulations. A successful engagement, a tooth rejection and delayed engagement are shown in Figure 4.8. Here, torque from experimental and simulative results is compared. Simulations showing delayed engagement are performed with rounded tooth edges. The tooth radius is measured on worn dog clutches. Validation of the multibody simulation model of the dog clutch is performed in two steps: event validation and knowledge-based validation.

4.3.3.1 Event validation

Through event validation, the occurrence of a determined event is controlled both in modelled and real system. For detailed procedure guidelines refer to Viehof and Winner [Vie17] or Balci [Bal90] and Sargent [Sar10]. This type of validation suits perfectly for assessing the general be-

haviour of the CCDC, as the outcome of a shift can be either successful engagement, delayed engagement or tooth rejection. To achieve this, different load combinations (i.e. speed difference between clutch bodies and relative axial velocity) shall be evaluated experimentally. At the test-rig, the overlapping of tooth tips when a tooth-vs-tooth position occurs generally follows a uniform continuous distribution, whose bounds are 0 % and 100 %. In order to achieve acceptable reliability of the experimental results, 10 cycle repetitions per load step are performed. Depending on the load, either a successful / delayed engagement or a tooth rejection occurs. Simulations are performed with according loads, considering three overlapping positions of the dog clutch at tooth-vs-tooth position (10 %, 50 % and 90 %). A schematic representation is shown in Figure 4.9.

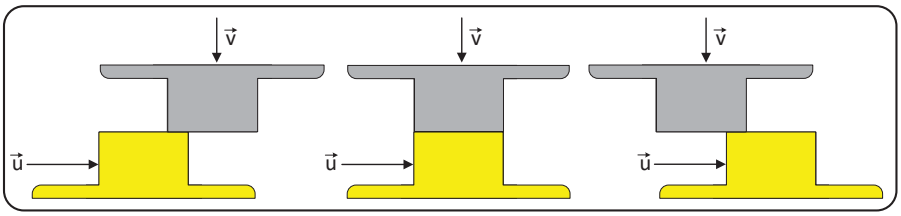

Figure 4.9: Schematic representation of considered starting positions with different overlapping toot-vs-tooth positions. From left to right: 10 %, 50 % and 90 % overlap

The simulation model is not capable of depicting a delayed engagement without rounded tooth edges. Hence, although experiments may show delayed engagement, corresponding simulations will always show tooth rejection. Delayed engagements shall be thus evaluated as an unsuccessful engagement.

4.3.3.2 Knowledge-based validation

Beside event validation, results provided by the simulation model must describe physical phenomena occurring during engagement correctly. Accordingly, all phases of the process are analysed critically, their physical feasibility assessed and eventually their correspondence with experiments proven. According to the description of Murray-Smith [Mur98], all of this falls under the process of knowledge-based validation. For instance, such test can be used to prove if the time intercurring between the moment the teeth meet their corresponding gaps and the instant the flanks come into contact and start transmitting torque. The test shall be performed for all available datasets, in order to prove model robustness.

4.3.4 Determination of influencing parameters

Once the simulation model is successfully validated, it can be used to determine the influence of design and load parameters on engagement behaviour. In particular, design parameters are fixed and peculiar of the clutch, while load parameters are actively varied during operation. Hence, geometric and design parameters influence performance and comfort of a positive clutch, load parameters are used to determine performance or comfort of a peculiar design.

4.3.4.1 Load parameters

Load parameters can be divided substantially into speed/velocity and force/torque. In particular, they are:

- Speed difference: The rotational speed mismatch between the two dog clutch bodies before engagement. In case of CCDC, it corresponds to the rotational speed of the inner dog clutch body, as the shifting element is a brake and the outer carrier stands still. The speed difference determines in turn a tangential velocity at the teeth. A too high tangential velocity can lead to tooth rejection.
- Axial piston velocity: The velocity with which the piston, and thus the connected outer dog clutch body, advances towards the rotating and axially-fixed, inner dog clutch body. The axial piston velocity is essential when the teeth of the outer clutch body meet the corresponding gaps of the inner clutch body. A too low axial speed causes the outer clutch body to advance too slowly, so that only a very limited surface overlaps when the tooth flanks meet. This may cause the axially movable outer dog clutch body to be rejected, depending on tooth geometry.
- Axial force: While the torque transmitted by the dog clutch is not determined by axial force, as happens in friction clutches, a determined axial force is necessary to engage the dog clutch and hold the engaged position. Indeed, the transmitted torque generates friction between the splines of cone and dog clutch and the corresponding carrier. Additionally, when teeth and gaps meet, if the axially movable outer dog clutch body is not able to completely shift through before the flanks come into contact, an additional friction force in axial direction is generated. Generally, the lower the radius of those sliding surfaces, the higher the friction force to be overtaken.
- Static torque: This parameter represents the torque which has to be transmitted by the shifting element independently of the shifting process. As described in Section 2.1.1, automatic transmissions are capable of powershifting. The additional torque deriving from mass synchronisation is to be delivered by the friction clutch. Furthermore, torque generates friction forces in axial direction at the splines (refer to Equation 4.13). Thus, it partly correlates with the axial force to be applied to the dog clutch for correct engagement.

Even though axial force and torque play a crucial role in determining the performance of a shifting element, their identification is not complex. Indeed, maximum static torque while shifting depends kinematically on the maximum engine torque. Those torques are linked by the constant transmission ratio between ICE output shaft and inner carrier of the clutch, except for power losses on this path. The axial force necessary to perform a successful engagement can be decomposed into different factors, as is expressed in Equation 4.13.

$$F_{ax} = F_{ax,s,f,i} + F_{ax,s,f,o} + F_{ax,s,d,i} + F_{ax,s,d,o} + F_{ax,s,d,t} + F_{spring} \tag{4.13}$$

F_{ax}	N	Total axial force	F_{spring}	N	Reaction force of wave spring
$F_{ax,s,f,o}$	N	Friction force between splines of carrier and outer friction cone(s)	$F_{ax,s,d,i}$	N	Friction force between splines of carrier and inner dog clutch body
$F_{ax,s,d,o}$	N	Friction force between splines of carrier and outer dog clutch body	$F_{ax,s,d,t}$	N	Friction force between tooth flanks of dog clutch
$F_{ax,s,f,i}$	N	Friction force between splines of carrier and inner friction cone(s)	–		

Once a dog clutch geometry has been selected, one or more load parameters can be varied. Especially speed difference and piston velocity play a crucial role in determining engagement performance of the dog clutch itself and enable comparisons between different clutch geometries.

4.3.4.2 Design & geometric parameters

Design and geometric parameters have also an important impact on engagement performance. Those parameters can be purposefully set or happen to change during operation. Thanks to the proposed method, each geometry can be characterised, allowing those parameters to be investigated and their influence on engagement performance individuated. For CCDC, the parameters described in the following were taken into account.

- Number of teeth. The influence of this design parameter on performance of the dog clutch is limited to negligible. It however influences the mechanical stability of the dog clutch. The latter can be determined for constant torque transmission with traditional finite element analyses. Conversely, the dynamic torque deriving from jerks during engagement cannot be estimated with standard tools and shall be determined e.g. through multibody analyses. Generally it can be stated that a higher number of theeth has positive effects on wear and bending stresses within the teeth, as normal contact pressure on tooth flanks - i.e. pressure in circumferential direction - is diminished by an increased overall surface. Hence, while the number of teeth has a direct influence on mechanical stability and wear, it hardly affects engagement performance of the dog clutch. Reducing number of teeth may become necessary if a too high backlash value is required.
- Tooth flank angle (γ_f). Tooth flanks may be characterised by an angle w.r.t. the axial direction in order to either facilitate or prevent disengagement during toque transmission (see Figure 5.31a). A negative flank angle, i.e. an undercut, is usually employed e.g. in synchronizers, where a disengagement during operation is not acceptable. On the other hand, dog clutches that need to operate in fail-safe mode, i.e. a disengagement has to be provided even under torque transmission, are usually characterised by positive flank angles. Be this the case, amplitude of such an angle depends mainly on self-locking of the teeth. According to Table 2.1, CCDC is characterised by flat flanks, as fail-safe operation is guaranteed by the release springs. Only variants with no backlash in fully engaged position boast a flank angle, in order to still have a backlash of 0.4° when the dog clutch

bodies are in tooth-vs.-tooth position. In this case the axial force has to be increased with respect to the variants with flat flanks. Also in this case, no appreciable effect of tooth flank angle is recognised with reference to the engagement performance, as defined above.

- Backlash S_V. It is defined as the difference between the angle of the tooth gap and the angle of one tooth. It thus determines how much play the clutch has between opposite flanks of each tooth or gap. According to the definition of limit relative engagement angle given in Equation 4.17, the circular backlash has indeed a direct influence on engagement performance. It is hence possible to determine the effect of circular backlash on engagement performance by determining, ceteris paribus, engagement performance for different circular backlash values. An increase in circular backlash in order to increase working regions and performance of the dog clutch is effective until a certain point. An optimal backlash value has to be chosen depending on specific requirements of the system in terms of needed working conditions and acceptable comfort. Indeed, an increased backlash causes the dog clutch to have more rotational play. This in turn can lead to higher jolts during both engagement and torque reversing.
- Tooth face shape. This parameter can sensibly influence engagement performance. However every tooth shape may also show drawbacks in terms of comfort, wear, costs, etc. For instance, the Maybach tooth geometry presented in Section 2.2.2, while facilitating engagement by giving the actuated dog clutch body an initial axial speed during the tooth-vs.-tooth phase, can only engage under definite speed differences of the shafts and are subject to increased wear rates. Similar geometries of tooth faces are to be found in splined clutches, e.g. in synchronizers. Flat tooth face shapes are not capable of directing the movable dog clutch body during tooth-vs.-tooth phases, yet they are cost-effective and robust. Additionally, they can be operated indistinctly with positive and negative rotational speed differences. Because on the many cross influencing parameters, determination of the influence of tooth face shape on engagement performance is not feasible by means of one analytical equation, as is done for backlash.
- Tooth edge rounding (r_f). Rounding of tooth edges may be performed purposefully (see Figure 5.33). However, the main reason for this parameter to exist is wear, which in turn means that said rounding generally appears and increases during operation. Therefore, this parameter has to be considered during design and initial performance assessment of the dog clutch geometry. Especially rounding of tooth edges, whose corresponding flanks are torque-transmitting, is responsible for performance reduction. In fact, the minimum axial tooth-flank overlap (see Equation 4.17) has to be increased when rounding of tooth edges is present. On the contrary, perfectly sharp edges can transmit torque over the whole axial length of tooth flanks. Indeed, rounding of tooth edges can be assimilated to a ramp, which generates a torque-induced friction force opposing to the actuator force. In this case, the engagement performance depends on the derivative of the curvature.

For better evaluation of this effect, the radius of the rounding must be known. The most reliable method for determination of wear effects is to perform several misuse shifts at the test-rig under severe load conditions. After the experiment, the radius of the wear-induced curvature can be measured and transferred to the 3D model. A new performance limit can be eventually determined through simulation and the possibly-diminished performance evaluated.

4.3.5 Engagement performance

Generally, coefficients of friction of steel-vs.-steel contacts between splines and tooth flanks are of difficult determination and depend on many factors. Additionally, torque splitting between cone and dog clutch is not analytically determinable. It is hence advisable to determine the necessary axial force experimentally, taking care of adding a sufficient reserve.

On the other hand, velocity parameters have a predominant impact on engagement performance of the dog clutch. Furthermore, rotational speed is difficult to control, as it depends on several kinematic and dynamic factors, which in general are different at every gearchange. Finally, axial speed of the piston is controlled by the TCU, yet circumferentially the relative position occurs randomly. For this very reason, it is important to determine the maximum allowable speed difference and the minimum required axial velocity. This way, the performance of the dog clutch can be guaranteed for safe operation in all working conditions.

4.3.5.1 Relative engagement angle

Even though axial velocity and circumferential speed difference are originated from independent sources, their interaction determines whether an engagement is going to be successful or not. In order to better understand said interaction, two points P and P' are defined on the axially movable and the rotating dog clutch body, respectively, as shown in Figure 4.10. Those points coincide when a full engagement of the clutch has taken place. No angular accelerations are considered until before engagement jolt. As a starting time, the instant is considered when two adjacent, non-torque-transmitting flanks have the same angle (marked red in Figure 4.10). In the following, let the circumferential speed of the rotating dog clutch body be identified by the vector $\vec{u}$ and the axial velocity of the actuated dog clutch body be identified by the vector $\vec{v}$. Accordingly, the point P is characterised by velocity $\vec{v}$, while P' is characterised by velocity $\vec{u}$. A schematic representation of those parameters can be appreciated in Figure 4.10. Here, the initial instant t is considered, as well as the time increment Δt necessary for the torque-transmitting tooth flanks to come into contact. For better comprehensibility, an arc of the clutch including 3 teeth is represented as straight.

In general, when the two dog clutch bodies meet at this point, two starting conditions can be met before engagement: Either tooth-vs.-toot or tooth-vs.-gap position can occur. Depending on the circular tooth backlash, as described at the beginning of Section 4.3, probability of one event

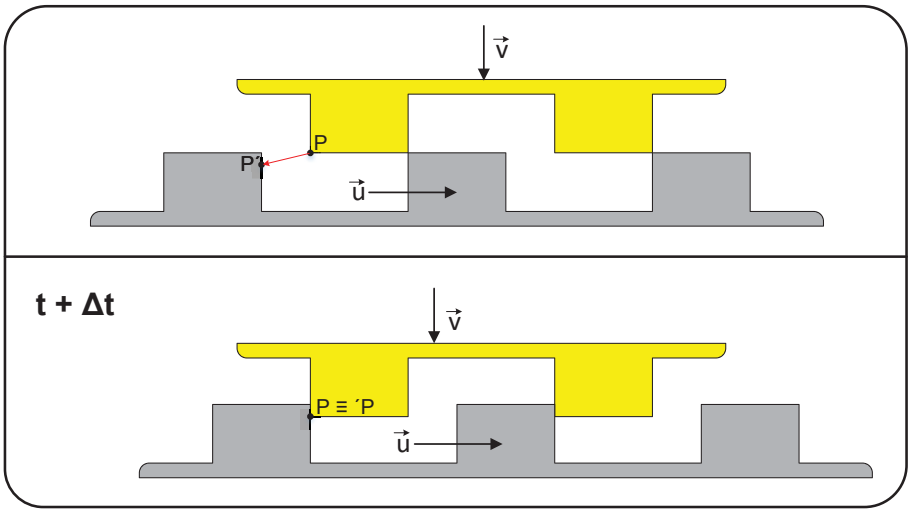

Figure 4.10: Representation of the tooth engagement process. The axially movable dog clutch body (yellow) moves toward the rotating dog clutch body (grey). At time instant $t + \Delta t$, the torque transmitting flanks come into contact

rather than the other varies. However, if after a tooth-vs.-gap position the overlapping surface of flanks is too limited and contact pressure is too high, a tooth rejection can occur. Indeed, wear and manufacturing tolerances can cause the axially movable dog clutch body to be rejected again to eventually engage in the following gap. If this is the case, a tooth-vs.-tooth position can be considered as a second starting condition of the engagement. Otherwise, the dog clutch has successfully engaged. Both starting conditions can thus be led back to a tooth-vs.-tooth position in the worst-case scenario. In such a case, the starting position is the same as shown in Figure 4.10.

Considering the vectors $\vec{u}$ and $\vec{v}$, it appears clear that their module - taken singularly - does not affect engagement behaviour, rather than the combination of both vectors. Let $\overrightarrow{P'P}$ be the vector that unites the points P and P'. The module of said vector is maximum at the starting position (time instant t) and equals zero when engagement is complete. The time derivative of vector $\overrightarrow{P'P}$ represents in turn the velocity of P' relative to P, or vice versa. It can be also expressed as the vector difference between $\vec{v}$ and $\vec{u}$, since constant velocities and thus no accelerations are considered. Let this latter vector be $\vec{w}$.

$$\vec{w} = \vec{v} - \vec{u} = \frac{d}{dt}(\overrightarrow{P'P}) \tag{4.14}$$

Generally, point P can be determined geometrically by intersecting the trajectory of P' relative to P and the equation of the tooth flank. The reference system is positioned on the contact tooth flank at its root. When point P coincides with the origin of said reference system, a full engagement occurs. Position of point P depends on different geometric quantities (such as tooth flank height, inclination, angular backlash) and on vectors $\vec{u}$ and $\vec{v}$. Mathematically, the general coordinates of P with reference to the aforementioned reference system are expressed in Equation 4.15. The setup is shown in Figure 5.31a.

$$\begin{cases} x_P = \dfrac{\left[\frac{|\vec{v}|}{|\vec{u}|}\cdot\left(S_V\cdot r_{DC,o}+h_t\cdot tan(\gamma_f)\right)-h_t\right]}{\frac{|\vec{v}|}{|\vec{u}|}+cotg(\gamma_f)} \\ y_P = \dfrac{\left[\frac{|\vec{v}|}{|\vec{u}|}\cdot\left(S_V\cdot r_{DC,o}+h_t\cdot tan(\gamma_f)\right)-h_t\right]}{\frac{|\vec{v}|}{|\vec{u}|}\cdot tan(\gamma_f)+1} \end{cases} \tag{4.15}$$

$\vec{u}$	m/s	Circumferential speed	$\vec{v}$	m/s	Piston axial velocity
γ_f	rad	Tooth flank inclination angle	S_V	rad	Angular backlash (fully engaged)
$r_{DC,o}$	m	Dog clutch outer radius	h_t	m	Overlap with fully engaged teeth

The direction of vector $\vec{w}$ appears hence to be a sufficient parameter to determine if an engagement is to be successful rather than not. The absolute value of the vector has no influence on the engagement performance of the clutch, but withal on its comfort. For instance, engagement may occur under increased rotational speed on condition that high enough axial velocity be provided. Conversely, its direction determines the approach line between P and P' and is essential to evaluate performance of the clutch. For better understanding, in the following, the direction of vector $\vec{w}$ is defined through the angle between $\vec{w}$ and $-\vec{u}$, as represented in Figure 4.11 and expressed in Equation 4.16. Let said angle ε be the relative engagement angle.

$$\varepsilon = arctg\left(\frac{|\vec{v}|}{|\vec{u}|}\right) \tag{4.16}$$

According to this definition, the relative engagement angle ε can be used for performance assessment of a dog clutch. In fact, the lowest possible relative engagement angle can be identified as the limit beneath which tooth rejection occurs. The angle - hereinafter ε_{lim} - can be determined analytically as in Equation 4.17.

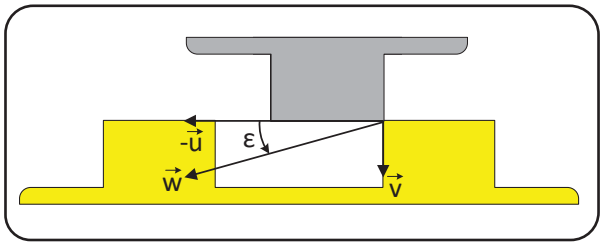

Figure 4.11: Schematic representation of velocities and ε during engagement

$$\varepsilon_{lim} = arctg\left(\frac{l_{min}\cdot\Delta t}{\widehat{S_V}\cdot r\cdot\Delta t}\right) \tag{4.17}$$

ε_{lim}	rad	Limit relative engagement angle	l_{min}	m	Minimum axial tooth-flank overlap
$\widehat{S_V}$	rad	Circular backlash	r_m	m	Average tooth radius
Δt	s	Engagement time	$-$		

However, even if the limit angle is determinable analytically, the minimum axial tooth flank overlap which avoids rejection is to be determined otherwise. In the proposed method, the aforementioned simulation model is used, after a thorough validation with experimental data. Given fixed geometry and design, as well as load torque and axial force, determination of ε_{lim} is performed as follows. Simulations are started with a definite value of axial velocity of the piston,

that is of the absolute value of vector $\vec{v}$. Such value shall be acceptable and realisable by the hydraulics of the system. With the axial velocity fixed, one rotational speed of the rotating clutch body is guessed, i.e. absolute values for vector $\vec{u}$ is set.

After performing the according simulation, if successful engagement is achieved, the rotational speed is further increased, until a simulation showing tooth rejection occurs. From this point on, the greatest speed value showing clutch engagement, i.e. the smallest speed value causing tooth rejection, can be determined with a chosen accuracy. For limit engagement angle determination of the dog clutch of CCDC, an accuracy of $\pm$ 1 rpm is used. The same procedure is to be repeated for different values of the piston axial velocity, in order to increase the final accuracy in determining ε_{lim}. Given the linear correlation between $|\vec{u}|$ and $|\vec{v}|$ for finding ε_{lim} (see Equation 4.17), the initial rotational speed for the subsequent step can be more closely guessed.

Once a sufficient number of limit points of $|\vec{u}|$ and $|\vec{v}|$ have been determined, they can be plotted against each other and a linear regression performed. Due to the linear nature of the correlation, the gradient of said function corresponds to the tangent of ε_{lim}.

4.3.5.2 Optimisation

The parameter ε_{lim} can be used to assess defined geometries and to compare them with others, or to perform sensitivity analyses, e.g. on design parameters. It thus provides an objective criterium to perform optimisation of the working field.

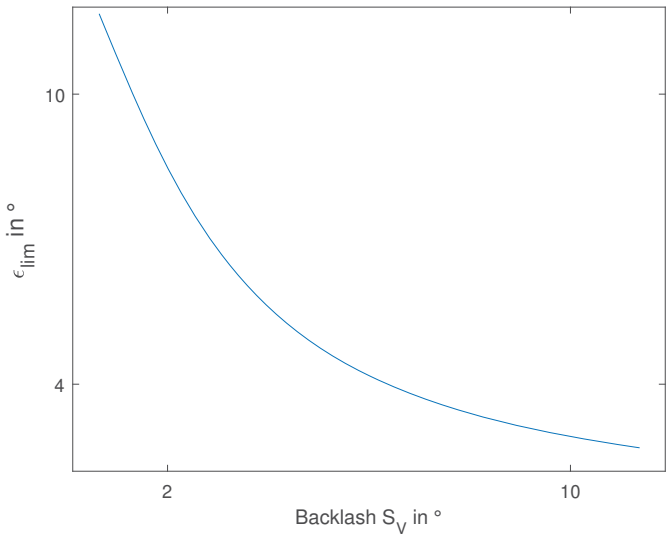

Figure 4.12: Exemplary plot of limit relative engagement angle ε_{lim} vs. backlash S_V

It is observed that the parameters described above, while all having an influence on engagement behaviour, impact differently on performance. The aim of operational optimisation is designing a dog clutch geometry capable of providing fair engagement behaviour both at low axial velocities and high rotational speeds. Such optimisation is, however, subject to boundaries. In particular, the clutch has to meet high comfort standards, as a worsening of shifting comfort is not acceptable for CCDC. On the other hand, also mechanical stability may become an issue, if, for instance, the number of teeth has to be reduced as a consequence of an increased backlash.

The first parameter to consider is indeed circular backlash. Its influence on engagement behaviour is to be carefully considered, especially at very low values. As is exemplarily shown in Figure 4.12, influence on the relative limit engagement angle ε_{lim} decreases with increas-

ing values of backlash, as the curve flattens. How fast the curve flattens depends in turn on the minimum tooth-flank axial overlap l_{min} and on the average tooth radius. According to the analytical equation formulated in Equation 4.17 and to experimental and simulative results, an optimal backlash value $S_{V,opt}$ is defined. Beyond said value, an increase in backlash would not lead to appreciable improvements in terms of engagement performance. Conversely, smaller values of $S_{V,opt}$ would lead to a considerable reduction of engagement performance. The value of $S_{V,opt}$ is determined by solving Relation 4.18.

$$\left.\frac{d\varepsilon_{lim}}{dS_V}\right|_{S_{V,opt}} \in (-4;-2) \tag{4.18}$$

Depending on working conditions, such as direction of speed difference and of torque, different tooth face shapes may be designed. Contrary to backlash, tooth face shape cannot be expressed by just one parameter. Hence, basing on known conditions, several dog clutch geometries are to be designed and evaluated. Evaluation of performance occurs subsequently through parameter ε_{lim}. Indeed, also tooth face shape has an impact on the minimum tooth-flank axial overlap l_{min}. Once a geometry with sufficiently low values of ε_{lim} is found, the benefits in terms of engagement performance are to be weighed versus manufacturing costs (deriving e.g. from tooth flank angle) and possible early degradation of the dog clutch.

4.3.6 Comfort optimisation

Comfort optimisation refers to the improvement of the driver's feeling during a gearshift when the positive-fit clutch engages. Due to the nature of CCDC, the dog clutch is not only to engage under speed difference, but also under a load torque, which diversifies it from e.g. classic synchronizers. As comfort refers to a subjective feeling, parameters are to be defined, which can well and objectively replicate said feeling. In order to perform a comfort optimisation, seven parameters directly correlated with a powershift are defined as representative for CCDC. They are listed in the following.

- Shifting time t_s. A comfortable gearchange is theoretically characterised by a long shifting time, in order to seamlessly unite the output torques generated by going and coming transmission ratios. However, increasing the shifting time implies increasing the slipping time of the clutch. While shifting time does not affect friction loss in shifts with traction interruption, it very well does when powershifts are considered. Hence, when performing powershifts with long sliding times, the friction clutch may reach its performance limits. Additionally, long shifting times affect the psychoacoustic perception of the driver, suggesting a slow response to the gearchange.

- Specific friction loss of disengaging clutch q_D. As mentioned above, increased sliding time imply higher friction losses when powershifts are considered. Hence, even though it is not

a comfort parameter, friction loss at the disengaging clutch in the automatic transmission is evaluated in order to determine if a shift is within the performance of the friction clutch. In case of a downshift from 5th to 4th speed in reference AT, clutch D disengages (refer to Table A.1).

- Maximum specific friction power at CCDC during dog clutch engagement $\dot{q}_{CCDC}$. For dog clutch engagement, a relative rotation between dog clutch bodies is necessary when a tooth-vs.-tooth position occurs. The higher the circumferential overlap, the higher such rotation is, which occurs in correspondence of the maximum axial force at the cone clutch. In addition to rotation, the maximum speed mismatch reached is also crucial for friction power determination. The entity of speed mismatch is in turn dependent on actuator force control. The maximum friction power - which occurs immediately before tooth flanks come into contact - is hence also considered as control parameter, as it gives information on the feasibility of the chosen shifting strategy, depending on the thermomechanical performance limits of the cone clutch.

- Torque gradient ΔT. When tooth flanks come into contact, the rotating shaft comes to an abrupt halt and torque can be transmitted to the transmission's output. Due to the presence of a dog clutch, the reaction torque insisting on CCDC is not limited by friction. Thus it depends only on the amount of torque reduction at the disengaging clutch. For instance, in the extreme case of an infinitely slow friction torque reduction at the disengaging clutch, ΔT = 0 Nm. On the contrary, should the disengaging clutch be completely released during dog clutch engagement ΔT would be maximum and correspond to the load torque. Hence, ΔT gives an idea on the shifting control at both CCDC and disengaging clutch.

- Gradient of actuator force of disengaging clutch ∇F_D. Unlike performance tests, gearshifts in automatic transmissions are carried out by letting the coming and going clutches interact with each other. This prevents the transmission to deliver negative torque for a short time during the shift, allowing a seamless gearchange. Precise control of the correct actuator force gradient of the clutch determines success and comfort of the gearchange. In general, the flatter the force curve versus time, the more comfortable the gearshift, as the shifting time increases. However, higher force gradients may be needed to perform quicker shifts, especially when performing sporty gearchanges.

- ICE overshoot or flare Δn_{ICE}. When engagement of the dog clutch occurs, the - albeit small - speed difference is instantaneously reduced to zero. Considering the transmission ratio between shifting element and transmission input shaft and neglecting damping of the torque converter, this causes an overshoot at the ICE, which is not easily controllable by the engine control unit. This phenomenon is usually perceived as negative by the driver and is to be reduced to a minimum.

- Rotatum ζ. This value represents the variation of torque with respect to time immediately after dog clutch engagement. It can be, in this particular case, assimilated to rotational and eventually longitudinal jolt at CCDC and the vehicle, respectively. Analytically, jolt is defined as the derivative of acceleration. In CCDC, jolt is mainly generated concomitant with dog clutch engagement. Due to the nature of this inelastic collision, rotational acceleration gradients tend to be very high, amplifying possible measurement or simulation errors. It is hence chosen to evaluate jolt basing on the torque step steepness arising during engagement of the dog clutch and consequent torque takeover.

While experimental determination of those parameters is very laborious if possible, it is less time-consuming with a simulation model. In fact, while experiments would require a vehicle with an already working CCDC, different simulation environments can be combined to create a vehicle model. In particular, for determination of the aforementioned parameters, parts of the existing and validated model of the shifting element are integrated in the AT-system, replacing the target multiple disc wet clutch. The multibody simulation model of the reference automatic transmission is built by assembling the epicyclic gear sets and connecting their suns, carriers and rings to each other, the shifting elements or the housing, according to the transmission design. Torsional elasticities are evaluated by considering the cross sections of the shafts analytically. Mesh stiffnesses of all gears are calculated utilising the FVA software STPlus and are accordingly implemented in the multibody simulation models of the planetary gearsets. For this purpose, the mean value of mesh stiffness per unit face width c_γ is used. For more detailed information on determination of mesh stiffness, refer to Otto et al. [Ott17]. The transmission is driven by an ICE, which is modelled according to literature values referring to the chosen reference vehicle. As modelling of the ICE is not part of this study, the model is kept fairly simple. Controlling of the ICE during gearchanges is performed in Matlab-Simulink. On the other hand, the output shaft of the transmission drives the rear wheels of a vehicle model. Representative vehicle data can be retrieved from the OEM. Thanks to the vehicle model, capable of representing longitudinal and lateral dynamic behaviour, accelerations deriving from gearshifts can be simulated.

Once the simulation model is correctly set up, a reference is to be determined by performing simulations with the original system. In this case, all shifting elements of the reference automatic transmission are modelled as multiple disc wet clutches. Eventually, the chosen shifting element is replaced with a CCDC and the same simulations are performed. Thanks to comparison and analysis of the aforementioned comfort parameters, a comfort rating relative to the original system can be computed. Due to the simplifications undertaken, a comfort assessment basing on absolute values is not recommended. Comparative performance optimisation shall eventually lead to a shifting element design being no less comfortable than the original one.

In order to perform comparisons between original multiple disc wet clutch and CCDC, reference

gearshifts are to be defined. In general, load conditions of said gearshifts are to be assumed in worst-case scenarios. As TCUs are programmed to avoid gearshifts in conditions that would damage the transmission, a manually triggered gearshift is utilised for this purpose. Depending on it being either an upshift or a downshift, appropriate starting conditions are to be set. However, as load toque has a major impact on engagement comfort, it has to be assumed at its maximum value. Initial speed difference between inner and outer carrier is of less importance to engagement behaviour, as it is reduced by the cone clutch. It however has to be chosen in a range to allow the ICE to still be capable of delivering maximum torque at new speed determined by the coming transmission ratio.

Once transmission input speed and torque are chosen, parameters of the shift control have to be set. Particularly, the torque overlapping of opening and closing shifting elements, along with the gradient of axial piston force at the disengaging clutch. Setting of those parameters is arbitrary within a limited range, as they determine if the performed gearshifts are perceived smoother rather than more sporty. For automatically triggered shifts, such setting depends also on the driver's behaviour. In order to cover all possible scenarios, three gearshift types are defined. They are classified as reference, comfort and sport shift, depending on the torque gradient insisting on the engaging shifting element. While a comfortable and thus smooth gearchange is characterised by lower torque gradient, i.e. by an increased shifting time, a sporty gearchange features a rapid torque increase and as a consequence possibly a perceivable jolt. Even though such jolt is a drawback deriving with rapid toque takeover between shifting elements, it is generally not rated as negative, as it gives the driver a feeling of increased sportiness. This is confirmed, amongst others, by Robinette et al. [Rob14, Rob15], Ranogajec et al. [Ran18] and van Berkel et al. [van14]. Control of opening and closing shifting elements is implemented basing on Fischer et al. [Fis15]. Indeed, ICE intervention during shifts is state-of-the-art for modern automatic transmissions. Accordingly, the model proposed by Förster et al. [För91] is not pursued further, for it does not consider engine support. An optimisation algorithm is not part of this work, yet many studies have been performed on this subject. For more accurate information, refer to the aforementioned literature.

Simulation results can be eventually used to compute the comfort rating parameters presented above. A comparison can be made between powershifts with CCDC and ones with a standard multiple disc wet clutch. If all simulated shifts with CCDC cannot match the comfort performance of the original multiple disc wet clutch, a further system optimisation is to be performed. In particular, the circular backlash may be reduced or teeth geometry modified in order to achieve a two-step engagement. Nonetheless, it appears clear that the main factor influencing powershift control is its control. State-of-the-art TCU can overcome to such highly dynamic and precise demands without difficulty.

4.4 Summary

In the present Chapter, a method for designing and optimising coupled cone and dog clutches for automotive applications is presented. As the functionality of the novel shifting element is split into two parts with different tasks, so are the optimisation methods. In fact, being the tasks of synchronising shafts and transferring static torque taken over by two different clutches, their optimisation can to a great extent be performed independently.

Task of the cone clutch is to synchronise inner and outer carrier by means of friction torque. Friction torque is generated by axial force made available by the TCU-controlled actuator. Like torque generated with a conventional multiple disc clutch it is proportional to the actuator force, yet it is increased by a factor determined by the cone angle (cf. Section 2.2.3). While such torque increase is beneficial as it allows friction surface and hence drag loss reduction, it results in higher specific friction loss and power, possibly leading to hotspots. In order to prove that CCDC is not affected by such phenomenon within its working region, a novel method for thermomechanical performance determination is proposed. Firstly, a finite element simulation model is set up. It combines undemanding mechanical and thermal finite element analyses. The highly unsteady synchronisation process is divided into time intervals whose duration is sufficiently small to perform quasi-static simulations, enhancing linearisation of a strongly non-linear problem. Results of the thermomechanical simulations are utilised to compute temperature and strain/stress distributions within the whole clutch. Every simulation is set up considering initial speed difference, axial force and reduced inertia as input parameters. Simulative data is utilised for training an a neural network. Inputs form simulations are generated aleatory, in order to improve training and reduce risk of overfitting. Results are used to calculate performance curves by identifying which load parameter combinations result in temperatures higher than the critical one. Critical temperature is identified when experimental and simulative results start to diverge and is consistent with values found in literature.

Dynamic engagement performance optimisation of the positive clutch is performed parallelly to thermomechanical performance optimisation. Performance limits of the dog clutch are identified by setting up a multibody simulation model. Its validity is proved with test-rig experiments. The validated simulation model can be eventually utilised to determine engagement performance limits of the dog clutch. Performance is evaluated by means of allowed minimum axial piston velocity and maximum tangential teeth velocity, i.e. speed difference. Those values are analytically combined, resulting in the engagement angle ε. Accordingly, the limit engagement angle ε_{lim} determines the performance of the dog clutch, i.e. the maximum allowable speed difference or the minimum necessary axial speed between claw bodies that still allow correct engagement to occur. In turn, ε_{lim} depends on a number of design parameters, the most predominant being circular backlash. As ε_{lim} defines the performance of each dog clutch design, it is used to compare different dog clutch designs and enable improvements. It can be further utilised to describe degradation effects, such as wear.

Finally, comfort optimisation is performed. It consists of evaluation of selected parameters that give information about behaviour of CCDC during engagement and its effects on the driver. However, being comfort subjective to the driver, those parameters are to be confronted with the same resulting from gearchanges with conventional multiple disc wet clutches. Comfort rating parameters are calculated by developing a simulation model of the whole reference vehicle. A reference gearshift is chosen. The selected gearchange is simulated with two further driving modes, which emphasise sportiness and comfort, respectively. Improving shifting comfort by acting on the design of CCDC has generally negative effects on both thermomechanical and engagement performance, as these functions are in conflict with comfort. Notwithstanding this, limited improvements in the control logic can effortlessly obviate minor comfort reduction issues.

The steps to follow for method application are shortly summarised here.

Thermomechanical optimisation

1. Define a valid simulative setup for thermomechanical simulation utilising an easily parametrisable finite element simulation and plausibilise it through appropriate convergence analyses.
2. Define an experimental setup which allows multiple temperature measurements under variation of the operational parameters J_{red}, v_g and p_{avg}.
3. Validate the simulation model by comparing simulations with experiments and identify critical operational conditions of the friction clutch.
4. With the validated parametric simulation model, perform multiple calculations within defined working regions to train a validate neural network.
5. Define critical working regions by utilising the limit values found in 3 (e.g. ϑ_{crit}). By time-effective result extrapolation, postprocess results and identify optimal designs.

Dynamic optimisation

1. Define a valid simulative setup for dynamic simulation utilising an easily parametrisable multibody simulation and plausibilise it through appropriate convergence analyses.
2. Define an experimental setup which allows engagement performance evaluation under variation of the operational parameters $\vec{v}$ and $\vec{u}$.
3. Validate the simulation model by comparing simulations with experiments and identify critical operational conditions under which engagement cannot be guaranteed.
4. By applying the proposed analytical approach, define each design variant of the dog clutch by its limit relative engagement angle.
5. Easily compare multiple dog clutch designs and identify those which fit best the requirements of the system.
6. As a last step, create a robust multibody simulation model of the reference transmission and assess shifting comfort of the designed CCDC.

5 Method application

The method for performance assessment and optimisation for coupled cone and dog clutches presented in Chapter 4 is applied to CCDC in order to prove its effectiveness. Results are presented in the present chapter.

In the first section, the cone clutch is analysed. The thermomechanical simulation model will be shown into detail, as well as its validation with experimental results. Performance limits of the friction clutch will be calculated and identified thanks to the trained neural network. According to obtained results, effects of design parameters will be investigated. Eventually, in the last section, design recommendations in order to achieve an optimal design will be presented.

In the second section, engagement performance of the dog clutch will be analysed. It will be compared to performance obtained by varying selected design parameters, in order to establish their effects on engagement performance and choose an optimal solution.

5.1 Thermomechanical performance of CCDC

In the present section, thermomechanical performance of CCDC is determined according to the method presented in Chapter 4. First the simulation model of the cone clutch is presented. The cone clutch of the second CCDC variant is selected for method application. An experimental validation with the new geometry is necessary, for the second design variant of CCDC features a reduction of friction surfaces and a position switch of cone and dog clutch in the axial force flow. Furthermore, the non-rotating piston of the actuator acts directly on the rotating inner ring, creating de facto another friction surface. Friction generated on such a surface is small, as it is designed to serve as an axial sliding bearing, yet it is not negligible.

5.1.1 Simulation model

In order to gain in computational efficiency, only the mere cone clutch and the relative axial fixation parts are considered. The latter are the piston and a locking ring for inner and outer cone, respectively. In order to guarantee maximum flexibility for parametric studies, all dimensions and material parameters can be adjusted independently of each other. Inner and outer carrier are not modelled. Material of all bodies is steel, but for the friction lining. The latter is a HC310 dual layer carbon friction lining, which presents outstanding qualities in terms of friction stability, wear resistance, load capability and lubricant compatibility. Material properties for both materials are summarised in Table 5.1.

Friction power is completely converted into heat flux, according to Equation 4.8. As mentioned above, friction occurs both between the cones of the cone clutch and between inner cone and piston. Coefficient of friction varies depending on material and lubrication of the friction partners. Coefficient of friction of partners steel and HC310 carbon lining is determined experimentally through endurance shifting tests. For this purpose, braking shifts with the first variant of CCDC

Parameter	Symbol	Unit	Steel	HC310
Young's modulus	E	N/m^2	210·10^9	1.1·10^9
Poisson's coefficient	ν	–	0.30	0.25
Density	ρ	kg/m^3	7770	1200
Thermal expansion coefficient	α	K^{-1}	13.3 · 10^{-6}	70.0·10^{-6}
Specific thermal capacity	c_p	kJ/(kg·K)	0.58	1.50
Thermal conductivity	λ	W/(m·K)	43.5	0.325

Table 5.1: Main characteristics of CCDC in its second design variant

are utilised, as no other sources of torsional friction are present in the system. As can be appreciated in Figure 5.1b, coefficient of friction shows a slight dependency on tangential speed. However, for simulation purposes it is kept constant and its average value μ_{avg} considered. Reference endurance test for CoF determination is run for 10,000 cycles. Oil temperature is set to ϑ_{oil} = 80 °C. As can be appreciated in Figure 5.1a, a nearly constant value of μ_{avg} = 0.10 is measured during the whole test. Running-in effects, which extinguish within the first 500 shifts, may be neglected. Also load-dependent variations in coefficient of friction are not considered. Finally, also friction behaviour degradation is not considered, as none could be observed during endurance tests with CCDC. In [Sto20], Stockinger et al. identify the value $\mu_{min,Grad}$ as the one of the decisive factors for describing degradation of friction behaviour in cone clutches. $\mu_{min,Grad}$ is defined as the negative gradient of minimum coefficient of friction μ_{min} in the range between 33 % and 100 % of the number of cycles. For the reference endurance test, $\mu_{min,Grad}$ almost equals zero, as can be seen in Figure 5.1.

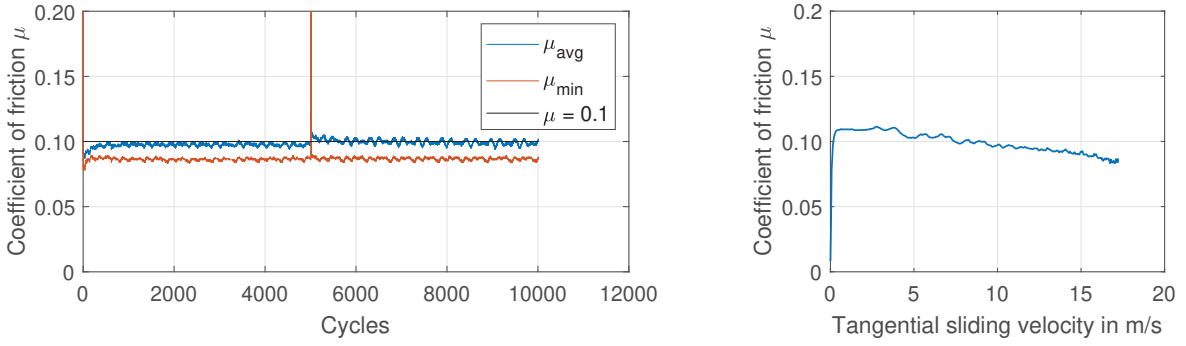

(a) Trend plot of average and minimum coefficients of friction during endurance test

(b) Coefficeint of friction vs. sliding speed at shift 10,000

Figure 5.1: Measured signals of coefficient of friction for endurance test with p_{avg} = 2 N/mm^2, q = 1 J/mm^2 and $v_{g,0}$ = 17.2 m/s. Oil temperature ϑ_{oil} = 80 °C

Long term degradation of friction according to Stockinger et al. can be observed during purposely performed misuse endurance tests. Notwithstanding importance of such results, they are not considered for determination of coefficient of friction. Indeed, misuse shifts are not expected to occur several times, so to cause degeneration of friction behaviour.

For the second friction surface of the system (i.e. steel cone vs. piston), material of both

sliding partners is steel. In this case, provided lubrication is sufficient to avoid scuffing, the experimentally determined coefficient of friction μ_{steel} = 0.05. Considering a cone angle of α = 10°, it can be stated that at least 92 % of friction torque is transmitted through the cone clutch. With such settings, simulations are performed. In order to save memory, only selected results are saved during simulation as text files. The latter are in particular: Thermal and mechanical stresses and strains in radial, axial and circumferential direction, node temperatures and friction surface contact pressure. Post-processing of the results is done with Matlab. This way, the key results can be visualised in a compact and effective way. Of particular interest is the evaluation of such outputs at the friction surface, where they are expected to reach their maximum values. Additionally, their distribution over the axial width of the surface can be easily determined. For instance, in Figure 5.2, simulated temperature at the friction surface for different load cases is shown versus time. It can be appreciated that increased load conditions, while leading to higher maximum temperature, also cause the latter to concentrate on a different portion of the friction surface.

Further, it can be noted that the temperature concentration is more acute in shifts with higher friction power, rather than in shifts with increased friction loss. Such information is utilised to visually validate the hotspot position by confronting simulations with marks on the steel cone of the clutch subjected to misuse shifts.

5.1.2 Experimental setup

Experiments are carried out at the braking test-rig ZF/FZG KLP-260. A schematic representation of the KLP-260 along with its main characteristics can be appreciated in Appendix A.4. Being the KLP-260 a braking rig, the outer carrier is fixed to the housing, whilst the inner carrier can rotate. The rig can operate either in braking or in slipping mode. In the first case, a selectable inertia is mounted on the shaft and hence connected to the inner carrier. An electric motor accelerates the shaft with its inertia to the desired speed and disconnects through a magnetic clutch. Only then the clutch is actuated by the hydraulic piston, accordingly braking shaft and inertia. In slipping mode, the rig is connected to a transmission and a different electric motor via a dog clutch. Being mentioned transmission ratio relatively high, the motor can transmit extremely high torque at relatively low speed.

Experiments for testing thermomechanical performance of the cone clutch are performed in the first mode. With the KLP-260, the whole shifting element can be tested. Two shafts are connected to inner and outer carrier, respectively. The outer carrier does not rotate. A load cell with a fixed lever arm reacts to the transmitted torque. The inner carrier is connected to the rotating shaft, to which a tuned inertial mass can be connected. The piston is actuated hydraulically. Its force is measured via a load cell, which is interposed between hydraulics and the piston itself. Along with force, the axial displacement is also measured.

Experiments for thermomechanical stability determination are carried out without engagement

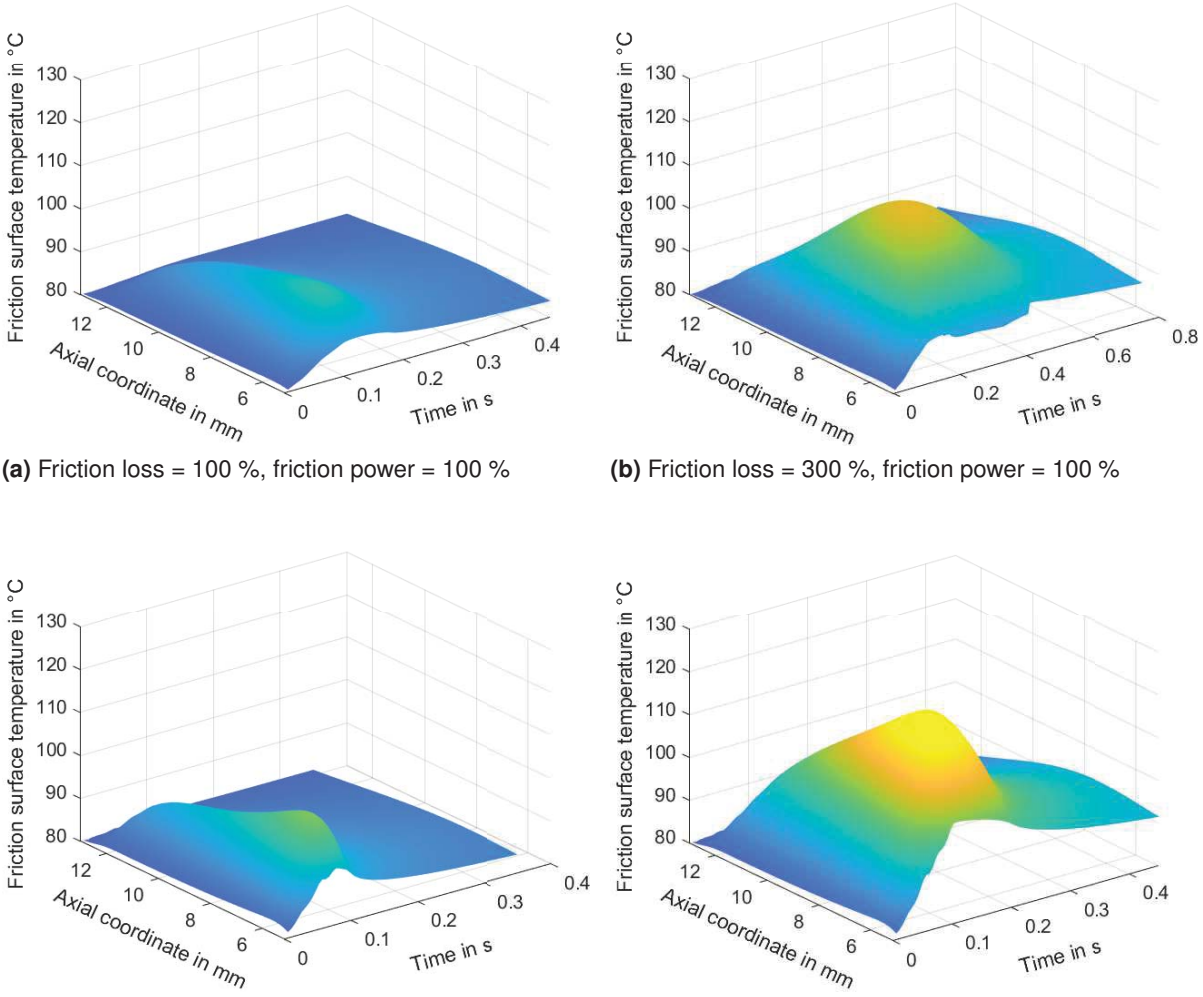

(a) Friction loss = 100 %, friction power = 100 %

(b) Friction loss = 300 %, friction power = 100 %

(c) Friction loss = 100 %, friction power = 140 %

(d) Friction loss = 300 %, friction power = 140 %

Figure 5.2: Simulated maximum temperature at friction surface arising during synchronisation vs. time and surface axial length. Starting temperature ϑ_0 = 80 °C

of the dog clutch. In fact, the axial force is not increased after synchronisation is completed and the prestressed spring prevents the piston to advance further.

5.1.2.1 Temperature measurement

Core element of such experiments is the temperature measurement. Temperature measurements through thermocouples are chosen due to their accuracy and effectiveness. Sensors are applied to the non-rotating clutch body. Measurements on the rotating body would be ineffective, as due to the low thermal conductivity of the friction layer, almost no energy flows to the inner ring. Additionally, an expensive wireless telemetry would be required to collect signals. The only surface accessible through the outer carrier is the external side of the outer steel ring. Being the thickness in radial direction of the outer steel cone limited, the thermocouples cannot be integrated within the clutch body. For this very design setup, a solution is chosen, with thermocouples directly applied to the surface. The application of the thermocouples on the outer

surface is shown in Figure 5.3.

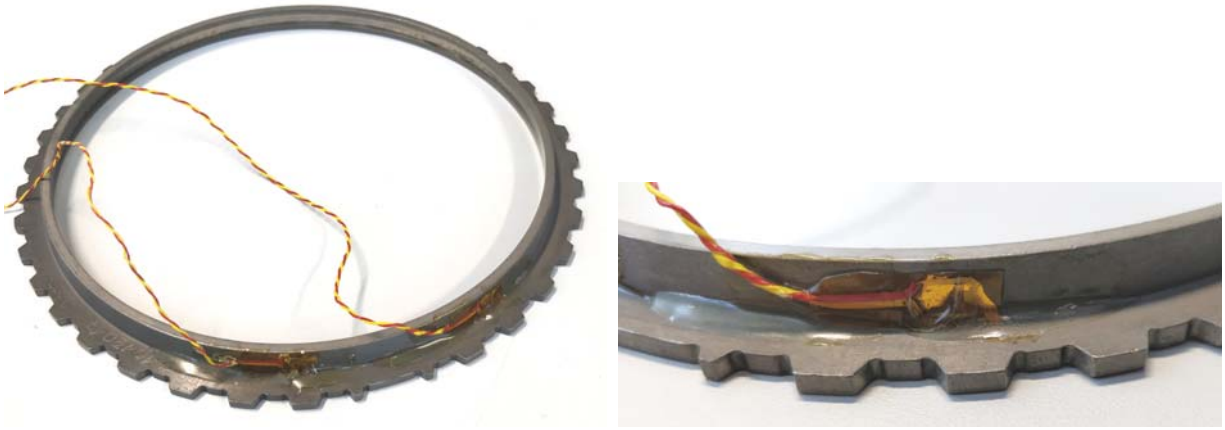

(a) Disposition of the thermocouples **(b)** Detail of the application

Figure 5.3: Application of thermocouples on the outer ring of CCDC in its second variant

The application of the sensors to the friction surface is an extremely delicate process. Indeed, any air intrusion between sensor and steel body has to be avoided, in order to avoid increase in thermal resistance. This would on one hand lead to lower measured temperatures, and on the other hand to a sensible time delay between real and measured value. The contact between sensor and clutch body is improved by using a heat transfer medium in form of a paste. It is essential that the flash point of the paste itself is never exceeded to avoid burning byproducts, which would in turn deteriorate the heat transfer qualities. For this reason, as high temperatures are to be expected during testing, a paste on a gallium basis is chosen. Beside excellent resistance to high temperatures, the paste shows high thermal conductivity compared to other similar products. Another important parameter to take into account is response time of the sensor itself. Indeed, as the synchronisation process is characterised by a duration in the order of some hundred milliseconds, the response time of the sensor is to be adequate. In order to characterise sensor response velocity, the 90 %-response time is used. The measured signal is deemed to be reproduced when 90 % of the real signal is reached. A too long response time would substantially lead to an underestimated temperature peak and to an error in the temporal determination of the latter. For all investigations, cement-on-surface foil thermocouples produced by Omega Engineering are utilised (Type CO4-K-40). The ultra-fast response time is at maximum 10 ms, being the thermal inertia of the sensors extremely low. In fact, the alloy junction thickness equals 50 μm. The maximum measurable temperature for short duration (10 h) amounts to 370 ^{o}C, being sufficient for the experiments carried out.

In order to guarantee validity and reproducibility of experiments, two temperature sensors are applied to the cone clutch contemporaneously at different angular positions (see Figure 5.3a). Before starting experiments, half of the cone clutch is submerged in hot lubricant with known temperature. Sensors are hold symmetrically on the top part and are not submerged in oil. The resulting measurement gives information about goodness of the application of the sensor and of possible delays in the signal.

Experiments are carried out in order to achieve a progressive increase of temperature on the friction surface. Oil temperature is set to ϑ_{oil} = 80 °C for all experiments. According to Section 4.2.3.2, ten cycles are performed per load stage. After performing each cycle, at least 60 s are to elapse, in order to let the oil cool down all components to mass temperature of ϑ_{oil} = 80 °C. Oil flow is set to $\dot{Q}_{oil}$ = 2.5 l/min for all tests, according to typical conditions in automatic transmissions. Investigated loads are plotted in Figure 5.4.

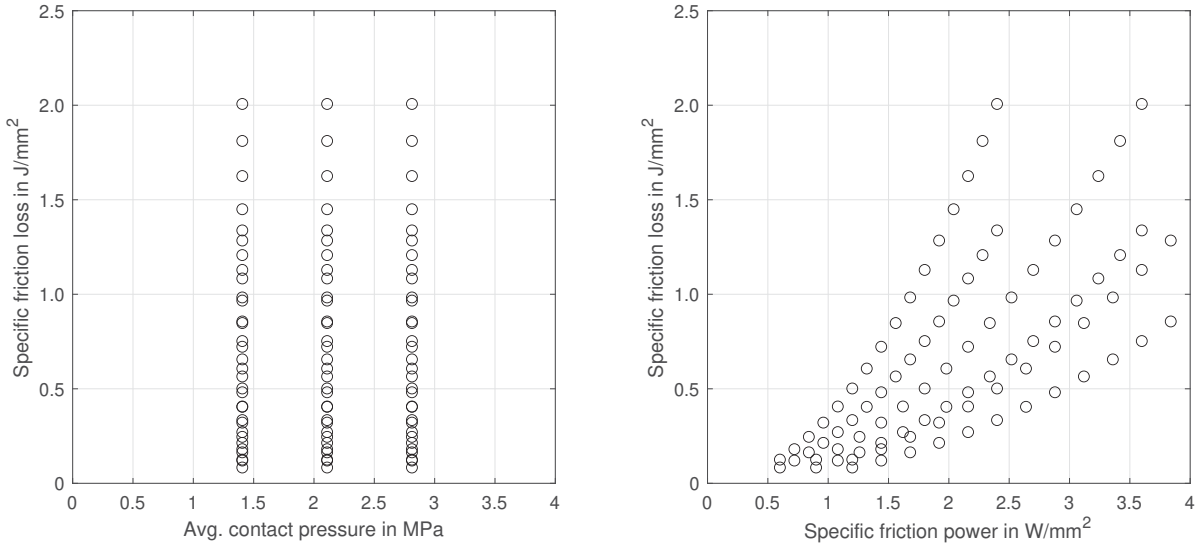

Figure 5.4: Load conditions of experiments for validation of the thermomechanical simulation model

5.1.2.2 Experimental results

For each load condition, all cycles are evaluated and all temperature curves averaged. Averaging is performed by referencing all data to speed difference. In fact, identifying the time instant the synchronisation process begins does not allow to take into account fluctuations in terms of axial force and coefficient of friction. Measurement results from an exemplary load stage are

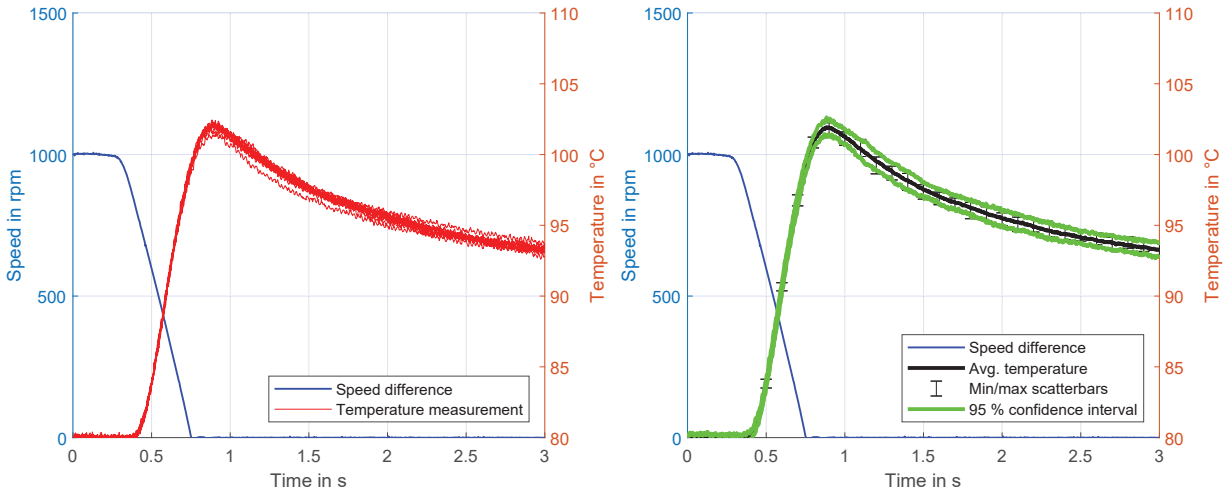

(a) Measured temperature signals for all experiment repetitions

(b) Average temperature with relative min/max scatterbars and 95 % CI

Figure 5.5: Temperature measurement for all experiment repetitions of an exemplary load stage with F_{ax} = 1500 N, p_{avg} = 2.1 MPa, Δn_0 = 1000 rpm

shown in Figure 5.5. For further experimental results refer to the appendix. In particular, in Figure 5.5a, all measurement repetitions are shown, while Figure 5.5b represents the averaged temperature curve with scatterbars and the limits of the 95 % confidence interval of the measurement. The maximum temperature and the temperature time-gradient are shown in Figures 5.6 and 5.7 for all experimental results. Here, the aforementioned values - measured at the outer steel surface - are plotted against friction loss for two values of reduced inertia J_{red}.

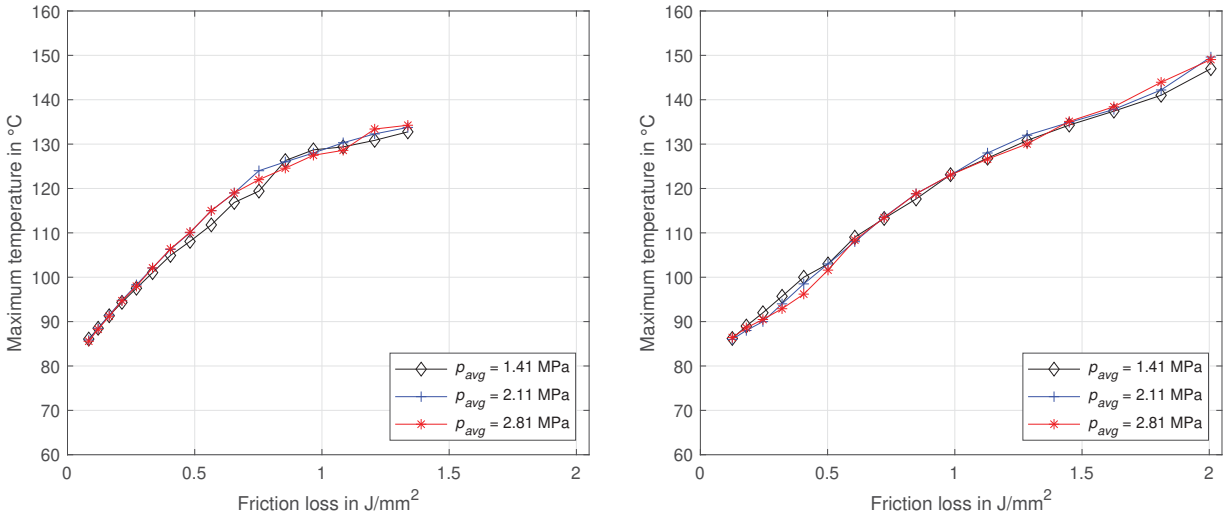

(a) Reduced inertia of J_{red} = 0.250 kgm^2 **(b)** Reduced inertia of J_{red} = 0.375 kgm^2

Figure 5.6: Measured maximum temperature for all performed experiments

In Figure 5.6, it can be appreciated that the influence of contact pressure on maximum temperature is almost negligible at the outer friction surface of the steel cone. Some temperature differences arise when higher friction energies are transmitted. This suggests contact pressure, and thus friction power, has almost no influence on temperature rise at the outer surface of the steel cone, while a sensible difference can be appreciated at the friction surface. This is confirmed both by literature and simulative results. The influence on friction power is likely to manifest with increasing sliding times, as is also suggested by Figure 5.6b. In fact, while an increase of the inertia to brake down linearly affects friction loss, it does not influence friction power. Ceteris paribus, this results in an increase in sliding time, which in turn allows the heat to distribute within the steel cone.

In Figure 5.7, the maximum temperature gradient with respect to time is shown for all performed experiments. The maximum temperature gradient is calculated from the average temperature curve, as shown e.g. in Figure 5.5b. The maximum values occur in correspondence with the initial part of the linear temperature increase during synchronisation. Differently from the maximum temperature curves, a clear influence of contact pressure on temperature gradient is recognisable. In fact, temperature gradient depends mainly of friction power rather than loss.

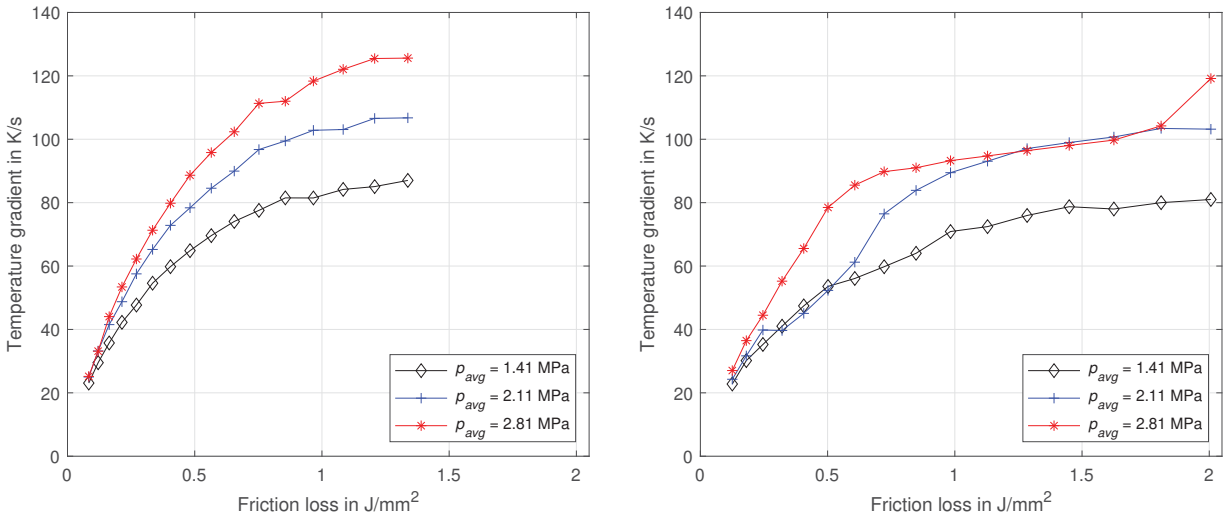

(a) Reduced inertia of J_{red} = 0.250 kgm^2 **(b)** Reduced inertia of J_{red} = 0.375 kgm^2

Figure 5.7: Measured maximum temperature gradient for all performed experiments

5.1.3 Model validation

In this section, the described simulation model is confronted with the experimental results. In a first part, the data-based validation is performed by showing maximum temperature and temperature gradient at the outer friction surface of the steel cone for simulation and experiment. In a second step, the steel cone is visually inspected in order to identify the regions affected by hotspots. These results are also compared to simulations.

5.1.3.1 Data-based validation

In this section, the correspondence between simulation and experiment is proved. In order to compactly display results, only the maximum temperature and the temperature gradient w.r.t. time in the first linear part of the shifting process are plotted. The latter value is obtained by evaluating the slope of the average temperature curve in the time domain in a region between 5 % and 75 % of the maximum temperature rise and relative to the starting temperature. All experiments and simulations are performed at starting temperature of ϑ_0 = 80 °C. Plots with a comparison of temperature curves in the time domain are shown in Appendix A.5. As test results in terms of maximum temperature do not show appreciable differences when plotted against friction loss, the data-based validation comparison is performed for each curve singularly. In Figure 5.8, the comparisons between simulated and measured maximum temperature at the outer surface of the steel ring (compare Figure 5.3) for all data-based validation points are plotted. The curves show that the simulation model is able to excellently reproduce thermomechanical behaviour of the synchronisation process for friction loss values of up to q = 1.0 J/mm^2, this value being subject to small contact-pressure-dependent variations. All curves show a growing divergence starting from such critical energy level. The corresponding maximum temperature at the friction surface is utilised in a second step for performance determination, as

described in 4.2.4.

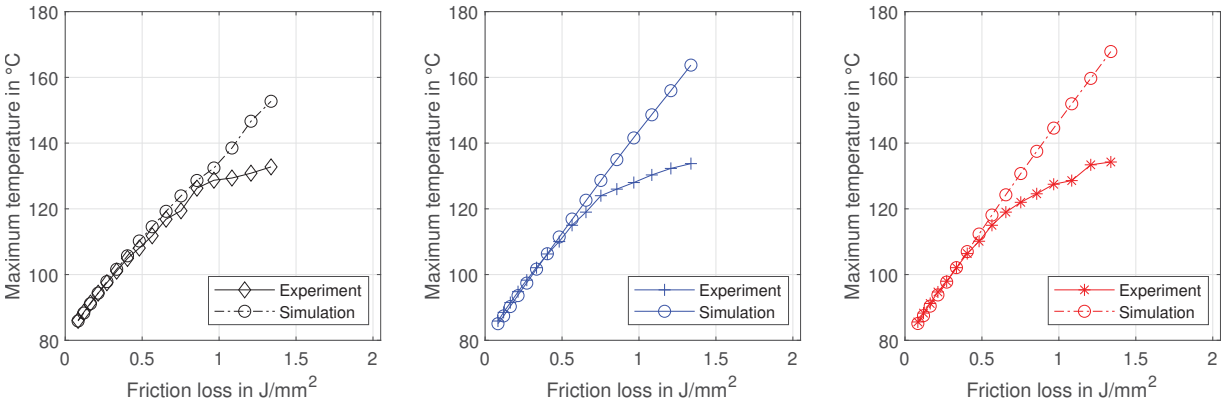

(a) J_{red} = 0.250 kgm^2; p_{avg} = 1.41 MPa **(b)** J_{red} = 0.250 kgm^2; p_{avg} = 2.11 MPa **(c)** J_{red} = 0.250 kgm^2; p_{avg} = 2.81 MPa

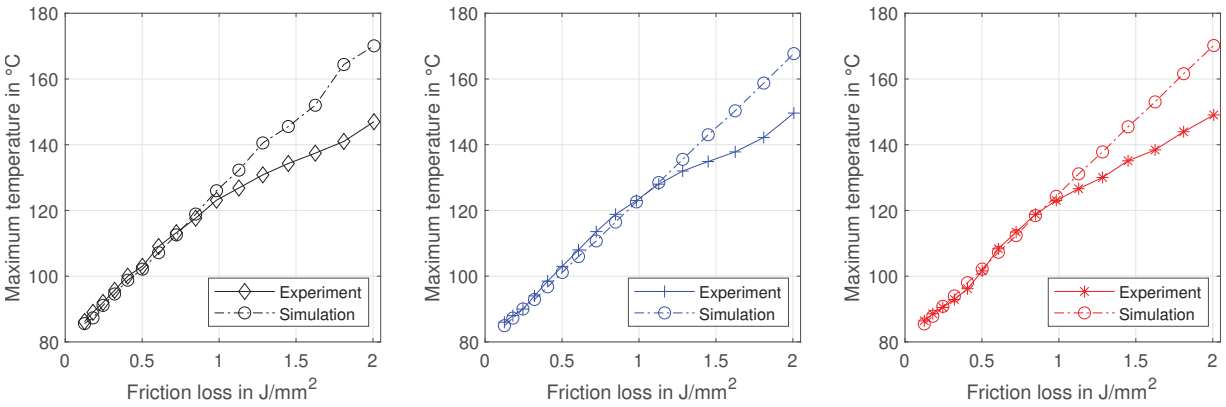

(d) J_{red} = 0.375 kgm^2; p_{avg} = 1.41 MPa **(e)** J_{red} = 0.375 kgm^2; p_{avg} = 2.11 MPa **(f)** J_{red} = 0.375 kgm^2; p_{avg} = 2.81 MPa

Figure 5.8: Comparison between simulated and measured maximum temperatures at the outer surface of the steel cone

Figure 5.8 shows that while the effect of contact pressure on maximum temperature at the external surface of the steel cone is evidenced by simulative results for the lower inertia, no appreciable difference can be noted in experiments with higher inertia (and, hence, sliding time). In fact, the latter curves show approximately the same gradient w.r.t. friction loss.

Figure 5.9 shows the data-based validation by confronting the temperature gradient with respect to time in the early linear phase of synchronisation, when the friction power is maximal. Correspondence between simulation and experiment is excellent and - differently from maximum temperature results shown above - holds for all validation load cases. Indeed, the temperature gradient gives information about friction power at an early phase, where possible critical temperatures are not reached yet.

Validation load points with smaller inertia (upper row of Figure 5.9) show a slightly diverging behaviour for increasing temperature gradients, while such behaviour is not present for higher inertia values. As for the case of maximum temperatures, such diverging behaviour is supposed to be caused, amongst others, by thermal resistances between steel cone and sensor itself.

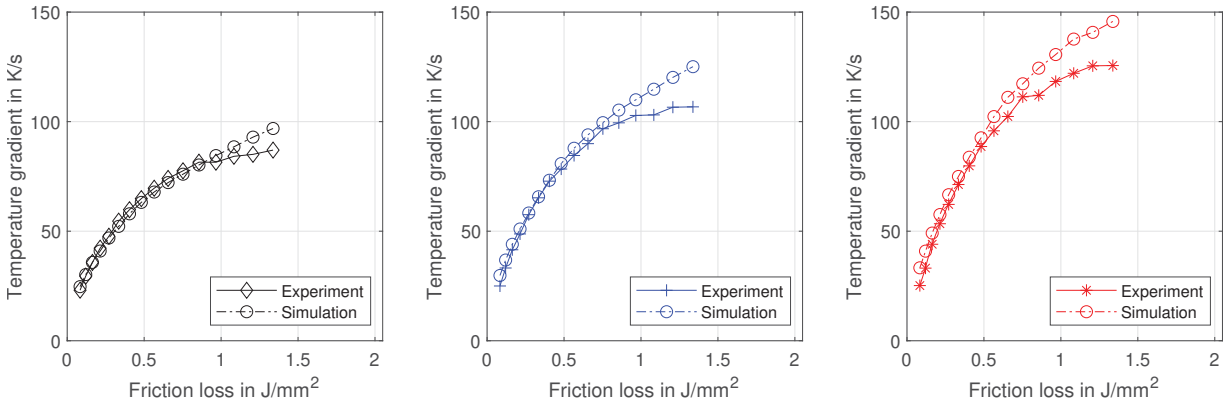

(a) J_{red} = 0.250 kgm^2; p_{avg} = 1.41 MPa **(b)** J_{red} = 0.250 kgm^2; p_{avg} = 2.11 MPa **(c)** J_{red} = 0.250 kgm^2; p_{avg} = 2.81 MPa

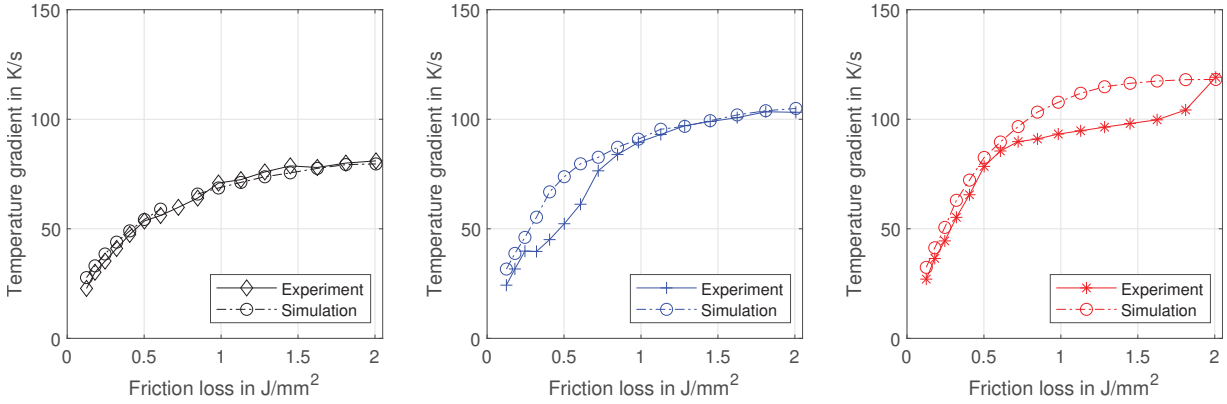

(d) J_{red} = 0.375 kgm^2; p_{avg} = 1.41 MPa **(e)** J_{red} = 0.375 kgm^2; p_{avg} = 2.11 MPa **(f)** J_{red} = 0.375 kgm^2; p_{avg} = 2.81 MPa

Figure 5.9: Comparison between simulated and measured maximum temperature gradients at the outer surface of the steel cone

Additionally, albeit sensors are chosen with appropriate response time, shorter sliding times may introduce a sensible delay in signals, which result in lower measured values. Measured temperature gradient datapoints shown in Figure 5.9e assume a noteworthy trend between corresponding friction loss values of q = 0.32 and q = 0.61 J/mm^2. Such behaviour is not plausible and may be caused by sensor deterioration during measurement.

5.1.4 Results

In this section, thermomechanical performance of CCDC will be evaluated according to the method described in Chapter 4. Before presenting the results deriving from the developed algorithm, the neural network and its working parameters will be described into more detail. Further, an evaluation of the error and a convergence analysis will be shown, proving robustness of the chosen structure. In a second part, performance of the cone clutch will be calculated within its working regions and in terms of bearable loads. Finally, geometric factors of the clutch and their impact on performance and thermomechanical stability are investigated.

5.1.4.1 Neural network

Generally, results delivered by the thermomechanical simulation model can be directly utilised to analyse temperatures within the bodies of all friction partners. However, while validated simulations are less cost-intensive and time-consuming than experiments and can additionally forecast the temperature at the friction surface, a definite number of simulation points is required in order to clearly identify existing correlations between load and design parameters. Being the required prevision preciseness high, the feasible solutions to achieve a performance plot are either to create a DOE-based simulative plan, or to interpolate and/or extrapolate existing simulation results through an AI algorithm. As described in Chapter 4, it is chosen to utilise a neural network to solve the problem. In fact, a NN-based computation of performance limits of a defined friction clutch geometry requires about 50 % of the time of following the purely simulative approach. In the latter case, performance evaluation of the same clutch would require about 200 simulation hours on an appropriate workstation, provided 4 simulations can be run parallelly. In this section, the created neural network and its robustness are presented.

The neural network is developed within the Matlab built-in Neural Network Toolbox. The network is mainly characterised by the employed training algorithm, the number of hidden layers and the number of neurons composing each hidden layer. Also important is the number of input and output data used for training the algorithm, in order to get reliable and robust results. As independent input variables, the same load parameters as in the simulations were used, i.e. axial force, reduced inertia and initial speed difference. As output, the maximum temperature arising at the friction surface during synchronisation is used. Training data is obtained by randomly generating load points within the three-dimensional space of input variables. After according thermomechanical simulations are performed, results are post-processed and maximum temperatures evaluated.

In order to identify optimal values of network size and constitution, nine validation points are chosen close to the borders and in the middle of the input variables space. These points, along with the according simulation results in terms of maximum temperature, are not used for training or validation of the neural network. They are summarised in Table 5.2.

	J_{red} in kgm^2	F_{ax} in N	Δn_0 in rpm	ϑ_{max} in °C		J_{red} in kgm^2	F_{ax} in N	Δn_0 in rpm	ϑ_{max} in °C
1	0.13	1300	700	109.7	6	0.37	1300	2300	672.6
2	0.13	1300	2300	471.0	7	0.37	3700	700	163.7
3	0.13	3700	700	123.5	8	0.37	3700	2300	1334.9
4	0.13	3700	2300	604.2	9	0.25	2500	1500	379.6
5	0.37	1300	700	144.4					

Table 5.2: Loads for neural network validation and corresponding simulated maximum temperatures at the friction surface

The difference between simulated maximum temperature of such points and temperature prevision provided by the neural network is used as an indicator for algorithm goodness. In particular, the mean squared error (MSE) of each load point i indicated in Table 5.2, relative to its respective temperature rise, is utilised. As the datasets for training and validation of the neural network are chosen stochastically at each training of the network, it is decided to perform the training for 100 times and evaluate the average values both for model convergence analysis and for results. According to this procedure, the averaged MSE - $MSE_{\Theta,avg}$ - is evaluated as expressed in Equation 5.1.

$$MSE_{\vartheta,avg} = \frac{\sum_{k=1}^{n_{nn}} \sum_{i=1}^{n_{sim}} \left(\frac{\vartheta_{max,nn,i,k} - \vartheta_{max,sim,i}}{\vartheta_{max,sim,i} - \vartheta_0} \right)^2}{n_{nn} \cdot n_{sim}} \tag{5.1}$$

n_{nn}	-	Number of performed NN trainings	n_{sim}	-	Number of validation simulations
$\vartheta_{max,nn,i,k}$	K	Maximum temperature evaluated with k-th NN for i-th validation load	$\vartheta_{max,sim,i}$	K	Maximum temperature simulated for i-th validation load

The averaged MSE offers the advantage of giving information about both the deviation of predicted temperatures with the neural network and their bias with reference to the corresponding simulated value.

As a training algorithm for the neural network, the Bayesian regularisation is used. In fact, better results in terms of both computational effort and results preciseness can be achieved in comparison with the mere Levenberg-Marquardt algorithm (see Figure 5.11a). For a more exhaustive description of such training algorithms, refer to Faul and Tipping [Fau02], Burden and Winkler [Bur08], Neal [Nea95] or Du and Swamy [Du 06].

As shown in Figure 5.11a, the averaged MSE is used - amongst others - to find the optimal hidden layer size and the number of training datasets necessary for a robust neural network. It is further used to compare the chosen training algorithm and prove its suitability. According to the curve shown in Figure 5.10a, a hidden layer size of 15 neurons is chosen, as a minimum error is reached for such value. If such value is further increased the neural network tends to show a slight overfitting, being additionally more complex and requiring more computational effort.

While this curve is reproduced for different training dataset dimensions, it is here shown only for a training dataset of 300 elements, which is the number of simulations necessary to achieve satisfying preciseness of predicted temperatures. In fact, as can be appreciated in Figure 5.10b, the averaged MSE shows a digressive yet monotonically decreasing behaviour within the tested limits. It is however decided to limit the training datasets to a value necessary to achieve an averaged relative error of less than 1 % for all validation loads. The averaged relative error,

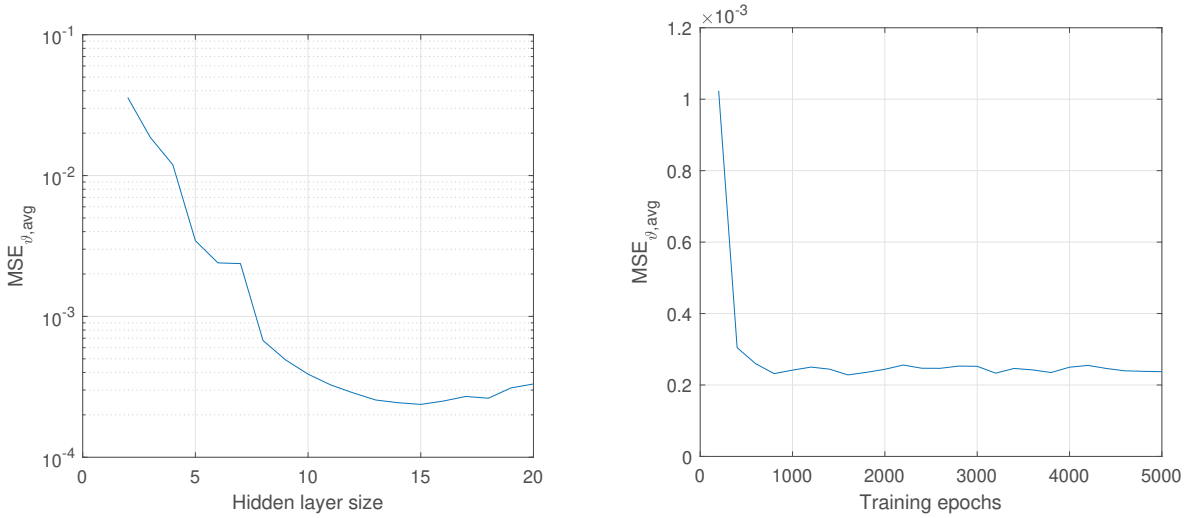

(a) $MSE_{\vartheta,avg}$ vs. hidden layer size

(b) $MSE_{\vartheta,avg}$ vs. training epochs

Figure 5.10: Identification of optimal neural network architecture through identification of hidden layer size and maximum number of training epochs

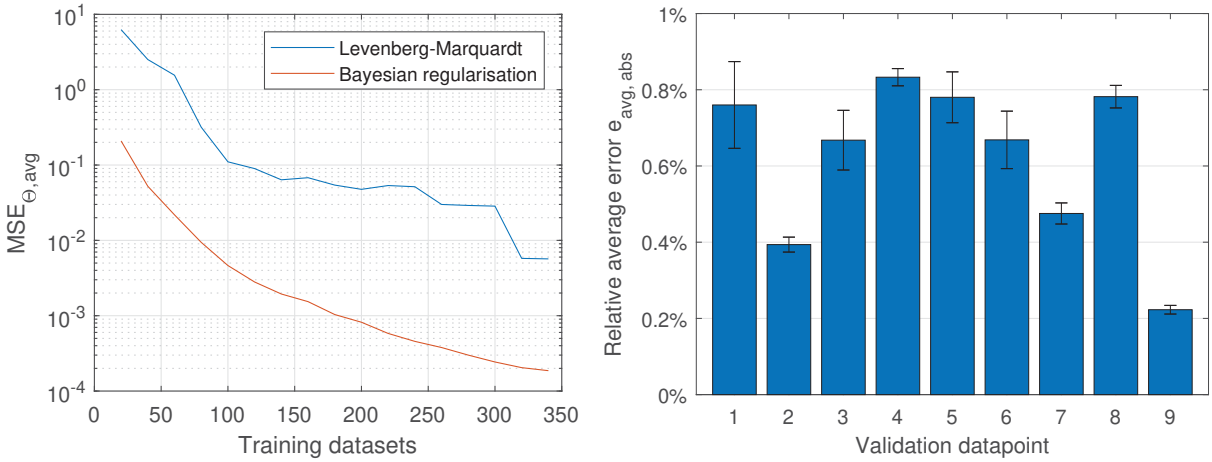

(a) $MSE_{\Theta,avg}$ vs. hidden layer size

(b) Absolute value of relative error (300 training datasets)

Figure 5.11: Averaged MSE for growing number of training datasets (left) and absolute value of relative error evaluated at all validation datapoints (refer to Table 5.2 for the chosen datapoint definition)

including the according 95 % confidence intervals, can be appreciated in Figure 5.11b for all validation datapoints. Also in this case, the values are obtained by training the network 100 times. In the following, if not further specified, the hidden layer size of the neural network is 15 neurons, while the training datasets equal 300. As the inputs to the problem are limited, just one hidden layer is considered.

5.1.4.2 Thermomechanical limits

As shown in Section 5.1.3, experimental and simulated maximum temperatures start to diverge when a critical friction loss is reached. Simulative results allow to determine the corresponding

temperature at the friction surface. For CCDC, a temperature of 400 °C is identified as critical. When such critical temperature ϑ_{crit} is reached at the friction surface, the merely linear finite element simulation model is not capable of representing non-linear effects typical of thermomechanical instability. In this Section, the effect of operational variables on the cone clutch and its thermomechanical behaviour will be analysed in detail. During powershifts, a clutch must synchronise two masses and hence reduce their speed mismatch to zero. Generally, the synchronisation process can be fully described by the three independent variables v_0 (initial sliding speed), p_{avg} (average contact pressure) and J_{red} (reduced inertia at the clutch), the load torque being included in the reduced inertia value (refer to Appendix A.6). For the according equations, refer to Section 4.2.1.2. While initial sliding speed and average contact pressure are specific quantities, the reduced inertia is independent of clutch geometry. It is calculated a priori, adding the component given by rotating masses to the one derived by dividing load torque by speed difference reduction rate. Those terms are evaluated with a 1D analytical differential equations system based on the kinematic transmission analysis, as described in Section 2.1.1.1. The system is built up in Simulink and described into more detail in Appendix A.6. On the contrary, independent variable v_0 depends on initial speed difference and average radius, while independent variable p_{avg} depends on axial force and friction surface. Even though axial force and speed difference are used as loads for experiments and simulations, v_0 and p_{avg} are used to show results, in order to obtain a more general understanding of physical phenomena regardless of geometry.

A graphical representation of performance limits of the clutch as defined in Section 4.2.4 is challenging, as four variables are to be represented simultaneously. In literature, performance limits are generally plotted in a friction power vs. friction loss plane, reducing the input variables to two. However, as power and loss are not linearly independent of each other, it is not possible to unequivocally determine the corresponding loads. In the following, it is hence decided to first show performance limits of the cone clutch in a v_0 vs. J_{red} plane for a discrete number of average contact pressure values. In fact, both v_0 vs. J_{red} are quantities virtually known before the synchronisation process takes place, and are not changeable unless engine torque is artificially reduced. Conversely, axial force (and thus average contact pressure p_{avg}) can be varied and is controlled by the TCU.

According to the procedure described in Section 4.2.4, 100 neural networks are generated for the same input data, in order to increase significance of results. Each of the trained networks is then used to compute maximum temperature at designated loadpoints. For this purpose, a relatively fine mesh is chosen, resulting in more than 34 million combinations of v_0, J_{red} and p_{avg} per network. Nonetheless, the computational effort is negligible.

Once maximum temperatures at the friction surface are evaluated, performance limits are evaluated. For doing so, one variable is kept constant, while temperatures equalling ϑ_{crit} are evaluated. The so obtained curves are then transposed in order to obtain the performance limits,

which are shown in Figure 5.12 for the second variant of CCDC.

The figure is divided into two regions, delimited by a number of iso-pressure curves. Above each of this curves is the region where performance limits are exceeded for that very average pressure. Conversely, every load combination underneath each of the curves denotes the region for safe operation of the clutch. Performance values are plotted for a range of average contact pressures varying from p_{avg} = 1.4 MPa to p_{avg} = 5.6 MPa. All curves show a monotonously decreasing behaviour for rising inertia, converging asymptotically to definite values. Asymptotic values - i.e. values where the effect of inertia is negligible - coincide with creep operation under constant load. Indeed, for the purpose of simulative modelling, a creep drive can be considered as a mass with infinite moment of inertia. However, the proposed simulation looses in preciseness when considering such cases, as sliding time increases and no heat dissipation mechanisms are modelled.

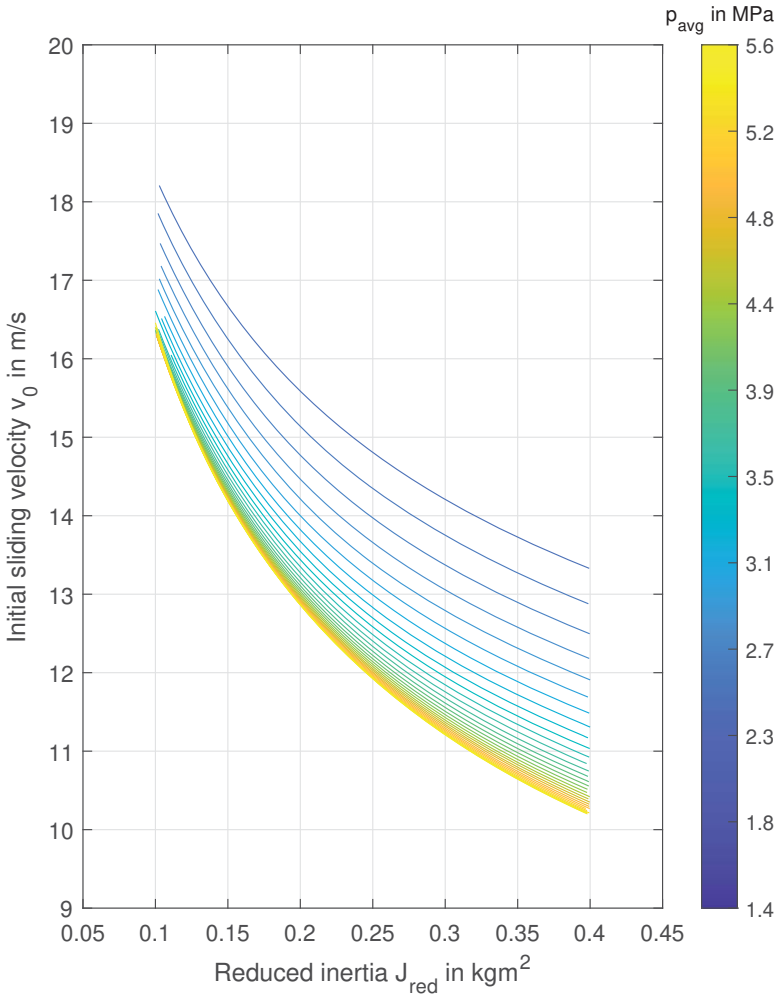

Figure 5.12: Thermomechanical performance limits in the J_{red} vs. v_0 plane

The change of performance limits for varying pressure values is also noteworthy. In fact, no limit can be recognised for decreasing average pressures. By decreasing average pressure, the performance field shown in the v_0 vs. J_{red} plane can be enlarged and become virtually infinite for average contact pressure p_{avg} = 0 MPa. This is physically plausible and aligns with the thesis of Strebel [Str17], as lower average pressure results in higher sliding times, which in turn allow the heat to distribute more evenly within the components. On the other side, increasing the contact pressure has an effect on thermomechanical performance of the clutch only up to a certain point. As can be appreciated in Figure 5.12, all curves converge to a line where increasing contact pressure does not reduce the performance region anymore. Consequently, underneath such

curve, average contact pressure could be increased at will without affecting thermomechanical performance of the clutch. That is, the curve divides the region where safe operation of the clutch always occurs from the region where a contact pressure diminution is necessary in order not to reach temperatures at the friction surface higher than the critical one. Considering the ordinate, a critical sliding velocity is identified with reference to reduced inertia. Such velocity is generally not to be exceeded. Strebel [Str17] does not identify the critical velocity as he does not consider average contact pressures higher than 3 MPa. Instead, a critical velocity curve independent of average contact pressure is typical of TEI-based analyses, as described in several sources cited in Section 2.5.1. Clearly, this considerations are only valid as long as the mechanical solicitation is negligible with respect to strength of the clutch.

The same performance limits are plotted in a specific friction power vs. specific friction loss plane, as shown in Figure 5.13a. Here, a hyperbolic trend is recognisable, that is, performance limit curves flatten towards higher specific friction loss values. This behaviour is confirmed in literature, e.g. by Strebel [Str17]. It can be noted that the inclination of curves decreases with average contact pressure. The upper end of each curve is limited by maximum reduced inertia. Further increasing the value of inertia and decreasing initial sliding speed at the same time would mathematically lead all curves to converge at a point where continuous slip can be assumed. It is however to note that for extremely high value of friction loss, the curves tend asymptotically to the ordinate, as the model is adiabatic and no heat dissipation is considered. However, those regions do not represent typical operation conditions of automotive transmissions and can be neglected.

In Figure 5.13b, the same performance limits are plotted against sliding time, which can be obtained by integrating Equation 2.6. Also in this case, a constant coefficient of friction of μ = 0.10 is used for calculations. The curves show an excellent accordance to the results presented by Strebel [Str17] and Schneider et al. [Sch19a], who identify two performance limit curves for contact pressures lower than 0.5 MPa and higher than 1 MPa, respectively. The constant offset between curves is most probably effected by different clutch geometry (i.e. multiple disc vs. cone clutch). Figure 5.13b shows that an almost linear trend of the curves can be assumed, especially for lower average contact pressure values. It however also shows that higher average contact pressure (i.e. lower sliding time) has a significant effect on the slope of limit curves.

It is to be expected that curves with very high values of average contact pressure will lead to extremely low values of bearable friction loss. Sliding time equalling zero serves as a peculiar case. Physically, a sliding time of zero can be only achieved with infinite contact pressure (the trivial case in which the speed mismatch is zero be not considered here). Neglecting mechanics, an infinite contact pressure would in turn result in infinite heat flux. It is hence assumed that all performance curves cut the axes in the origin. This means performance curves at constant p_{avg} can be considered linear only for sliding times that are high enough. In the considered case, bending of the curves towards zero sliding time is clearly visible for values less than $t_S \approx 0.4$ s.

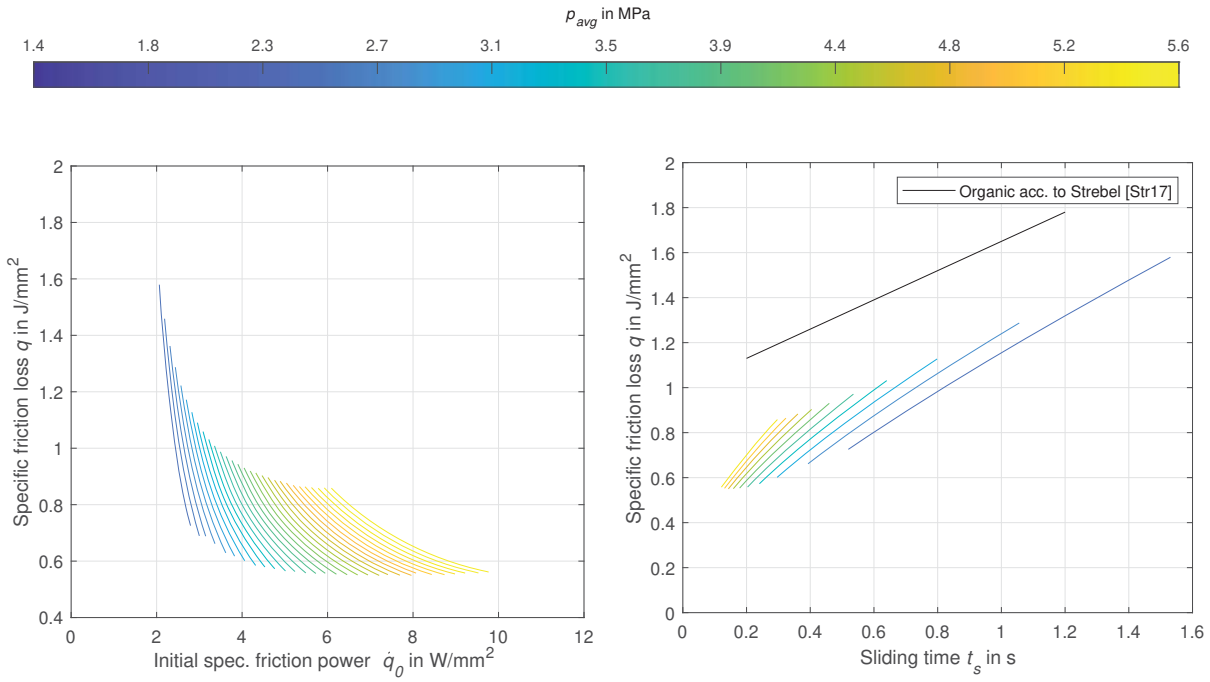

(b) Performance in q vs. $\dot{q}_0$ plane

(c) Performance in q vs. t_S plane

Figure 5.13: Thermomechanical performance in the q vs. $\dot{q}_0$ (a) and q vs. t_S (b) planes

Identification of performance curves and according discussion shown here are valid for the reference variant of CCDC, which has been manufactured as a prototype and tested. All curves are generated with one set of 100 neural networks. Such networks are trained with stochastically chosen training data derived from thermomechanical simulations, which are experimentally validated. For generating Figures 5.12 and 5.13, 30,000,000 combinations of v_0, J_{red} and p_{avg} have been evaluated, with moderate computational effort. However, as the neural network is a function of those input variables, real-time calculation of performance limits in transmission control units would be effortless and significantly more efficient than saving data tables.

5.1.4.3 Load-independent effects

In the previous section, effects of load variables v_0, J_{red} and p_{avg} or q and $\dot{q}_0$ were analysed. In this section, the same performance curves are generated for design modifications of CCDC. In section 4.2.5, thermomechanical design optimisation is presented. The proposed methods include variations of sheet thickness, clutch stiffness, cone angle difference and friction surface size. However, design modifications are limited by geometric and load constraints and performance conflicts. For instance, increasing the friction surface has a beneficial effect on reducing specific quantities. However, it implies also increasing drag torque. Additionally, as CCDC is designed to fit an existing reference automatic transmission, external diameter and width of the clutch cannot be freely modified. Hence, it will not be treated in this discussion. Also cone angle difference between inner and outer cone is not treated into detail due to the higher elasticity of the system with respect to traditional cone clutches. Conversely, a sensibility analysis on sheet thickness is of great interest, as increased thickness increases both clutch rigidity and thermal

mass.

Due to its compactness, increasing steel cone strength of CCDC represents a feasible solution within volume available in the reference AT. In the proposed study, three design variants are considered and their thermomechanical performance assessed. In addition to the standard geometry, a variant with increased and one with decreased thickness are presented. A schematic representation can be appreciated in Figure 5.14. Results are shown in Figures A.28 and A.29 in the Appendix. Of more interest is the comparison between sheet thicknesses and the effect on thermomechanical performance. In Figure 5.15a, results are plotted in a J_{red} vs. v_0 plane. Only three values of average contact pressure are shown in order to more clearly render results. In particular, a high and a low value of simulated average contact pressure are shown, i.e. p_{avg} = 2.2 MPa and p_{avg} = 5.6 MPa, respectively.

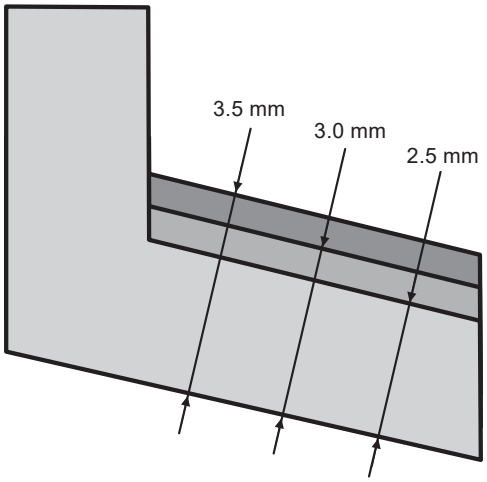

Figure 5.14: Schematic cross section of the analysed sheet thickness variations of the outer cone

In Figure 5.15b, performance limit curves are plotted for the same average contact pressure values in the q vs. $\dot{q}_0$ plane. As expected, an increased thermal mass has higher capacity, resulting in lower maximum temperatures also at the friction surface.

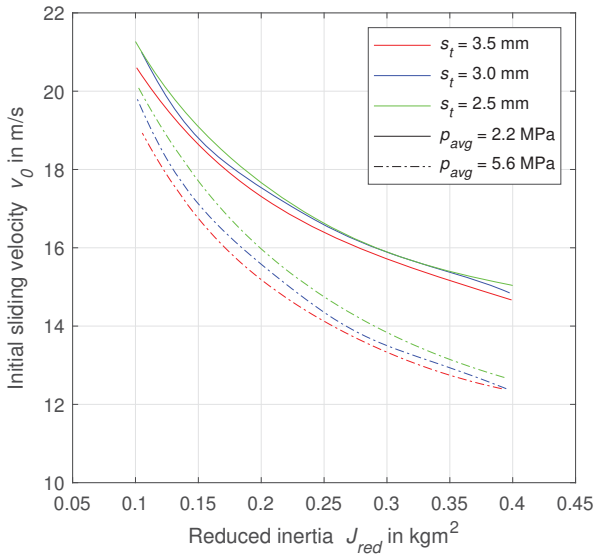

(a) Performance in J_{red} vs. v_0 plane

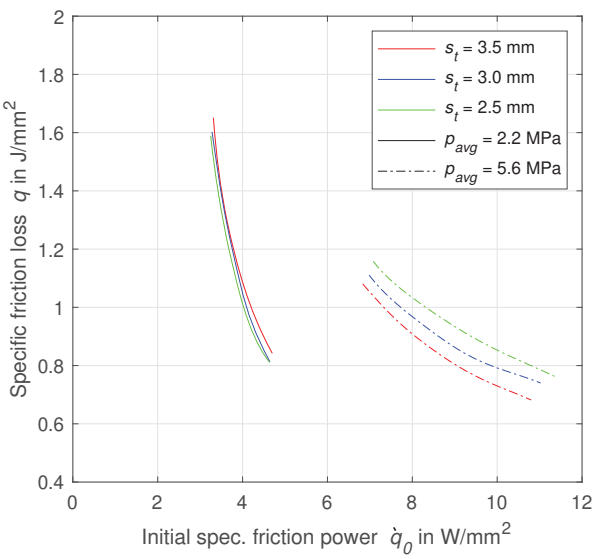

(b) Performance in q vs. $\dot{q}_0$ plane

Figure 5.15: Thermomechanical performance limits evaluated for different values of sheet thickness of the cone clutch in the J_{red} vs. v_0 (a) and q vs. $\dot{q}_0$ (b) planes

However, as can be appreciated in 5.15b, curves with high values of average contact pressure tend to diverge. in this region, differently from curves with lower average contact pressure, mechanical stability and stiffness are key factors to increase performance of the cone clutch.

However, an increase in sheet thickness leads to higher mass and production costs.

The working region and the accordingly needed average contact pressure shall be hence evaluated carefully in order to find a satisfying compromise between costs and performance.

5.2 Dynamic performance of CCDC

In this section, the method presented in Section 4.3 is applied to the dog clutch geometries of CCDC in its first variant. Results are compared to the optimised design of the second variant and recommendations eventually derived.

Initially, a short overview on the simulation model is given, according to Section 4.3.1. Next, the experimental setup for validation of the model is presented. Results of experiments are discussed and utilised to validate the simulation model. In a second part, the simulation model is employed to determine engagement performance of all dog clutch variants. Additionally influencing parameters, as described in Section 4.3.5, are singularly analysed.

5.2.1 Multibody simulation model

Two multibody simulation models of CCDC are developed according to the description in Section 4.3.1. Even though the simulated dog clutch geometries do not differ, carriers and shafts do. In fact, for result validation, the test-rig is modelled to a great extent, in order to replicate its increased stiffness compared to the reference automatic transmission. On the contrary, especially for determination of shifting comfort, a model approximating the real system is utilised. For performance evaluation, the test-rig approximating model is employed, due to its increased computational efficiency. Indeed, while many simulations are needed to compute engagement performance curves, torsional stiffness of shafts and components is not as important as when it comes to shifting comfort determination.

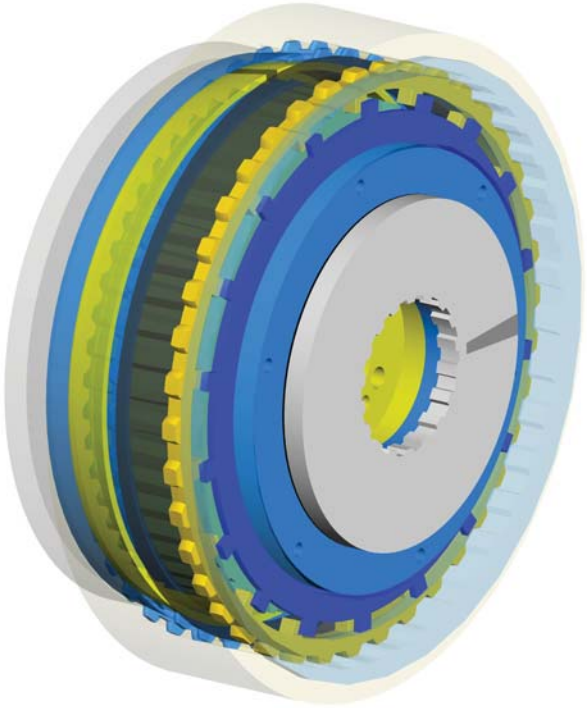

Figure 5.16: Representation of the multibody simulation model

5.2.1.1 Model description

The multibody simulation model in the test-rig variant reproduces the testing interface of the ZF/FZG KLP-260, which is detailedly described in Appendix A.4.

A representation of the simulation model is shown in Figure 5.16. All components included in

the simulation model can be also appreciated in the cross section in Figure A.4. In particular, the system is cut at the interface between driving shaft and slip clutch lamellae. The axial load which determines the slip torque is obtained through a constant force element instead of a plate spring. Thanks to the introduction of the slip clutch, experimental measurements can be directly compared to simulative results. Also torque measurement is implemented similarly to the test-rig. In fact, the outer carrier, which is connected to the external housing through an adapter, is free to spin about its axis. Large rotation is, however, impeded by a highly stiff spring characterised, which represents the employed load cell. All parts between mentioned interfaces are built up as described in Chapter 4.

5.2.1.2 Model optimisation

After the simulation model is complete, a further step is taken in order to optimise and improve its computing efficiency. For this very purpose, the real-time-factor (RTF) is used. This factor is calculated as the ratio between computational time and simulated time. In this multibody model of CCDC, most of the computational effort is caused by the contact simulation. Especially simulations with many high-energy impacts tend to increase the computational time and, hence, RTF. Generally, after discretisation and polygonisation optimisation is performed, a value of RTF = 1500 could be reached. For a standard engagement, this corresponds to a computational time of about 9 minutes.

5.2.2 Experimental setup

As mentioned in Section 4.3.2, the test-rig is operated in creep drive mode. In this operating mode, static torque (i.e. full torque with still-standing shafts) cannot be transmitted, which is necessary when full engagement of the dog clutch is reached. In fact, the creep drive is speed-controlled, which collides with the halt of the shaft occurring when the dog clutch engages. In order to deliver a constant static torque to the dog clutch, an on-purpose designed slip clutch is interposed between drive and dog clutch. The slip clutch is constructed as a disc clutch with two friction surfaces. Axial force - and hence slip torque - is obtained by loosening or tightening screws. A disc spring behind the slip clutch allows exact force setting by defining its prestress. A section cut of the slip clutch is shown in the appendix in both Figure A.4 for CCDC variant 1 (elements 12, 14, 14, 16) and Figure A.5 for variant 2 (element 9).

Validation experiments are carried out according to the experimental plan shown in Table 5.3. All geometries are tested successively. Results are utilised to validate the simulation model. Unless tooth rejection occurs, experiments are repeated 10 times for each load stage, in order to minimise risk of false successful engagements. A load stage is deemed as successful only if all cycles are.

As discussed in Section 4.3.3, three possible outcomes of a shift are observed. Results will be discussed into more detail in the following sections. Engagement experiment results confirm the performance expectations for all geometries. In fact, increased backlash leads to higher

Quantity	Symbol	Unit	Values
Axial force	F_{ax}	N	7500, 8500
Speed difference	Δn	rpm	1, 25, 50, 75, 100
Axial velocity	v_f	mm/s	10, 20, 30

Table 5.3: Tested combinations of axial force, speed difference and axial velocity for model validation, resulting, in sum, in 30 load stages

engagement performance, allowing up to more than 100 rpm speed difference between clutch bodies at shifting velocities of at least 20 mm/s. All clutch bodies are inspected and documented before and after testing. While tooth flanks do not show appreciable signs of wear, the same does not hold for the edges between flank and face. Here, the once sharp edges are characterised by radii which are observed to be as great as 0.3 mm after misuse shifts are performed purposedly. Influence of wear of tooth edges on engagement performance is dealt with in Section 5.3.2.1.

5.2.2.1 Dog clutch engagement behaviour

Engagement behaviour of all dog clutch designs is assessed by applying the criteria of successful engagement vs. tooth rejection. Also delayed engagements are considered, even though this phenomenon can be only observed in experiments. Indeed, finite rigidness of the test-rig and elasticities of the actuation system contribute to enhance engagement, even if the conditions would theoretically not. Based on results, it can be stated that delayed engagement usually appears in regions very close to the performance limits of the dog clutch. It is further observed, that usually of all cycles of a load stage showing delayed engagement, about 50 % show a successful engagement. Experimental results are summarised in Figure 5.20. For all tested combinations of axial velocity and speed difference, all cycles are evaluated singularly. If all of the 10 repetitions show engagement of the dog clutch, the load step is considered as passed. Conversely, it is sufficient that one of the 10 cycles shows delayed engagement or tooth rejection to categorise it as not passed.

5.2.2.2 Positive form-fit generation

For load stages where sufficiently high axial velocity or sufficiently low speed difference can be guaranteed, a successful form-fit generation can be observed. In general, for all geometries, a positive form-fit generation can be achieved with very low speed differences in combination with any of the tested axial velocities. The lowest tested speed difference is Δn = 1 rpm. However, such speed difference is not representative of a real AT system, as it would require a too sophisticated control with precise speed measurement as feedback signal. The highest tested speed difference is Δn = 100 rpm, under which only Variant V1, with a circular backlash of 18°, could still engage correctly. In the following, representative signals of shifts showing successful engagement are analysed. In particular, differences caused by backlash and tooth edge are shown. Speed difference of Δn = 1 rpm is chosen for all shown geometries (in particular, V1,

V2, V3, V4 and V5), in order to allow comparability of results. Axial velocity of the piston during engagement varies between 5 mm/s and 30 mm/s. In Figure 5.17, measured signals of axial force, torque, piston position and speed difference are shown for an engagement experiment performed with dog clutch variant V1. From the measured signals, all relative positions of the dog teeth can be appreciated due to the low speed difference and high backlash. In general, considering constant speed difference over the whole engagement process, the time necessary for the rotating clutch to cover an angle $\Delta\xi$ can be expressed as shown in Equation 5.2.

$$\Delta t_{\Delta\xi} = \frac{\Delta\xi \cdot \pi/180}{\Delta\omega} = \frac{\Delta\xi \cdot 30 \cdot \pi}{180 \cdot \Delta n \cdot \pi} = \frac{\Delta\xi}{6 \cdot \Delta n} \tag{5.2}$$

$\Delta t_{\Delta\xi}$	s	Time necessary for rotating of an angle $\Delta\alpha$	$\Delta\xi$	°	Angle of considered rotation
$\Delta\omega$	rad/s	Angular speed difference	Δn	rpm	Speed difference

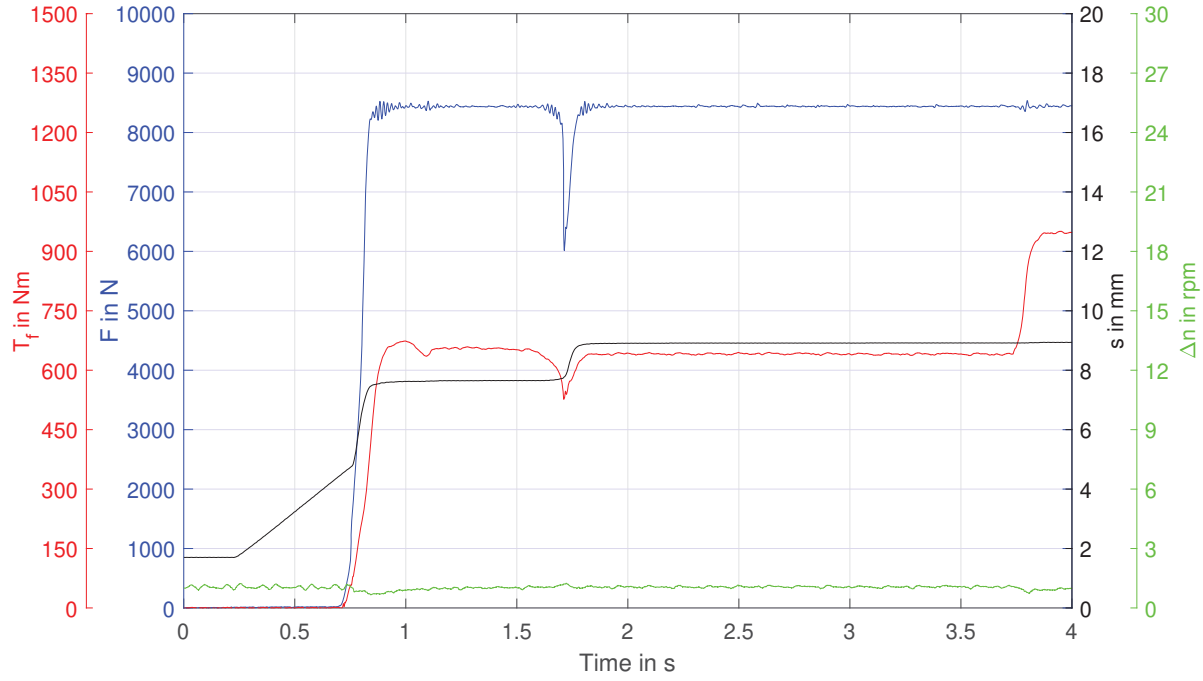

Figure 5.17: Measured signals of a successful engagement of dog clutch variant V1. Δn = 1 rpm, v_f = 20 mm/s, F_{ax} = 8500 N

For the cycle shown in Figure 5.17, after clearing the axial gap between teeth of the clutch bodies, the same come into contact in a tooth-vs-tooth position at time t = 0.850 s. Reversing Equation 5.2, the angle can be evaluated, of which the rotating clutch body has to turn for the tooth to meet the adjacent gap. In this case, the gap is met at time t = 1.712 s, which is clearly recognisable by the sudden fall in axial force. The tooth-vs-tooth position is kept for an angle of $\Delta\xi$ = 5.2°, which results in a circumferential overlap of about 65 % (refer to Table 2.1). After the tooth-vs-gap position is reached, the dog clutch can engage. According to the considerable backlash of S_V = 12°, full torque is transmitted through the tooth flanks only at time t = 3.723 s.

The difference in time of Δt = 2.011 s correlates well with the analytic value obtainable with Equation 5.2, with a relative discrepancy of 0.55 %. Variants V3 and V2, with a backlash of 2° and 1°, respectively, show the effects of reduced backlash on engagement behaviour and performance. As soon as the tooth-vs-gap position is met, variant V2, characterised by a smaller circular backlash, has less time to reach the final engagement position, before the torque-transmitting tooth flanks come into contact. In Figures A.32 and A.33 (see Appendix), such time difference can be appreciated. Furthermore, it can be observed, that for dog clutch V2, the final position is not completely reached. Indeed, the axially movable dog clutch body stops about 0.3 mm before reaching its end position. This is caused by axial friction on tooth flanks, which in turn derives from transmitted torque. In real transmission systems, vibrations and load interruptions would enhance and support the engagement process. Hence, such engagement is considered as successful.

Dog clutch variant V4 differs from the above mentioned variant V2 because of the tooth face shape. In fact, V4 is characterised by convex teeth, which are meant to improve engagement behaviour. A comparison between tooth shape of variants V2 and V4 can be appreciated considering Figures 5.31a and 4.11. Curvature of the tooth face introduces an axial velocity component already during the face-vs-face sliding phase, reducing the energy needed to axially accelerate piston and dog clutch body. The effect is clearly visible when low speed differences are considered, such as in Figure A.34. A more detailed analysis of this very design parameter is given in Section 5.3.1.

Finally, an engagement with variant V5 is considered. This variant is characterised by zero play in the fully engaged position, and thus provides ideal conditions for maximum driving comfort when torque alternation is concerned. Due to the tooth flank angle of γ_f = 14°, a circular backlash of S_V = 0.4° exists when the dog clutch is disengaged. This translates in a circumferential clearance of about 0.55 mm. Also in this case the tooth face is characterised by a curvature, analogously to variant V4. As can be seen in Figure A.35, an axial velocity begins to generate already in the tooth-vs-tooth phase. Due to the very limited backlash and also considering the flank angle, torque-transmitting flanks come into contact after about 42 ms. Such value can be determined geometrically as the intersection of the tooth flank of one clutch body and the relative trajectory of the corresponding and foremost point of the other clutch body. Measured time confirms calculations and amounts to around 45 ms. Such short time interval prevents the torque to drop as sensibly as observed with the other variants, which turns into a distinct increase in shifting comfort. However, already under low speed differences a complete shifting through cannot be guaranteed with those shifting conditions. Indeed, the axially movable clutch body can advance of about 0.88 mm before being stopped by axial friction. Inclined flanks exacerbate such behaviour, as they also introduce an axial component of torque-induced normal pressure between tooth flanks, which acts against the piston force.

5.2.2.3 Delayed engagement and tooth rejection

In this section, selected test results showing unsuccessful engagements will be shown and analysed. A shift can be rated as unsuccessful either when tooth rejection or when a delayed engagement occurs. In both cases, the full load torque cannot be transmitted through the tooth flanks at once, as the axially moving dog clutch body is not capable of sufficiently filling the tooth gap until the next tooth arrives. Depending on clutch geometry and speed difference, tooth rejection manifests itself as torque variations with different frequency. In the following, one experiment with tooth rejection and one with delayed engagement are considered. In Figure

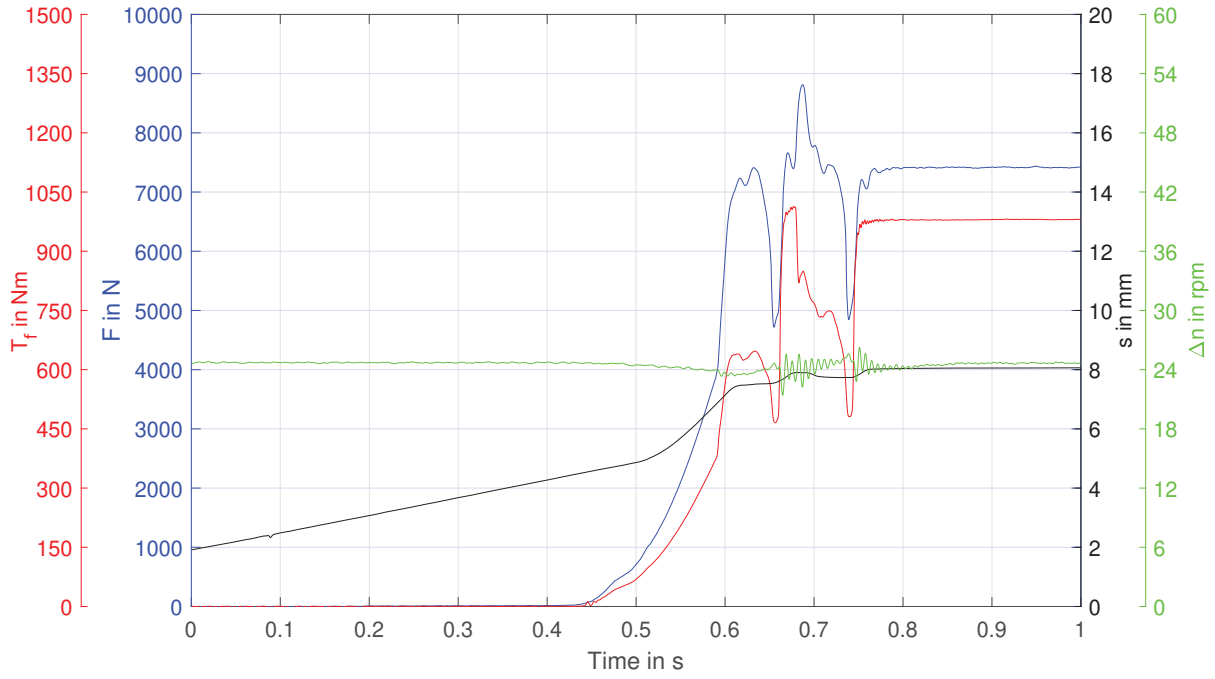

Figure 5.18: Measured signals of delayed engagement of dog clutch variant V4. Δn = 25 rpm, v_f = 20 mm/s, F_{ax} = 7500 N

5.18, a delayed engagement is shown. In this very case, teeth are rejected only once. At about time t = 0.6 s, the tooth-vs-tooth position is reached for the first time. As soon as the teeth meet the next gaps, the axially movable dog clutch body can translate. However, due to the combination of limited gap and relatively high speed difference, an overlap of just 0.35 mm can be achieved in this case. For a very limited amount of time, even though the tooth flank contact is characterised by extremely high contact pressures (about 7 times higher than nominal pressure), the dog clutch is able to transmit torque. However, at time t = 0.68 s, teeth are rejected and the dog clutch is again in tooth-vs-tooth position. When the next tooth gap is met, the axially movable dog clutch body advances to the slightly more as before. This time, the overlap is 0.44 mm and the teeth are not rejected. Nonetheless, such condition appears to be highly unstable, as an even slight increase in load torque could determine an ulterior tooth rejection.

If - ceteris paribus - the speed difference is further increased, form fit generation is not possible anymore. An example is shown in Figure 5.19. Here, the dog clutch engagement behaviour is tested with a speed difference of Δn = 50 rpm. The maximum measured tooth flank overlap that is achieved during experiments corresponds to 0.15 mm, which is not enough to keep the engaged position with a load torque of 500 Nm. The pattern described for the delayed engagement is here repeated several times, until the dog clutch is opened again. The effects of such behaviour are vibrations and an according noise, which is clearly distinguishable and is characterised by specific frequency. Frequency determination is not only dependent on speed difference and tooth number (i.e. geometry), bus also on the time static torque is transmitted during each tooth rejection. In this very case, such frequency equals 12.4 Hz.

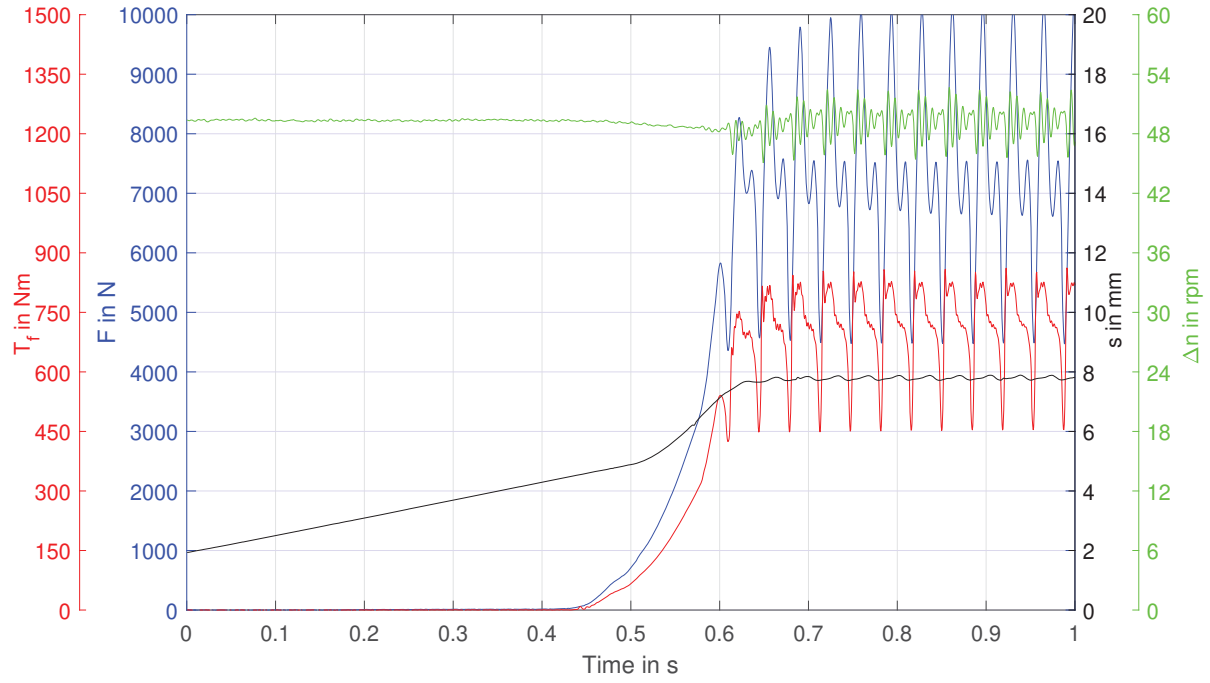

Figure 5.19: Measured signals of tooth rejection of dog clutch variant V4. Δn = 50 rpm, v_f = 20 mm/s, F_{ax} = 7500 N

Effects of tooth rejection-induced noise are not pursued further, as tooth rejection is to be avoided in any case in the transmission. Besides, the clearly distinguishable torque ripple would translate in repeated longitudinal jolts, which can be perceived by the driver and invalidate stability of the vehicle. For further experimental results of unsuccessful shifts characterised by tooth rejection refer to the Appendix A.8. Effects of tooth rejection on comfort are analysed in Chapter 6.

5.2.3 Model validation

Experiments are performed to prove functionality of the interlocking clutch and to study its engagement behaviour in the first design phase. Additionally, they are employed for validating the multibody simulation model, as described in Section 4.3.3. In fact, proved validity of such dy-

namic model is necessary to allow precise and significant behaviour predictions. Even though extensive experimentation is particularly time consuming, it improves conspicuously robustness and goodness of the multibody simulation model. For validation, the multibody simulation model represents the whole CCDC system as it is tested in the test-rig. Accordingly, static torque is generated with a slip clutch at the inner carrier. Torque is evaluated at the outer carrier, which is rotably mounted and held in place by a high-stiffness spring at the diameter the load cell would measure reaction force in the real system.

5.2.3.1 Event validation

According to the procedure described in section 4.3.3, a number of load points are to be defined for event validation. For CCDC, the event to be validated is whether an engagement occurs or not under defined load conditions. For validation, only one force level is employed, while five speed differences and three piston velocities are varied for each dog clutch geometry. All variation parameters are chosen in a range typical for automatic transmissions. If all of the 10 performed experiments per load stage show successful engagement, the test is considered as passed. The very same holds for the corresponding simulations, which are tuned so to achieve initial tooth-vs-tooth overlap of 10 %, 50 % and 90 %, as depicted in Figure 4.9. In Figure

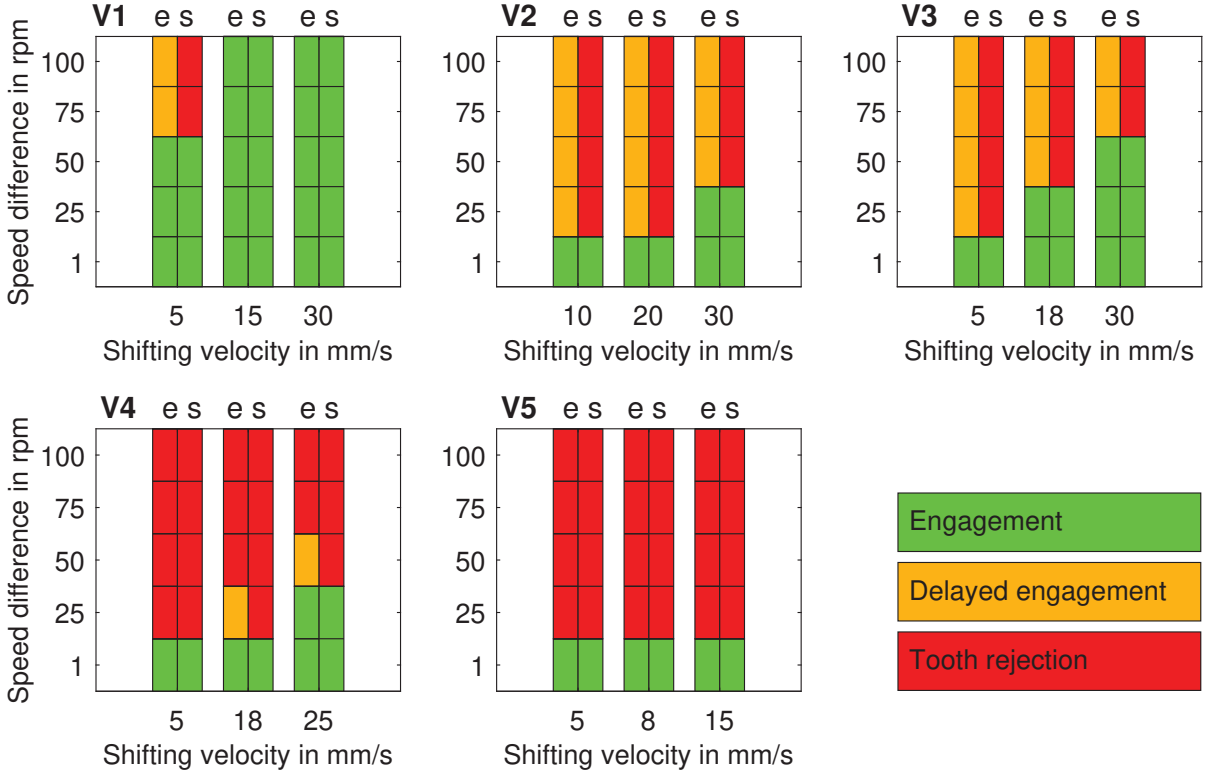

Figure 5.20: Event validation for all tested variants of CCDC version 1. The left bar summarises experimental results (e) while the right one summarises simulative results (s)

5.20, validation results are shown for all clutch geometries. It can be noted that all validation experiments show excellent correspondence with the according simulations for all variations of geometry, speed difference and axial velocity. Only minor differences arise for variants with

reduced backlash when delayed engagement occurs. As described in Chapter 4, the simulation model is not able to depict this phenomenon unless clutch and rig non-idealities are considered. Delayed engagement is considered analogously to tooth rejection for event validation purposes, yet it is colour-differentiated for a holistic understanding. Already from the comparison between experiment and simulation, a strong influence of angular backlash on engagement behaviour can be noted. Such influence generally overrules all design distinctions between dog clutch variants and will be covered into more detail in the next sections.

5.2.3.2 Knowledge-based validation

As described in Section 4.3.3, knowledge-based validation is performed by comparing simulation results with expected physical phenoemena. In particular, the time intercurring between the moment the teeth meet their corresponding gaps and the instant the flanks come into contact and start transmitting torque can be evaluated by applying Equation 5.2. The test is performed for all simulations automatically and shows excellent correspondence between simulated, measured and analytical values of time difference. Relative discrepancy between analytical and simulated results is less than 0.8 % for all performed simulations.

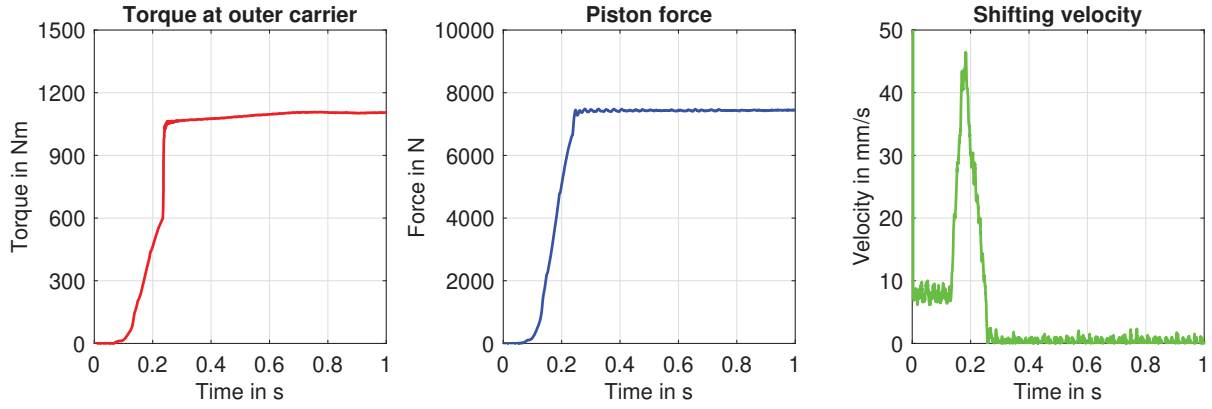

(a) Measured signals of engagement experiment

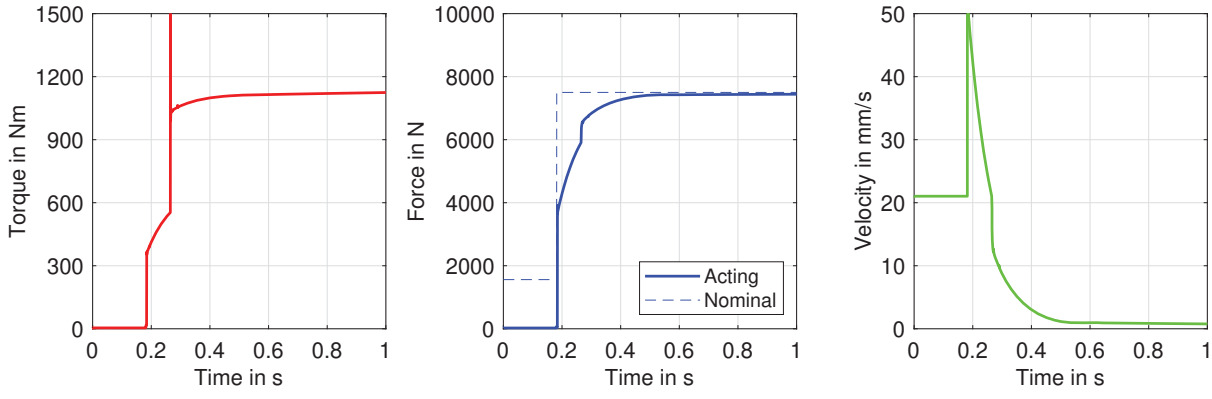

(b) Engagement simulation signals

Figure 5.21: Validation comparison between experiment and simulation of a direct engagement. Dog clutch variant V1, F_{ax} = 7500 N, v_f = 20 mm/s, Δn = 50 rpm

Additionally, through graphic comparison of simulated and measured signals, the capability of

the model to reflect physical phenomena occurring during engagement is assessed. The simulation model is able to reproduce all phenomena during engagement. In particular, the time dependent events, such as tooth contacts, engagement and rejections are reproduced exactly. Minor discrepancies are to be found in the first friction phase of the cone clutch. In fact, the overall torque is dependent on friction coefficient, which varies with increasing pressure. This results in a torque offset, which is maximal when the dog clutch is completely engaged. Further, the force increase cannot be depicted correctly in the first phase after the kiss point of the cone clutch is reached due to internal dynamics and control of the hydraulic piston. While both effects are known, they are not pursued further, as the main focus of dynamic investigations is laid on the engagement behaviour of the dog clutch. In Figure 5.21, a validation comparison

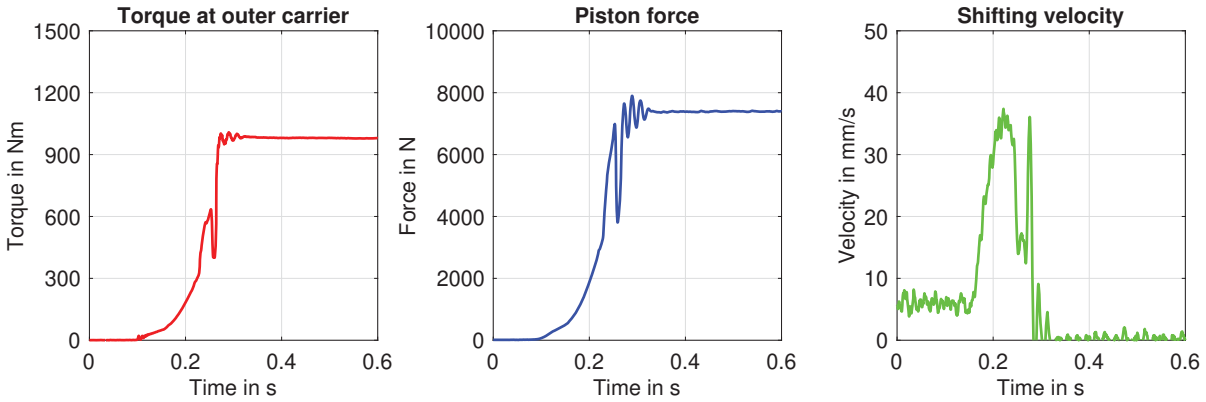

(a) Measured signals of engagement experiment

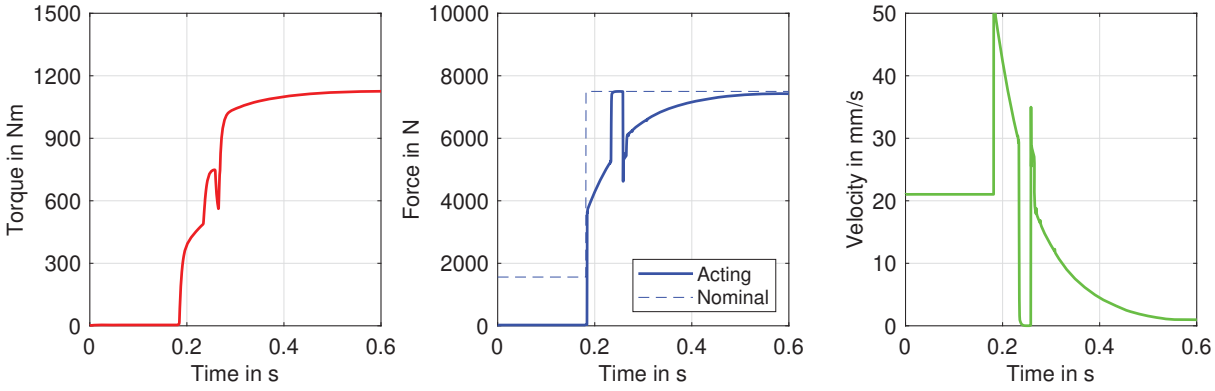

(b) Engagement simulation signals

Figure 5.22: Validation comparison between experiment and simulation of an engagement preceded by a tooth-vs-tooth position. Dog clutch variant V3, F_{ax} = 7500 N, v_f = 30 mm/s, Δn = 50 rpm

between experiment and simulation is shown for a direct engagement. As mentioned above, the simulation model is not able to exactly reproduce the force increase in the first shifting phase (until kiss point of the con clutch is reached). However, as soon as friction torque is generated at the cone clutch, torque signals coincide almost exactly. Due to the relatively high circular backlash of dog clutch variant V1 (S_V = 12°, in this specific case engagement occurs without the tooth tips of both clutches to come into contact. Because of this, axial force corresponds to the reaction of the reset spring, which in turn depends on its compression. Axial force abruptly

increases to its maximum value (at about time t = 0.22 s) when an additional reaction arises. Here, such force is generated by friction between tooth flanks. In fact, also full static torque is transmitted starting from this very moment. Due to the damping element utilised for piston modelling, the nominal axial force is reached with a slight delay. Finally, axial piston velocity curves also show excellent correspondence. Beginning from the kiss point, both curves show a degressive behaviour, induced by the increasing reaction force of the reset spring. After tooth flanks are in contact, simulated piston speed decreases degressively, to eventually reach the fully engaged position of the clutch. This phenomenon is not observed in experiments, possibly due to stick-slip phenomena and non idealities of tooth faces which increase axial friction force. Noteworthy is the simulated torque signal when the impact between tooth flanks occurs. Indeed, numerical instabilities due to the sudden deceleration of the rotating dog clutch body contribute to generate a torque superelevation. The high jolt cannot be eliminated, unless the contact model is tuned for this purpose, with drawbacks in terms of contact stiffness and damping. It is hence decided to accept said numerical instability.

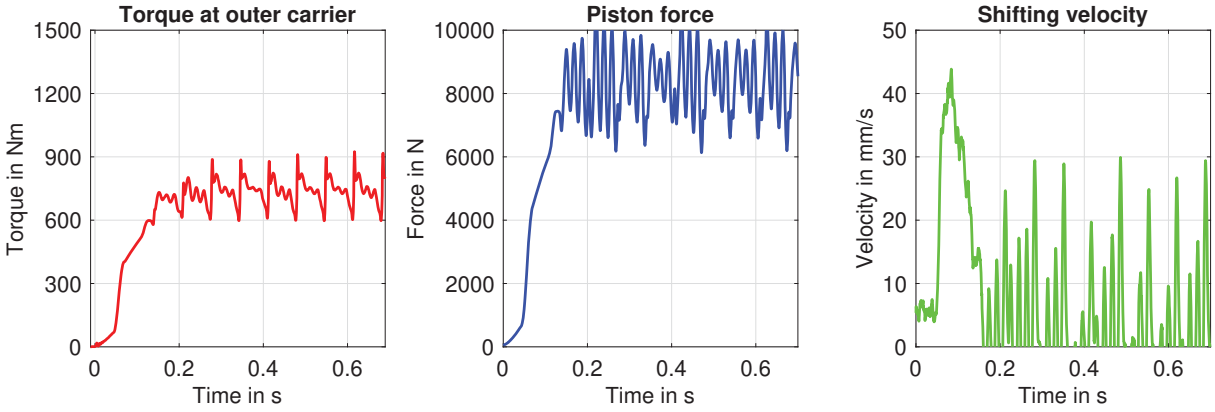

(a) Measured signals of engagement experiment

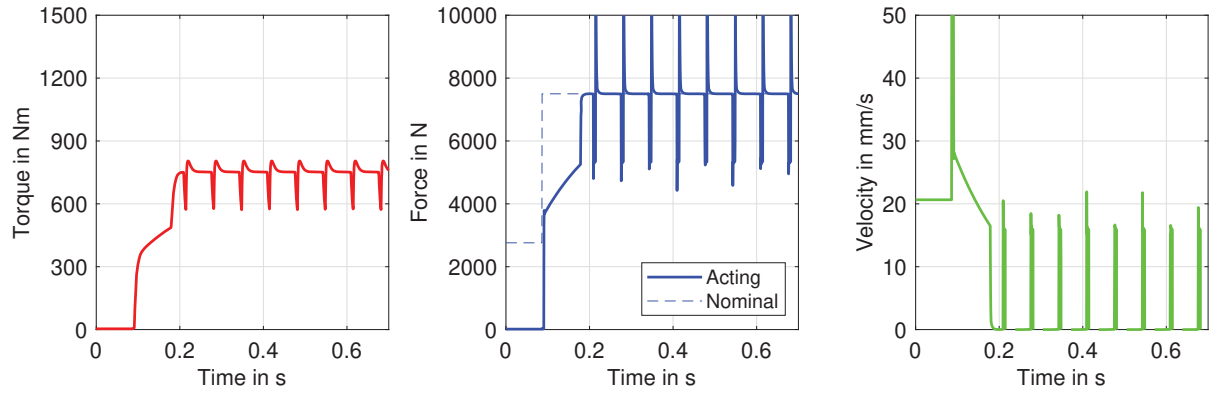

(b) Engagement simulation signals

Figure 5.23: Validation comparison between experiment and simulation of an engagement preceded by a tooth-vs-tooth position. Dog clutch variant V5, F_{ax} = 7500 N, v_f = 18 mm/s, Δn = 25 rpm

In Figure 5.22, an engagement comparison between experiment and simulation for dog clutch variant V3 is shown. In this case, successful engagement occurs after a tooth-vs-tooth position.

For the time the axially movable dog clutch body is unable to move further, velocity drops. In the multibody simulation model, where all bodies are ideal and rigid, velocity drops to zero. Conversely, from measured axial velocity it is visible that the piston does not come to a complete halt. This behaviour is determined by the very limited time the tooth-vs-tooth position is held and the elasticity of all bodies, and in particular of the cone clutch. Again, axial force reaches its maximum value with a delay caused by its damping component. Axial vibrations - visible both in torque and force signals - are determined by hydraulics control. In fact, increased axial velocities reduce stability of force control, especially when an abrupt halt occurs. This phenomenon is known, yet it will not be pursued further, as it can be solved by intervening on control parameters and strategy, as described in literature (refer to Chapter 2).

Finally, in Figure 5.23, a comparison of measured and simulated signals for a tooth rejection for dog clutch variant V5 is shown. Also in this case, all phenomena occurring during rejection are reproduced correctly. In fact, all signals show excellent correspondence in terms of both amplitudes and frequencies. For further engagement comparisons for knowledge-based validation refer to the Appendix.

5.3 Results

In this section, simulation results on engagement behaviour of the dog clutch variants V1 to V6 are presented. After having successfully validated the simulation model, the latter is utilised for determination of performance of the dog clutch, as well as to identify how geometric and design parameters impact on its limits.

5.3.1 Performance determination

In a first step, the simulation model is employed for performance determination of all dog clutch variants. According to the method described in Section 4.3.5, the sole limit relative engagement angle ε_{lim} is sufficient for this purpose.

Through a binary search, 20 points are identified, which represent either the highest possible speed difference with fixed axial velocity, or the lowest acceptable axial velocity with fixed speed difference for still guaranteeing a successful engagement. A linear regression is then performed and the according line is evaluated and plotted. Figure 5.24 shows the results for dog clutch variant V1. According to its relatively high circular backlash, engagement performance of the clutch is excellent. Indeed, for typical piston speeds of v_f = 30 mm/s, engagement can still occur with a speed difference of Δn = 300 rpm. On the contrary

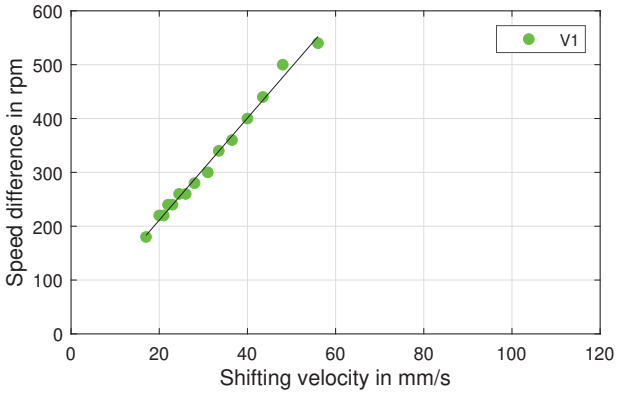

Figure 5.24: Engagement performance in the axial shifting velocity vs. speed difference plane. In black, the linear regression line is shown

engagement and driving comfort behaviours are expected to be poor, due to the considerable circular backlash. Regression line shows linear behaviour with a coefficient of determination that equals R^2 = 0.992.

In Figure 5.25, simulation results of performance evaluation are shown for dog clutch variant V3. The only difference to variant V1 is the reduced backlash and increased number of teeth. The latter parameter is neglected for dynamic analyses, as it is only relevant for load distribution on tooth flanks (see Section 4.3.5). Engagement performance is sensibly reduced, as the linear coefficient of the line - and hence ε_{lim} - decreases. Also in this case, coefficient of determination is very high (R^2 = 0.998).

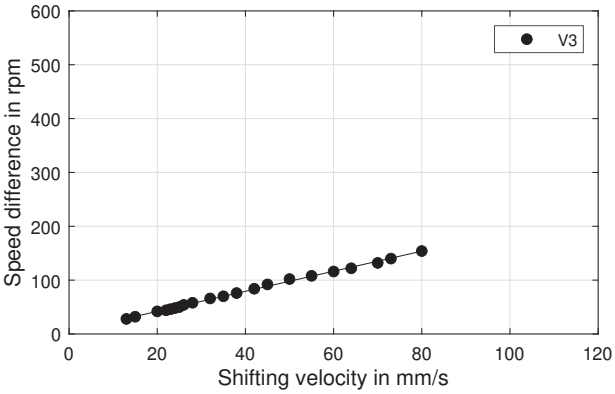

Figure 5.25: Engagement performance in the axial shifting velocity vs. speed difference plane. In black, the linear regression line is shown

Dog clutch variants V2 and V4, which are characterised by a further reduced angular backlash of S_V = 1°, show a visibly decreased engagement performance (see Figure 5.26). Already here, it is clear that the smaller circular backlash, the more influential a further reduction would be. Geometries of variants V2 and V4 differ from each other only for tooth tip shape.

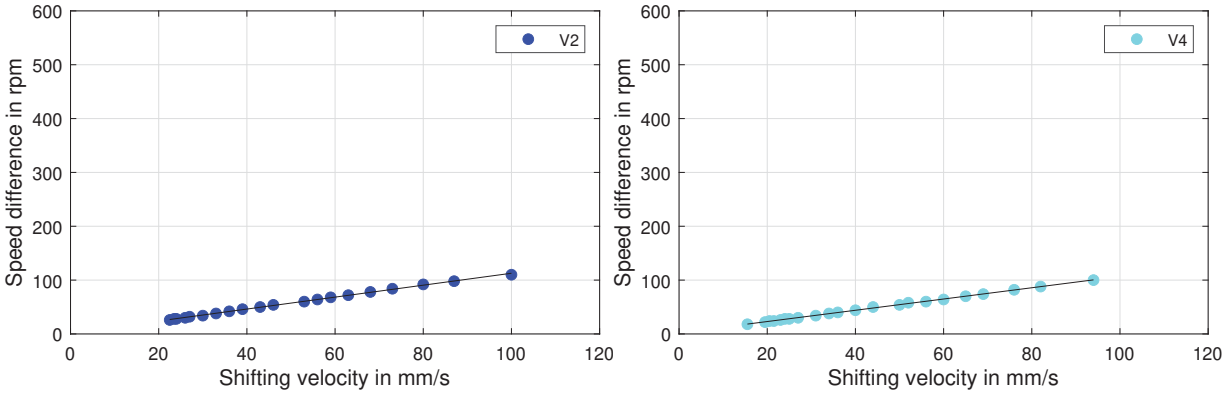

(a) Variant V2 - flat tooth face

(b) Variant V4 - convex tooth face

Figure 5.26: Engagement performance in the axial shifting velocity vs. speed difference plane. In black, the linear regression line is shown

While variant V2 has a flat tooth tip face, V4 is characterised by a convex shape, derived from DCT synchronizers. From an axial perspective, tooth faces are characterised by an arc of circumference with a radius of 40 mm. Effects of tooth face geometry will be analysed in further detail in Section 5.3.2.

Finally, engagement performance of dog clutch variants V5 and V6 can be appreciated in Figure 5.27. As both variants have an angular backlash S_V = 0.4° when disengaged due to their tooth flank inclination, engagement performance line flattens further in comparison to the other

variants. Additionally, tooth flanks are characterised by an angle γ_f = 14°, which allows a zero play angular coupling when fully engaged. Similar geometries are analysed e.g. by Jasnỳ et al [Jas20]. Such angle contributes to reduce initial backlash. Analogously to dog clutch variants V2 and V4, V5 and V6 differ from each other for their tooth face geometry.

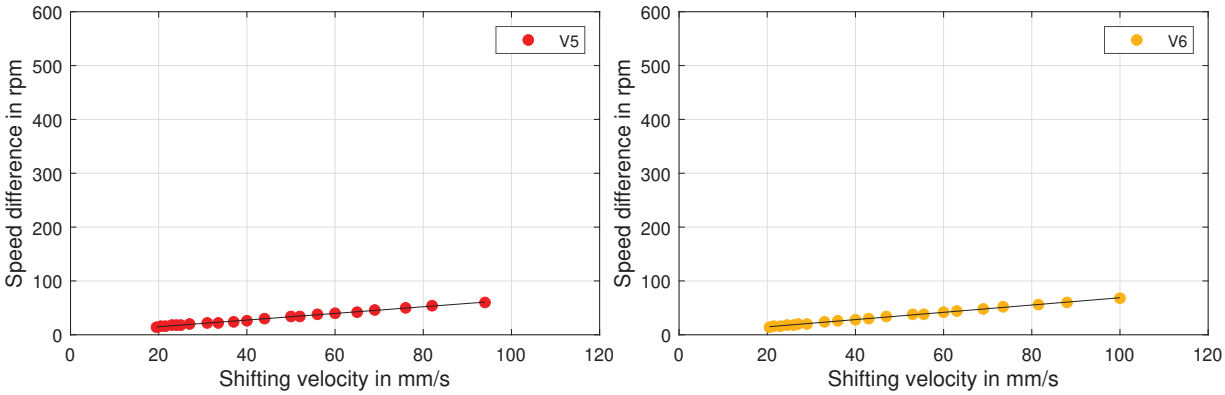

(a) Variant V5 - flat tooth face

(b) Variant V6 - convex tooth face

Figure 5.27: Engagement performance in the axial shifting velocity vs. speed difference plane. In black, the linear regression line is shown

In order to compactly compare engagement performance of all dog clutch variants, the limit engagement angle ε_{lim} is evaluated for all curves starting from regression lines as is expressed in Equation 4.17. Results are plotted in Figure 5.28a. For the derivative of the regression line, which is used for limit engagement angle computation, the standard deviation is computed. The latter is then transformed in angular terms and utilised for plotting a 99.5 % confidence interval for ε_{lim} (error bars).

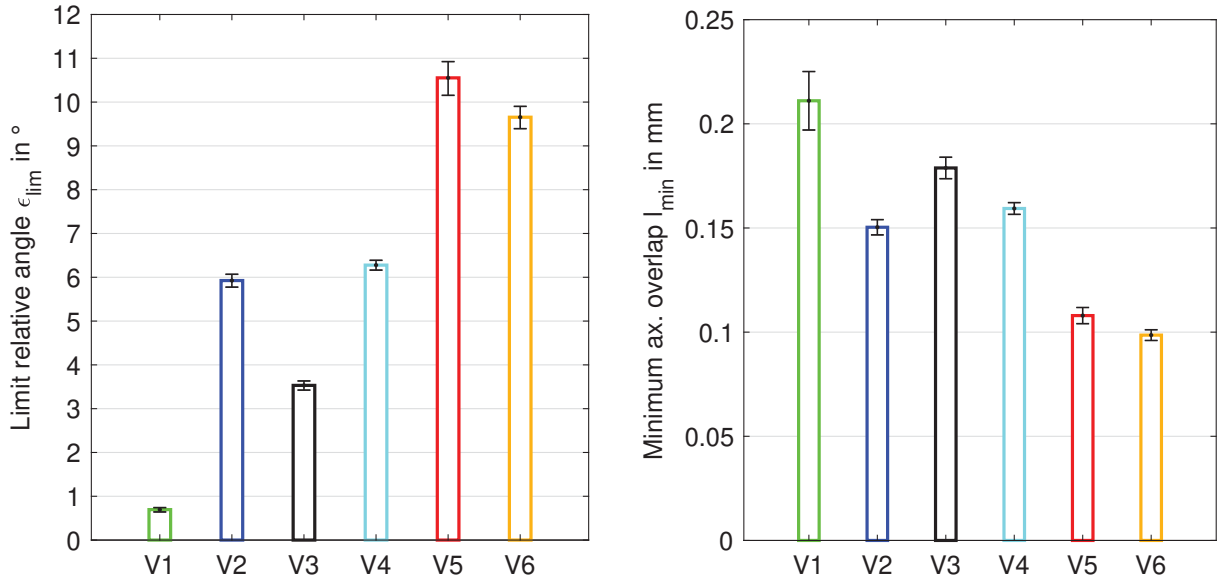

(a) Limit engagement angle ε_{lim}

(b) Minimum axial tooth flank overlapping l_{min} for successful engagement

Figure 5.28: Limit engagement angle and corresponding minimum axial tooth flank overlapping for all doc clutch variants. Error bars indicate the 99.5 % confidence interval

A high confidence interval is chosen in this case, as standard deviation of performance limits is

extremely low. From Figure 5.28a, correlations of engagement performance on geometric design parameters can be appreciated. It is clear that angular backlash strongly influences engagement behaviour. Dog clutch variants with identical backlash (i.e. V2-V4 and V5-V6) show the subordinate effect ot tooth face shape. It can be stated that a symmetric and convex tooth face slightly decreases engagement performance of the dog clutch.

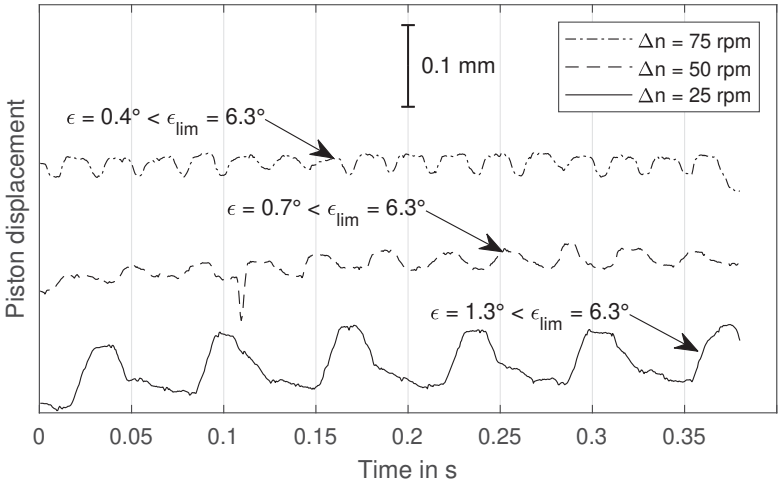

Figure 5.29: Piston axial rejection displacement for three engagement experiments performed with dog clutch variant V4. F_{ax} = 7500 N, T_r = 500 Nm, v_f = 5 mm/s

Figure 5.28b represents the minimum axial tooth flank overlap necessary for successful engagement, evaluated according to Equation 4.17. If the minimum overlap is not reached, tooth rejection occurs, due to the too high local contact pressures, which can reach values between 200 MPa and 300 MPa.

Dog clutch variant V1 shows a particularly high value of l_{min} because of its considerable circular backlash. Additionally, also jolts play a minor role in increasing contact pressure. As small backlash decreases jolt, variants with reduced backlash generally show smaller minimum axial tooth flank overlap.

If flank overlap is less than l_{min}, teeth will be rejected. For instance, in Figure 5.29, measured axial piston displacement is shown for three experiments performed with dog clutch variant V4. Axial piston velocity is set to v_f = 5 mm/s, while speed differences are set

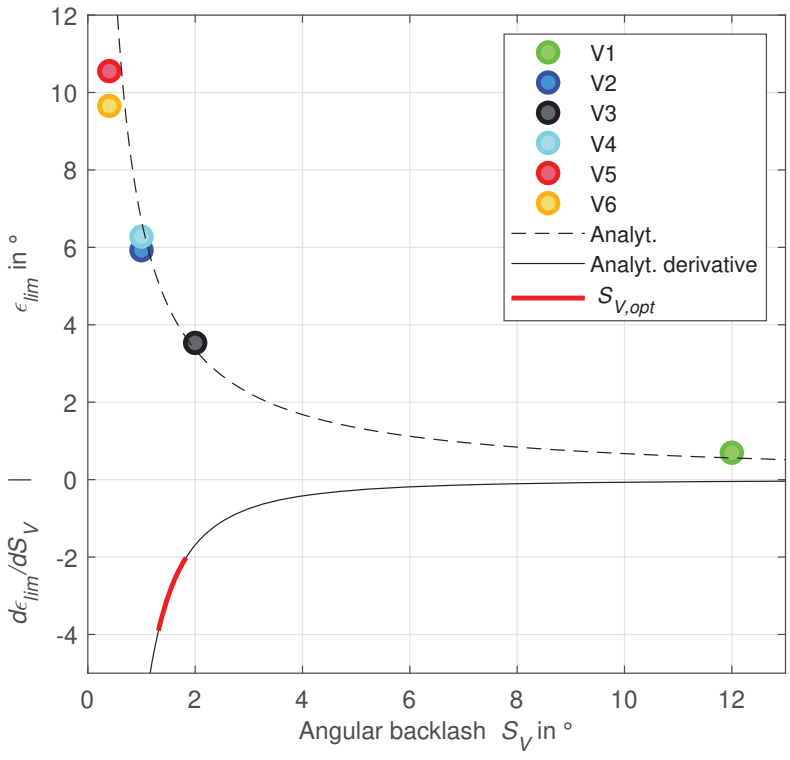

Figure 5.30: Engagement performance as a function of angular backlash S_V

to Δn = 25, 50, 75 rpm. In all experiments, tooth rejection occurs.

From amplitude of the three periodic curves, the tooth flank overlap can be deduced. According to results, the minimum axial overlap l_{min} is not reached for any of the experiments. Also, according to equations, the axial overlap decreases digressively with increasing speed difference.

Dependency of engagement performance on angular backlash can be also summarised in one diagram. Here, the degressive correlation is modulated by the arctangent function, as expressed in Equation 4.17. In Figure 5.30, analytic and simulative results are compared.

For computation of the analytic curve of relative limit engagement angle ε_{lim}, a minimum axial overlap length of l_{min} = 0.17 mm is chosen, according to results shown in 5.28b. The optimal region of circular backlash according to Equation 4.18 is highlighted in red.

5.3.2 Influence of tooth shape

According to results shown in the previous section, also tooth shape has an influence on engagement performance. Generally, tooth flank and tooth tip shapes can be distinguished for better characterisation. As only straight tooth flanks are analysed, only inclination of tooth flank is considered. Inclination angle γ_f is here defined through the angle between rotation axis and actual flank. A positive inclination would result in a tendency to self-open. Conversely, a negative tooth flank inclination, i.e. an undercut, would result in a self-locking dog clutch. Both geometries can be associated to a fail-safe functionality, depending on the desired behaviour of the clutch in case of piston hydraulics failure. As CCDC is to self-release in case of hydraulics failure, a negative angle shall be excluded. Despite torque-induced self-retention, an angle of zero is feasible, as a limited release force is guaranteed by the reset spring. On the other hand, with a positive flank angle, torque-induced disengagement force has to be compensated by hydraulics, thus reducing efficiency of the shifting element.

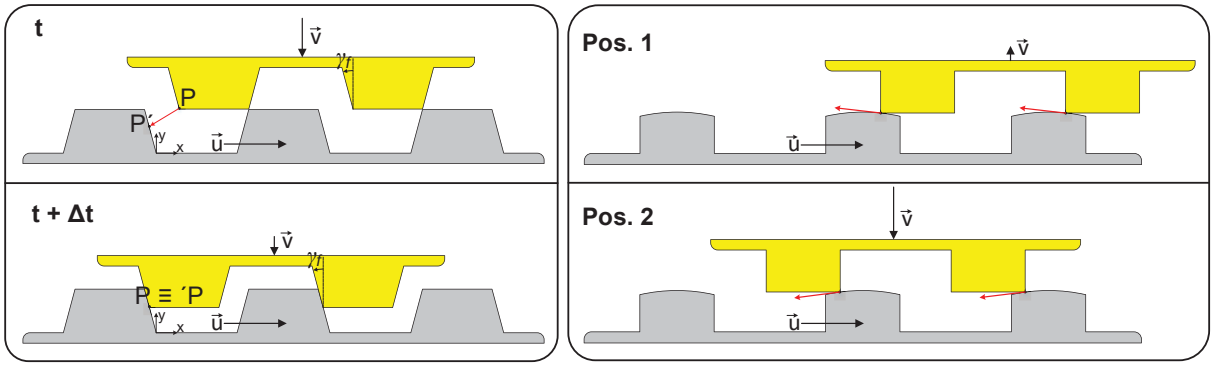

(a) Positive tooth flank angle **(b)** Convex tooth face shape

Figure 5.31: Schematic representation of engagement process with positive tooth flank angle (a) and with different circumferential overlaps for convex tooth face shape (b)

Experimentally, only flanks with an inclination angle of γ_f = 0° are considered, but for the zero play variant V5. In this latter case, in order to guarantee a minimum angular backlash of S_V

= 0.4° in disengaged position, a tooth flank angle of γ_f = 7° is chosen. Dog clutch variant V6, which bases on geometry of V5, presents the same flank angle. Concerning engagement performance, flank inclination can be traced back to angular backlash. In fact, referring to Figure 5.31a, it is necessary to calculate the intersection point between the linear trajectory of point P (determined by x_P and y_P) and the equation describing the corresponding tooth flank. For a general tooth flank inclination the intersection point is shown in Equation 4.15. Also, axial resistance to piston force increases. In particular, the term $F_{ax,s,d,t}$ is concerned (refer to Equation 4.13). Increase of the latter term depends on friction coefficient between teeth and inclination angle γ_f. The force increase due to tooth flank inclination is expressed in Equation 5.3.

$$\Delta F_{ax,s,d,t} = \frac{T_s}{r_m} \cdot \frac{sin(\gamma_f) + \mu_z}{cos(\gamma_f)} \tag{5.3}$$

Also convexity of tooth face has an influence on engagement behaviour, which cannot be traced back to angular backlash in performance determination. A schematic representation of tooth face convexity can be appreciated in Figure 5.31b.

As convexity is symmetric on the tooth face, maximum tooth height is in the middle of each face. During engagement, when tooth-vs-tooth position occurs, the axially movable dog clutch body starts to move forward once 50 % face overlap is passed. In such a way, convexity generates a component of axial velocity $\vec{v}$ before the corresponding tooth gap is met, virtually increasing the relative angle ε. Yet, as can be deduced from simulation results shown in Figure 5.28, engagement performance of dog clutch variants with convex tooth faces is reduced in comparison to variants with same geometry, but flat tooth face. Such behaviour is determined by the symmetric convexity and by dynamics in axial direction. In fact, when a tooth-vs-tooth position occurs with a face overlap of more than 50 %, in a first phase, the piston is rejected by the tooth shape. In this second case, engagement behaviour is slightly worsened. The effect sharpens when circumferential velocity is increased. Engagement performance may be increased with a non symmetric tooth face. However, this would imply that engagement is favoured just in one rotation direction. As CCDC is to be able to work in both rotation directions, such solution is not pursued further.

5.3.2.1 Influence of wear

Operation of a dog clutch is also associated to wear. Indeed, during engagement, tooth faces and flanks experience friction and jolts. While determination of wear phenomena and evolution during life of the component is not part of this work, its effects on engagement performance are analysed in this section. As described in Section 4.3.4.2, wear especially affects engagement behaviour of the dog clutch when it comes to tooth edge rounding.

Wear at tooth edges is mainly generated by tooth rejections. As the dog clutch is designed to avoid tooth rejection in any working condition, wear generation at the tooth flanks is very slow. The proposed method provides a procedure for wear generation. In particular, several misuse shifts are performed, which are characterised by tooth rejection. After performing these tests, dog clutch bodies are unmounted and analysed and wear at tooth edges measured.

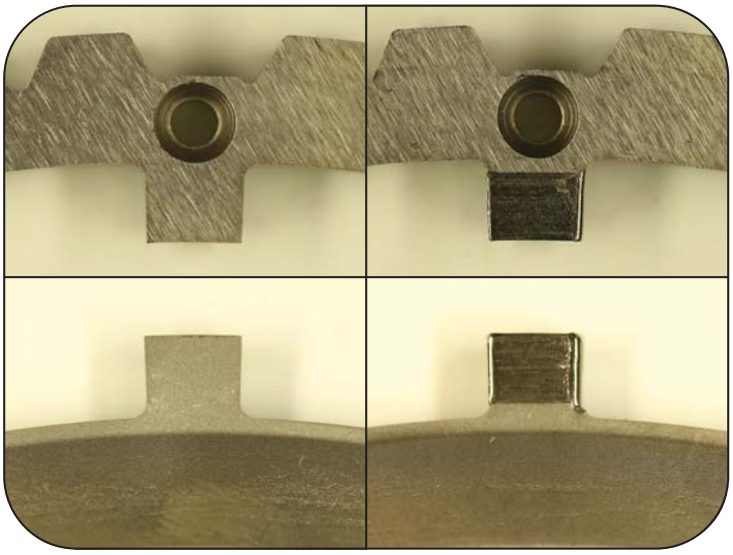

Figure 5.32: New (left) and worn (right) tooth, outer and inner dog clutch body on top and bottom, respectively

In Figure 5.32, the same tooth is shown in new and worn condition for both clutch bodies of variant V1. For photographic documentation of the remaining variants refer to Appendix A.9. Wear is modelled by introducing a fillet with a radius of r_f = 0.3 mm. Such value is an average of measured radii of all variants after having performed misuse shifts. In Figure 5.33, two different outcomes of a shift are represented, when the limit condition of two flanks coming into contact in the region of their rounding is met. Being this the case, the limit flank overlap l_{lim} is not further sufficient to foresee whether a successful engagement will occur or not. Additionally, Equation 5.3, which describes the additional axial force component introduced by an inclined tooth flank, is to be taken into account.

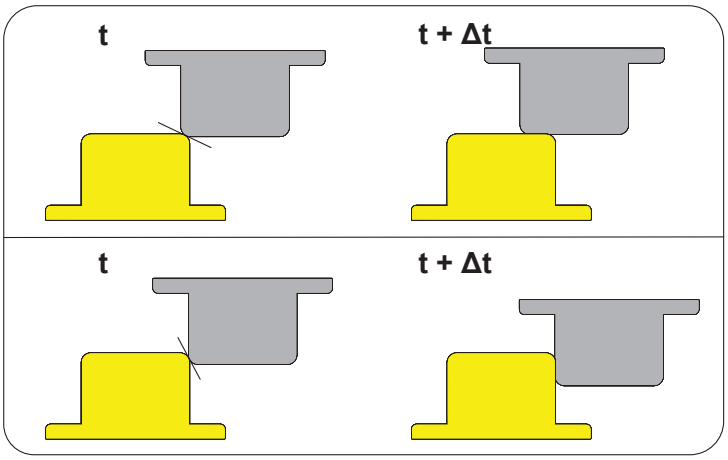

Figure 5.33: Schematic representation of the effect of rounded tooth edges on engagement behaviour

The inclination angle can be calculated by determining the line tangent to both curved geometries at the contact point, as schematised in Figure 5.33. If such inclination exceeds a critical value, teeth will be rejected. Analytical determination of such value is not straightforward, as it depends in turn on the minimum tooth overlap l_{min}. It is hence preferred to only determine the limit engagement angle ε_{lim} simulatively, and base performance assessments on these results.

Engagement performance curves are shown for all variants in Figure 5.34. It is clearly visible that wear of tooth edges has a major effect on engagement performance. A sensible diminution

is recognisable for all variants. Especially dog clutch variants with small angular backlash - i.e. V5 and V6 - are negatively affected by this phenomenon, as their performance decreases by more than 50 %. For all other variants, performance decrease due to a wear-induced tooth edge rounding of r_f = 0.3 mm amounts to about 25 % compared to sharp edged teeth.

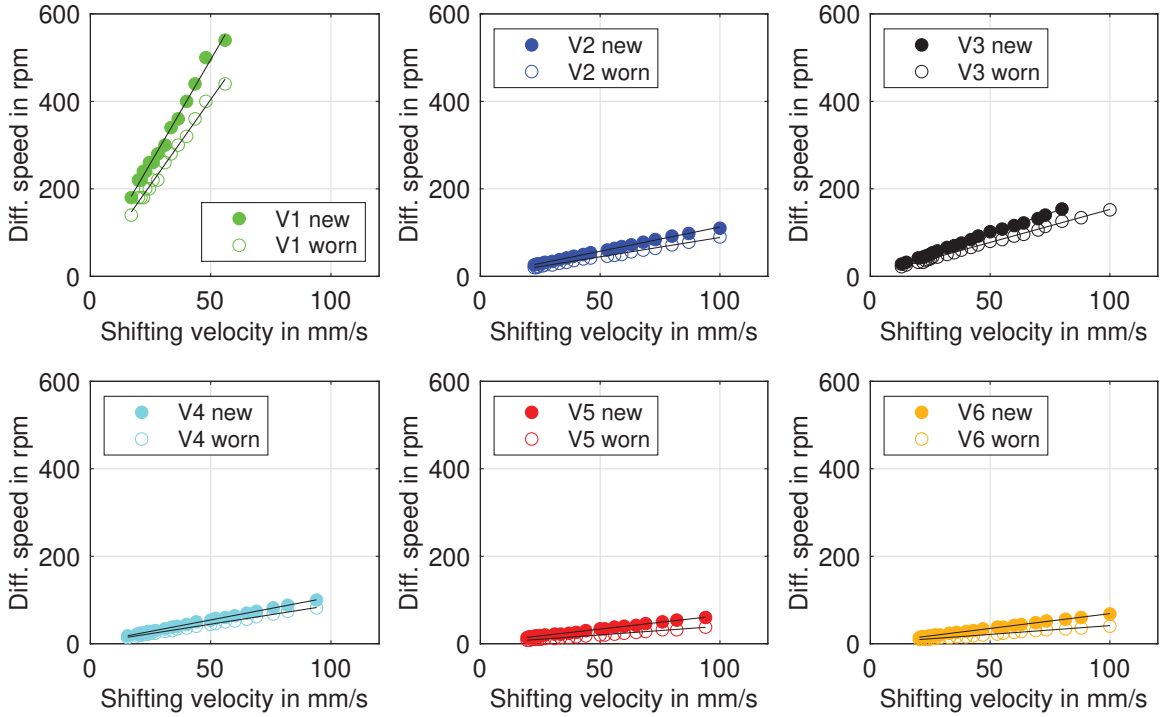

Figure 5.34: Engagement performance in the axial shifting velocity vs. speed difference plane of new (full dots) and worn (hollow dots) teeth. In black, the linear regression line is shown

Modelling of not perfectly sharp tooth edges also helps understanding the phenomenon of tooth skip and delayed engagement. In case a condition is met where engaging and rejecting forces reach an equilibrium condition for a brief interval of time, the full static torque can be transmitted.If such equilibrium proves to be unstable, rejecting forces prevail and force the axially movable dog clutch body to reverse. Such phenomenon recurs as often as a favourable axial tooth flank overlap is reached. However, since such overlap happens to be very close to the value of l_{lim}, the engagement experiment will be considered as not passed. The long-term, yet sensible decrease in engagement performance caused by wear on tooth edges is very well to be considered when designing a dog clutch for powershift engagement purposes. An increase of ε_{lim} of about 20 % is observed for variants with backlash and straight tooth flanks with a tooth edge rounding of r_f = 0.3 mm. Even though such radius is caused by numerous misuse shifts, which shall not occur during normal operation of the transmission, an engagement performance reduction of about 5 % is very likely to occur by end of life of the transmission.

5.4 Discussion and design recommendations

The method described in Chapter 4 is here applied to CCDC in order to prove its effectiveness. Results quantify both performance and limits of cone and dog clutch. Once such limits

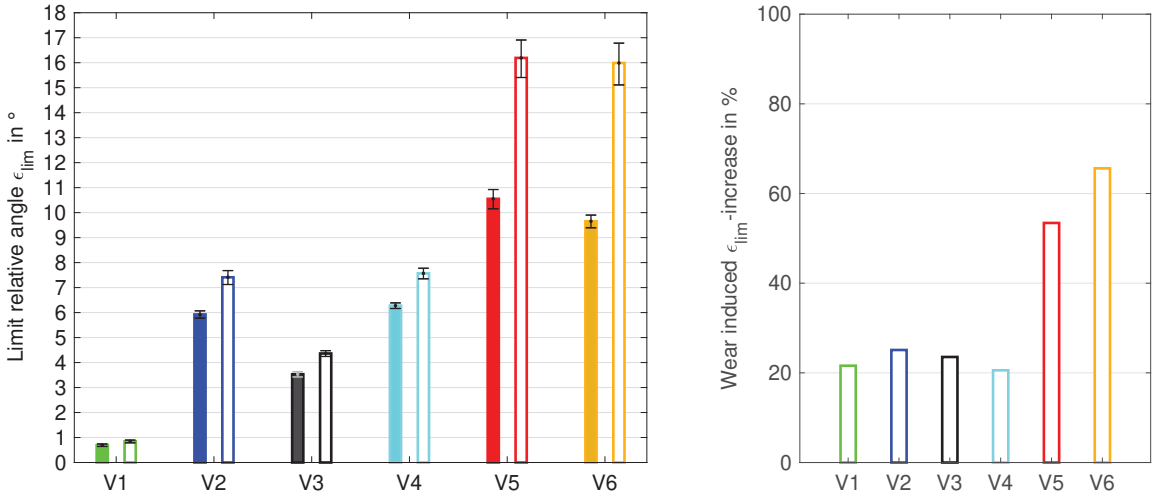

(a) Limit relative engagement angle ε_{lim} for sharp (filled bars) and rounded (hollow bars) tooth edges

(b) Increase of limit relative engagement angle ε_{lim} due to a rounded tooth edges

Figure 5.35: Limit relative engagement angle ε_{lim} for new (i.e. sharp) and worn (i.e. r_f = 0.3 mm) tooth edges (a) and its relative variation (b)

are computed, they can be compared to system requirements so that an optimisation can be performed.

5.4.1 Cone Clutc

Thermomechanical stability of the cone clutch is quantified in Figures 5.12 and 5.13 for CCDC in its second version. Within the validation limits, the neural network is capable of instantly evaluating maximum temperature for any combination of J_{red}, v_0 and p_{avg}. In order to optimise the cone clutch, sheet thickness may be varied as shown in Section 5.1.4.3. This way stiffness and thermal mass especially of the steel cone can be adjusted. The analysed version of CCDC is designed according to the described method and is hence already optimised. As can be appreciated from worst-case gearshift signals in Figure A.27 in the appendix, extreme shifting conditions are simulated and serve as proof of thermomechanical stability of the considered design. In this case, a traction downshift from 5th to 4th speed is considered, with T_{in} = 700 Nm and n_{in} = 2,000 rpm at the input shaft. The resulting friction loss of Q = 2.66 kJ can be converted into specific friction loss of q = 0.65 J/mm^2 and reduced inertia of J_{red} = 0.34 kgm^2. Considering internal kinematics (refer to Figure A.2), an initial sliding velocity at the clutch of v_0 = 10.1 m/s is computed. With J_{red} and v_0, one can see in Figure 5.12 that the performance limits are not overstepped for any value of p_{avg}. Albeit the sheet thickness may be decreased and so costs saved, it is advised to consider a safety factor between results and the critical velocity curve. Safety factor must not be high, as the critical velocity curve is already purposedly slightly overestimated. If the design of the cone clutch is overwhelmingly cost-driven, load combination beyond the critical velocity curve may be accepted, provided that pressure can be modulated

accordingly. On the other hand, increasing sheet thickness may not pe pursued unlimitedly, due to limiting factors such as packaging and manufacturability. Also, unless extremely shifting times $t_S > 2$ s are considered, sheet thickness increase proves limitedly useful beyond a certain value. Such value depends on application and dimension of the cone clutch and must be estimated for each design and application.

5.4.2 Dog Clutch

Dog clutch design is mainly driven by the required performance of the system. For instance, so called *dog boxes* for motorsport and rally applications feature mere dog clutches instead of synchronizers to speed up the gearchange process. As a tooth vs. tooth condition is not wanted either, dog clutch backlash can reach considerable values of S_V. Comfort does not play a role in those cases. The opposite holds for AT applications, generally targeted for the premium automotive sector.

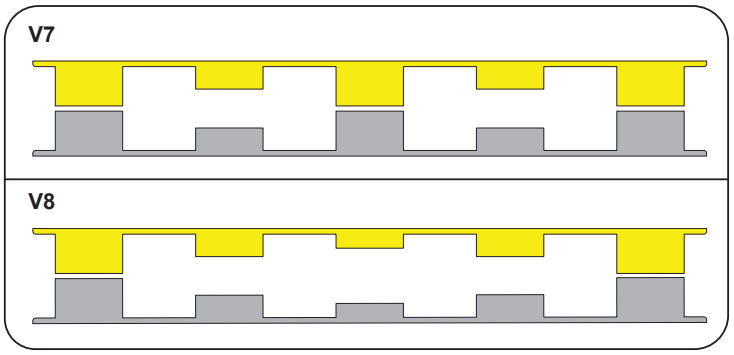

Figure 5.36: Dog clutch variants designed for the second design of CCDC

Hence, the dog clutch design should always start from analysing boundary conditions and chose a backlash as small as admissible and as high as allowable. This way, general requirements to the component are more likely to be met already for the first design. Wear shall also be considered as a limiting factor. Indeed, especially for high backlash values where engagement jolts are expected to be considerably higher, wear can sensibly decrease performance during lifetime. If the component is even subjected to misuse shifts, wear-induced degradation occurs much earlier. In a second step, tooth shape shall be considered in relation to external requirements. For instance, if a fail-safe application (in either way, i.e. hold or release) is required, tooth flank angle γ_f is changed accordingly.

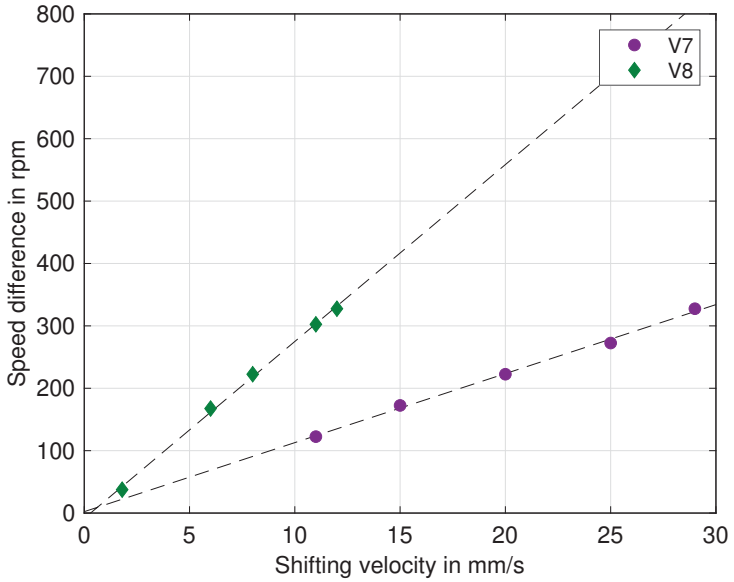

Figure 5.37: Performance of dog clutch variants V7 and V8 for the second CCDC version

In the present chapter, six dog clutch variants designed for CCDC in its first version are shown. Design of the dog clutch for the second version of CCDC is performed according to this method. According to Equation 4.18 and results shown in Figure 5.30, a backlash value of S_V = 1.4° is chosen. Due to the presence of the reset spring, a tooth flank angle γ_f = 0 can be chosen, while tooth tip convexity does not lead to appreciable improvements for the analysed application. Hence, it is decided to even reduce components by utilising splines of the inner carrier as teeth of the inner dog clutch body.

In a second step, the clutch is further optimised by creating a new variant which is realised by axially shortening every second teeth (refer to Figure 5.36). The angular backlash is in this case chosen at the lower limit of the optimal region and is hence as high as allowable for this application. In the engaged condition however, backlash equals again the original value S_V = 1.4°, maintaining same comfort when torque inversions are considered (i.e. traction and thrust). An optimised variant V8 is designed, which further increases virtual backlash and hence reduces ε_{lim}. As can be appreciated in Figure 5.37, engagement performance considerably benefits from the proposed dog clutch correction. If feasible and coherent with the considered design, such solution is hence recommended.

6 Exemplary application at vehicle level

In this chapter, functionality of the CCDC is shown at vehicle level through multibody simulation. In particular, the reference automatic transmission is modelled and linked to a vehicle model at the output. As input of the automatic transmission, speed and torque are set. A model of the internal combustion engine and its dynamics is not built. With the reference shifting element of the reference automatic transmission being substituted with CCDC, gearshifts are simulated and both thermomechanical and dynamic performance is assessed. Simulations are performed with the commercial software SIMpack. In the first section, the automatic transmission, shifting elements and vehicle model are described. In the second section, results obtained with this model are presented and discussed.

6.1 Transmission and vehicle simulation model

Daimler's 9-speed automatic transmission 9G-tronic serves as reference for performance evaluation of CCDC (refer to Appendix A.1). Due to its kinematics, the reference shifting element is chosen to be brake B06. Speed and torque ratios with reference to the input shaft can be appreciated in Figures A.2 and A.3, respectively . As can be seen in Figure A.2, the shifting element is disengaged in all upper speeds, starting from the fifth. Hence, the shifting element generates drag losses whenever the vehicle travels in the fifth gear or higher. Drag losses are even higher than average, due to the fact that the considered shifting element has the highest number of friction surfaces of all other clutches. In fact, as can be seen in Figure A.3, while load torque at the brake is relatively low during shifting, it considerably increases for stationary torque transfer at lower speeds. A shifting element with friction fit has to generate an according friction torque, which is in turn obtained by adding lamellae and thus sliding surface. Conversely, a previously engaged dog clutch is able to effortlessly transmit the high load torque of the first speed.

Transmission 9G-Tronic is composed of four planetary gear sets arranged successively on the main rotation axis. Beside rigid couplings in form of shafts, three clutches and three brakes serve as connection between input and output shafts, gear sets and housing. In the following, geometry and model of gear sets and shifting elements are described into more detail.

6.1.1 Planetary gear sets

Core of the multibody simulation model of the reference automatic transmission are four successive planetary gear sets (P1, P2, P3, P4). Each gear set consists of seven rigid bodies and is characterised by seven degrees of freedom (rotation around the respective axes): sun gear, carrier, ring gear and four identical planets equally distributed around the carrier. Planets are mounted into the carrier and can freely revolute around their axes. Figure 6.1 shows the gear sets in a rendering of the AT. Numbers of teeth are listed for each planetary gear set in Table

6.1 along with the corresponding fixed carrier transmission ratio i_{12}. Suns, planets and gear wheels are modelled as *Gear Wheels*. The same procedure is followed to model the splines between carriers and cone and dog clutch of CCDC (refer to Section 4.3.1). Accordingly, teeth contacts are modelled with *Gear Pair* force elements. In sum, for each planetary gear set, 8 force contacts are to be modelled, as four planets are meshing.

An overall description of the kinematics of the automatic transmission can be appreciated in Dörr et al. [Dör14], along with further technical details.

Gear set	Number of teeth			i_{12}
	Sun	Planet	Ring	
PS1	46	26	-98	-2.13
PS2	44	27	-100	-2.27
PS3	36	23	-84	-2.33
PS4	34	26	-86	-2.53

Table 6.1: Number of teeth of planetary gear sets obtained through reverse engineering

6.1.2 Shifting elements

The nine forward transmission ratios of automatic transmission 9G-tronic are obtained by opportunely actuating the six brakes and clutches. In order to kinematically define the transmission, three DoF have to be blocked in each gear, that is, three shifting elements are always engaged. During gearchange, one shifting element disengages while another engages, according to the desired transmission ratio.

Quantities and units			Shifting elements					
			Brakes			Clutches		
			A (B08)	B (B05)	C (B06)	D (K81)	E (K38)	F (K27)
Outer diameter	D_o	mm	199	195	181	165	166	139
Inner diameter	D_i	mm	184	170	165	140	150	121
Avg. frict. radius	r_m	mm	95.75	91.25	86.50	76.25	79.00	65.00
Frict. surface	A_f	mm²	4,512	7,167	4,348	5,989	3,971	3,676
No. of frict. surfaces	z	-	8	8	10	8	10	12
Total frict. Surface	$A_{f,tot}$	mm²	36,097	57,334	43,480	47,909	39,710	44,108

Table 6.2: Shifting elements of Daimler's 9G-tronic calculated through reverse engineering

All shifting elements of Daimler's 9G-tronic are multiple disc wet clutches / brakes. Names and essential technical data are compiled in Table 6.2. Inner lamellae consist of a steel disc on which linings are rigidly linked on both sides. Both inner and outer lamellae are composed of *Gear Wheel* and *Cylinder* elements for modelling the coupling with the according carrier and the friction surface, respectively. The sliding contact is modelled analogously to the contact between friction cones of CCDC, i.e. utilising the Polygonal Contact Model (PCM) presented in Section 4.3.1. Material parameters of the paper lining are taken from literature (see Table 6.3).

Based on measurements performed at the test-rig KLP-260, a dynamic coefficient of friction of $\mu = 0.13$ is chosen. The value is assumed to be constant and is consistent with values found in literature (e.g. refer to Meingaßner et al. [Mei15]).

Parameter	Symbol	Unit	Steel	Paper lining
Density	ρ	kg/m^3	7850	1700
Young's modulus	E	N/m^2	210·10^9	0.05·10^9
Poisson's coefficient	ν	-	0.30	0.20
Elastic layer thickness	b	mm	1.0	0.7

Table 6.3: Contact parameters and material properties [Omp11, Woh12]

.

6.1.3 Couplings and torque converter

Planetary gear sets and shifting elements are, as mentioned afore, linked to each other through shafts, which serve as couplings. All steel shafts are characterised by an intrinsic flexibility. In the proposed model, all shafts are defined as rigid and decoupled via torsional springs and dampers disposed parallelly, namely a Kelvin-Voigt model. The latter is characterised by a damper with linearly viscous fluid and a linearised elastic body. For further details on the model refer e.g. to Buličeк [Bul12]). The damper considers both internal damping, generated by friction within the solid, and external damping, deriving from viscous drag. The viscoelastic damper may be substituted with a Maxwell element if it becomes unstable. Determination of damping coefficients is not straightforward, hence they are chosen within a sensible range based on experience and computational effort optimisation according to Schecht [Sch11]. Conversely, once geometry is known, torsional stiffness is effortlessly determined through finite element calculations.

One last important component of the AT model is the torque converter. A complete modelling of the internal hydrodynamics is not pursued. The lack of torsional vibration decoupling between motor and transmission is considered acceptable, since a constant torque is generated at the input shaft. In general, it can be stated that the lock-up clutch is always engaged and the pump wheel is hence mechanically linked to the turbine wheel.

Figure 6.1: Model rendering of the automatic transmission, CCDC substituting brake C (B06)

6.1.4 Vehicle model

At the output of the transmission a vehicle model is set up. In particular, the components which follow the AT in the power flux are cardan shaft, which connects the AT to the final drive and differential, final drive and rear drive axle shafts. The rear axle shafts are in turn attached to the wheels and are linked to the vehicle through according bearings.

For the vehicle model, the lumped parameter approach is pursued, obtaining a 1-dimensional system. Hence, the mass of the vehicle is transformed into a reduced inertia, half of it being attached to each of the rear axle shafts. As the aim of this analysis it to determine shifting behaviour of the clutch, it is chosen to further simplify the model and consider moments of inertia of shafts, differential and wheels, through a mass markup factor, de facto reducing the degrees of freedom to one (see Figure 6.2).

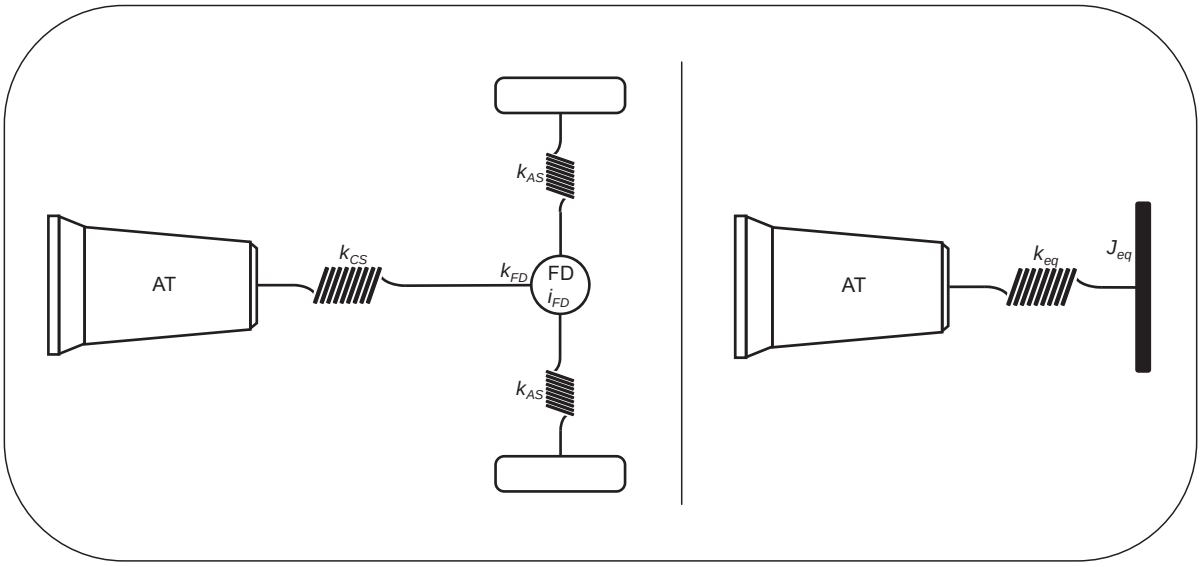

Figure 6.2: Schematic representation of the vehicle model

As a result of a kinetic energy balance, Equation 6.1 is obtained. A markup factor κ introduced for taking into account rotating masses.

$$J_{red} = \kappa \cdot m_V \cdot \left(\frac{r_{dyn}}{i_{FD}}\right)^2 \tag{6.1}$$

J_{red}	kgm^2	Reduced inertia	κ	-	Rotating mass markup factor
m_V	kg	Vehicle mass	r_{dyn}	m	Tyre rolling radius
i_{FD}	-	Final drive transmission ratio	–	-	-

As a consequence of considering the rotating masses with a markup factor, stiffness damping between transmission output and vehicle mass can be reduced to an equivalent torsional spring and damper, respectively. The latter is estimated according to the procedure described in the previous section. Equivalent torsional stiffness is determined by considering the machine ele-

ments that transfer power up to the vehicle reduced inertia through a balance of elastic potential energy and considering the effect of the final drive transmission ratio (see Equation 6.2)

$$k_{eq} = \frac{k_{CS} \cdot k_{FD} \cdot 2k_{AS}}{i_{FD}^2 \cdot k_{CS} \cdot k_{FD} + k_{CS} \cdot 2k_{AS} + k_{FD} \cdot 2k_{AS}} \tag{6.2}$$

$$\frac{1}{k_{eq}} = \frac{1}{k_{CS}} + \frac{1}{k_{FD}} + \frac{i_{FD}^2}{2k_{AS}} \simeq \frac{i_{FD}^2}{2k_{AS}} \tag{6.3}$$

k_{eq}	Nm/rad	Equivalent torsional stiffness	k_{CS}	Nm/rad	Trosional stiffness of cardan shaft
k_{FD}	Nm/rad	Trosional stiffness of final drive	k_{AS}	Nm/rad	Trosional stiffness of axle shafts

Stiffness values are evaluated by considering real geometries of according components. Based on results, Equation 6.2 is simplified to Equation 6.2 and both contributions of cardan shaft and final drive tooth stiffness neglected. In fact, the contribution to equivalent stiffness of cardan shaft and final drive is about 2.1 % and 0.02 %, respectively. According values are shown in Table 6.4. In order to assess performance of gearshifts of CCDC in the worst case scenarios, the maximum allowable input torque to the transmission is chosen, which is delivered by a Diesel ICE. Main vehicle information are summarised in Table 6.4.

Parameter	Symbol	Unit	Value
Vehicle mass	m_V	kg	2200
Final drive ratio	i_{FD}	-	2.47
Max. torque at AT input	T_{max}	Nm	700
Dynamic rolling radius	r_{dyn}	m	0.34
Mass markup factor	κ	-	1.11
Cardan shaft torsional stiffness	k_{CS}	Nm/rad	$9.68 \cdot 10^4$
Final drive torsional stiffness	k_{FD}	Nm/rad	$8.73 \cdot 10^6$
Axle shaft torsional stiffness	k_{AS}	Nm/rad	$1.25 \cdot 10^4$

Table 6.4: Vehicle information used for multibody simulation acc. to Woitysak [Woi20]

6.1.5 Assumptions

Aim of this analysis is to reference shifting behaviour of CCDC to a conventional multiple disc wet clutch, considering both friction and form-fit phases. It is hence necessary to describe the whole process with satisfying preciseness, yet keeping the model simple to result in acceptable computational effort. In order to do so, some assumptions are made, which do not significantly affect accuracy of final results. In particular:

- Most of the dimensions and properties of the described machine elements are either taken from literature or measured in situ. Were this is not possible, an educated guess is made.

- In order to decrease dimension of the problem, some degrees of freedom are actively constrained.
- Transmission input torque is kept constant during the whole powershift. As a reference, only the maximum value shown in Table 6.4 is considered. Effects of the torque converter are neglected as the lockup clutch is assumed to be engaged during the whole shifting process. Torsional vibrations caused by ICE are not modelled, hence the assumption is considered as acceptable.
- The hydraulic actuation system of the AT is not modelled, nor the control strategies for force application. Instead, time-dependent force profiles are predetermined. Clutch actuation control is kept fairly simple, as it depends on driving situation and is tuned based on several subjective parameters.
- Coefficient of friction of shifting elements is kept constant. This way, dependency on sliding speed is neglected, not allowing representation of phenomena such as vibrations or stick and slip.

6.2 Simulation results

In this section, results obtained with the above described model are presented and analysed. In a first step, a reference gearshift is defined, which allows direct comparisons between gearshifts with CCDC and the multiple disc wet clutch from series application. The reference powershift is simulated in three different situations, i.e. for standard, comfort and sporty driving modes. Finally a case where CCDC fails is presented.

6.2.1 Reference gearshift

The alternative shifting element CCDC substitutes the multiple disc brake C (B06) in the reference automatic transmission. The shifting scheme of the AT is shown in Appendix A.1. It shows that brake C is engaged in speeds 1 to 4 and disengaged in speeds 5 to 9. As a consequence, the 5-4 powershift is taken as reference. This corresponds to a condition where either the driver pushes the accelerator pedal sufficiently to trigger a downshift, or the latter is triggered manually. Due to the kinematics of the transmission, ICE torque can support the synchronisation process as soon as the opening clutch starts slipping. Conversely, a downshift while coasting is not supported by ICE torque, yet it is highly improbable and generally not allowed by TCU that such a gearshift is performed at high ICE speed. A power-downshift can be generally performed by positively or negatively overlapping friction torque of the shifting elements. A positive overlap, which occurs when both disengaging and engaging shifting elements generate friction torque for a definite time interval, is chosen for the reference gearshift. The advantage of this strategy is that an overrevving on the ICE may be completely avoided by correctly actuating the shifting elements. However, with a positive overlapping strategy, more friction energy is generated at the friction surfaces, as the sliding phase lasts longer. A simplified power-downshift with nega-

tively overlapping shifting strategy according to Fischer et al. [Fis15] is shown in Figure 6.3. A negatively overlapping strategy is generally used for coasting downshifts and will not be further considered.

As can be appreciated in Figure 6.3, the powershift is performed with both clutches generating friction torque. It begins with the disengaging clutch being slowly released to the point it starts sliding (phase II). Speed synchronisation occurs between II and III, as can be seen from the speed plot. Only at this point, the engaging shifting element is actuated, showing the aforementioned positive overlapping with the disengaging one (between IV and V). At point V, the gearshift is completed.

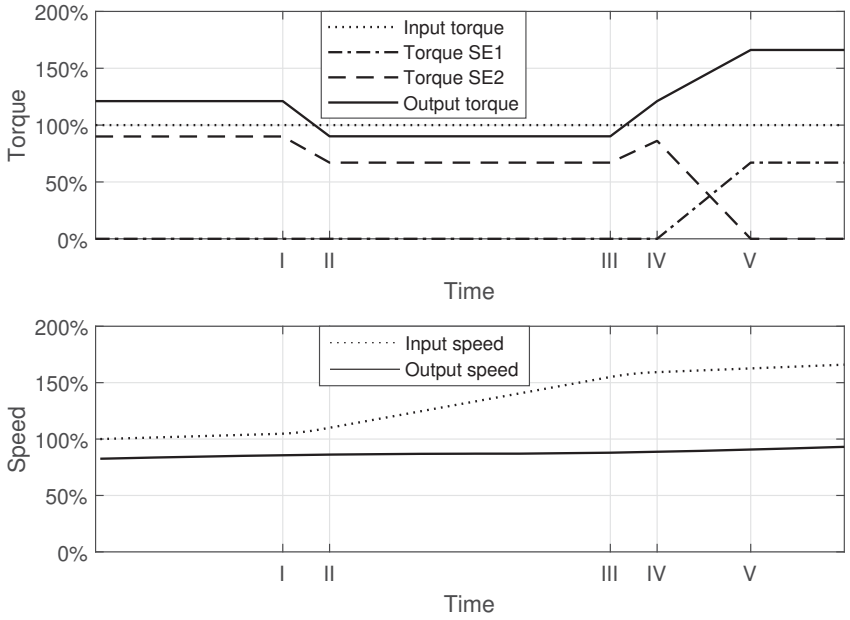

Figure 6.3: Schematic time-dependent representation of a power-downshift with positively overlapping shifting elements (SE1 and SE2)

With this setup being chosen, clutch D (K81) is the disengaging shifting element, while CCDC is the engaging one. Of particular importance is the definition of the time derivative of the actuating force at the disengaging shifting element during overlapping (phase IV - V), as it is directly proportional to the torque increase at CCDC. According to Equation 6.4, the force decrease rate at clutch D determines not only how fast the gearshift is, but also how steep the increase in torque at CCDC is. Indeed, if the torque increase rate is too high, sensible speed difference may build up again, resulting in more difficult dog clutch engagement and possibly to consequent jolts. Conversely, if force at clutch D is diminished more smoothly, the dog clutch is able to close the axial gap and engage before substantial speed difference builds up. However, a longer sliding time leads to higher friction loss. Hence, force gradient at clutch D $-\nabla F_D$ is used as a control parameter to discriminate between gearshifts.

$$\frac{d}{dt}T_{CCDC} \propto -\nabla F_D \tag{6.4}$$

Figure A.30 shows how different shifting strategies can be obtained by changing the actuator force gradient at the opening clutch D. In the following discussion, clutch control with the least steep gradient will be referred to as *comfort* gearchange. Conversely, the gearchange characterised by the shortest shifting time will be referred to as *dynamic*. The reference gearshift

represents a compromise between shifting comfort and a sufficient sportiness feeling.

6.2.2 Comfort rating

In this section, the comfort rating procedure presented in 4.3.6 is utilised in order to show effects of engagement position and gearshift type. All simulations are performed with the second and optimised version of CCDC.

6.2.2.1 Engagement position

Differently from friction clutches, final position of the dog clutch may change after synchronisation is completed, when tooth-vs-tooth position occurs. This means that, due to the torque acting at the CCDC, a speed difference is generated between dog clutch bodies until the next available gap is met. It is clear that such condition does not hold in case of a direct engagement. In order to show the effect of different relative circumferential positions of the dog clutch, a direct engagement, and tooth-vs-tooth overlap of 50 % and 90 % are considered (see Figure 6.4).

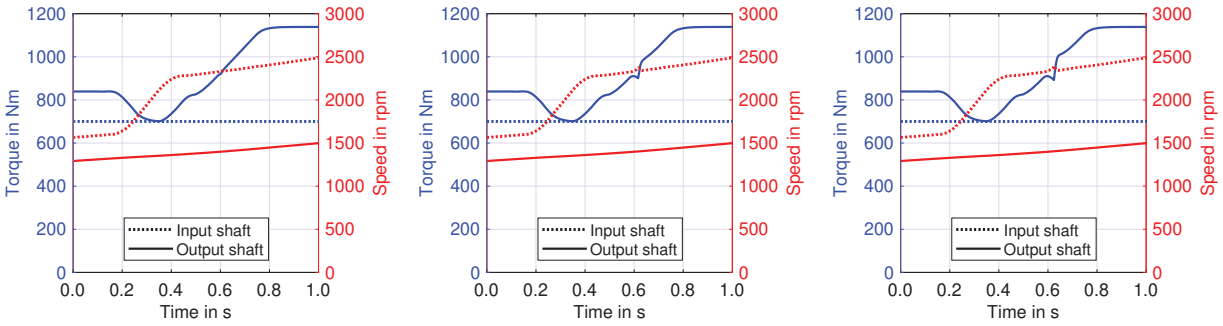

(a) Direct engagement **(b)** 50 % overlap **(c)** 90 % overlap

Figure 6.4: Simulated speed and torque signals of AT input and output shafts for different circumferential dog clutch overlaps

As long as tooth-vs-tooth position occurs and the tooth gap is not met, the dog clutch can only transmit friction torque deriving from cone clutch and - in small part - from tooth faces. Consequently, torque at CCDC remains about constant until the following tooth gap is met. However, friction torque at the disengaging clutch D is parallelly reduced, so that an instantaneous torque increase occurs at CCDC as soon as the piston moves forward and flanks come into contact. During this time interval, as no additional torque can be transferred through the shifting element, an acceleration occurs at the input shaft. Such acceleration determines in turn an overshoot (or flare) of the ICE, which is directly proportional to the time the tooth-vs-tooth position holds on. As can be appreciated in Figure 6.4c, the greatest possible circumferential overlap represents the worst case scenario for what concerns shifting comfort. In fact, the torque step following dog clutch engagement is maximum and determines a slight flare of the ICE. Especially this factor is to be accounted for, as a flare is generally not expected by the driver and causes additional wear at the engaging shifting element. It is however to be noted that ICE flare caused by a 90 % overlap of the dog clutch of CCDC is clearly lower than typical values shown in literature and caused by erroneous and too fast release of the disengaging clutch (refer e.g. to Kahlbau

and Bestle [Kah13b]). Also friction power derived from clutch sliding is relatively limited and expectedly increases with circumferential overlap. In Figure 6.5, friction power peaks, which occur concomitant to ICE flare, are plotted against overlap. It can be noted that specific friction power almost triples when considering 10 % and 90 % overlap. Such values, while negligible with reference to thermomechanically critical values (cfr. Section 5.1.4.2), may be of interest for wear rating and friction layer stability considerations, as sliding occurs with high contact pressure (p_{avg} > 7 MPa).

In order to schematise and objectify shifting comfort, a spider diagram comprising all parameters described in Section 4.3.6 is plotted and shown in Figure 6.6. Those parameters are evaluated for the three overlap situations described above and shown in Figure 6.4. As can be appreciated, friction loss at shifting element D does not change, as it is not influenced by tooth-vs-tooth position of CCDC's dog clutch. The same holds for the shifting time, which in this case depends only on the force increase or decrease rate at CCDC and disengaging clutch D, respectively. With an increased gap, the shifting time may increase, as dog teeth engage later. Also, the shifting control becomes more difficult and risk of noticeable flare significantly higher. Force gradient at clutch D is also constant and is independent of circumferential overlap.

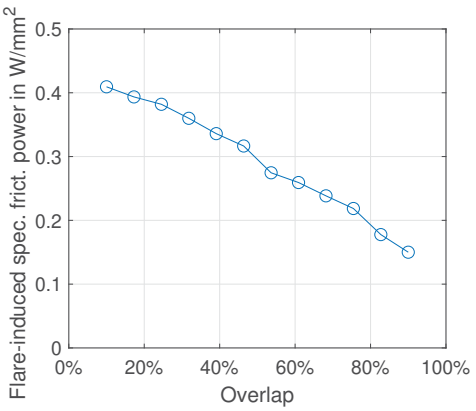

Figure 6.5: Flare-induced specific friction power at CCDC for different circumferential tooth overlap values

Flare, expressed as the momentary speed increase at the AT input shaft (i.e. at the ICE), cannot be completely avoided, unless the circumferential backlash of the dog clutch is set to zero. However, flare from a direct engagement can be generally neglected, while a maximum overlap generates a flare of about 50 rpm. Such value is to be considered overestimated, due to the higher stiffness of the model w.r.t. reality. Due to the low value and limited temporariness, it can be stated that flare is not noticed by the driver even when maximum overlap occurs.

A further drawback of prolonged tooth-vs-tooth position is the instantaneous torque increase when tooth flanks engage. The latter is proportional to the torque decrease at the disengaging clutch occurring during the time interval the tooth-vs-tooth position occurs and hence to the circumferential overlap. AT output torque is directly influenced by such torque increase, as is clearly visible in Figure 6.4. So is, in turn, the torque at the wheels, which has to be taken into account with the final drive ratio. Maximum rotatum ζ_{max} (see Equation 6.5) serves hence as objective indicator of the jolt perceived by the driver and is of particular importance for comfort rating. Direct proportionality between the two values is a consequence of nearly constant

shifting time.

$$\zeta_{max} = max\left(\frac{\partial T}{\partial t}\right) \tag{6.5}$$

All criteria chosen for comfort rating confirm the outstanding shifting performance of CCDC. While direct engagement of the dog clutch may be compared to a standard multiple disc wet clutch, a tooth-vs-tooth position causes only negligible loss of shifting comfort. According to simulation results, varying tooth-vs-tooth positions before engagement of the dog clutch do not represent a perceptible change in shifting comfort. Based on the ATZ Comfort Rating defined by Albers [Alb04] and proposed by Kahlbau [Kah13b], shifting comfort of the reference gearshift with maximum tooth overlap is rated with a performance index of 6, which is sufficient for passenger vehicles. A higher absolute value of ∇F_D causes the torque at CCDC's inner carrier to increase faster. As a consequence, the gearshift is concluded in a shorter amount of time, which is needed when sportiness is required.

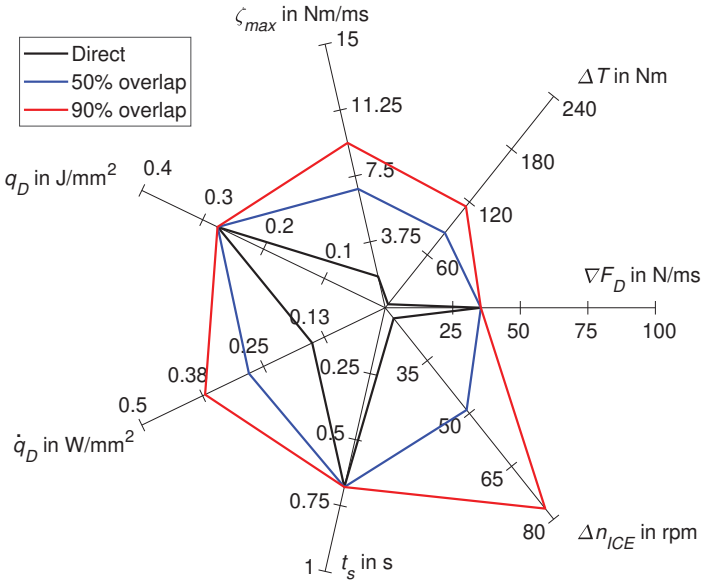

Figure 6.6: Spider diagram showing the effects of different initial tooth-vs-tooth overlaps on shifting comfort

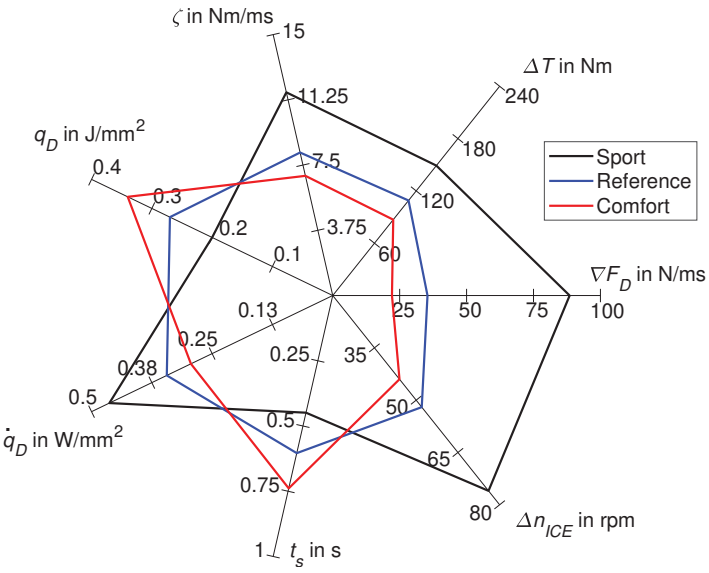

Figure 6.7: Spider diagram showing the effects of shifting strategy on shifting comfort

6.2.2.2 Shifting strategy

Also shifting strategy has a major effect on shifting comfort and is analysed in this section. Considering the reference gearshift, clutch D may be disengaged with a different force gradient, as is appreciable in Figure A.30.

In this very case, the driver expects an abrupt acceleration, so jolt is generally accepted as proof of sporty driving. Conversely, a lower absolute value of ∇F_D enables a more comfortable

gearshift. In fact, during the time interval needed by the dog clutch to engage, torque drop at disengaging clutch D and hence torque increase at engaging CCDC is considerably lower.

Simulation results for reference, sporty and comfort gearchange are shown in Figure A.30. As expected, sporty gearshifts are concluded considerably faster than reference or comfort shifts. Yet the driver will most probably experience a noticeable engagement jolt along with a short flare at ICE. Shifting time of comfort gearshift is increased by about 30 %, reaching t_s = 660 ms. Friction loss at disengaging clutch D increases accordingly. Conversely, due to the slower release of clutch D, flare and engagement jolt are reduced by almost 40 %, considerably increasing shifting comfort.

Finally, a comfort gearshift aims to minimise jolt and ICE flare by further reducing the absolute value of force release rate at disengaging clutch D. A very smooth gearshift may be expected. However, increased values of shifting time and specific friction loss at clutch D by about 25% have to be accepted. While shifting time of t_s = 790 ms may prove relatively long, an increased value of friction loss to up to q_D = 0.34 J/mm^2 is considerably lower than any performance limit identified in Chapter 5. Maximum flare settles at Δn_{ICE} = 40 rpm and is therefore negligible as shown e.g. by Wang et al. [Wan19].

Results for reference, sporty and comfort gearchange are shown in the spider diagram in Figure 6.7. As mentioned afore, it has to be taken into account that gearshift simulations are performed without including ICE support and worst-case scenario with 90 % tooth face overlap is considered. Yet, from results in Figure 6.7, it is clearly visible that CCDC is capable of providing good shifting comfort (rating 6) in all driving modes.

6.2.3 Incorrect gearshift

In order to fully understand the consequences of a failed gearshift a specific simulation is performed. In this case, the release force gradient of disengaging clutch D is further increased to a value of ∇F_D = -175 N/ms. If this is the case, toque increase at CCDC's inner carrier is too fast for the cone clutch to overcome it. Accordingly, the inner carrier begins to spin causing the speed difference to grow above the engagement limits computed in Chapter 5. Consequently, a tooth rejection of the dog clutch occurs, leading to a failed gearshift. Simulated signals are shown in Figure 6.9.

If the input torque would continue to act on the input shaft, the additional degree of freedom of disengaged CCDC would cause the internal shafts to accelerate, reducing output torque accordingly. It is however important to clarify that this example is merely academic. This condition would only occur in case of failure of the actuation system or of a TCU malfunction. It would lead to shift failure also in case a multiple disc clutch is employed as shifting element (refer, for instance, to Čoríc et al. [Čor17]).

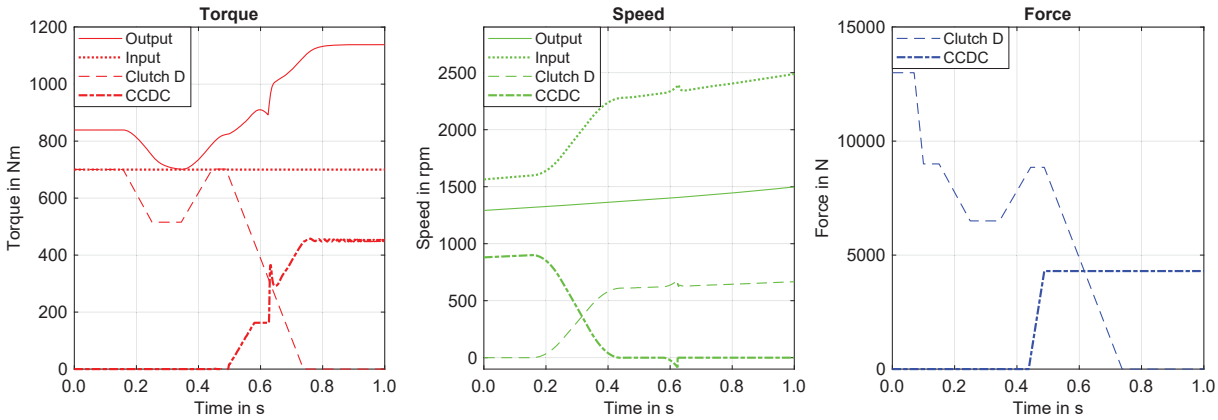

(a) Reference gearshift

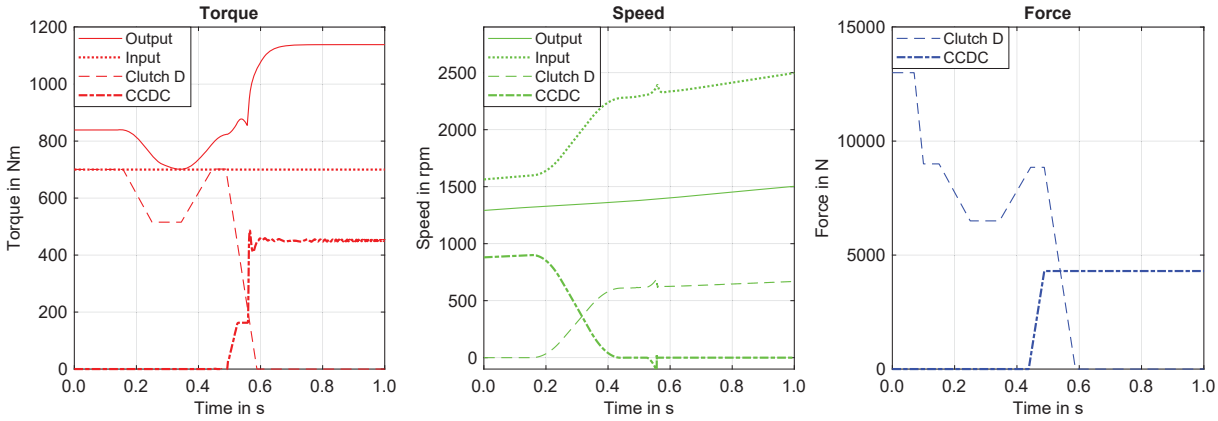

(b) Sporty gearshift

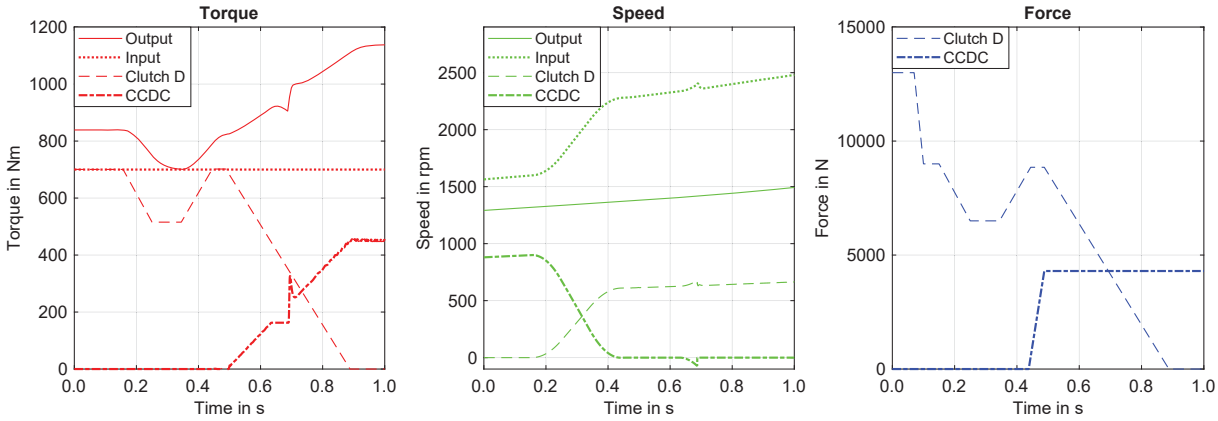

(c) Comfort gearshift

Figure 6.8: Simulated torque, speed and force signals at input and output shafts of the automatic transmission as well as at disengaging and engaging shifting elements

6.3 Conclusions

Employment of CCDC in existing automatic transmissions is generally possible without need of major structural changes of the transmission itself. The alternative shifting element is adapted to an existing packaging and integrated in the system. In particular, multiple disk wet clutch C (B06)

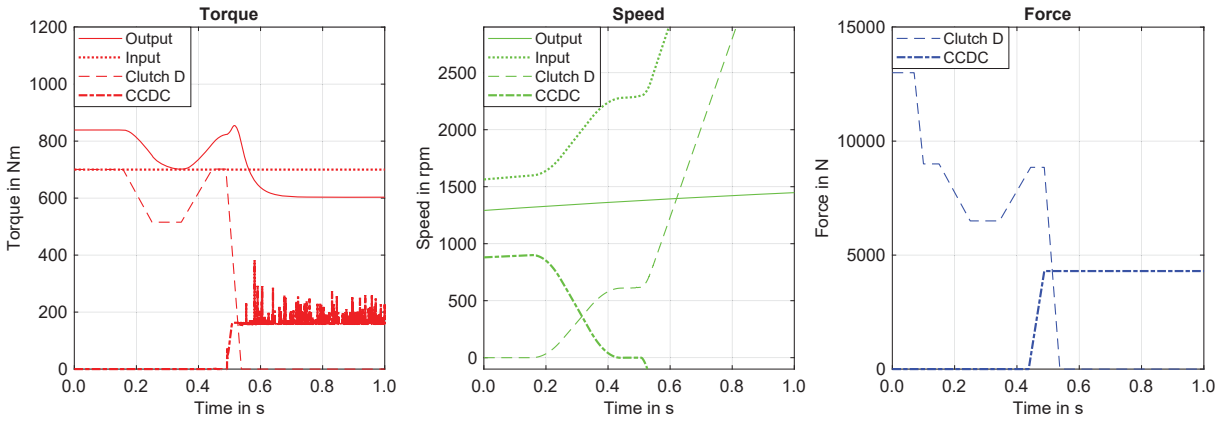

Figure 6.9: Simulated torque, speed and force signals at input and output shafts of the automatic transmission as well as at disengaging and engaging shifting elements for an incorrect gearshift

is substituted with CCDC, as such interface offers the most benefits of employing the alternative shifting element. After showing how the AT model is built, results from shifting simulations are shown. A manually triggered power-downshift 5-4 is chosen as a reference, as it proves to represent the worst case scenario. At the input shaft, the maximum allowable torque for the transmission is applied. No ICE support is considered during the gearshift. Shifting control of disengaging and engaging shifting elements is characterised by a positive overlap of friction torque. Shifting performance is rated through a number of parameters, which take into account both thermomechanical stability and engagement behaviour.

The effect of different tooth-vs-tooth circumferential positions during dog clutch engagement is analysed. It is shown that such effect is caused by the finite number of end positions of the dog clutch and cannot hardly be corrected, unless a very robust and purpose-created control is implemented in the TCU. A relative rotation of the dog clutch bodies after synchronisation completion is necessary to reach the final engagement position. As the amplitude of such rotation is aleatory and underlies a continuous uniform distribution, effects of different tooth-vs.tooth overlapping positions is shown and analysed. Results show that a difference between gearshifts exists indeed in terms of thermomechanical and dynamic solicitation. They however also point out that such shifting performance variation is hardly noticeable by the driver and is considered as innocuous for the shifting element itself.

Changing torque handover time between shifting elements - i.e. axial actuation force gradient - determines the overall shifting time and affects comfort. Indeed, three shifting modes are identified, which depend on the release force rate of disengaging clutch D. Equivalent shifting modes are widespread on the automotive marked and can be selected by the driver. Results show excellent performance of CCDC in any shifting condition. As expected, increasing shifting comfort leads to higher thermomechanical loads at the disengaging clutch D. Conversely, a sporty powershift leads to decreased shifting time and consequently thermal solicitation, yet increasing engagement rotatum. The latter converts into a perceptible jolt, which is however

associated to driving sportiness by the driver and thus accepted.

In all presented cases, CCDC is capable of engaging correctly and without delay or sensible comfort loss. Simulative results confirm that all critical parameters lay considerably below performance limits of both cone and dog clutches. Therefore, if definite boundary conditions for successful substitution and integration are met, CCDC proves to be a valid and efficient alternative to conventional multiple disc wet clutches.

A failed gearshift, caused by an extremely high force decrease rate at the disengaging clutch, is presented too. The extreme dynamicity of the process causes a tooth rejection of the dog clutch, due to the arisen speed difference between dog clutch bodies. While - differently form CCDC - a multiple disc clutch may be theoretically able to recover from such situation by generating sufficient friction torque, this condition is to be prevented by the transmission control system.

,

7 Summary and outlook

7.1 Summary

Modern drivetrain evolution is mainly driven by acting legislations aiming to reduce global CO_2 emissions. While development of hybrid and fully electric vehicles represents an opportunity to develop new higly-efficient concepts, classical drivetrains will continue to hold a considerable market share for the years to come. In both cases - and in the second rather than the first - efficiency increase is an imperative to reach emissions objectives within the fixed time constraints in order to avoid extremely costly penalty fines. Modern automatic transmissions (AT) are - similarly to every multispeed transmission characterised by friction shifting elements - affected by drag losses of disengaged clutches. Share of said losses can represent more than 60 % of the total. The development of a novel shifting element, alternative to standard multiple disk wet clutches, appears hence to be highly desirable to help reduce the vehicle's emissions. The alternative shifting element (CCDC) presented in this work represents one such solution for any powershiftable transmission. In fact, CCDC combines peculiarities and advantages of friction and dog clutches and compensates the respective drawbacks. The application field for CCDC ranges therefore from classic ATs to DHTs and multispeed transmissions for BEV.

CCDC consists of serially connected cone and dog clutch. The cone clutch is capable of increasing the axial force provided by the shifting actuator by a factor determined by the reciprocal of its sine. This allows an according reduction of friction interfaces, if the same friction torque is required. Friction surface reduction can reach values of up to 80 %. If the considered shifting element is designed for transferring even higher static torques (as is e.g. the case for Brake C(B06) in Daimler's 9G-Tronic AT), friction surface reduction can be pushed even further and reach values of up to 93 %. As widely confirmed in literature, such friction surface reduction directly influences drag losses, which can be more than halved. Experimental proof can be appreciated in Chapter 3. After synchronisation is completed, dog clutch engagement takes place. In order for this to happen, a speed difference between dog clutch bodies must exist.

Albeit CCDC proves to have both synchronisation and form-fit-generation capabilities, some aspects concerning both clutch types must be considered with extreme attention. Aim of this work is to develop a method, which accompanies the development process of combined cone and dog clutches for application in powershiftable transmissions. Peculiarity of CCDC's design allows to divide the development process into two subsequent phases, which chronologically follow the engagement process. Such division is taken on for method description.

Thermomechanical stability

Synchronisation is carried out on a strongly decreased friction surface. Accordingly, both specific friction pressure, loss and power increase, leading to more critical temperature values and distributions within the clutch itself. In line with literature, unfavourable thermal conditions may

lead to instabilities and friction surface hotspotting. As hotspots must be avoided, a validated and cost-effective method is developed, which is capable of assessing thermomechanical performance of the cone clutch and provides information on suitable working regions. Due to the strong and non-linear interaction between mechanical and thermal effects which induce spontaneous damages (in case of CCDC: hotspots), an experimental validation of the results is not omittable. However, since experiments are connected with high time-effort, determining performance limits of a given cone clutch and subsequently generalising the results is not a feasible solution. Instead, experimental results are utilised to validate a two-dimensional, axisymmetric finite element simulation model, which is capable of giving information on temperature and location of hotspots on the friction surface. Determination of performance limits is further implemented by developing an artificial intelligence (AI) algorithm. For such purpose, a neural network (NN) is chosen. Simulation results are utilised as training datasets with maximum temperature on the friction surface during synchronisation as output. In fact, maximum temperature is assumed to trigger thermomechanical instabilities on the friction surface. A threshold temperature is hence individuated by comparing performed experiments with simulative results and literature. Thermomechanical performance limits are computed for CCDC and are shown in Chapter 5.

Dynamic behaviour

Dog clutch engagement occurs after the synchronisation process is complete by overrunning a prestressed release spring. A speed difference between dog clutch bodies is necessary to provide a definite rotation. In line with the intrinsic nature of powershifts, engagement takes place under static torque, which at some point exceeds friction torque and causes the dog to gain speed difference. However, if load torque grows too fast, speed difference may grow beyond acceptable limits for successful engagements. Axial velocity of the piston plays a fundamental role in determining which rotational speed mismatch is bearable by a definite dog clutch design. A validated method is hence developed for dynamic performance assessment. Several engagement experiments under varying load conditions serve as validation data for a multibody simulation model which reproduce the employed test-rig. With the validated simulation model, dynamic performance limits of different dog clutch geometries can be determined and assessed. Performance curves can be described by one single parameter - the limit relative engagement angle ϵ_{lim}. The latter represents the direction of the vectorial difference between axial velocity and circumferential speed at the dog teeth. Furthermore, an analytical equation is developed, which allows to directly put performance limits in relation with design parameters of the dog clutch. In Chapter 5, engagement performance of CCDC is assessed for all investigated dog clutch variants. A study on effects of wear and tooth shape is shown. Two optimised dog clutch variants (V7 and V8) are designed and their performance assessed through the described method.

Utilising a multibody simulation model of the reference AT 9G-Tronic by Daimler, a holistic investigation on CCDC-gearchanges is performed. For this purpose, reference shifting element - brake C (B06) - is substituted with CCDC. Simple ICE and vehicle models are connected to input and output of the transmission's model, respectively. Seven critical parameters are defined and evaluated for different gearchange types. Thanks to such parameters, suitability and goodness of CCDC with respect to shifting comfort and thermomechanical stability is proved.

7.2 Outlook

The presented method supports development of a coupled cone and dog clutch for power-shiftable transmission systems. Each of both sub-methods may be employed singularly and in different development fields, as they are independent. With minor modifications, the method for thermomechanical performance assessment may be applied to all sort of friction clutches, as those systems are generally axisymmetric. In fact, the parametrised simulation model is easily adaptable to virtually every geometry. The neural network is not affected by changes and would need no adjustments. While having been subject to many improvements over the last years, the thermomechanical simulation model may be further optimised for faster computation. This would further increase preciseness of maximum temperature prediction during a sliding process. Also, it could be adapted and extended to include adjacent components or consider oil cooling also during the short synchronisation process. Result of the developed neural network is a black-box function. Although the user has no control on such function, it allows to describe phenomena not describable elseways. It is also capable to deliver temperature predictions way faster than real time. It could hence be easily integrated in transmission control systems to optimise each gearshift based on available data (speed and torque) and possibly avoid clutch degradation by e.g. adjusting shifting time.

The developed analytical equation of ϵ_{lim} links minimum tooth overlap and circular backlash with axial velocity and speed difference. It is a powerful tool which supports dog clutch development in an early phase by allowing a direct comparison between all desired geometries without the need of costly testing. Also in this case, thanks to the simplicity of the formula, a real time implementation in TCUs may result extremely helpful in preventing tooth rejections and related comfort issues. In fact, often the axial velocity of the piston determines the bottleneck of the system. For instance, utilising speed measurements at input and output shafts, the control system may decide to shortly reduce ICE torque or increase friction torque if an engagement is deemed to be unsuccessful.

References

Papers, Books, Dissertations, Thesises

[Abb14] Abbasi, S. ; Teimourimanesh, S. ; Vernersson, T. ; Sellgren, U. ; Olofsson, U. ; Lundén, R.: Temperature and thermoelastic instability at tread braking using cast iron friction material. In: *Wear* 314 (2014) Nr. 1-2, pp. 171–180.

[Abd16] Abdullah, O. I. ; Schlattmann, J.: Thermal behavior of friction clutch disc based on uniform pressure and uniform wear assumptions. In: *Friction* 4 (2016) Nr. 3, pp. 228–237. ISSN: 22237690.

[Abu] Abu Snima, K.: Kenngrößen und Belastungsgrenzen von nasslaufenden Lamellenkupplungen unter Dauerschlupfbeanspruchung: Dissertation. In:

[Ach14] Achtenová, G. ; Pakosta, J. ; El Morsy, M.: Smoothness of Maybach dog clutch shift in the automotive gearbox. In: *13th International CTI Symposium, Berlin* (2014).

[Ach18] Achtenová, G. ; Jasny, M. ; Pakosta, J.: Dog Clutch Without Circular Backlash. In: *SAE Technical Papers* Volume 2018-April (2018).

[Acu14] Acuner, R. ; Pflaum, H. ; Stahl, K.: Friction screening test for wet multiple disc clutches with paper type friction material. Society of Tribologists and Lubrication Engineers, 69th Annual Meeting & Exhibition, (2014).

[Acu16] Acuner, R.: Synchronisierungen mit Carbon-Reibwerkstoffen unter hohen und extremen Beanspruchungen: Dissertation. In: Nr. 213 (2016).

[Ai05] Ai, X. ; Anderson, S.: An Electro-Mechanical Infinitely Variable Transmission for Hybrid Electric Vehicles. In: *SAE Technical Papers, 2005-01-0281* (2005).

[Alb04] Albers, A.: Ermittlung und Objektivierung komfortrelevanter Gesamtsystemeigenschaften. In: *Ermittlung und Objektivierung komfortrelevanter Gesamtsystemeigenschaften,* (2004).

[Alb18] Albers, A. ; Ott, S. ; Kniel, J. ; Eisele, M. ; Basiewicz, M.: Investigation of the thermomechanical behaviour of clutches using fibre optic sensing technology with high spatial measurement density. In: *Proceedings of the Institution of Mechanical Engineers, Part J: Journal of Engineering Tribology* 232 (2018) Nr. 1, pp. 26–35. ISSN: 1350-6501.

[And90] Anderson, A. E. ; Knapp, R. A.: Hot spotting in automotive friction systems. In: *Wear* 135 (1990) Nr. 2, pp. 319–337.

[Aph06] Aphale, C. R. ; Cho, J. ; Schultz, W. W. ; Ceccio, S. L. ; Yoshioka, T. ; Hiraki, H.: Modeling and Parametric Study of Torque in Open Clutch Plates. In: *Journal of Tribology* 128 (2006) Nr. 2, p. 422. ISSN: 07424787.

[Aph10] Aphale, C. R. ; Schultz, W. W. ; Ceccio, S. L.: Aeration in lubrication flows with application to reduced disengaged drag torque in clutches. In: *7th International Conference on Multiphase Flow, Tampa, FL, USA* (2010).

[Ash93] Ashikawa, R. ; Naruse, T. ; Kurashina, H. ; Matsuoka, T. ; Adachi, T. ; Nakayama, T.: ATF Characteristics Required for the Latest Automatic Transmissions. In: *SAE Technical Paper Series 1993* (1993).

[Bac16] Back, O. ; Damm, A. ; Echtler, P.: Clutches with positive fit for Automatic Transmissions. In: *International VDI Congress - Drivetrain for Vehicles, VDI* (2016).

[Bal90] Balci, O.: Guidelines for successful simulation studies. In: *1990 Winter Simulation Conference, New Orleans, LA, USA* (1990), pp. 25–32.

[Bao16] Bao, K. ; Zhang, Z. ; Liao, R.-D.: Failure Physics Analysis of the Thermoelastic Instability in Automotive Wet Friction Disks Based on Pressure Distributions of Return Springs. In: *Prognostics and System Health Management Conference (PHM-Chengdu)* (2016).

[Bar67] Barber, J. R.: The influence of thermal expansion on the friction and wear process. In: *Wear* 10 (1967) Nr. 2, pp. 155–159.

[Bar69] Barber, J. R.: Thermoelastic Instabilities in the Sliding of Comforming Solids. In: *Proceedings of the Royal Society A: Mathematical, Physical and Engineering Sciences* 312 (1969) Nr. 1510, pp. 381–394. ISSN: 1364-5021.

[Bau11] Bauchau, O. A.: Flexible Multibody Dynamics. Vol. 176. Dordrecht: Springer Netherlands, (2011).

[Bau20] Baumgartner, A.: Friction Behavior of Wet Disk Clutches – Uncertainty of Measurement and Evaluation Methods. master's thesis, Cahir of Machine Elements, technical University of Munich, (2020).

[Ben72] Benkler, H.: Zur Auslegung bogenverzahnter Zahnkupplungen. In: *Konstruktion* 24 (1972), pp. 326–333.

[Bla96] Bland, J. M. ; Altman, D. G.: Statistics Notes: Measurement error. In: *BMJ* 313 (1996) Nr. 7059, p. 744. ISSN: 1468-5833.

[Bók10] Bóka, G. ; Márialigeti, J. ; Lovas, L. ; Trencséni, B.: Face dog clutch engagement at low mismatch speed. In: *Periodica Polytechnica Transportation Engineering* 38 (2010) Nr. 1, p. 29. ISSN: 0303-7800.

[Bók11] Bóka, G.: *Shifting Optimization of Face Dog Clutches in Heavy Duty Automated Mechanical Transmissions*. Ph.D. Thesis. (2011).

[Bos11] Boss, R. ; Gumpoltsberger, G. ; Freudenreich, H.-P.: Multi-stage gearbox. In: *Worldwide applications, Patent US8062164B2* (2011).

[Bre08] Breuer, S.: Getriebe. Wiesbaden: Springer Fachmedien, (2008).

[Buc13] Buchberger, R.: Synchronization methods of automated gearboxes for electric driven light commercial vehicles. In: *LMS European Vehicle Conference* (2013).

[Bul12] Bulíček, M. ; Málek, J. ; Rajagopal, K. R.: On Kelvin-Voigt model and its generalizations. In: *Evolution Equations and Control Theory* 1 (2012) Nr. 1, pp. 17–42. ISSN: 2163-2480.

[Bur08] Burden, F. ; Winkler, D.: Bayesian regularization of neural networks. In: *Methods in molecular biology (Clifton, N.J.)* 458 (2008), pp. 25–44. ISSN: 1064-3745.

[Bur73] Burton, R. A. ; Nerlikar, V. ; Kilaparti, S. R.: Thermoelastic instability in a seal-like configuration. In: *Wear* 24 (1973) Nr. 2, pp. 177–188.

[Cam13] Camilleri, R. ; Armstrong, P. ; Ewin, N. ; Richardson, R. ; Howey, D. A. ; McCulloch, M. D.: The value of a clutch mechanism in electric vehicles. In: *International battery hybrid and fuel cell electric vehicle symposium* (2013), pp. 1–11.

[Cav19] Cavallino, C. ; Santis, S. de ; Riemer, P.: HRAM : hybrid rear axle module, an innovative hybrid differential for P3 and P4 applications. In: *CTI Symposium USA, Novi* (2019).

[Che11] Chen, L. ; Zhu, F. ; Zhang, M. ; Huo, Y. ; Yin, C. ; Peng, H.: Design and Analysis of an Electrical Variable Transmission for a Series–Parallel Hybrid Electric Vehicle. In: *IEEE Transactions on Vehicular Technology* 60 (2011) Nr. 5, pp. 2354–2363. ISSN: 0018-9545.

[Che15] Cheli, F. ; Diana, G.: Advanced Dynamics of Mechanical Systems. Cham and s.l.: Springer International Publishing, (2015).

[Cho14] Chopra, V.: *Design of innovative clutching mechanisms for hybrid automotive transmissions*. PhD Thesis. McGill University, Montreal, (2014).

[Coo90] Cook, R. D. ; Malkus, D. S. ; Plesha, M. E.: Concepts and applications of finite element analysis. 3. ed. Chichester: Wiley, (1990).

[Čor17] Čorić, M. ; Ranogajec, V. ; Deur, J. ; Ivanović, V. ; Eric Tseng, H.: Optimization of Shift Control Trajectories for Step Gear Automatic Transmissions. In: *Journal of Dynamic Systems, Measurement, and Control* 139 (2017) Nr. 6. ISSN: 0022-0434.

[Dav21] Davis, S. C. ; Boundy, R. G.: Transportation Energy Data Book. In: *Office of Energy Efficiency and Renewable Energy - U.S. Department of Energy* (2021).

[Dec01] Decuzzi, P. ; Ciaverella, M. ; Monno, G.: Frictionally Excited Thermoelastic Instability in Multi-Disk Clutches and Brakes. In: *Journal of Tribology* 123 (2001) Nr. 4, p. 865. ISSN: 07424787.

[Dem18] Dempfle, A. ; Binder, J. ; Echtler, P.: Switching device for a motor vehicle and motor vehicle transmission. In: *Worldwide applications, Patent US20180266493A1* (2018).

[Dem19] Dempfle, A. ; Fischer, P. ; Echtler, P. ; Damm, A. ; Matthies, F. ; Müller, J. ; Rüden, K. von ; Köhler, T.: Evaluation of shift quality for conical shifting elements with form fit for powershift automatic transmissions. In: *VDI-Fachtagung Kupplungen und Kupplungssysteme in Antrieben, Ettlingen* (2019).

[Die05] Dietz, P.: Kupplungen und Bremsen. In: *Dubbel, Taschenbuch für den Maschinenbau* 24 (2005), G65–G81.

[Dör14] Dörr, C. ; Kalczynski, H. ; Rink, A. ; Sommer, M.: Nine-Speed Automatic Transmission 9G-Tronic by Mercedes-Benz. In: *ATZ worldwide* 116 (2014) Nr. 1, pp. 20–25.

[Dow72] Dow, T. ; Burton, R. A.: Thermoelastic instability of sliding contact in the absence of wear. In: *Wear* 19 (1972) Nr. 3, pp. 315–328.

[Dow73] Dow, T. A. ; Burton, R. A.: The Role of Wear in the Initiation of Thermoelastic Instabilities of Rubbing Contact. In: *Journal of Lubrication Technology* 95 (1973) Nr. 1, pp. 71–75. ISSN: 0022-2305.

[Dow78] Dow, T. A.: PREVENTING HOT SPOTS IN SLIDING CONTACT. In: *Machine Design* 50 (1978) Nr. 2, pp. 94–102.

[Drä16] Dräxl, T. ; Pflaum, H. ; Stahl, K.: Wirkungsgradverbesserung durch Reduzierung der Schleppverluste an Lamellenkupplungen: FVA-Nr. 671 - Heft 1177. In: *Forschungsvereinigung Antriebstechnik e.V., Frankfurt/Main* (2016).

[Du 06] Du, K.-L., Swamy, M.N.S.: Neural Networks in a Softcomputing Framework. London: Springer-Verlag, (2006).

[Dua14] Duan, C.: Analytical Study of a Dog Clutch in Automatic Transmission Application. In: *SAE International Journal of Passenger Cars - Mechanical Systems* 7 (2014) Nr. 3, pp. 1155–1162. ISSN: 1946-4002.

[Dum77] Duminy, J. ; Federn, K.: Ermittlung der Leistungsgrenzen der Reibpaarung Stahl/Sinterbronze in Ölgeschmierten Reibungskupplungen unter Berücksichtigung der Kühl- und Schmiermittel. In: *Abschlussbericht, FVA-Heft Nr. 52* (1977).

[Dyc04] Dyck, G. ; Dries, P. ; BagherpourJohn, M. ; Czepak, J.: “Electro-mechanical continuously variable transmission”. US7008342B2. (2004).

[Ech17] Echtler, P. ; Mileti, M. ; Damm, A.: TorqueLINE - Konische Kupplung mit Formschluss als alternatives Schaltelement für Automatikgetriebe. In: *VDI-Fachtagung Kupplungen und Kupplungssysteme in Antrieben, Ettlingen* (2017).

[Eur19] European Parliament and the Council of the European Union: Setting CO2 emission performance standards for new passenger cars and for new light commercial vehicles: Regulation 2019/631. (2019).

[Fai01] Fairbank, D. ; Maruo, K. ; Du, S. ; Newcomb, T.: ATF Additive Effects on Hot Spot Formation in Wet Clutches. In: *SAE Technical Paper Series*. SAE Technical Paper Series. SAE International400 Commonwealth Drive, Warrendale, PA, United States, (2001).

[Fau02] Faul, A. ; Tipping, M.: Advances in neural information processing systems 14. In: (2002).

[Fis15] Fischer, R. ; Pollak, B. ; Kücükay, F. ; Jürgens, G. ; Najork, R.: The automotive transmission book. Powertrain. Cham: Springer, (2015).

[Fis17] Fischer, P. ; Pflaum, H. ; Stahl, K.: Ist das Getriebe noch zu retten?. In: *6. Augsburger Technologietransfer-Kongress* (2017).

[För91] Förster, H. J.: Automatische Fahrzeuggetriebe: Grundlagen, Bauformen, Eigenschaften, Besonderheiten. Berlin, Heidelberg: Springer Berlin Heidelberg, (1991).

[Fre14] Frey, D.: Wet Multi Disk Clutches and Brakes. In: *Mang (Hg.) 2014 – Encyclopedia of Lubricants and Lubrication* (2014), pp. 2347–2362.

[Gae13] Gaertner, L. ; Ebenhoch, M.: The ZF Automatic Transmission 9HP48 Transmission System, Design and Mechanical Parts. In: *SAE International Journal of Passenger Cars - Mechanical Systems* 6 (2013) Nr. 2, pp. 908–917. ISSN: 1946-4002.

[Goe03] Goetz, M. ; Levesley, M. C. ; Crolla, D. A.: Dynamic Modelling of a Twin Clutch Transmission for Controller Design. In: *Materials Science Forum* 440-441 (2003), pp. 253–260.

[Gop16] Goppelt, G.: Das DHT Hybridgetriebe neu definiert. In: *ATZ - Automobiltechnische Zeitschrift* 118 (2016) Nr. 7-8, pp. 8–13. ISSN: 0001-2785.

[Gra12] Graf, M. ; Ostermeyer, G.-P.: Hot bands and hot spots: Some direct solutions of continuous thermoelastic systems with friction. In: *Physical Mesomechanics* 15 (2012) Nr. 5-6, pp. 306–315. ISSN: 1029-9599.

[Gre07] Grewe, T. M. ; Conlon, B. M. ; Holmes, A. G.: Defining the General Motors 2-Mode Hybrid Transmission. In: *SAE Technical Papers, 2007-01-0273* (2007).

[Grö20] Grötsch, D. ; Niedenthal, R. ; Völkel. K ; Pflaum, H. ; Stahl, K.: Volume of Fluid vs. Cavitation CFD-Models to Calculate Drag Torque in Multi-Plate Clutches. In: *SAE Technical Paper Series 2020* (2020).

[Gup15] Gupta, A. K. ; Kartik, V. ; Ramanarayanan, C. P.: Design, development and performance evaluation of a light diesel hybrid electric pickup vehicle using a new parallel hybrid transmission system. In: *2015 IEEE International Transportation Electrification Conference (ITEC)* (2015), pp. 1–10.

[Hab96] Haberhauer, H. ; Bodenstein, F.: Elemente der drehenden Bewegung. In: *Maschinenelemente* (1996).

[Häg15] Häggström, D. ; Sellgren, U. ; Stenström, W. ; Björklund, S.: A Verified and Validated Model for Simulation-Driven Design of Heavy Duty Truck Synchronizers. In: *ASME 2015 International Design Engineering Technical Conferences and Computers and Information in Engineering Conference* (2015).

[Häg18a] Häggström, D.: *Towards model-based development of heavy truck synchronizers*. PhD Thesis. Stockhol, Sweden: KTH Royal Institute of Technology, (2018).

[Häg18b] Häggström, D. ; Sellgren, U. ; Björklund, S.: Evaluation of synchronizer loading parameters and their ability to predict failure. In: *Proceedings of the Institution of Mechanical Engineers, Part J: Journal of Engineering Tribology* 232 (2018) Nr. 9, pp. 1093–1104. ISSN: 1350-6501.

[Häg18c] Häggström, D. ; Sellgren, U. ; Björklund, S.: The effect of manufacturing tolerances on the thermomechanical load of gearbox synchronizers. In: *Procedia CIRP* 72 (2018), pp. 1202–1207. ISSN: 22128271.

[Hen14] Hensel, M.: *Thermische Beanspruchbarkeit und Lebensdauerverhalten von nasslaufenden Lamellenkupplungen*. Dissertation. Technische Universität München, (2014).

[Hip04a] Hippmann, G.: *Modellierung von Kontakten komplex geformter Körper in der Mehrkörperdynamik*. Dissertation. (2004).

[Hip04b] Hippmann, G.: An Algorithm for Compliant Contact Between Complexly Shaped Bodies. In: *Multibody System Dynamics* 12 (2004) Nr. 4, pp. 345–362. ISSN: 1384-5640.

[Hir07] Hirano, T. ; Maruo, K. ; Gu, X. ; Fujii, T.: Development of Friction Material and Quantitative Analysis for Hot Spot Phenomenon in Wet Clutch System. In: *SAE Technical Paper Series*. SAE Technical Paper Series. SAE International400 Commonwealth Drive, Warrendale, PA, United States, (2007).

[Hua04] Huang, Q. ; Wang, H.: Fundamental Study of Jerk: Evaluation of Shift Quality and Ride Comfort. In: *SAE Technical Paper 2004-01-2065* (2004).

[Irf18] Irfan, M. ; Berbyuk, V. ; Johansson, H.: Performance improvement of a transmission synchronizer via sensitivity analysis and Pareto optimization. In: *Cogent Engineering* 5 (2018) Nr. 1, p. 89.

[Jan02] Jang, J. Y. ; Khonsari, M. M.: On the Formation of Hot Spots in Wet Clutch Systems. In: *Journal of Tribology* 124 (2002) Nr. 2, p. 336. ISSN: 07424787.

[Jan03] Jang, J. Y. ; Khonsari, M. M.: A generalized thermoelastic instability analysis. In: *Proceedings of the Royal Society A: Mathematical, Physical and Engineering Sciences* 459 (2003) Nr. 2030, pp. 309–329. ISSN: 1364-5021.

[Jas20] Jasný, M. ; Hajžman, M. ; Bulín, R.: DOG CLUTCH WITHOUT CIRCULARDog Clutch without circular backlash - Design optimization using multi-body simulation. In: *FISITA World Automotive Congress* (2020).

[Kah04] Kahraman, A. ; Ligata, H. ; Kienzle, K. ; Zini, D. M.: A Kinematics and Power Flow Analysis Methodology for Automatic Transmission Planetary Gear Trains. In: *Journal of Mechanical Design* 126 (2004) Nr. 6, pp. 1071–1081. ISSN: 1083-4435.

[Kah13a] Kahlbau, S.: *Mehrkriterielle Optimierung des Schaltablaufs von Automatikgetrieben*. Dissertation. Technische Universität Cottbus, (2013).

[Kah13b] Kahlbau, S. ; Bestle, D.: Optimal Shift Control for Automatic Transmission. In: *Mechanics Based Design of Structures and Machines* 41 (2013) Nr. 3, pp. 259–273. ISSN: 1539-7734.

[Kin99] Kinugasa, T.: Thermal analysis of the synchronizer friction surface and its application to the synchronizer durability improvement. In: *JSAE Review* 20 (1999) Nr. 2, pp. 217–222. ISSN: 03894304.

[Kit03] Kitabayashi, H. ; Li, C. Y. ; Hiraki, H.: Analysis of the Various Factors Affecting Drag Torque in Multiple-Plate Wet Clutches. In: *JSAE/SAE International Spring Fuels and Lubricants Meeting* (2003).

[Kle17] Klement, W.: Hybridfahrzeuge: Getriebetechnologie an Beispielen. München: Fachbuchverlag Leipzig im Carl Hanser Verlag, (2017).

[Kle62] Klein, H.: Die Planetenrad-Umlaufrädergetriebe. Hanser Verlag, München, (1962).

[Klu99] Kluger, M. A. ; Long, D. M.: An Overview of Current Automatic, Manual and Continuously Variable Transmission Efficiencies and Their Projected Future Improvements. In: *SAE Technical Papers* (1999).

[Kön12] König, D. ; Gilgenbach, V. ; Rinderknecht, S.: Design and model based control of a dog clutch for electrified vehicles. In: *CTI Symposium Germany, Berlin* (2012).

[Kön14] König, D. H. ; Riemann, B. ; Bohning, M. ; Syrnik, R. ; Rinderknecht, S.: Robust anti-jerk control for electric vehicles with multi-speed transmission. In: *53rd IEEE Conference on Decision and Control* (2014), pp. 3298–3303.

[Kön16] König, R. ; Rinderknecht, S. ; Viehmann, A.: Investigation of Gear Shifts and Hybrid Mode Changes in an Innovative Parallel-Series Hybrid Powertrain with Dog Clutches. In: *FISITA World Automotive Congress, Busan* (2016).

[Kre08] Krempaszky, C. ; Werner, E.: Frictionally excited thermoelastic instabilities of multi-disc clutches. In: *Australian Journal of Mechanical Engineering* 6 (2008) Nr. 1, pp. 15–20. ISSN: 1448-4846.

[Kun17] Kuncz, D.: Schaltzeitverkürzung im schweren Nutzfahrzeug mittels Synchronisation durch eine induzierte Antriebsstrangschwingung. Wiesbaden, (2017).

[Kut27] Kutzbach, K.: Mehrgliedrige Radgetriebe und ihre Gesetze. In: *Maschinenbau* 6 (1927), p. 1080.

[Lai90] Laird, M. P. B. ; Lawton, B. ; Gregory, R. P.: Dog clutches for rapid gear changes in automotive gearboxes. In: (1990).

[Lay11] Layher, M.: *Einfluss der Schmierstoffadditivierung auf das Reibungsverhalten nasslaufender Reibschaltelemente*. Dissertation. (2011).

[Leb76] Lebeck, A. O.: Theory of Thermoelastic Instability of Rotating Rings in Sliding Contact With Wear. In: *Journal of Lubrication Technology* 98 (1976) Nr. 2, pp. 277–284. ISSN: 0022-2305.

[Lee93] Lee, K. ; Barber, J. R.: Frictionally Excited Thermoelastic Instability in Automotive Disk Brakes. In: *Journal of Tribology* 115 (1993) Nr. 4, p. 607. ISSN: 07424787.

[Lei19] Leighton, M. ; Morris, N. ; Trimmer, G. ; King, P. D. ; Rahnejat, H.: Efficiency of disengaged wet brake packs. In: *Proceedings of the Institution of Mechanical Engineers, Part D: Journal of Automobile Engineering* 233 (2019) Nr. 6, pp. 1562–1569. ISSN: 0954-4070.

[Lie18] Liebold, J. ; Rueden, K. von ; Danzer, D. ; Hirschbeck, T. ; Müller, T.: 1, 2 or 3 - how much it would be? Evaluating the need of multispeed electric drives coming from different perspectives. In: *17th International CTI Symposium, Berlin* (2018).

[Lin19] Lin, S. ; Li, B. ; Jiao, W.: Gearshift performance improvement for an electromagnetic gearshift system based on optimized active disturbance rejection control method. In: *Advances in Mechanical Engineering* 11 (2019) Nr. 2, p. 168781401982746. ISSN: 1687-8140.

[Lov06] Lovas, L. ; Play, D. ; Marialigeti, J. ; Rigal, J. F.: Mechanical Behaviour Simulation for Synchromesh Mechanism Improvements. In: *Proceedings of the Institution of Mechanical Engineers, Part D: Journal of Automobile Engineering* 220 (2006) Nr. 7, pp. 919–945. ISSN: 0954-4070.

[Man21] Mann, R. ; Magnier, V. ; Brunel, J. F. ; Dufrénoy, P. ; Henrion, M. ; Guillet-Revol, E.: Thermomechanical characterization of high-speed train braking materials to improve models: Numerical validation via a comparison with an experimental braking test. In: *Tribology International* 156 (2021), p. 106818. ISSN: 0301679X.

[Mas06] Mastinu, G. ; Gobbi, M. ; Miano, C.: Optimal Design of a Double-Cone Synchroniser. In: *Mastinu et al. (Hg.) 2006 – Optimal Design of Complex Mechanical Systems* (2006), pp. 245–262.

[Mas14] Mastinu, G. ; Plöchl, M. (eds.): Road and off-road vehicle system dynamics handbook. Boca Raton, Fla.: CRC Press, (2014).

[Mei15] Meingaßner, G. J. ; Pflaum, H. ; Stahl, K.: Test-Rig Based Evaluation of Performance Data of Wet Disk Clutches. In: *CTI Symposium Germany, Berlin* (2015).

[Mei17] Meingaßner, G. J.: *Methodik zur Untersuchung des Reibungsverhaltens nasslaufender Lamellenkupplungen bei Langsamlauf- und Mikroschlupf*. Dissertation. Technische Universität München, (2017).

[Mer19] Merkel, H.: Solutions for increased power density at shifting clutches. In: *International VDI Congress, Dritev - Drivetrain for Vehicles* (2019).

[MEw49] M'Ewen, E.: The Theory of Gear-changing. In: *Proceedings of the Institution of Mechanical Engineers: Automobile Division* 3 (1949) Nr. 1, pp. 30–40. ISSN: 0367-8822.

[Mil18a] Mileti, M. ; Strobl, P. ; Pflaum, H. ; Stahl, K.: Speed4E - Design of a hyper-high-speed Powertrain for EV to achieve maximum ranges. In: *CTI Symposium Germany, Berlin* (2018).

[Mil18b] Mileti, M. ; Pflaum, H. ; Stahl, K.: Alternative Schaltelemente für Automatikgetriebe. In: *Abschlussbericht - Bayerische Forschungsstiftung* (2018).

[Mil18c] Mileti, M. ; Pflaum, H. ; Stahl, K.: TorqueLINE Cone Clutch: Thermo-Mechanical Stability of Cone Clutches for ATs. In: *International VDI Congress, Dritev - Drivetrain for Vehicles, VDI* (2018).

[Mil19a] Mileti, M. ; Schweigert, D. ; Pflaum, H. ; Stahl, K.: Speed4E: Hyper-High-Speed Driveline and Gearbox for BEVs. In: *CTI Symposium USA, Novi* (2019).

[Mil19b] Mileti, M. ; Pointner, L. ; Fischer, P. ; Pflaum, H. ; Stahl, K.: TorqueLINE Cone Clutch: Performance Analysis of Highly Dynamic Form-Fit Shifts in Automatic Transmissions. In: *International Journal of Powertrains* (2019).

[Mil21] Mileti, M. ; Pointner, L. ; Fischer, P. ; Pflaum, H. ; Stahl, K.: Dynamic Analysis of Powershifts with Form-Fit Clutches in Automatic Transmissions. In: *International Journal of Powertrains* (2021).

[Mor19] Morris, N. ; Davies, J. ; Leighton, M. ; King, P. D. ; Rahnejat, H.: Oil film separation and drag torque in disengaged wet brakes. In: *Proceedings of the Institution of Mechanical Engineers, Part D: Journal of Automobile Engineering* 233 (2019), p. 095440701984435. ISSN: 0954-4070.

[Mül98] Müller, H. W.: Die Grundgesetze der Umlaufgetriebe. Vol. 28. Springer-Verlag Berlin Heidelberg, (1998).

[Mur98] Murray-Smith, D. J.: Methods for the external validation of contiuous system simulation models:a review. In: *Mathematical and Computer Modelling of Dynamical Systems* 4 (1998) Nr. 1, pp. 5–31. ISSN: 1387-3954.

[Nau07] Naunheimer, H. ; Bertsche, B. ; Lechner, G. ; Ryborz, J.: Fahrzeuggetriebe: Grundlagen, Auswahl, Auslegung und Konstruktion. 2., bearb. und erw. Aufl. Berlin, Heidelberg, (2007).

[Nea95] Neal, R. M.: *Bayesian Learning for Neural Networks*. PhD Thesis. University of Toronto, (1995).

[Neu08] Neudörfer, S.: *Thermomechanische Einflüsse auf die Tribologie von Synchronisierungen*. Dissertation. Hannover, (2008).

[Neu19] Neupert, T. ; Bartel, D.: High-resolution 3D CFD multiphase simulation of the flow and the drag torque of wet clutch discs considering free surfaces. In: *Tribology International* 129 (2019), pp. 283–296. ISSN: 0301679X.

[Nez15] Nezhadali, V. ; Eriksson, L.: A framework for modeling and optimal control of automatic transmission systems. In: *IFAC-PapersOnLine* 48 (2015) Nr. 15, pp. 285–291. ISSN: 24058963.

[Omp11] Ompusunggu, A. P. ; Janssens, T. ; Al-Bender, F. ; Sas, P. ; van Brussel, H.: Engagement behavior of degrading wet friction clutches. In: *IEEE/ASME International Conference on Advanced Intelligent Mechatronics (AIM), Hungary* (2011), pp. 271–276.

[Ost13] Ostermeyer, G.-P. ; Graf, M.: Influence of wear on thermoelastic instabilities in automotive brakes. In: *Wear* 308 (2013) Nr. 1-2, pp. 113–120.

[Ott17] Otto, M. ; Fromberger, M. ; Stahl, K.: Gear Mesh Resonance and Stiffness Validated in Calculation and Experiment. In: *24th International Congress on Sound and Vibration, London* (2017).

[Pac12] Pacejka, H. B.: Tire and Vehicle Dynamics. Elsevier, (2012).

[Pan04] Panier, S. ; Dufrénoy, P. ; Weichert, D.: An experimental investigation of hot spots in railway disc brakes. In: *Wear* 256 (2004) Nr. 7-8, pp. 764–773.

[Pen19] Peng, H. ; Zhu, B. ; Zhang, N. ; Liang, G. ; Yan, W. ; Rao, M.: Research on Three-Parameter Shift Schedule of Pure Electric Vehicle Based on Fuzzy Control. In: *International Conference on Advanced Vehicle Powertrains, Hefei, China* (2019).

[Pin92] Pinnekamp, B.: *Das Schaltverhalten von PKW-Getriebesynchronisierungen*. Dissertation. TU München, (1992).

[Poi19] Pointner, L. ; Mileti, M. ; Pflaum, H. ; Stahl, K.: Characterization of High-dynamic Form-fit Shifts in Automatic Transmissions. In: *ATZ worldwide* 121 (2019) Nr. 10, pp. 64–69.

[Pol03] Poll, G. ; Spreckels, M.: Influence of temperature distribution on the tribological performance of automotive synchronisers. In: *In: Tribological Research and Design for Engineering Systems* 41 (2003), pp. 613–621.

[Pos39] Postlewaite, D. E. ; Selby, J. ; Shisler, G. D.: The Motor World for 1940. In: *Ohio State Engineer: Volume 23, no. 2* (1939).

[Ran18] Ranogajec, V. ; Coric, M. ; Deur, J. ; Ivanovic, V.: Multi-objective Parameter Optimization of Automatic Transmission Shift Control Profiles. In: *SAE Technical Paper Series*. SAE Technical Paper Series. SAE International400 Commonwealth Drive, Warrendale, PA, United States, (2018).

[Rob14] Robinette, D.: A Two Degree of Freedom, Lumped Inertia Model for Automatic Transmission Clutch-to-Clutch Shift Dynamics. In: *SAE International Journal of Passenger Cars - Mechanical Systems* 7 (2014) Nr. 3, pp. 1163–1174. ISSN: 1946-4002.

[Rob15] Robinette, D. ; Gibson, G. ; Szpara, D. ; Tehansky, E.: Performance Characterization of Automatic Transmission Upshifts with Reduced Shift Times. In: *SAE International Journal of Engines* 8 (2015) Nr. 3, pp. 1359–1373. ISSN: 1946-3944.

[Ros06] Rossmanith, H. P. ; Loibnegger, F. ; Huber, R.: Thermomechanical fatigue fracture due to repeated braking of railway wheels. (2006).

[Sam12] Samie, F. ; Millerman, A. ; Lee, C. J.: “Synchronizer in electro-mechanical transmission”. (2012).

[Sar10] Sargent, R. G.: Verification and validation of simulation models. In: *Simulation Conference (WSC), Proceedings of the 2010 Winter*. Piscataway, N.J.: IEEE, (2010), pp. 166–183.

[Sch11] Schlecht, B.: Getriebe - Verzahnungen - Lagerungen. [Nachdr.] Vol. 2. Ing - Maschinenbau. München: Pearson Studium, (2011).

[Sch19a] Schneider, T. ; Strebel, M. ; Pflaum, H. ; Stahl, K.: Spontaneous damage to wet-running multi-plate clutches with organic and metallic friction linings. In: *Forschung im Ingenieurwesen* 83 (2019) Nr. 2, pp. 199–207.

[Sch19b] Schöneberger, D. ; Mileti, M. ; Stahl, K. ; Rinderknecht, S.: Development of an Innovative Shift Actuator for Electrified Multispeed Transmissions. In: *International Journal of Powertrains* (2019).

[Sch19c] Schweigert, D. ; Mileti, M. ; Morhard, B. ; Sedlmair, M. ; Fromberger, M. ; Otto, M. ; Lohner, T. ; Stahl, K.: Innovative transmission concept for hyper-high-speed electromechanical powertrains. In: *International VDI Congress, Dritev - Drivetrain for Vehicles* (2019).

[Sed17] Sedlmair, M. ; Fischer, P. ; Lohner, T. ; Pflaum, H. ; Stahl, K.: Holistic Investigations on the innovative high-speed powertrain Speed2E for electric vehicles. In: *CTI Symposium Germany, Berlin* (2017).

[Sha20] Shabana, A. A.: Dynamics of multibody systems. Fifth edition. New York: Cambridge University Press, (2020).

[Shi19] Shiotsu, I. ; Tani, H. ; Kimura, M. ; Nozawa, Y. ; Honda, A. ; Tabuchi, M. ; Yoshino, H. ; Kanzaki, K.: Development of high efficiency dog clutch with one-way mechanism for stepped automatic transmissions. In: *International Journal of Automotive Engineering* 10 (2019) Nr. 2, pp. 156–161.

[Sla14] Slapak, D.: “Gearbox for vehicle and vehicle, including such a gearbox”. (2014).

[Sme18] Smejkal, T. ; Wirth, C.: Innovative transmission topologies using the example of a P2-hybridtransmission for front-transverse applications. In: *International VDI Congress, Dritev - Drivetrain for Vehicles* (2018).

[Soc68] Socin, R. J. ; Walters, L. K.: Manual Transmission Synchronizers. In: *SAE Technical Paper Series, 680008* (1968).

[Son19] Song, X. ; Spitas, C. ; Mohammad-Pour, M. ; Shahbakhti, Mahdi: Xu, Liangfei ; Prucka, R. ; Montanaro, U.: Evolutionary Electrification of Powertrains for More Efficient and Intelligent Vehicles. In: *International Journal of Powertrains* (2019).

[Sta07] Stangl, M.: *Methodik zur kinematischen und kinetischen Berechnung mehrwelliger Planeten-Koppelgetriebe*. Dissertation. (2007).

[Sta14] Stahl, K. ; Acuner, R. ; Pflaum, H.: Synchronizer. In: *Mang (Hg.) 2014 – Encyclopedia of Lubricants and Lubrication* (2014), pp. 2020–2030.

[Sto18] Stockinger, U. ; Pflaum, H. ; Stahl, K.: Friction screening tests for wet multi-plate clutches - Variation of lubricant and friction lining. In: *Malaysian Tribology Society (Hg.) 2018 – Proceedings of Asia International Conference* (2018).

[Sto20] Stockinger, U. ; Schneider, T. ; Pflaum, H. ; Stahl, K.: Single vs. multi-cone synchronizers with carbon friction lining—a comparison of load limits and deterioration behavior. In: *Forschung im Ingenieurwesen* (2020). ISSN: 0015-7899.

[Str14] Strebel, M. ; Wirth, M. ; Pflaum, H. ; Stahl, K.: Schleppverluste in Synchronisierungen. In: *GETLUB - Tribologie- und Schmierstoffkongress* 1 (2014), pp. 232–242.

[Str17] Strebel, M.: Spontanschäden an nasslaufenden Lamellenkupplungen: Dissertation. In: (2017).

[Tak92] Takezaki, K. ; Kubota, M.: Thermal and Mechanical Damage of Paper Wet Friction Material Induced by Non-Uniform Contact. In: *SAE Technical Paper Series 1992* (1992).

[Tim61] Timoshenko, S. P. ; Gere, J. M.: Theory of Elastic Stability. Courier Corporation, (1961).

[Toc68] Tochtermann, W. ; Bodenstein, F.: Konstruktionselemente des Maschinenbaues. Berlin, Heidelberg: Springer Berlin Heidelberg, (1968).

[Ton15] Tonius, N. ; Bertsche, B. ; Dörr, C.: Dog clutches as innovative shifting elements for automatic transmissions: Friedrichshafen, June 16-17, 2015 ; [15th International VDI Congress Drivetrain for Vehicles 2015, 4th VDI Conference Transmissions in Commercial Vehicles, 2nd VDI Conference Control Solutions for Transmissions. Vol. 2256. VDI-Berichte. Düsseldorf, (2015).

[Vac18] Vacca, F. ; Capilli, G. ; Sorniotti, A. ; Cavallino, C. ; Fracchia, M. ; Remondin, T. ; Bottiglione, F.: A novel hybridized automated manual transmission for high performance cars. In: *IEEE International Workshop on Advanced Motion Control (AMC)* (2018), pp. 517–522.

[van14] van Berkel, K. ; Hofman, T. ; Serrarens, A. ; Steinbuch, M.: Fast and smooth clutch engagement control for dual-clutch transmissions. In: *Control Engineering Practice* 22 (2014), pp. 57–68. ISSN: 09670661.

[VDI12] VDI: VDI Guideline 2157, Planetary gear drives Definitions, symbols, designs, calculations. (2012).

[Vie17] Viehof, M. ; Winner, H.: *Stand der Technik und der Wissenschaft: Modellvalidierung im Anwendungsbereich der Fahrdynamiksimulation*. Research report. (2017).

[Vil04] Vileneuve, A. ; Mendes, P.: Dual Mode Electric Infinitely Variable Transmission. In: *SAE Technical Papers, 2004-40-0019* (2004).

[Wal15] Walker, P. ; Roser, H. ; Zhang, N. ; Fang, Y.: Comparison of Powertrain System Configurations for Electric Passenger Vehicles. In: *SAE Technical Papers, 2015-01-0052* (2015).

[Wan19] Wang, S. ; Liu, Y. ; Wang, Z. ; Dong, P. ; Cheng, Y. ; Xu, X. ; Tenberge, P.: Adaptive fuzzy iterative control strategy for the wet-clutch filling of automatic transmission. In: *Mechanical Systems and Signal Processing* 130 (2019), pp. 164–182. ISSN: 08883270.

[Wil70] Willis, R.: Principles of mechanism. Cambridge: J. and J.J. Deighton, (1870).

[Win85] Winkelmann, S. ; Harmuth, H.: Schaltbare Reibkupplungen: Grundlagen, Eigenschaften, Konstruktionen. Vol. 34. Konstruktionsbücher. Berlin: Springer, (1985).

[Wis08] Wishart, J. ; Zhou, Y. L. ; Dong, Z.: Review of multi-regime hybrid vehicle powertrain architecture. In: *IJEHV, International Journal of Electric and Hybrid Vehicles* (2008).

[Woh12] Wohlleber, F.: Thermischer Haushalt nasslaufender Lamellenkupplungen: Dissertation. (2012).

[Woi20] Woitysak, T.: Das Modellangebot zum Start der S-Klasse3. In: *Sonderprojekte ATZ/MTZ* 25 (2020) Nr. S1, p. 7. ISSN: 2509-4602.

[Wol58] Wolf, A.: Die Grundgesetze der Umlaufgetriebe. Schriftenreihe Antriebstechnik, H. 14. Braunschweig, (1958).

[Xu18] Xu, X. ; Dong, P. ; Liu, Y. ; Zhang, H.: Progress in Automotive Transmission Technology. In: *Automotive Innovation* 1 (2018) Nr. 3, pp. 187–210. ISSN: 2096-4250.

[Yan19] Yang, L. ; Huang, Y. ; Zhao, W.: Coordination Control for Dual-mode Power-split Hybrid Electrical Vehicle. In: *International Journal of Powertrains* (2019).

[Zab13] Zabala, P.: High Efficiency Power Shift System - MSYS 3 Speed Electric Vehicle Transmission. In: *CTI Symposium Germany, Berlin* (2013).

[Zag03] Zagrodzki, P. ; Truncone, S. A.: Generation of hot spots in a wet multidisk clutch during short-term engagement. In: *Wear* 254 (2003) Nr. 5-6, pp. 474–491.

[Zag08] Zagrodzki, P.: Thermoelastic instability in friction clutches and brakes – Transient modal analysis revealing mechanisms of excitation of unstable modes. In: *International Journal of Solids and Structures* (2008), pp. 2463–2476. ISSN: 00207683.

[Zel19] Zelentsov, V. B. ; Mitrin, B. I.: Thermoelastic Instability in the Quasi-Static Coupled Thermoelasticity Problem Dealt with the Sliding Contact with Frictional Heating. In: *Mechanics of Solids* 54 (2019) Nr. 1, pp. 58–69. ISSN: 0025-6544.

[Zha05] Zhang, Y. ; Lin, H. ; Zhang, B. ; Mi, C.: Performance Modeling and Optimization of a Novel Multi-mode Hybrid Powertrain. In: *Journal of Mechanical Design* 128 (2005) Nr. 1, pp. 79–89. ISSN: 1083-4435.

[Zhu15] Zhu, B. ; Zhang, N. ; Walker, P. ; Zhou, X. ; Zhan, W. ; Wei, Y. ; Ke, N.: Gear shift schedule design for multi-speed pure electric vehicles. In: *Proceedings of the Institution of Mechanical Engineers, Part D: Journal of Automobile Engineering* 229 (2015) Nr. 1, pp. 70–82. ISSN: 0954-4070.

[Zir17] Zirn, O.: Elektrifizierung in der Fahrzeugtechnik: Grundlagen und Anwendungen. München: Fachbuchverlag Leipzig im Carl Hanser Verlag, (2017).

Supervised theses relevant for this work

Following theses were scientifically supervised by the author during his work at the Chair for Machine Elements, Gear Research Centre, Technical University of Munich. The present work partially bases on results and data originated in the context of such theses.

- Pointner-Gabriel, Lukas: Multibody Simulation for Characterisation of High-dynamic Form-fit Shifts of Alternative Shifting Elements for Automatic Transmissions, master's thesis, Chair of Machine Elements, Technical University of Munich, 2018
- Pointner-Gabriel, Lukas: Multibody Dynamic Simulations of the Behaviour of Clutches: Optimization and Implementation of an Existing Model, semester's thesis, Chair of Machine Elements, Technical University of Munich, 2017
- Peteler, Franziska: Gearshift Characterisation of a high-dynamic Dog Clutch through Multibody Simulation, semester's thesis, Chair of Machine Elements, Technical University of Munich, 2019
- Maurer, Alexander: Validation of a FE Simulation Model for the Thermomechanical Analysis of the TorqueLINE Cone Clutch, semester's thesis, Chair of Machine Elements, Technical University of Munich, 2019
- Bombelli, Alexander: Method for Time-Efficient Performance Evaluation of Cone Clutches for Automatic Transmissions, semester's thesis, Chair of Machine Elements, Technical University of Munich, 2021
- Estaller, Julian: Design and Optimization of Shifting Strategies for EVs to Achieve Maximum Ranges, semester's thesis, Chair of Machine Elements, Technical University of Munich, 2019
- Estaller, Julian: Thermo-Mechanical Finite Elment Simulation of Alternative Shifting Elements for Automatic Transmissions, bachelor's thesis, Chair of Machine Elements, Technical University of Munich, 2017
- Bruckmoser, Maximilian: FE Thermo-mechanical Simulation to Optimize Alternative Shifting Elements for AT, semester's thesis, Chair of Machine Elements, Technical University of Munich, 2018

- Strobl, Patrick: Design of a Hyper-High-Speed Gearbox for EV Drivetrains, master's thesis, Chair of Machine Elements, Technical University of Munich, 2019

Further documents

This work bases on data and results developed during the 36-month project "Alternative Shifting Elements for Automatic Transmissions" performed in cooperation between Gear Research Centre (FZG) and HOERBIGER ANTRIEBSTECHNIK HOLDING GmbH. The project has been funded by the Bavarian Research Foundation (German: Bayerische Forschungsstiftung). For the final project report refer to [Mil18a]. Selected contents of the final project report are utilised in this work.

A Appendix

A.1 Evaluation of shaft speeds of an AT

Daimler's 9G-Tronic transmission serves in this section as example for computation of speed of all shafts. A schematic representation of the transmission is shown in Figure A.1

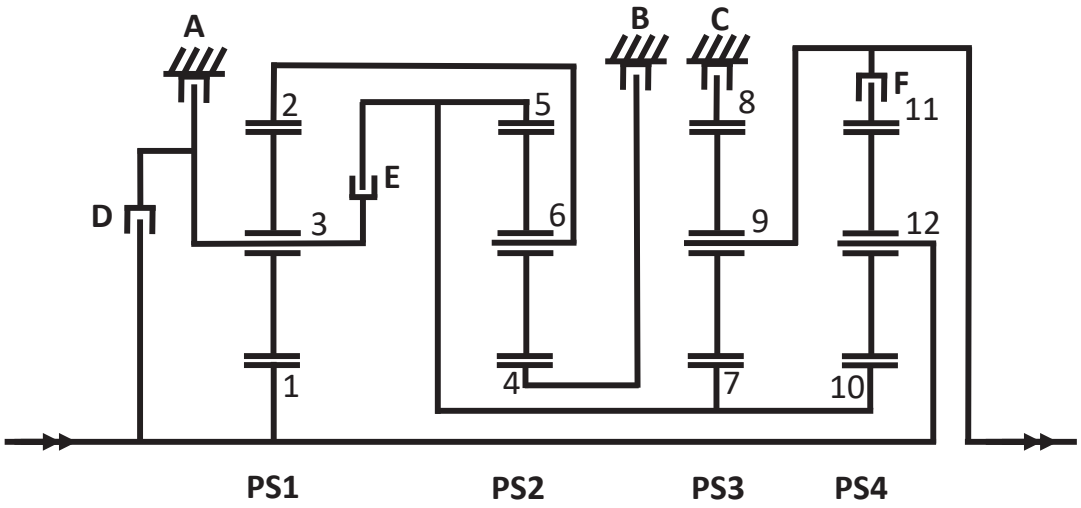

Figure A.1: Schematic representation of AT 9G-Tronic, based on [Dör14]

In Table A.1, the shifting pattern of the transmission is shown.

Speed	Tr. ratio	Brakes			Clutches		
		A	B	C	D	E	F
R	-4.932	•	•	•			
1	5.503		•	•		•	
2	3.333			•	•	•	
3	2.315		•	•	•		
4	1.661		•	•			•
5	1.211		•		•		•
6	1.000				•	•	•
7	0.865		•			•	•
8	0.717	•				•	•
9	0.601	•	•				•

Table A.1: Shifting scheme and according transmission ratios of automatic transmission 9G-Tronic

All transmission elements, i.e. planetary gearboxes, shifting elements and shafts, are num-

bered. This way, an automated routine can compile the Jacobian matrix $\mathbf{A}$ of the velocities for every transmission ratio. The latter has to have as many rows as the shafts in the system. In particular, it includes the Willis equations for every planetary gearbox, the couplings between shafts and the actuated shifting elements for each transmission ratio. On the example of the transmission ratio of the first gear (shifting elements B, C and E are engaged), equations are computed and matrix $\mathbf{A}$ derived accordingly.

First, the Willis equations for all planetary gear sets are computed.

$$\begin{cases} n_1 - i_{12,PS1} \cdot n_2 - (1 - i_{12,PS1}) \cdot n_3 = 0 \\ n_4 - i_{12,PS2} \cdot n_5 - (1 - i_{12,PS2}) \cdot n_6 = 0 \\ n_7 - i_{12,PS3} \cdot n_8 - (1 - i_{12,PS3}) \cdot n_9 = 0 \\ n_{10} - i_{12,PS4} \cdot n_{11} - (1 - i_{12,PS4}) \cdot n_{12} = 0 \end{cases}$$

Second, equations deriving from couplings between planetary gear sets are computed.

$$\begin{cases} n_1 = n_{12} \\ n_3 = n_{n6} \\ n_5 = n_7 \\ n_7 = n_{10} \end{cases}$$

Finally, the connections derived from engaged shifting elements for the considered transmission ratio are computed.

$$\begin{cases} n_4 - 0 \\ n_8 = 0 \\ n_3 = n_5 \end{cases}$$

The missing equation has to be a known velocity. In this case it is chosen to set the input speed to 1, in order to reference all other values to input speed. The aforementioned equations generate a linear system, which in turn can be rewritten in matrix form. The known vector $\vec{b}$ includes the input velocity - that is, the velocity of shaft 1. All other known terms are set to 0, according to the equations of the linear system.

$$\vec{b} = \begin{bmatrix} 0 & 0 & 0 & 0 & 0 & 0 & 0 & 0 & 0 & 0 & 0 & 1 \end{bmatrix}^T \tag{A.1}$$

Matrix $\mathbf{A}$ results in:

$$\begin{bmatrix}
-1 & i_{12,PS1} & 1-i_{12,PS1} & 0 & 0 & 0 & 0 & 0 & 0 & 0 & 0 \\
0 & 0 & 0 & -1 & i_{12,PS2} & 1-i_{12,PS2} & 0 & 0 & 0 & 0 & 0 \\
0 & 0 & 0 & 0 & 0 & 0 & -1 & i_{12,PS3} & 1-i_{12,PS3} & 0 & 0 \\
0 & 0 & 0 & 0 & 0 & 0 & 0 & 0 & -1 & i_{12,PS4} & 1-i_{12,PS4} \\
1 & 0 & 0 & 0 & 0 & 0 & 0 & 0 & 0 & 0 & -1 \\
0 & 1 & 0 & 0 & 0 & -1 & 0 & 0 & 0 & 0 & 0 \\
0 & 0 & 0 & 0 & 1 & 0 & -1 & 0 & 0 & 0 & 0 \\
0 & 0 & 0 & 0 & 0 & 0 & 1 & 0 & 0 & -1 & 0 \\
0 & 0 & 0 & 1 & 0 & 0 & 0 & 0 & 0 & 0 & 0 \\
0 & 0 & 0 & 0 & 0 & 0 & 0 & 1 & 0 & 0 & 0 \\
0 & 0 & 1 & 0 & -1 & 0 & 0 & 0 & 0 & 0 & 0 \\
1 & 0 & 0 & 0 & 0 & 0 & 0 & 0 & 0 & 0 & 0
\end{bmatrix} \tag{A.2}$$

Eventually, the linear system can be solved and the velocities of all shafts found. All velocities are related to the input speed, which is set conventionally to 1.

$$\vec{n} = \mathbf{A}^{-1}\,\vec{b} = \begin{bmatrix} 1 & 0.42 & 0.61 & 0 & 0.61 & 0.42 & 0.61 & 0 & 0.19 & 0.61 & 1.16 & 1 \end{bmatrix}^T \tag{A.3}$$

The same procedure can be applied to torque calculation. In this case, the Willis formulae are substituted by torque equilibrium and power conservation equations. Efficiency of all gear sets is set to 1. Relative results in terms of speed and torque at the shifting elements of reference AT 9G-Tronic are represented in Figures A.2 and A.3.

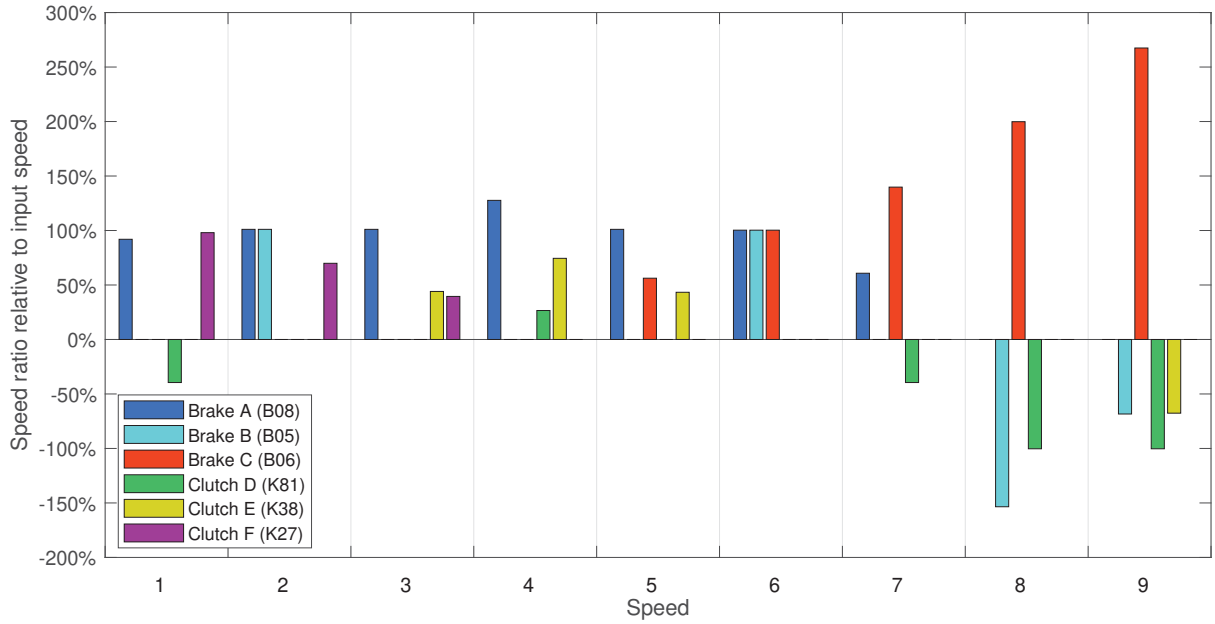

Figure A.2: Speed at shifting elements referenced to transmission input speed of AT 9G-Tronic for all forward speeds

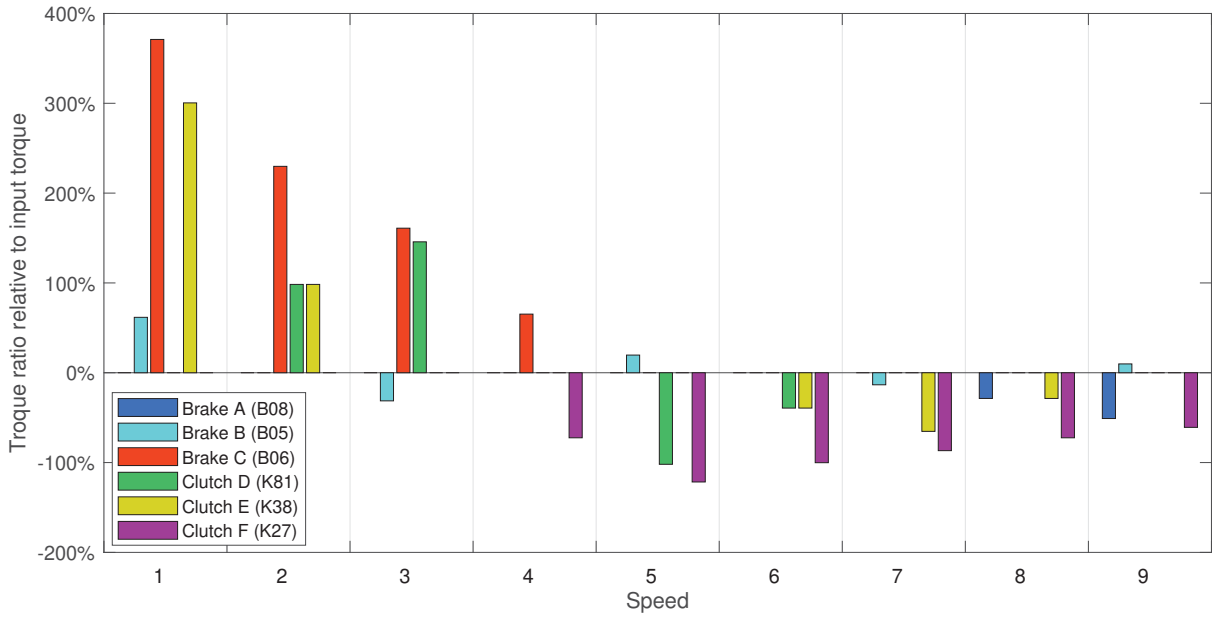

Figure A.3: Torque at shifting elements referenced to transmission input torque of AT 9G-Tronic for all forward speeds

.

A.2 CCDC design

A.2.1 CCDC design variant 1

Cross section of CCDC variant 1 in its test-rig configuration.

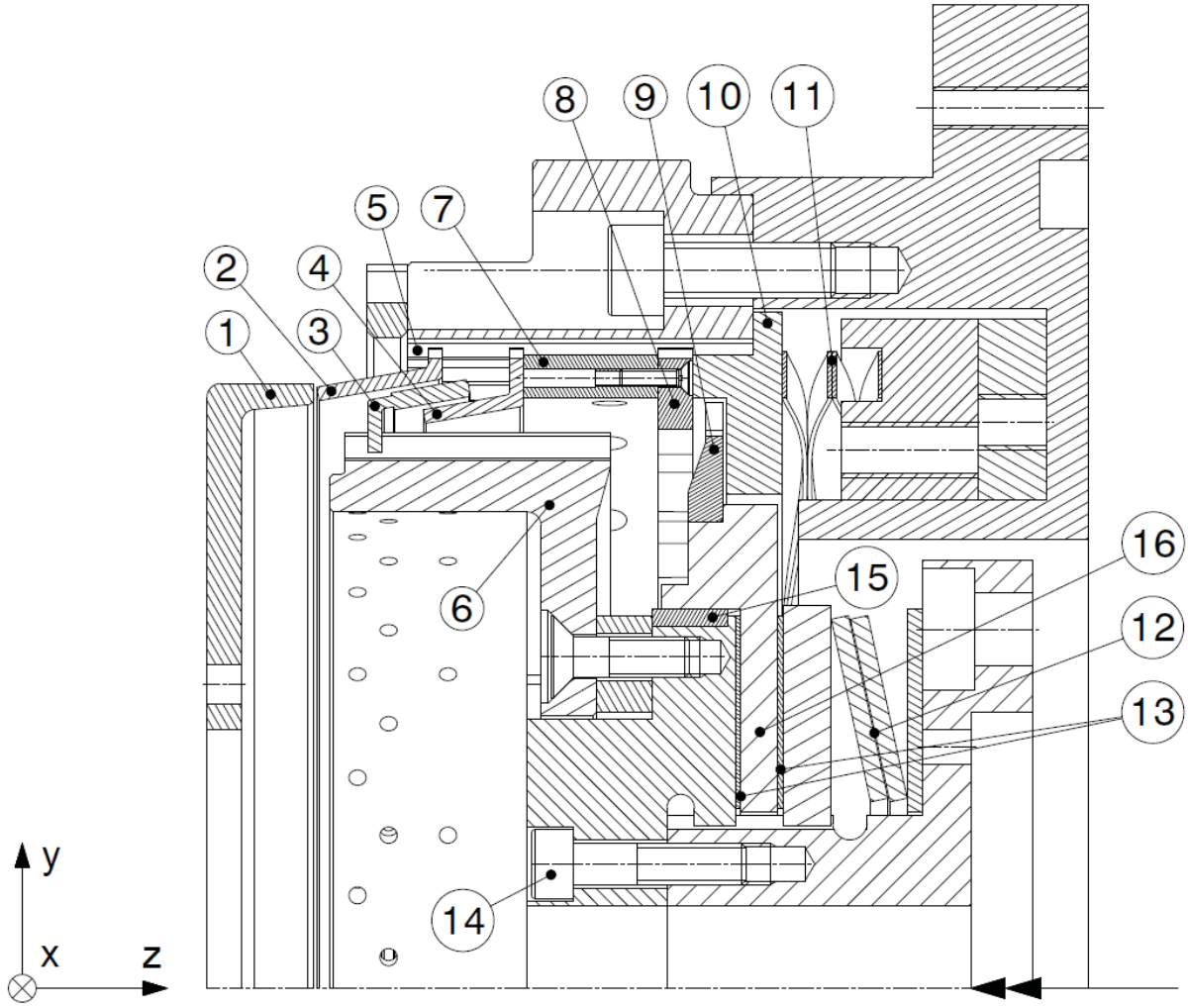

Figure A.4: The following components are marked: (1) piston, (2) outer steel cone, (3) intermediate friction cone, (4) inner steel cone, (5) outer carrier, (6) inner carrier, (7) distancer, (8) axially movable dog clutch body, (9) fixed dog clutch body, (10) spring-prestress plate, (11) wave reset-spring, (12) plate spring for slip clutch, (13) friction lining of slip clutch, (14) screw for slip clutch setting, (15) bushing, (16) dog-clutch support

A.2.2 CCDC design variant 2

Cross section of CCDC variant 2 in its test-rig configuration.

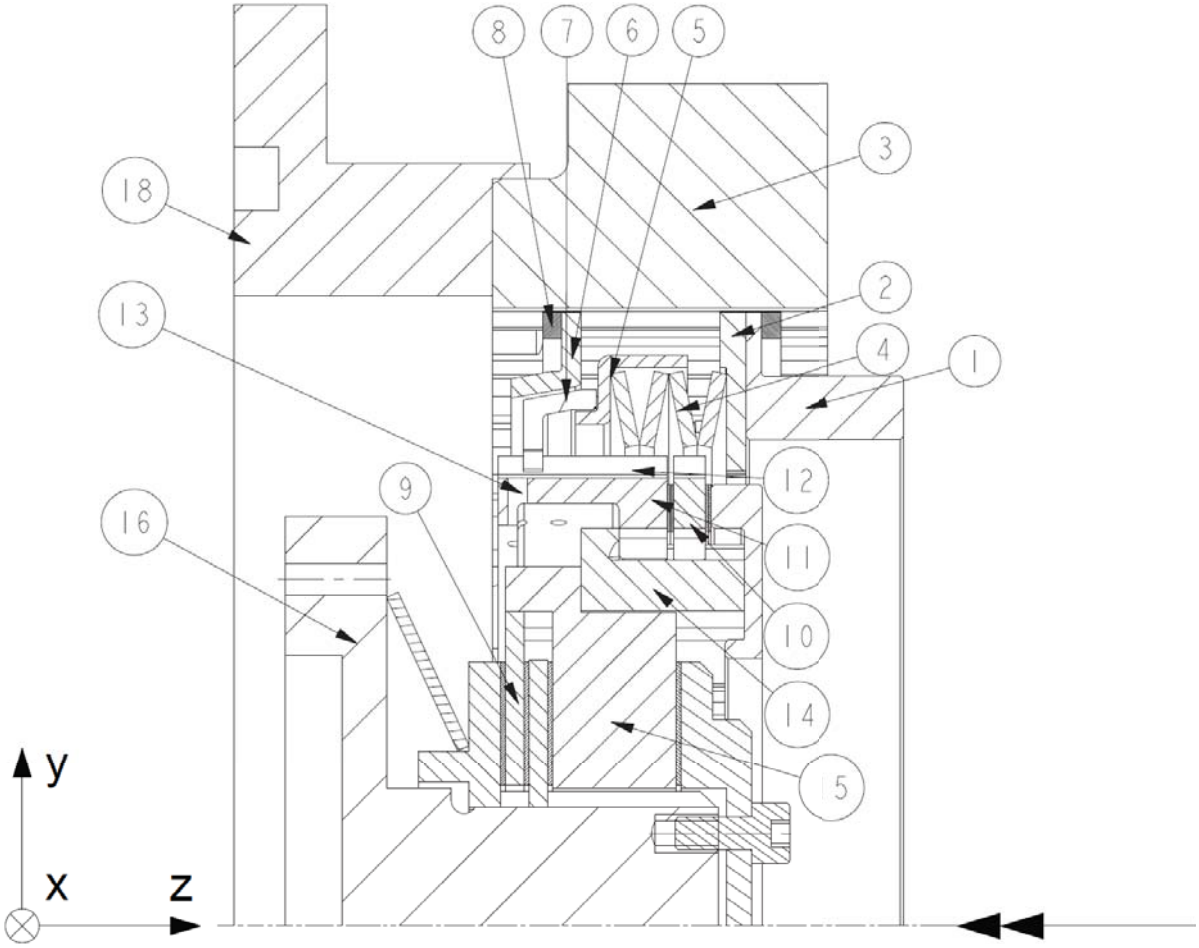

Figure A.5: The following components are marked: (1) piston, (2) outer dog clutch body, (3) outer carrier, (4) prestressed reset-spring, (5) spring holder, (6) outer friction cone, (7) inner friction cone, (8) snap-ring as axial stop, (9) slip clutch system (3 friction surfaces and a preload spring), (10) inner dog clutch body, (11) inner carrier, (12) splines of inner carrier, (13) hole in inner carrier for centrifugal lubricant injection, (14) inner carrier and inner dog clutch body holder, (15) outer carrier of slip clutch connected to inner carrier of CCDC, (16) adapter to tes rig shaft, (18) adapter to test rig hollow shaft (still standing)

.

A.3 FEM convergence analysis

As described in Section 4.2.1, mesh refinement and time increment of the thermomechanical simulation model are key parameters to set in order to obtain satisfying and robust results. The chosen mesh type is - thanks to the relatively simple geometry - almost completely structured. An exemplarily representation of the meshed geometry can be appreciated in Figure A.6. Additionally to the grid, the system's mechanical boundary conditions (as described in Section 4.2.1.1) are schematised.

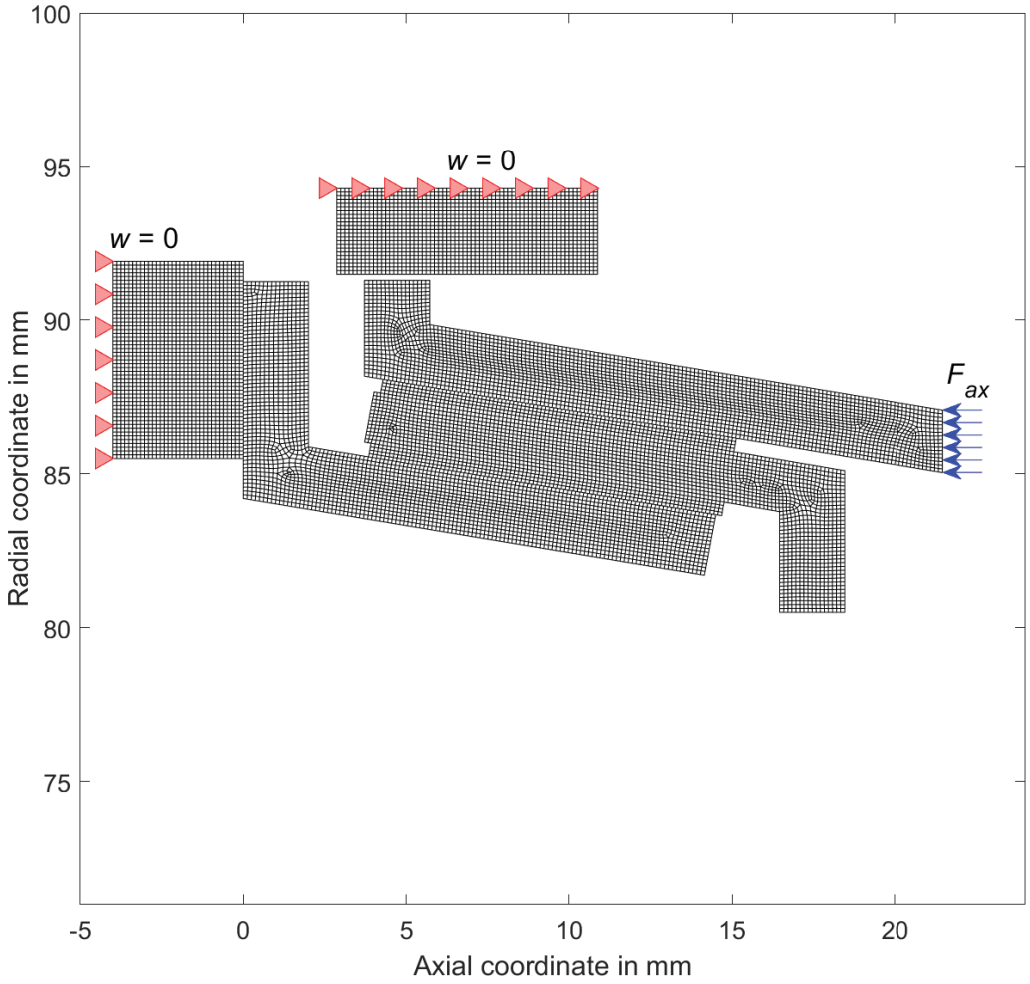

Figure A.6: Cross section of CCDC variant 1 with a mesh thickness of h_{el} = 50 μm. Mechanical boundary conditions are represented exemplarily

.

Final mesh thickness, described through parameter h_{el} is determined through a convergence analysis. The same holds for time increment Δt. Maximum temperature is used as control parameter for simulation goodness. The load conditions listed in Table A.2 are used for convergence analysis simulations.

Simulations for convergence analysis are performed with varying time increments and element

Symbol	J	F_{ax}	Δn_0	μ	v_s	p_{avg}	q	$\dot{q}_0$
Unit	kgm^2	N	rpm	-	m/s	MPa	J/mm^2	W/mm^2
Value	0.5	2000	2000	0.1	18.1	2.0	1.0	1.8

Table A.2: Load parameters utilised for convergence analysis with CCDC variant 1

lengths. In particular, time increments between Δt = 0.5 ms to Δt = 10 ms are considered. Higher values are not taken into account in order to achieve sufficient time discretization for results postprocessing. Element length is varied in a range between h_{el} = 0.01 mm to h_{el} = 0.3 mm. In Table A.3, maximum temperature results are plotted relative to converged maximum temperature (i.e. simulation with Δt = 0.5 ms and h_{el} = 0.01 mm). Results show a clear convergence towards a more refined mesh, while the influence of time increment is not as dominant.

ϑ_{max} variation w.r.t. converged simulation in %		h_{el} in mm									
		0.3	**0.25**	**0.2**	**0.15**	**0.125**	**0.1**	**0.075**	**0.05**	**0.025**	**0.01**
Δt in ms	**10**	-27.6	-21.3	-19.5	-10.9	-10.2	-8.3	-6.3	-4.5	-3.4	-2.6
	5	-27.3	-20.5	-19.0	-9.9	-10.5	-7.2	-4.5	-3.6	-2.2	-1.6
	2	-27.0	-20.0	-18.8	-9.2	-9.4	-6.3	-3.8	-2.6	-1.5	-1.0
	1	-26.9	-19.6	-18.6	-9.0	-8.3	-6.1	-3.4	-2.0	-0.7	0.0
	0.5	-26.7	-19.4	-18.5	-8.8	-8.1	-6.0	-3.3	-1.9	-0.6	0.0

Table A.3: Convergence analysis in terms of maximum simulated temperature relative to converged maximum temperature

.

Due to the digressive tendency to converged results with decreasing element length, the value of h_{el} = 0.05 mm is chosen as satisfying. A more refined mesh is not pursued. In fact, it would lead to minor result quality improvements, while quadratically increasing computational effort.

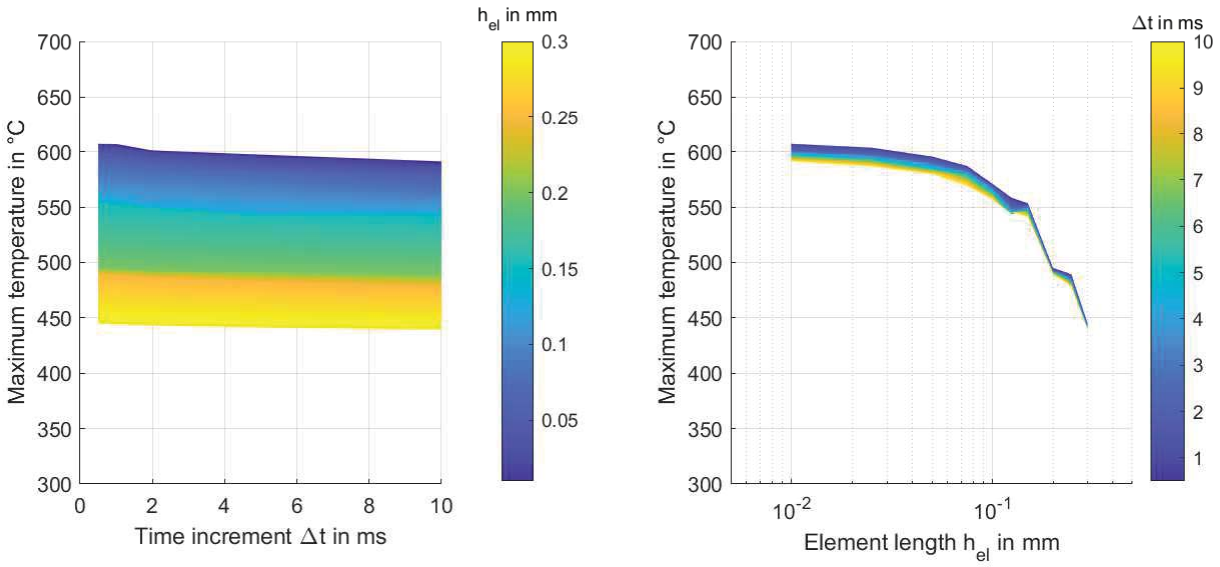

Figure A.7: Maximum temperature values considered for convergence analysis

.

Influence of time increment is less dominant in correspondence of a more coarse mesh. A plot

of maximum simulated temperatures for convergence analysis can be appreciated in Figure A.7. Here the aforementioned values are shown with reference to both element length and time increment. According to shown values and to required computational effort, it is decided to consider a relatively refined mesh thickness with an element length of h_{el} = 0.05 mm and a time increment of Δt = 1 ms. As a compromise between acceptable computation times and results preciseness a 2 % deviation of maximum simulated temperature is rated as satisfying.

A.4 Test-rig ZF/FZG KLP-260

The test-rig ZF/FZG KLP-260 is employed for research on multiple-disc and positive clutches and synchronizers. Depending on the operation mode - i.e. baking powershifts or slip - friction, endurance and wear behaviour can be tested. Additionally, engagement behaviour of positive clutches can be tested. A photograph of the test-rig can be appreciated in Figure A.8. For

Figure A.8: Photograph of the test-rig ZF/FZG KLP-260 according to [Mei15]

experiments relevant for this work, both braking and slip mode are employed. As each type of experiment focuses on different measured parameters and in different measurement regions, two separate measurement uncertainty considerations are discussed.

A.4.1 Temperature measurements

Validation experiments with according temperature measurements are performed in braking mode. This means that a preset inertial mass is accelerated until the desired speed difference that must be braked is reached. Immediately before clutch engagement, a magnetic clutch, which connects the driving electric motor to the shaft, disengages. As temperature is the only parameter of interest for validation tests, expanded measurement uncertainty considerations according to GUM guideline are done only for this signal. For detailed considerations about expanded measurement uncertainty of load cells for axial force and torque measurements, refer to Baumgartner [Bau20]. Under the assumption that the indicated value is saved as is and so no error occurs at this stage, the elements generating uncertainty in the measurement chain are in turn the sensor itself and the voltage supply module. As the module is manufactured by National Instruments, all values referring to it are characterised by apex *NI*.

The real voltage signal differs from the indicated one by a defined uncertainty value, as expressed in Equation A.4.

$$U_{real} = U_{ind} - \delta U_{tc} - \delta U_{NI,g} - \delta U_{NI,n} - \delta U_{NI,r} \tag{A.4}$$

U_{real}	V	Real voltage signal	U_{ind}	V	Indicated voltage signal
U_{tc}	V	Thermocouple signal error	$U_{NI,g}$	V	NI-module gain error
$U_{NI,n}$	V	NI-module noise error	$U_{NI,r}$	V	NI-module resolution error

Knowing that the voltage supply module operates in a range of $\pm$ 10.4 V and has a resolution of 16 Bit, appropriate error probability distribution functions (PDF) are assumed and according deviations considered, based on datasheets. In particular:

- Signal error caused by the thermocouple itself is retrieved from sensor's specifications. The error is assumed to be continuously uniform distributed and the value of a half interval is fixed at 0.75 % of the indicated value.
- Because of the voltage gain added by the NI-module during analogue to digital signal conversion, an error is generated. Also in this case, it is considered continuously uniform distributed. according to specifications, a half interval value of 0.02 % of the indicated value is considered.
- According to specifications, noise-induced error is normally distributed around the expected value of 0, the standard deviation amounting to 120 % of the least significant bit (LSB). The voltage span amounts to twice 10.4 V, divided into 2^{16} intervals.
- Resolution error amounts to half a LSB and possesses a continuous uniform distribution.

Values are summarised in Table A.4.

Parameter	Symbol	Unit	Expected value	PDF	Std. deviation
Indicated voltage	U_{ind}	V	U_{ind}	-	-
Thermocouple signal error	U_{tc}	V	0	Uniform	$\sigma = \frac{0.0075 \cdot U_{ind}}{\sqrt{3}}$
NI-module gain error	$U_{NI,g}$	V	0	Uniform	$\sigma = \frac{0.0002 \cdot U_{ind}}{\sqrt{3}}$
NI-module noise error	$U_{NI,n}$	V	0	Nomal	$\sigma = \frac{1.2 \cdot (2 \cdot 10.4V)}{2^{16}}$
NI-module resolution error	$U_{NI,r}$	V	0	Uniform	$\sigma = \frac{0.5 \cdot (2 \cdot 10.4V)}{2^{16} \cdot \sqrt{3}}$

Table A.4: Summary of all uncertainty values in the measurement chain

For instance, for the maximum measured temperature of ϑ = 155 °C (U_{ind} = 3.22 V), the relative measurement uncertainty results as in Equation A.5.

$$U_{\vartheta,rel} = \frac{U_{\vartheta}}{U_{ind}} = \frac{\sqrt{{\sigma_{\mathrm{tc}}}^2 {\sigma_{\mathrm{NI,g}}}^2 + {\sigma_{\mathrm{NI,n}}}^2 + {\sigma_{\mathrm{NI,r}}}^2}}{U_{ind}} = \frac{\pm 0.013}{3.22} = \pm 0.43\% \tag{A.5}$$

Assuming the values of the uncertainty chain are distributed normally, the 95 % confidence interval for the determined value is expressed in Equation A.6.

$$\vartheta_{real} = 155\ ^{\circ}\mathrm{C} \pm 1.96 \cdot 0.013\ \mathrm{V} \cdot 48.07\ \frac{^{\circ}\mathrm{C}}{\mathrm{V}} = 155 \pm 1.22\ ^{\circ}\mathrm{C} \tag{A.6}$$

A.4.2 Torque measurements

Relevant signals from dog clutch engagement experiments are especially torque and position. Detailed measurement uncertainty considerations on position sensor are neglected in this section. As the position of measurement of interest is at the dog clutch body, all elasticities in the force flow from actuator to dog clutch are assumed to have an unknown influence which is at least two orders of magnitude higher than the ones caused by measurement errors. Torque measurement is performed by force measurement vie a load cell tangentially oriented with reference to the rotation axis and with known lever arm. As the load cell for torque measurement is calibrated before each new set of experiments, uncertainties deriving from calibration itself have to be considered too. Voltage supply, gain, noise and resolution of the NI-measurement system are analogous to the ones employed for temperature measurement. Deviations at the load cell itself are generated only by temperature, while deviations induced by torque inversion are neglected. Indeed, a considerable amount of the total measured torque is delivered by the cone clutch, so that engagement jolts are not capable of inverting the torque itself. These uncertainty sources shall however be considered when a torque inversion occurs. Temperature-induced measurement uncertainty deviation at the load cell is expressed as in Equation A.7. Ambient temperature utilised as reference is assumed to be ϑ_{amb} = 23 °C.

$$\sigma_{T,\vartheta} = \frac{10^{-4}}{\mathrm{K}} \cdot (\vartheta_{sensor} - \vartheta_{amb}) \cdot U_{ind} \tag{A.7}$$

Calibration torques are generated by applying known lever-weight combinations to the outer carrier externally. Hence, the torque uncertainty is a combination of mass weight and lever length. Both quantities are distributed continuously uniform. In order to determine the combined effect of weight and length uncertainty on torque, the first order sensitivity coefficients are used to weigh the according standard deviations. While different masses are utilised to generate according calibration torques (measured variable m_{ind}), the lever arm - and hence its length - remain constant. Sensitivity coefficients are determined as partial derivatives of the calibration torque, as expressed in Table A.5.

Parameter	Symbol	Value	Sensitivity coeff.	PDF	Std. deviation
Lever arm	l_{cal}	1.5 ± 0.014 m	$\frac{\partial}{\partial l_{cal}}(m_{ind}\cdot l_{cal}\cdot g) = g\cdot m_{ind}$	Uniform	$\sigma = \frac{0.014}{\sqrt{3}} = 0.0081$ m
Weight	m_{ind}	m_{ind} ± 0.01 kg	$\frac{\partial}{\partial m_{ind}}(m_{ind}\cdot l_{cal}\cdot g) = g\cdot l_{cal}$	Uniform	$\sigma = \frac{0.01}{\sqrt{3}} = 0.0058$ kg

Table A.5: Summary of all uncertainty values in the measurement chain

According to these values, measurement uncertainty of calibration setup can be determined as expressed in Equation A.8. As a set of different masses is employed for calibration curves determination, the smallest calibration weight of m_{ind} = 5.034 kg is considered, which causes the greatest relative uncertainty. Such mass generates a torque at the load cell of T_{ind} = 74 Nm.

$$U_{T,cal,rel} = \frac{U_{T,cal}}{T_{ind}} = \frac{\sqrt{(\sigma_{l_{cal}}\cdot c_{l_{cal}})^2 + (\sigma_{m_{cal}}\cdot c_{m_{cal}})^2}}{T_{ind}} = \frac{\pm 0.094}{74} = \pm 0.13\% \tag{A.8}$$

Finally, uncertainty deriving from calibration and influencing the calibration factor can be associated in an analogous way to uncertainties in the measurement chain induced by temperature, noise, resolution and gain of the NI-module. As an example, the extended relative uncertainty is determined for the maximal torque arising during experiments, which equals 1300 Nm. The according mathematics is expressed in Equation A.9

$$U_{T,rel} = \frac{U_{cal}}{U_{ind}} = \frac{\sqrt{\sigma^2_{T,\vartheta} + \sigma^2_{NI,g} + \sigma^2_{NI,n} + \sigma^2_{NI,r} + (U_{T,cal,rel}\cdot U_{ind})^2}}{U_{ind}} = \frac{\pm 0.02}{6.25} = \pm 0.33\% \tag{A.9}$$

Hence, the real torque T_{real} and its according confidence interval of 95 % can be expressed as shown in Equation A.10.

$$T_{real} = 1300\ \mathrm{Nm} \pm 1.96 \cdot 0.02\ \mathrm{V} \cdot 208\ \frac{\mathrm{Nm}}{\mathrm{V}} = 1300 \pm 4.3\ \mathrm{Nm} \tag{A.10}$$

A.5 Temperature measurements

Temperature measurements obtained from validation experiments are plotted in this section. All temperature curves are referenced to each other by the speed difference signal. Each plot includes a speed difference curve as well as the average temperature (obtained as mean of at least 10 measurements), according min-max scatterbars and the 95 % confidence interval.

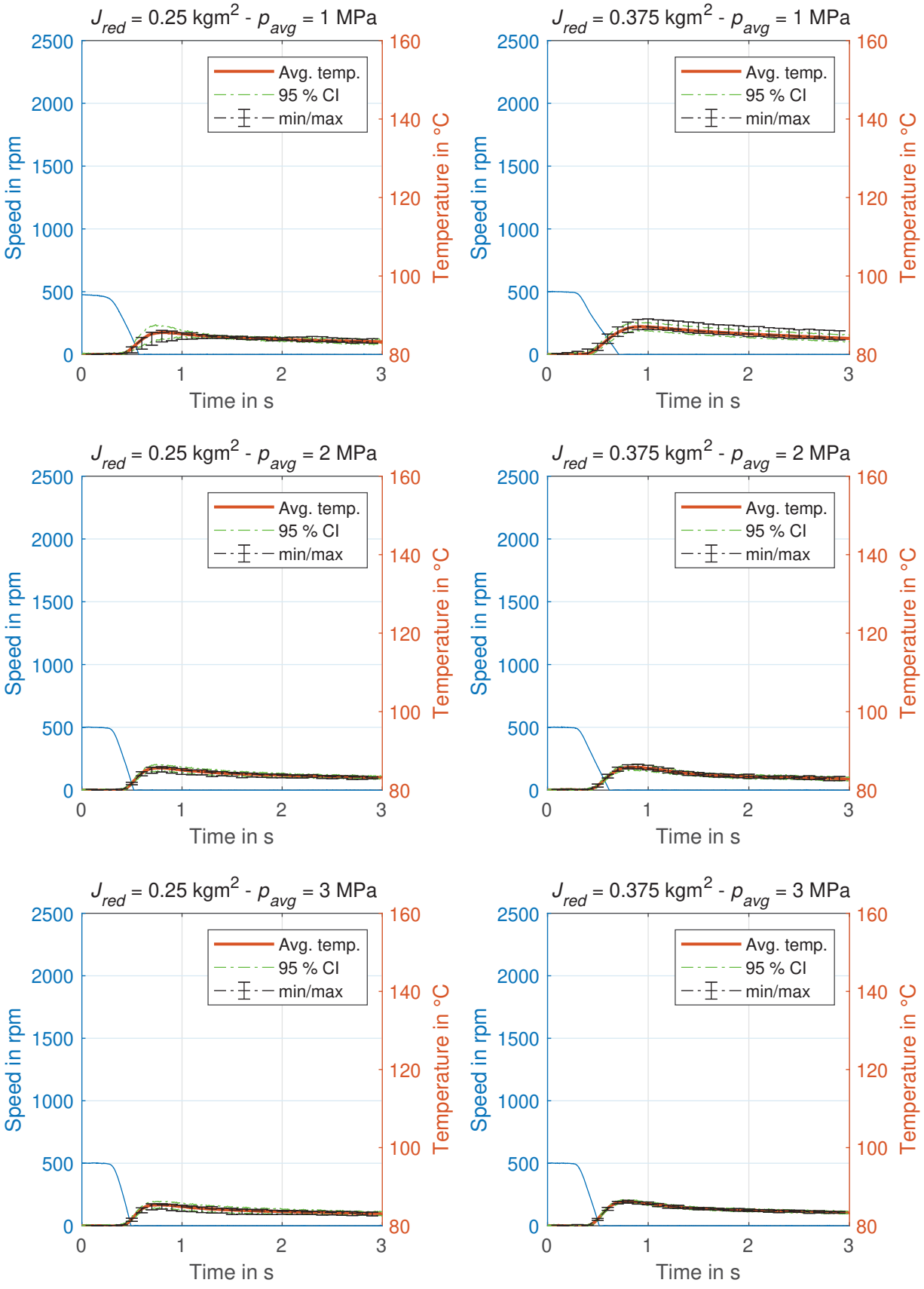

Figure A.9: Measured temperatures for experiments with initial sliding velocity of v_0 = 4.2 m/s

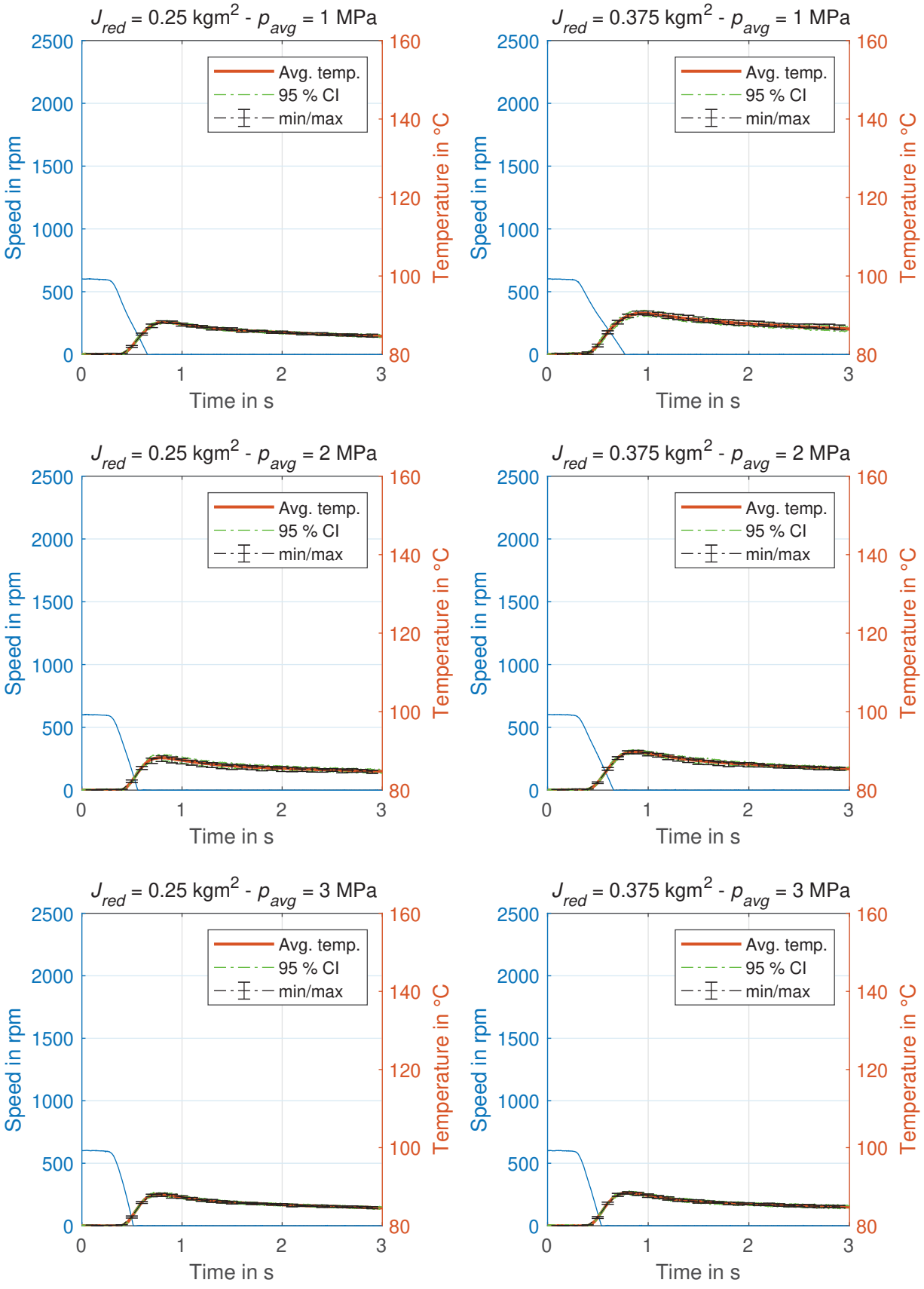

Figure A.10: Measured temperatures for experiments with initial sliding velocity of v_0 = 5.0 m/s

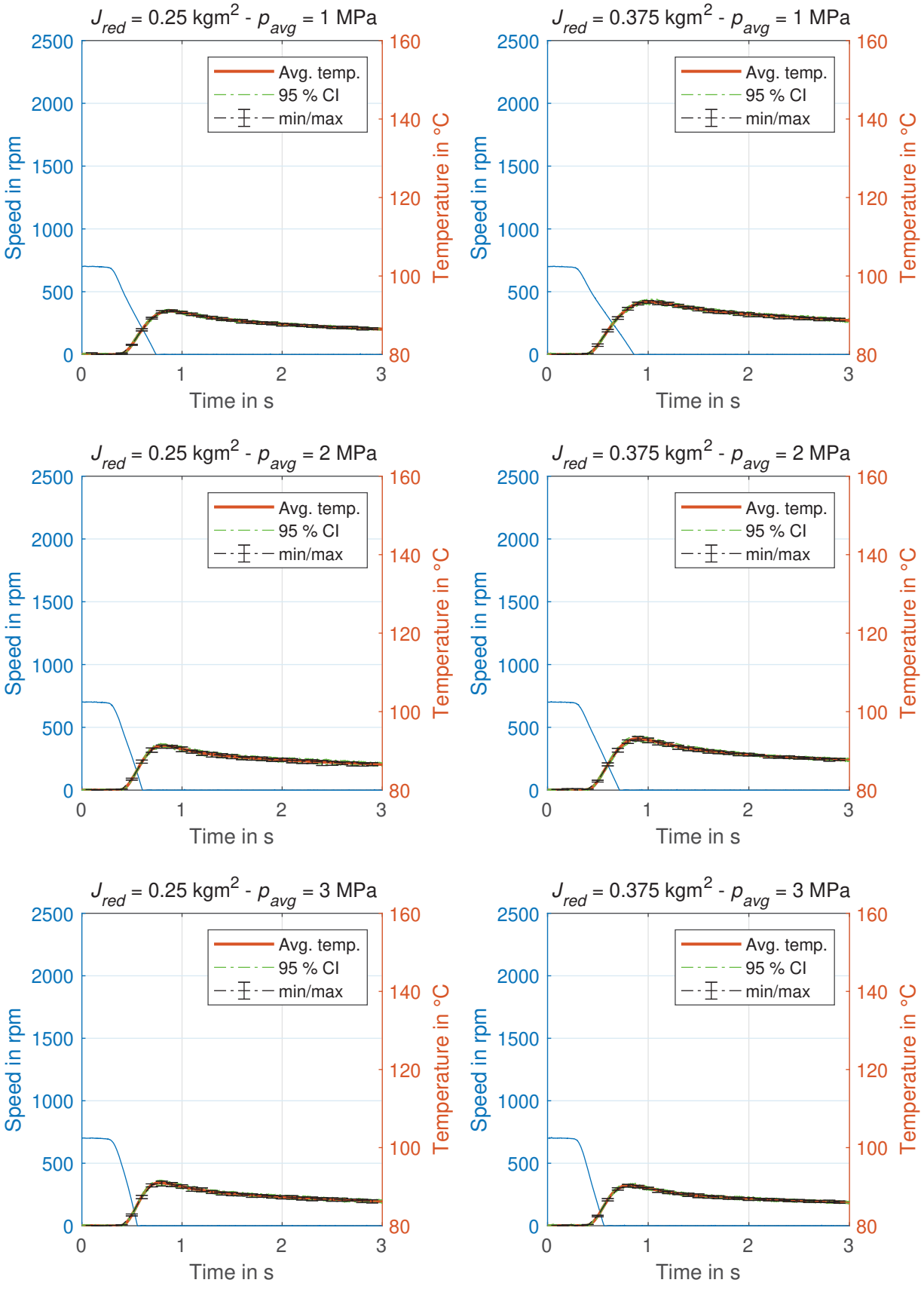

Figure A.11: Measured temperatures for experiments with initial sliding velocity of v_0 = 5.9 m/s

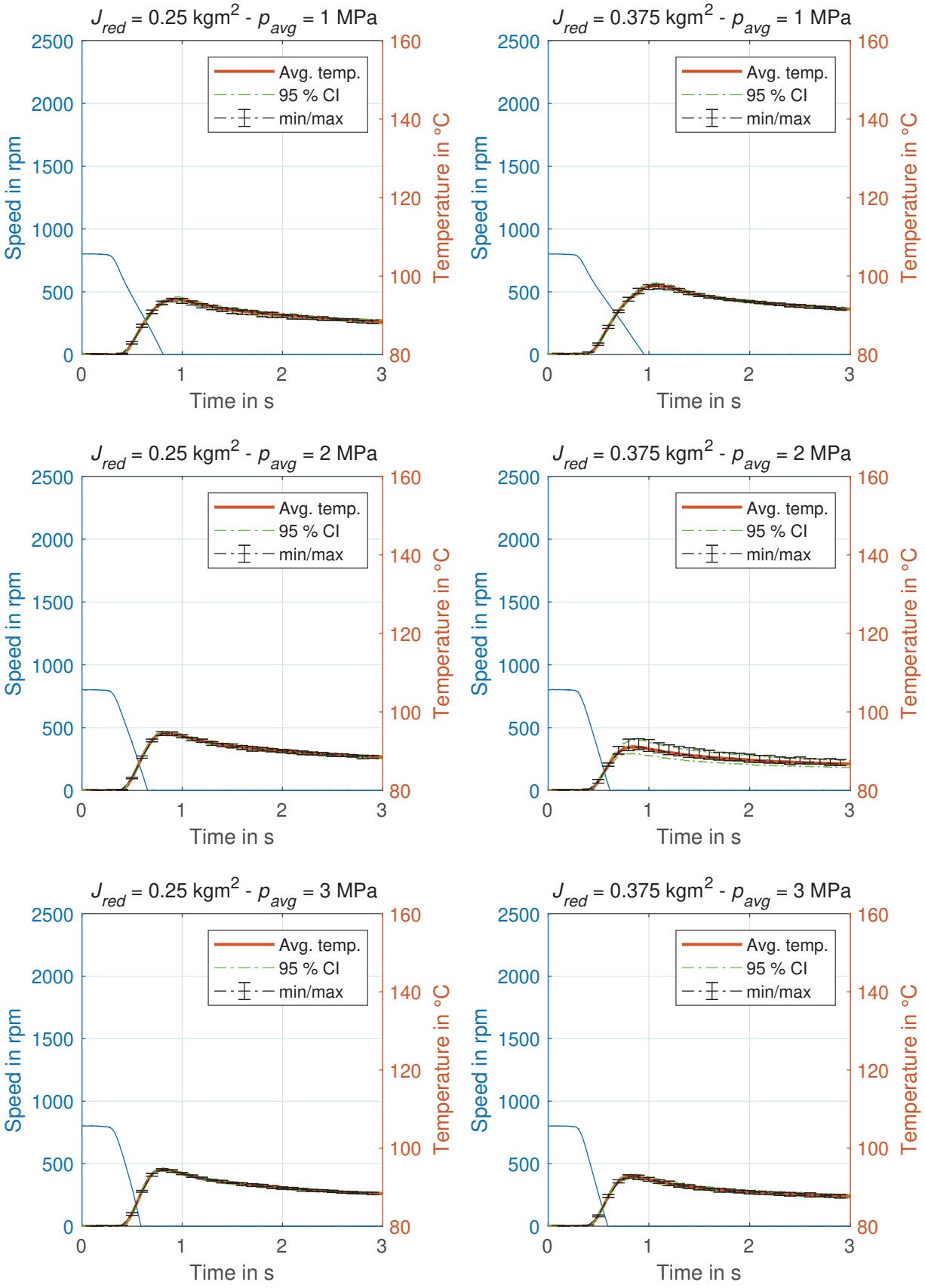

Figure A.12: Measured temperatures for experiments with initial sliding velocity of v_0 = 6.7 m/s

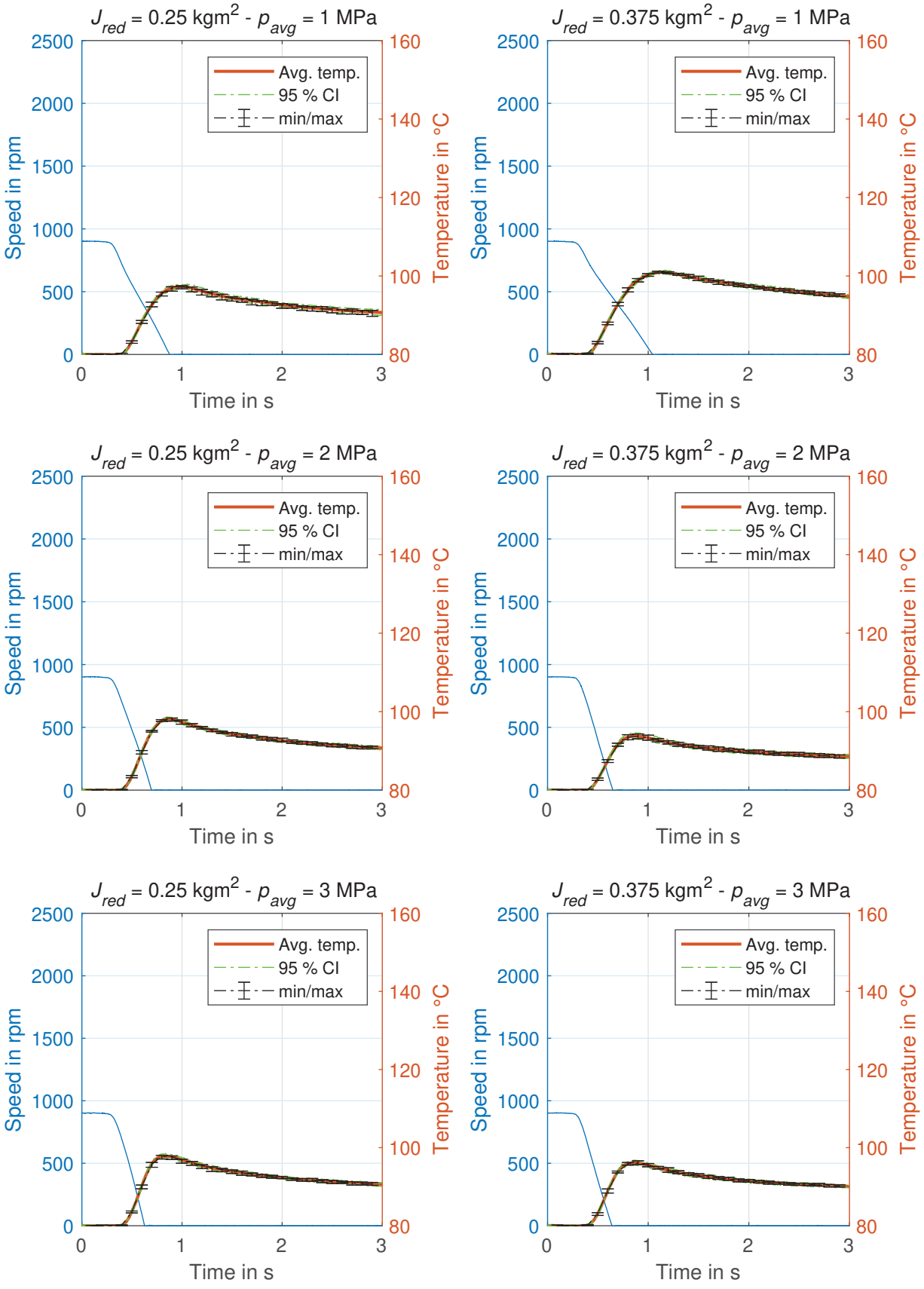

Figure A.13: Measured temperatures for experiments with initial sliding velocity of v_0 = 7.5 m/s

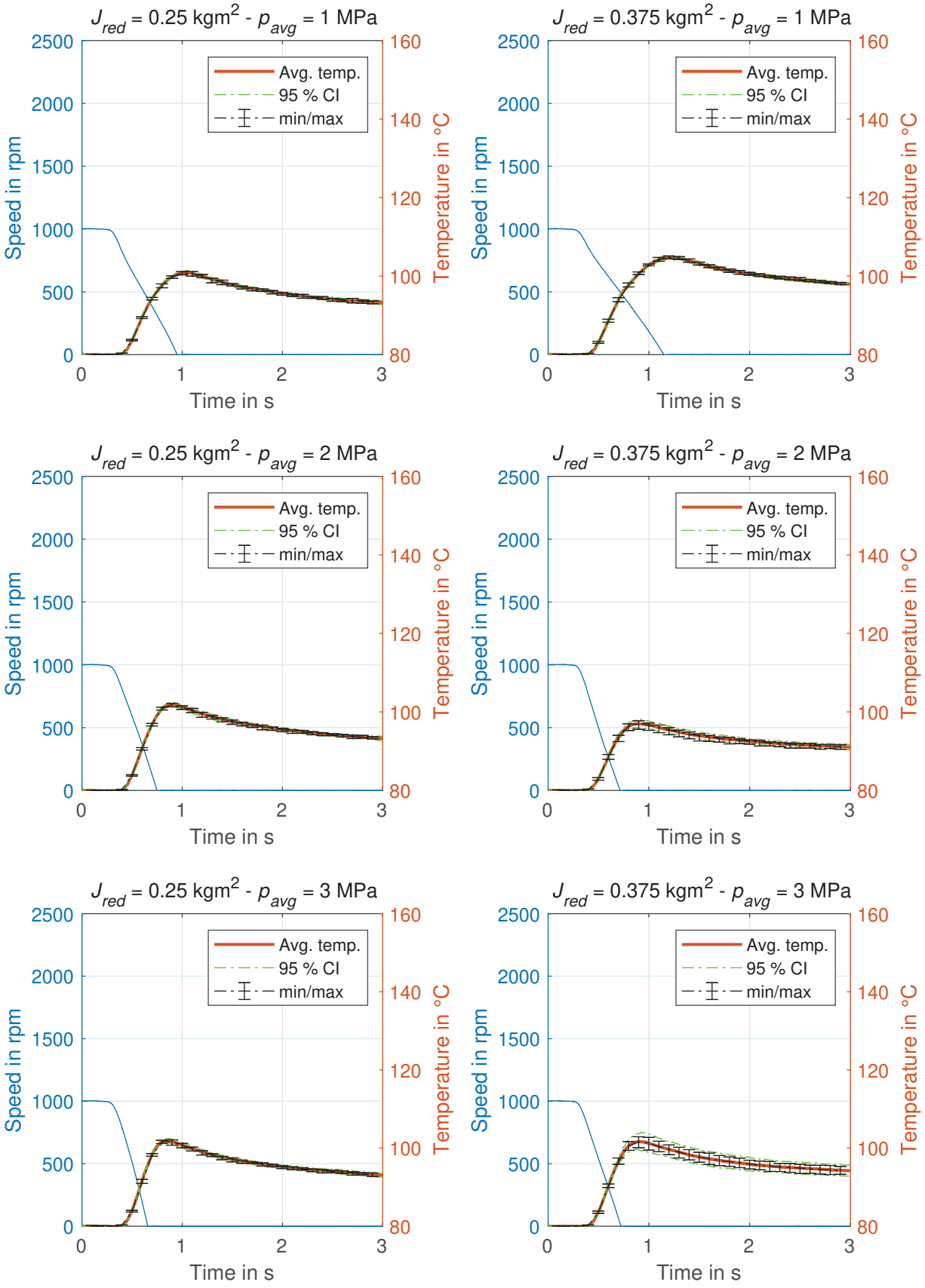

Figure A.14: Measured temperatures for experiments with initial sliding velocity of v_0 = 8.4 m/s

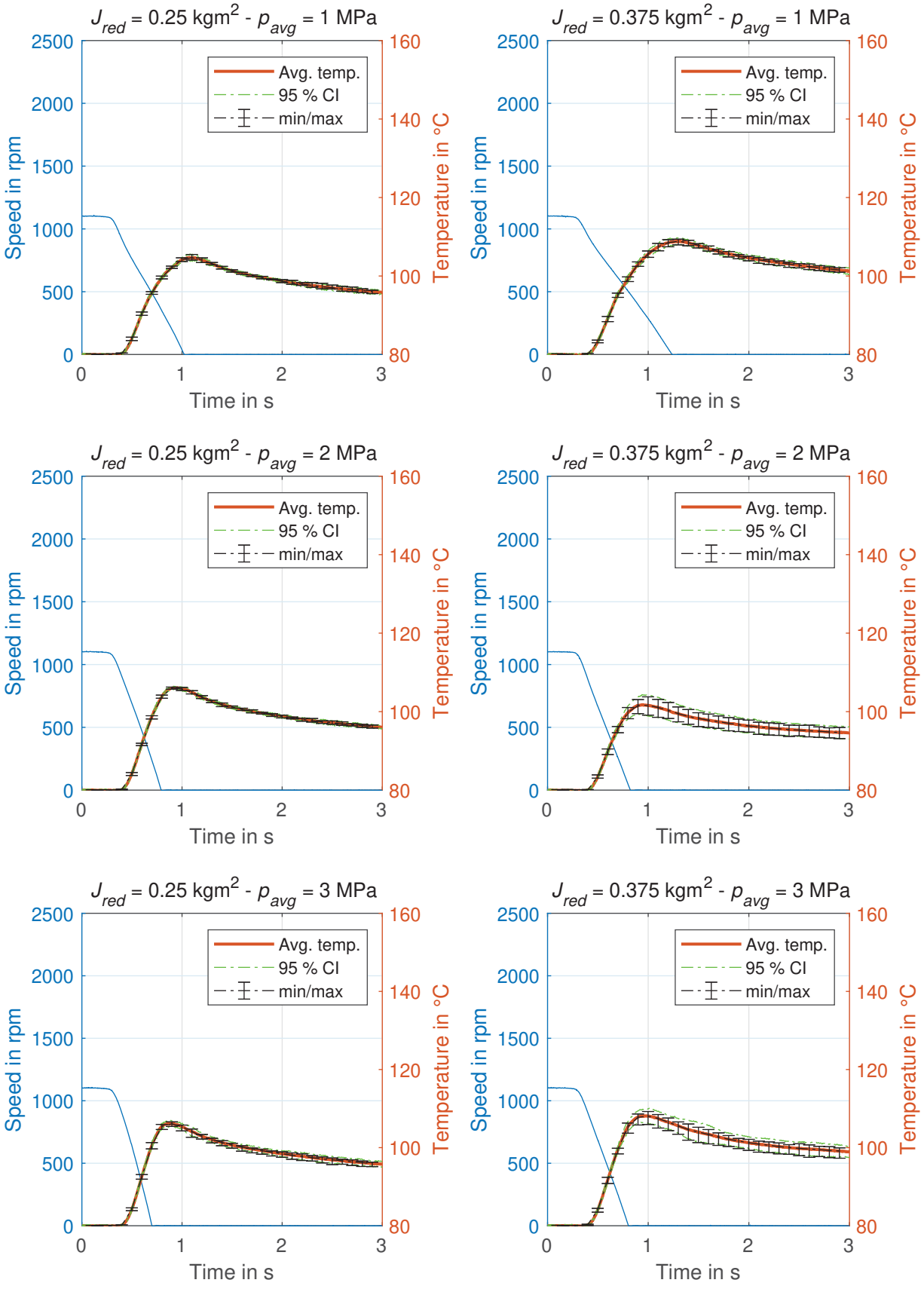

Figure A.15: Measured temperatures for experiments with initial sliding velocity of v_0 = 9.2 m/s

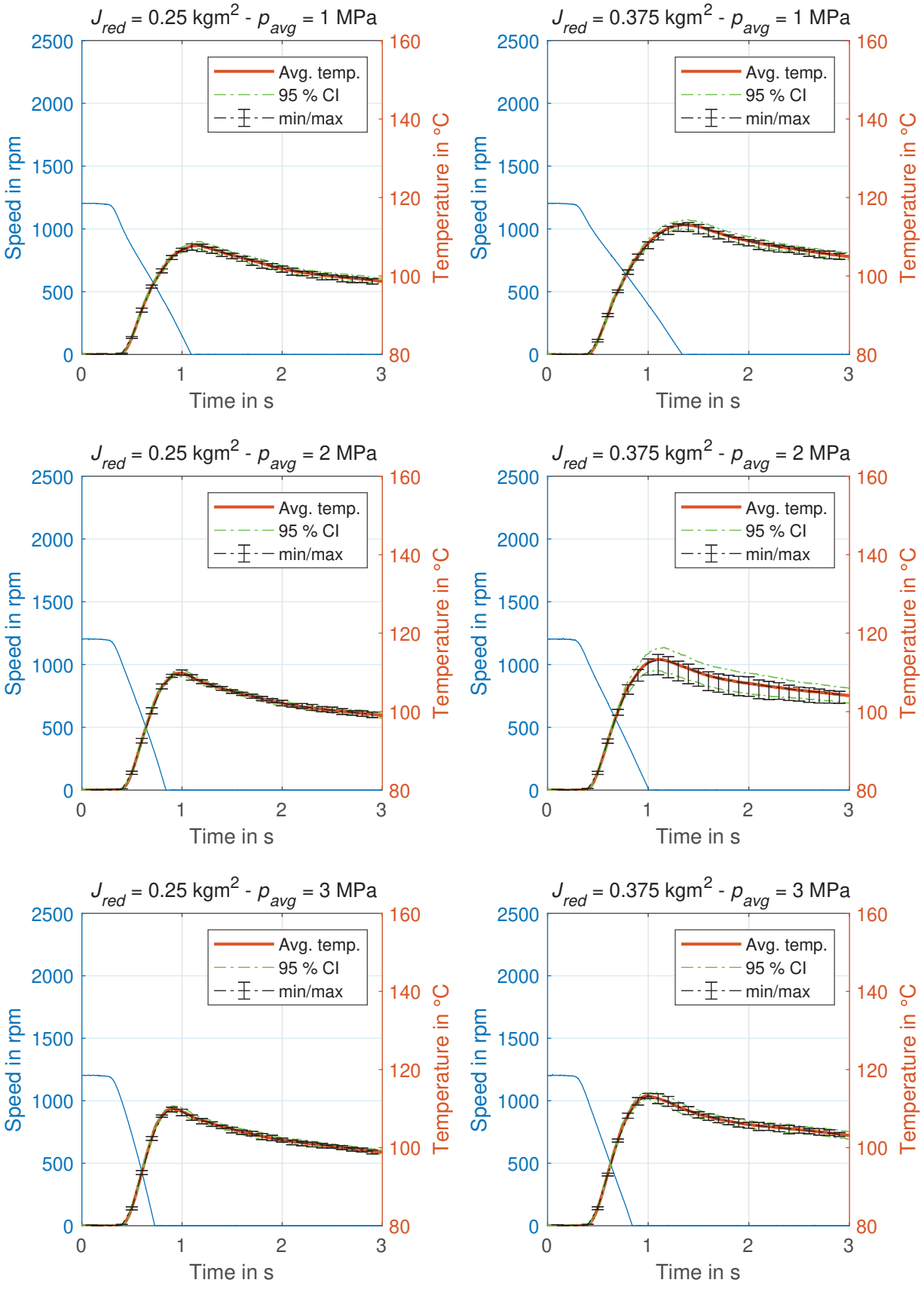

Figure A.16: Measured temperatures for experiments with initial sliding velocity of v_0 = 10.1 m/s

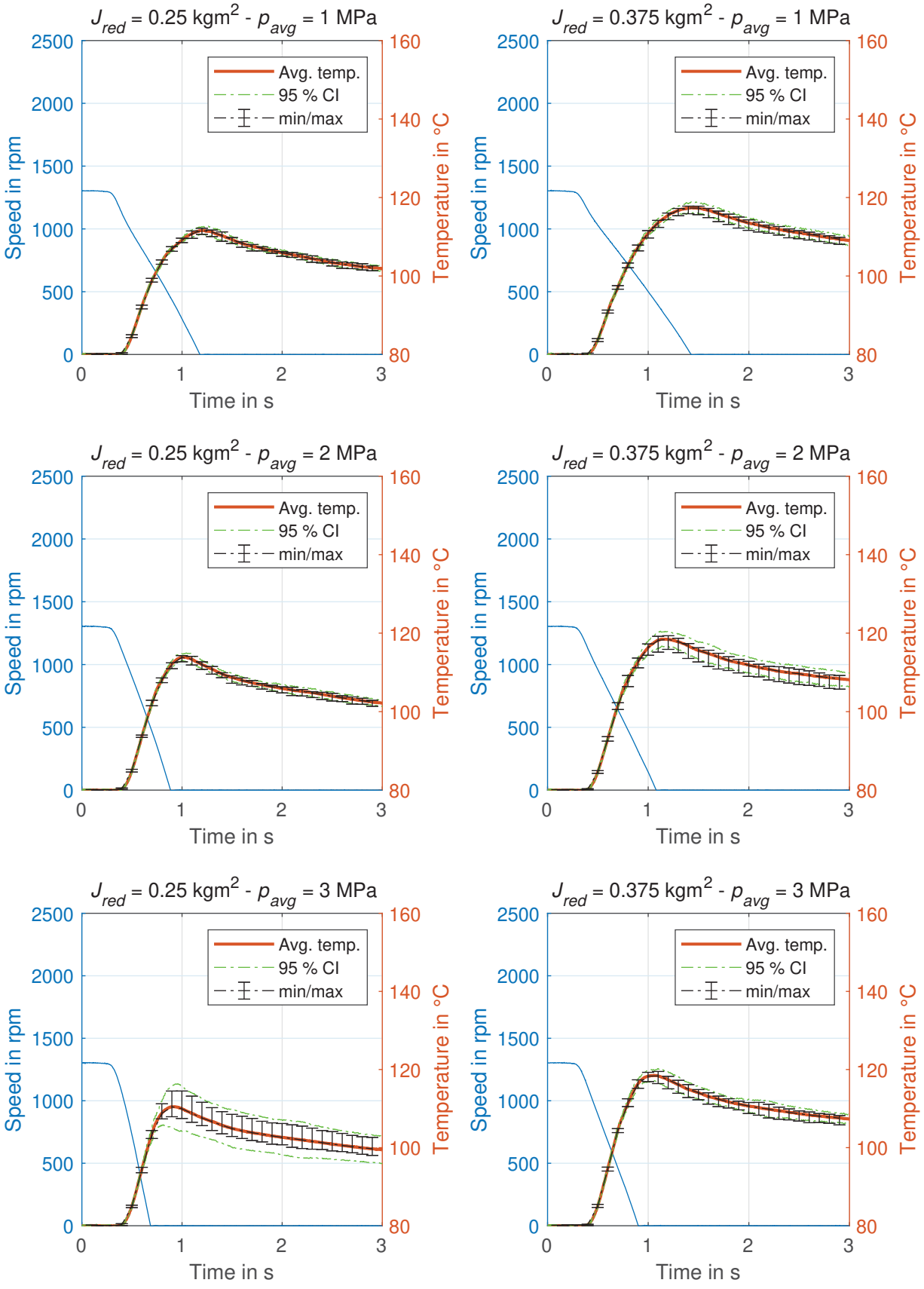

Figure A.17: Measured temperatures for experiments with initial sliding velocity of v_0 = 10.9 m/s

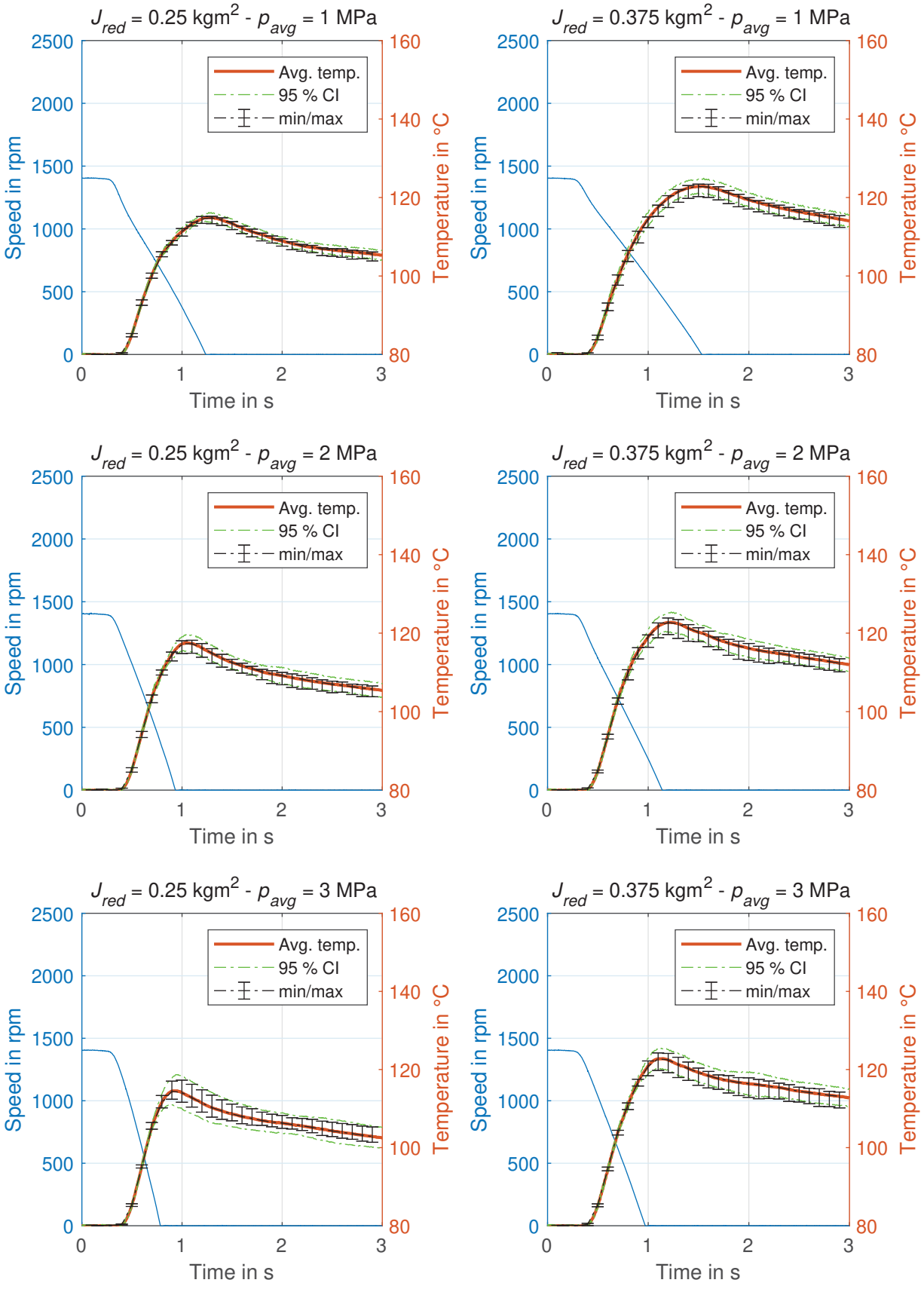

Figure A.18: Measured temperatures for experiments with initial sliding velocity of v_0 = 11.7 m/s

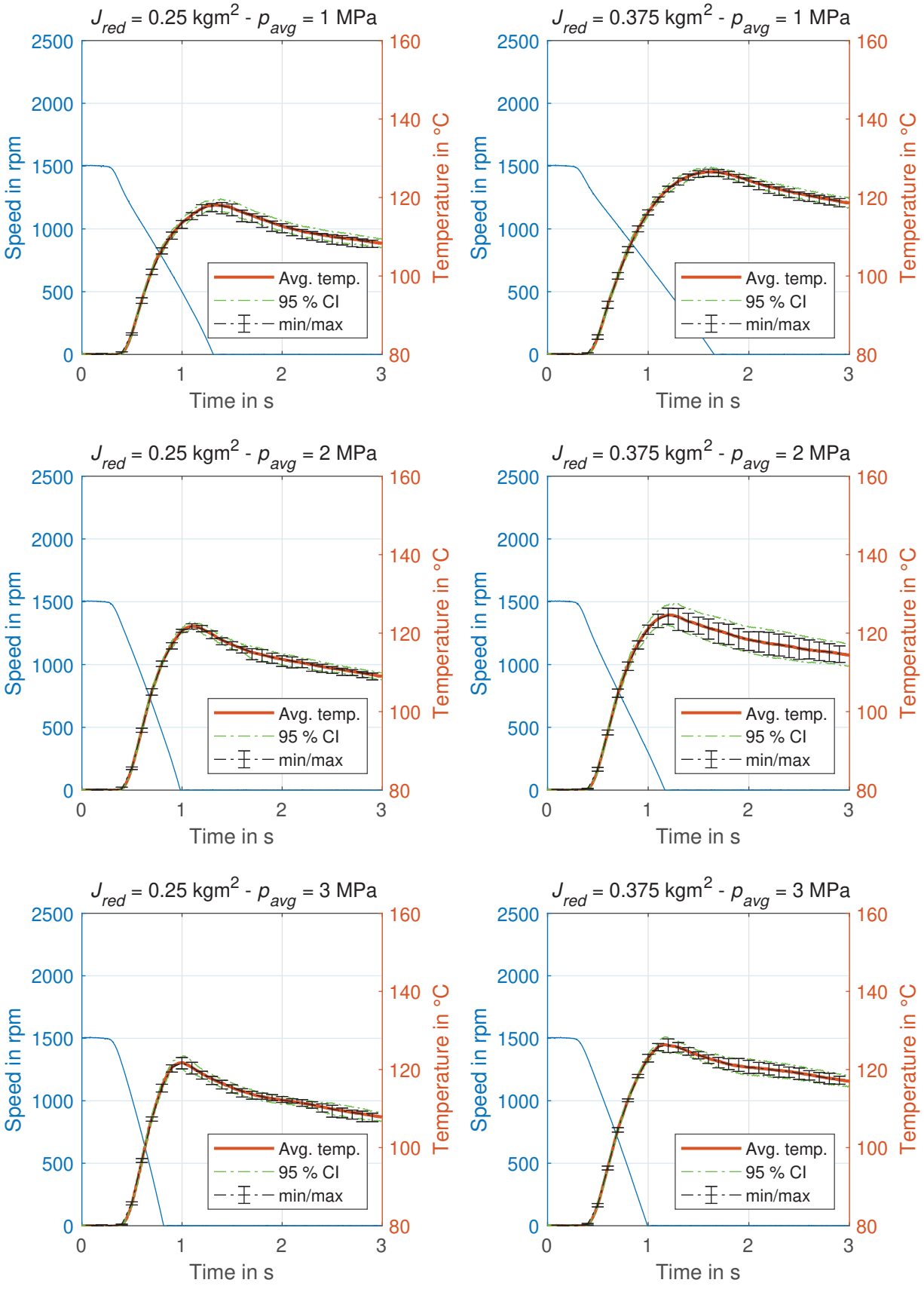

Figure A.19: Measured temperatures for experiments with initial sliding velocity of v_0 = 12.6 m/s

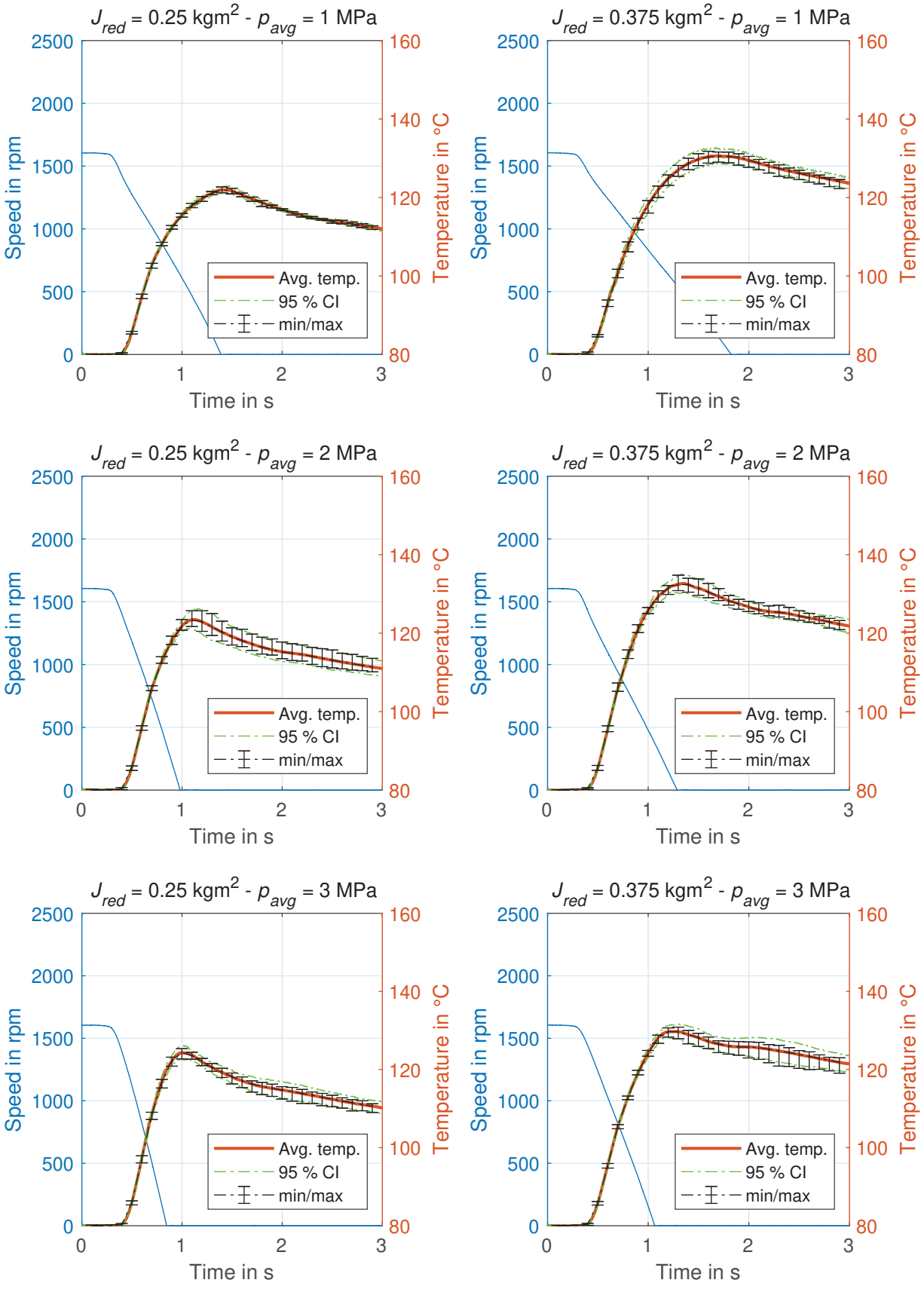

Figure A.20: Measured temperatures for experiments with initial sliding velocity of v_0 = 13.4 m/s

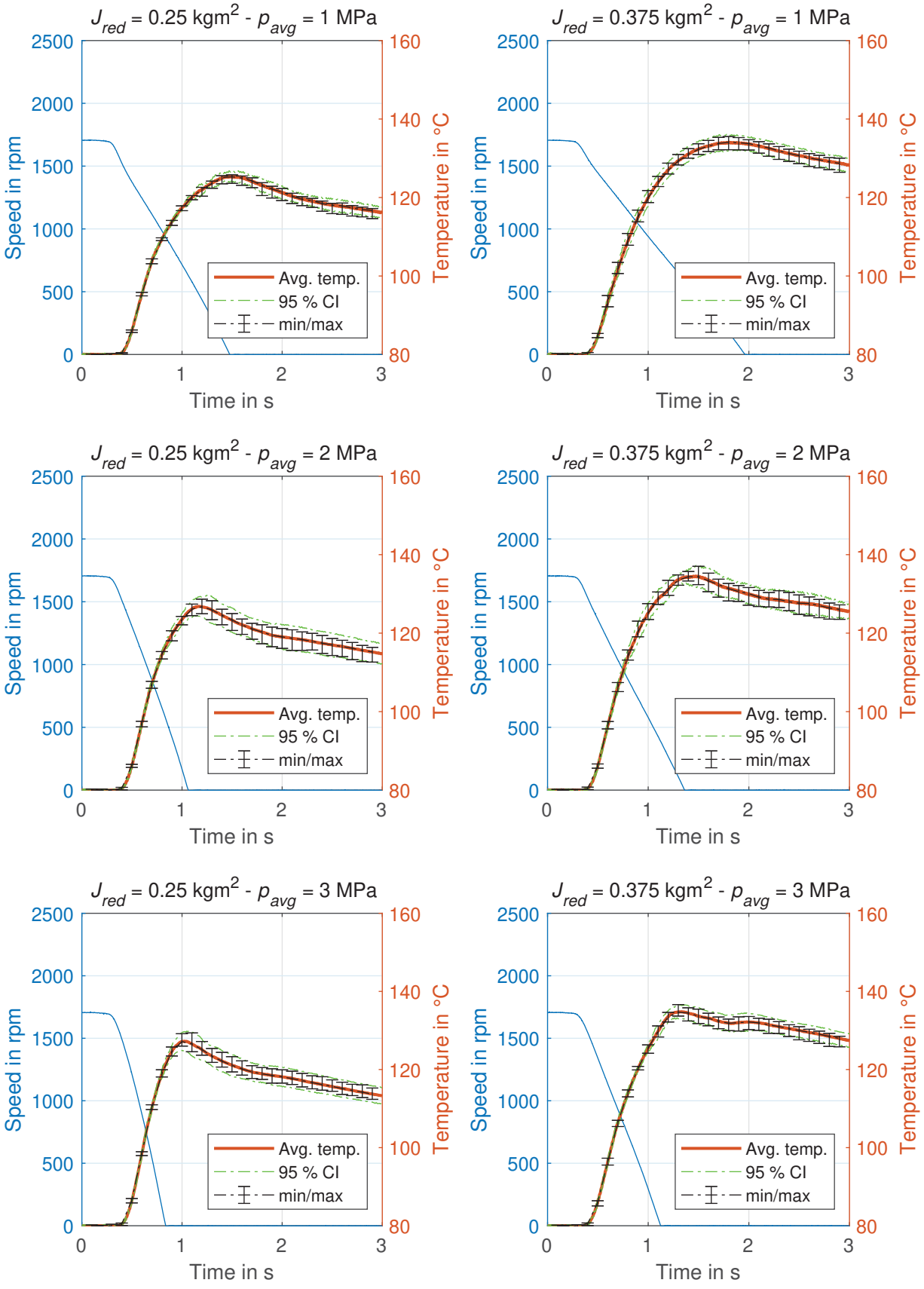

Figure A.21: Measured temperatures for experiments with initial sliding velocity of v_0 = 14.2 m/s

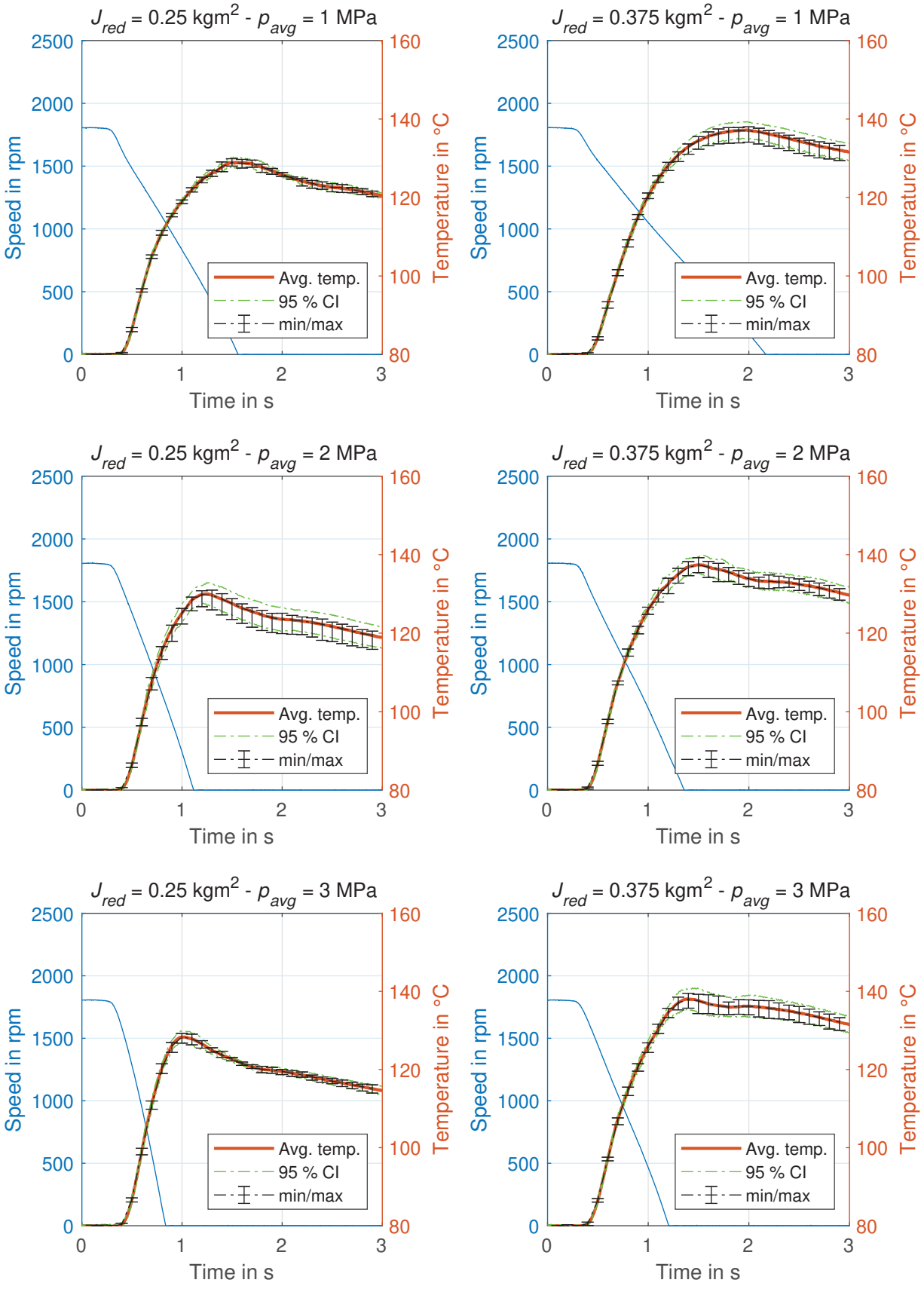

Figure A.22: Measured temperatures for experiments with initial sliding velocity of v_0 = 15.1 m/s

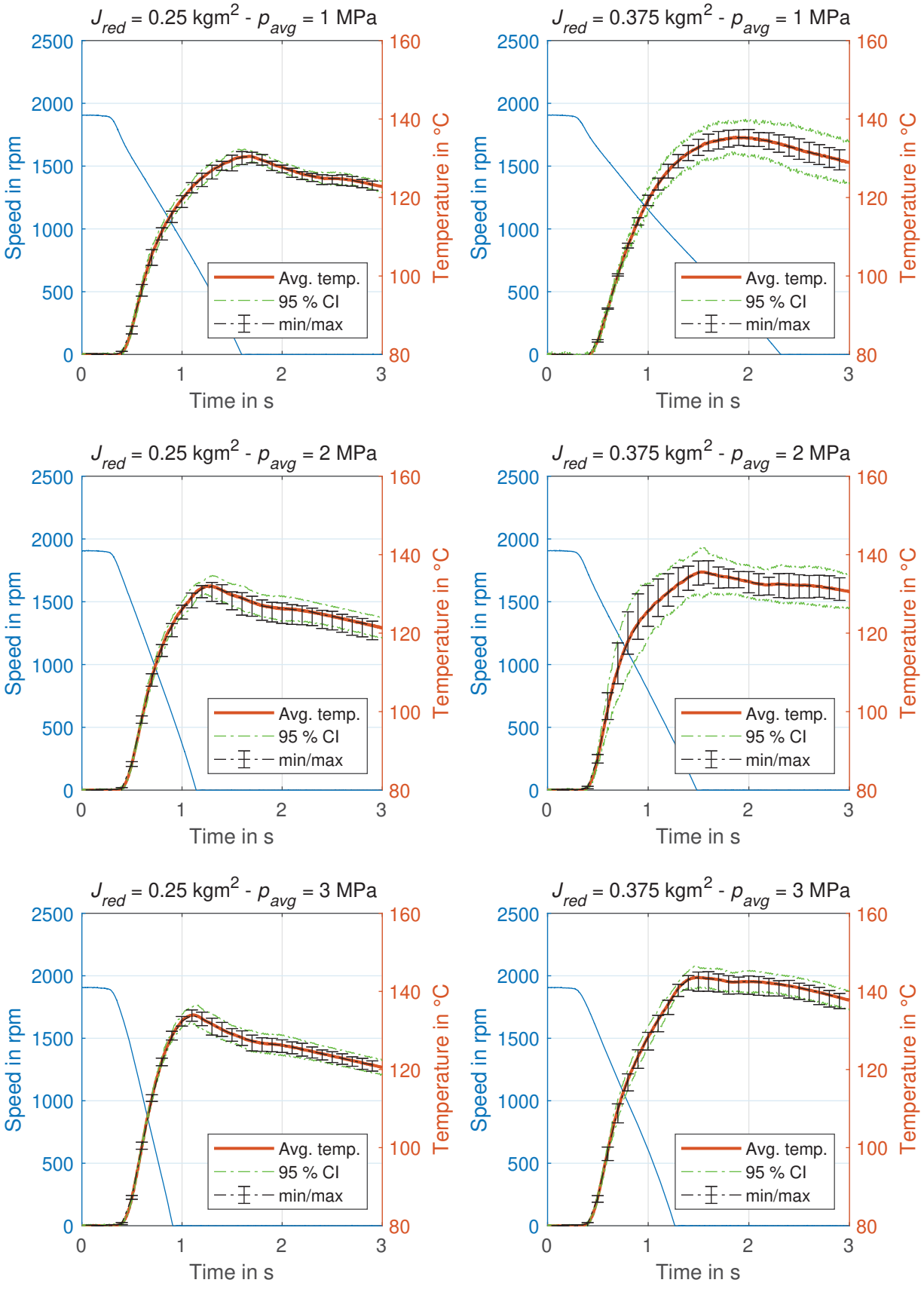

Figure A.23: Measured temperatures for experiments with initial sliding velocity of v_0 = 15.9 m/s

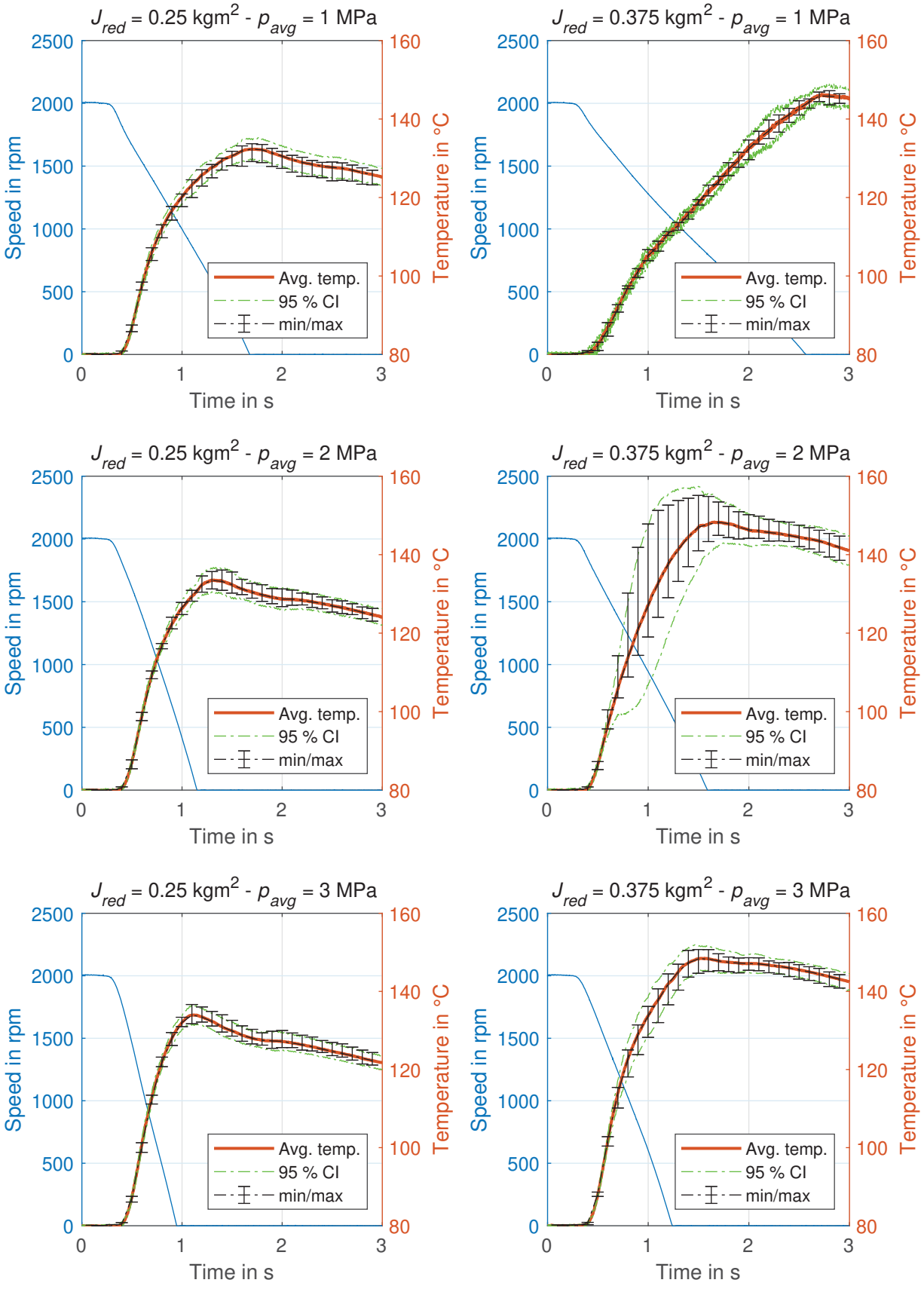

Figure A.24: Measured temperatures for experiments with initial sliding velocity of v_0 = 16.8 m/s

A.6 Simulink transmission model

A preliminary investigation on the most widespread AT on the market and the respective shifting elements is conducted for identifying shifting elements suitable for being substituted with CCDC. For this purpose, a 1D multibody simulation model is built in Simulink to support and validate calculations shown in Appendix A.1. The Simulink model is easily adaptable to virtually every series AT on the market by adapting the respective geometry. Shifting scheme and strategy is implemented in a Matlab program. In the context of this work, ATs 8HP70 & 9HP48 by ZF, 8GL90 by GM, F22 by AISIN and 7G-Tronic & 9G-Tronic by Daimler are modelled. In the following, only Daimler's 9G-Tronic is exemplary shown (see Figure A.25).

Each AT model is composed of these main blocks:

- ICE: This simplified block represents the driving engine and defines torque and speed at the input shaft of the transmission. Albeit a complex ICE model may be implemented for model improvement, such approach is not followed in this case, as the disadvantages in terms of programming, tuning and computational effort clearly overrule the advantages. Instead, a pure torque and speed source is considered sufficient for computing the pursued quantities.

- AT: The transmission is composed of planetary or epicyclic gear sets, their rigid couplings and the shifting elements. Moments of inertia of the shafts are educatedly guessed according to CAD data. The transmission block receives speed and torque of the shaft and pressure signals at the actuators as inputs. Speed and torque signals at every shaft are saved as outputs of the block. The AT block for Daimler's 9G-Tronic is represented in Figure A.26.

- Vehicle model: Also in this case, the vehicle model as simple as possible. Vehicle mass and moments of inertia of cardan shaft and differential are considered along with wind drag, street inclination and rolling resistance. Wheels are modelled into more detail, the Magic Formula by Pacejka [Pac12] being considered for tyre-street interaction.

- Actuator pressure: This block determines the hydraulic oil pressure and hence axial force exerted by acutators on their respective shifting elements. It receives inputs directly form Matlab workspace and computes the time dependent pressure curves depending on gearchange type (up/down, traction/thrust), shifting mode and target shifting time.

Simulations results for an exemplary shift are shown in Figure A.27 for the reference transmission (9G-Tronic) and reference shifting element (brake C(B06)). A traction downshift is considered from 5^{th} to 4^{th} speed. Input parameters are worst-case scenario, i.e. maximum allowable input torque of T_{in} = 700 Nm and an initial input speed of n_{in} = 2,000 rpm. Form torque and speed signals at the shifting element, friction loss and power at CCDC can be evaluated. In

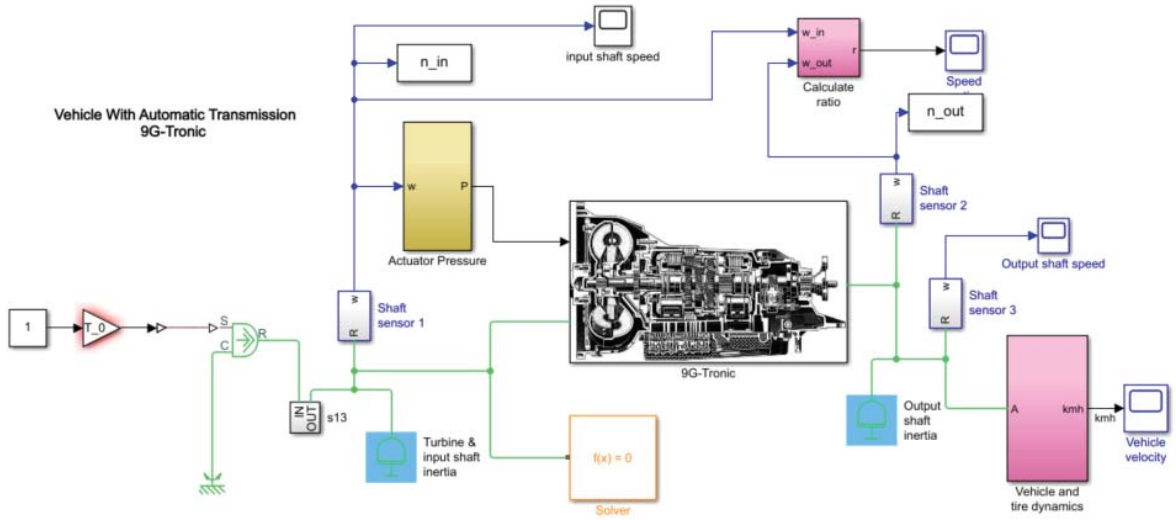

Figure A.25: Representation of the Simulink driveline model

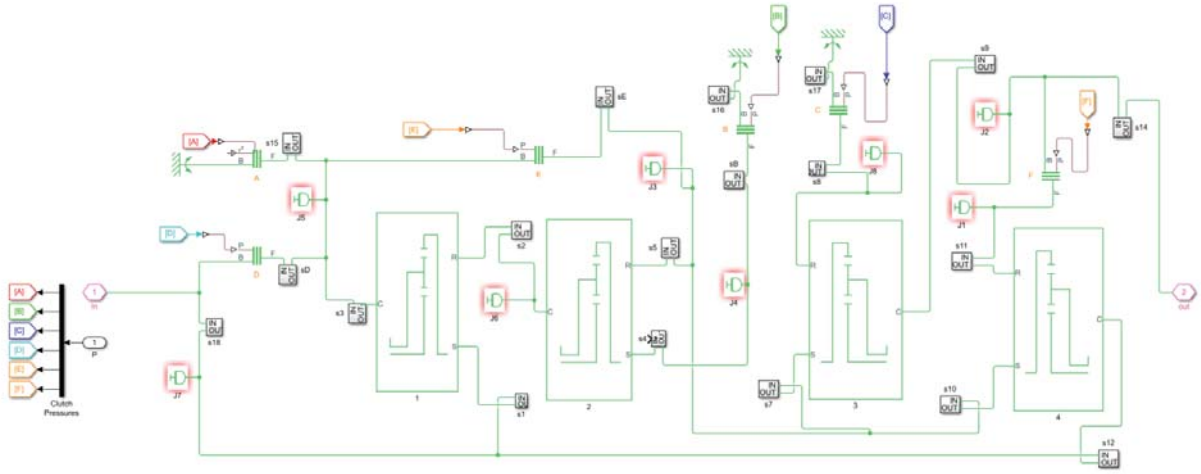

Figure A.26: Representation of the Simulink AT model

particular, utilising friction loss and rearranging the kinetic energy equation, one obtains the reduced inertia J_{red}.

$$J_{red} = \frac{2Q}{\Delta\omega_0^2} \tag{A.11}$$

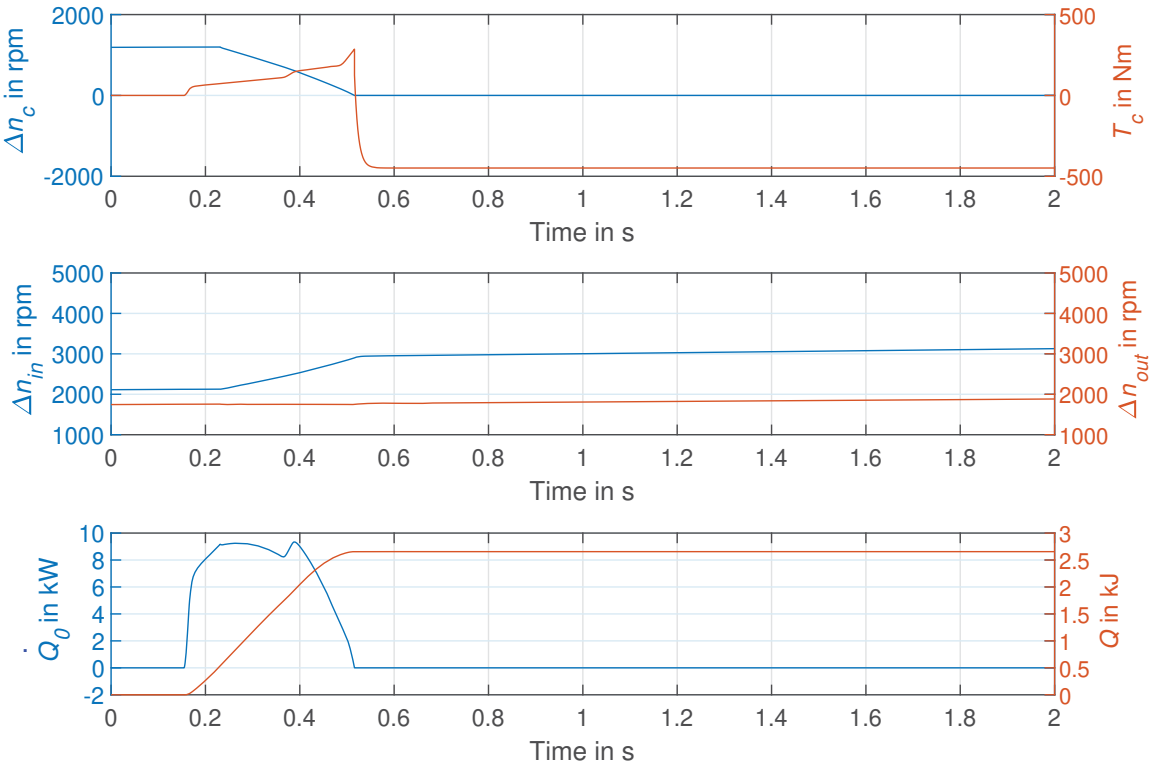

Figure A.27: Simulative gearchange signals at Brake C (B06) of Daimler's 9G-Tronic. T_{in} = 700 Nm and n_{in} = 2,000 rpm

A.7 Sheet thickness variation study

Effect of sheet thickness variation on computed temperature at validation datapoints (refer to Table 5.2). Standard sheet thickness of s_t = 3.0 mm and according thickness variations of s_t = 2.5 mm and s_t = 3.5 mm.

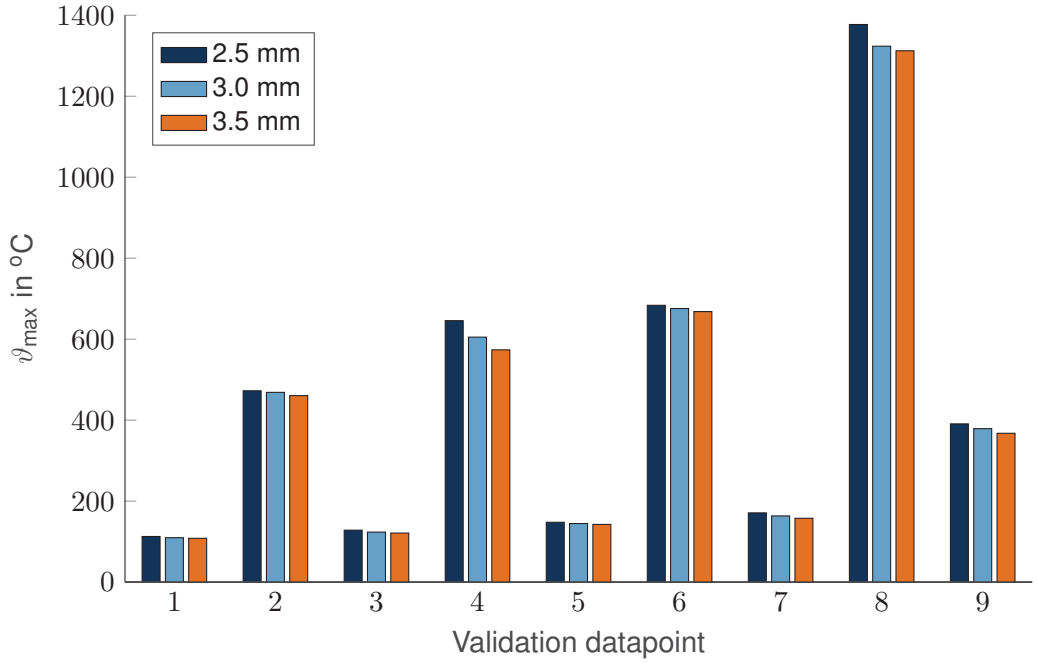

Figure A.28: Comparison of absolute temperature rise evaluated at validation datapoints for different sheet thicknesses

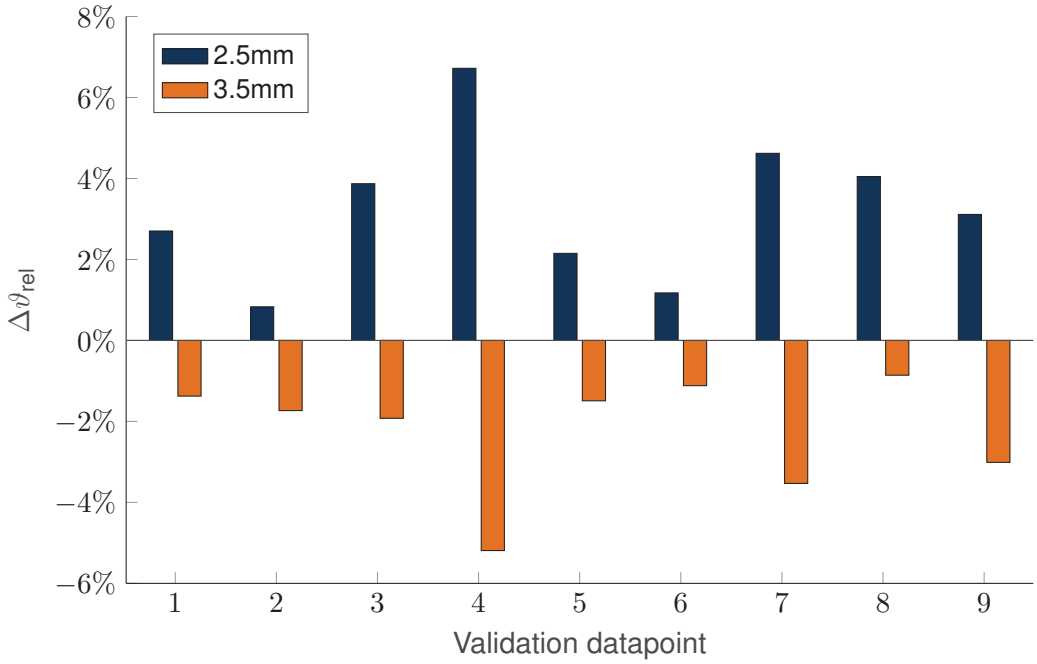

Figure A.29: Comparison of temperature rise relative to standard sheet thickness evaluated at validation datapoints for different sheet thicknesses

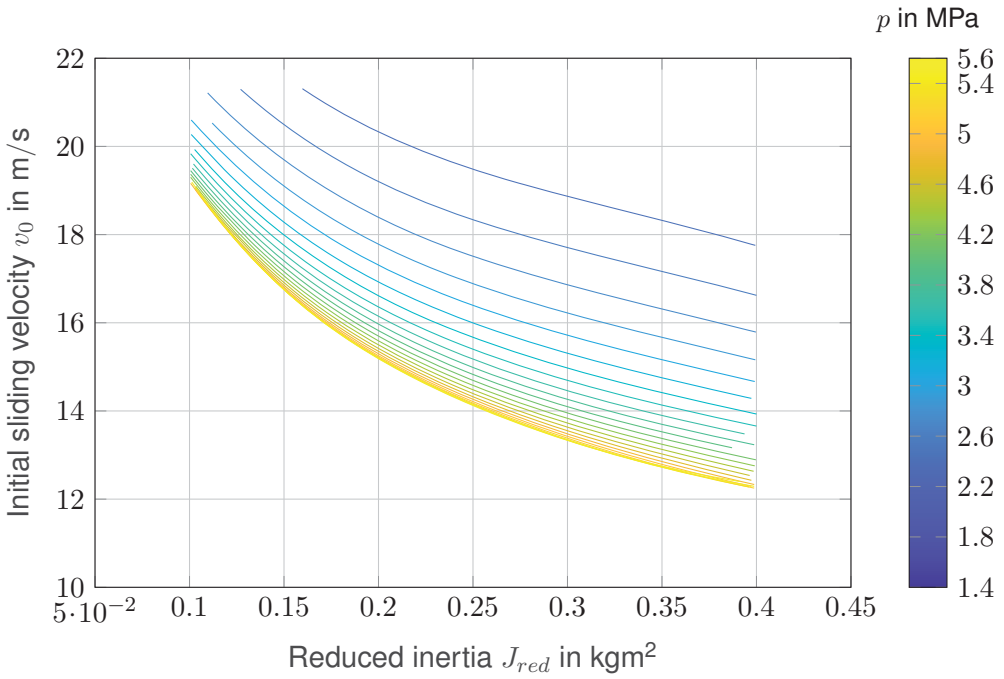

(a) s_t = 2.5 mm

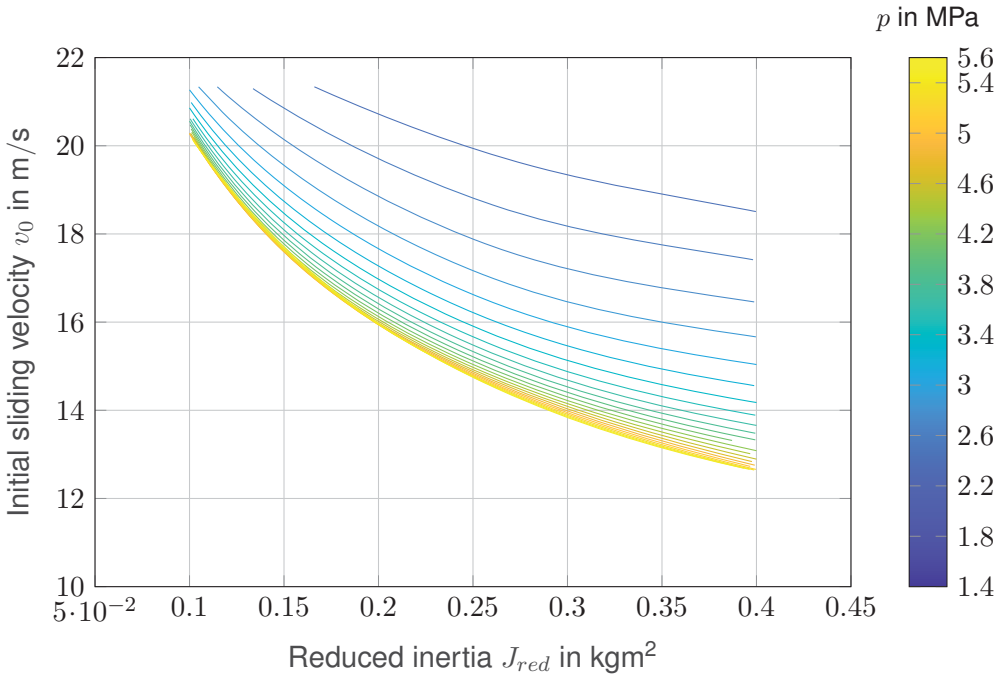

(b) s_t = 3.5 mm

Figure A.30: Thermomechanical performance limits evaluated for sheet thickness of the cone clutch of s_t = 2.5 mm (a) and s_t = 3.5 mm (b)

A.8 Dog clutch engagement experiments

Plots show time signals of measured reaction torque T_r, axial force F_{ax}, piston position s and speed difference Δn.

A.8.1 Successful engagement

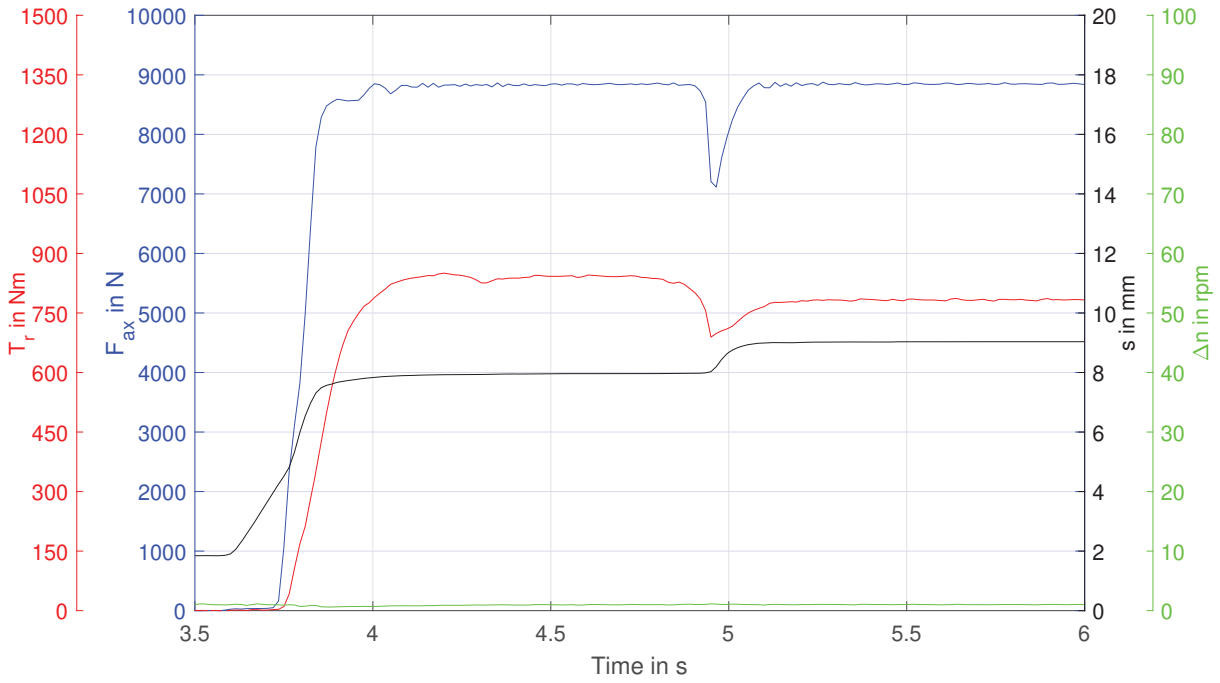

Figure A.31: Measured signal from test FFSK0106. Dog clutch variant V1, F_{ax} = 8500 N, Δn = 1 rpm, v_f = 5 mm/s

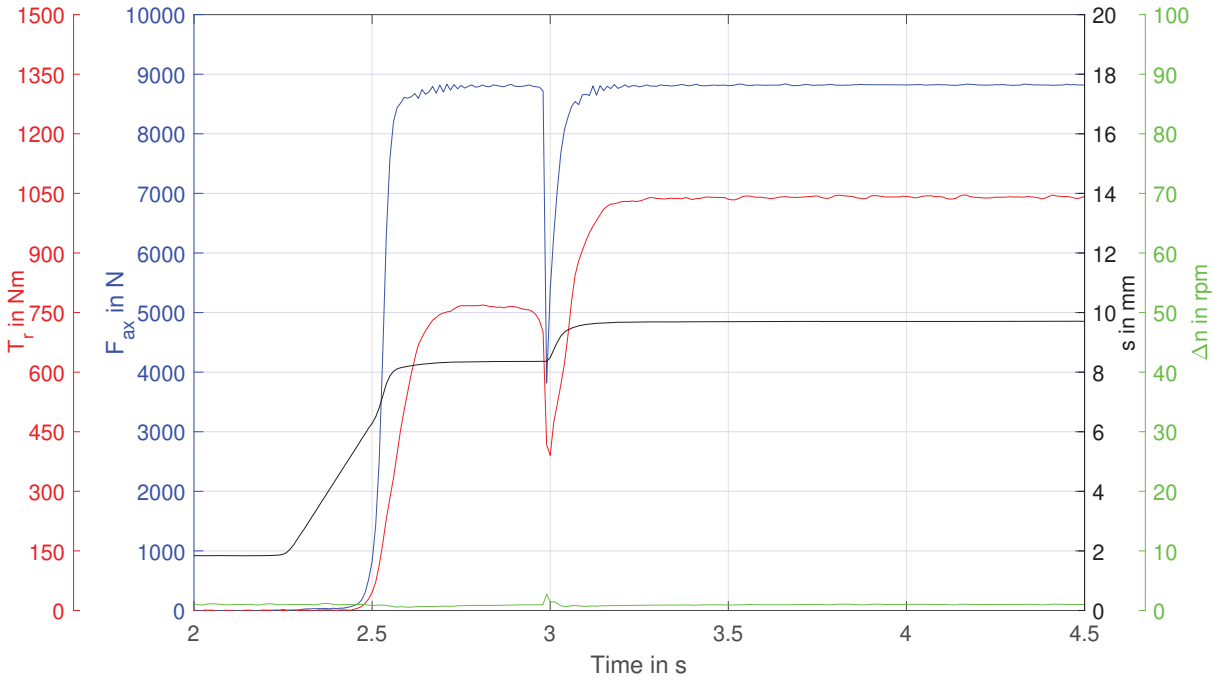

Figure A.32: Measured signal from test FFSK0126. Dog clutch variant V2, F_{ax} = 8500 N, Δn = 1 rpm, v_f = 5 mm/s

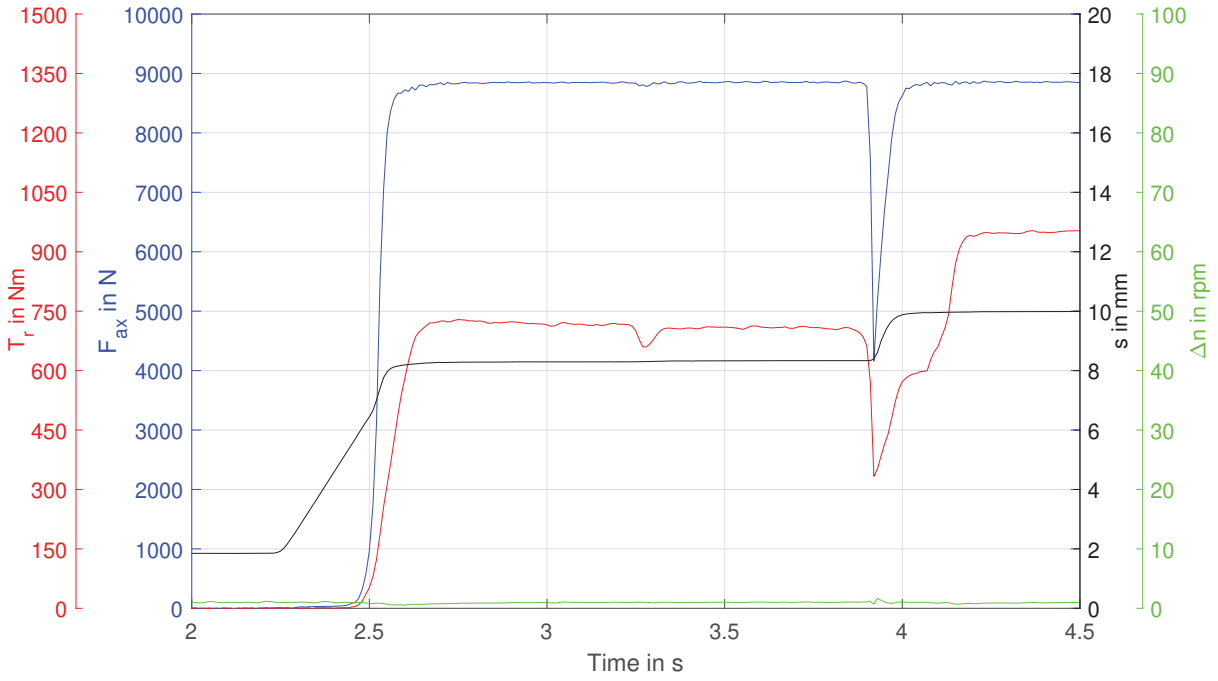

Figure A.33: Measured signal from test FFSK0146. Dog clutch variant V3, F_{ax} = 8500 N, Δn = 1 rpm, v_f = 5 mm/s

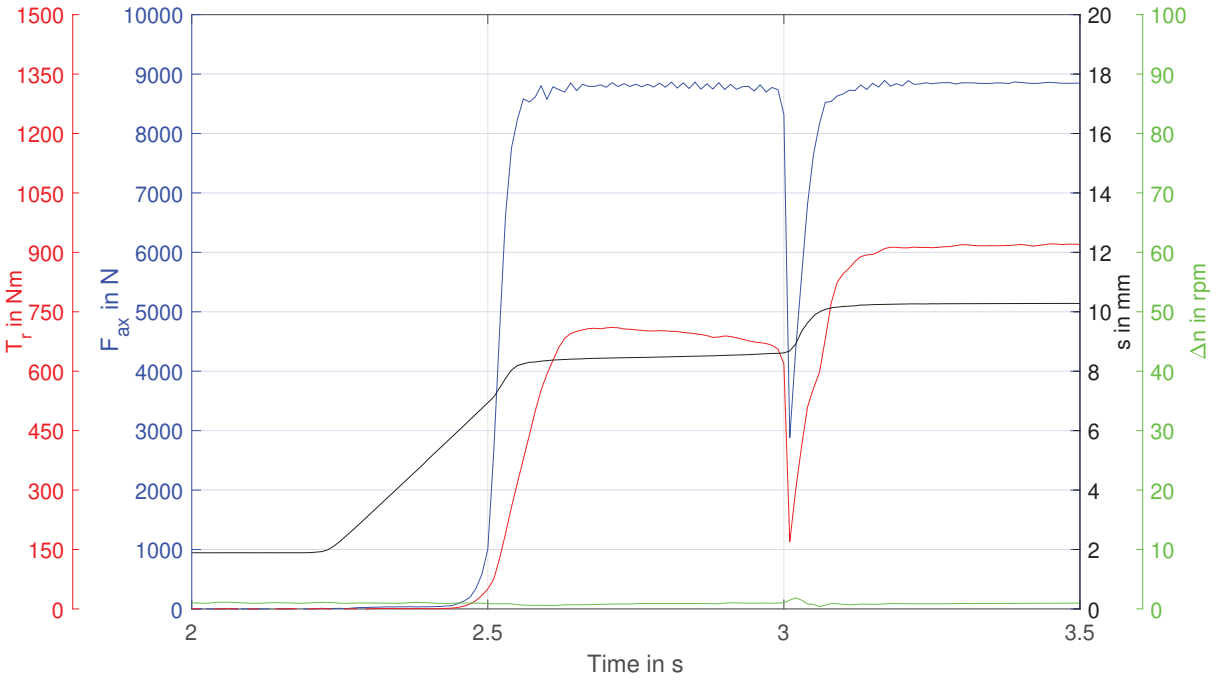

Figure A.34: Measured signal from test FFSK0166. Dog clutch variant V4, F_{ax} = 8500 N, Δn = 1 rpm, v_f = 5 mm/s

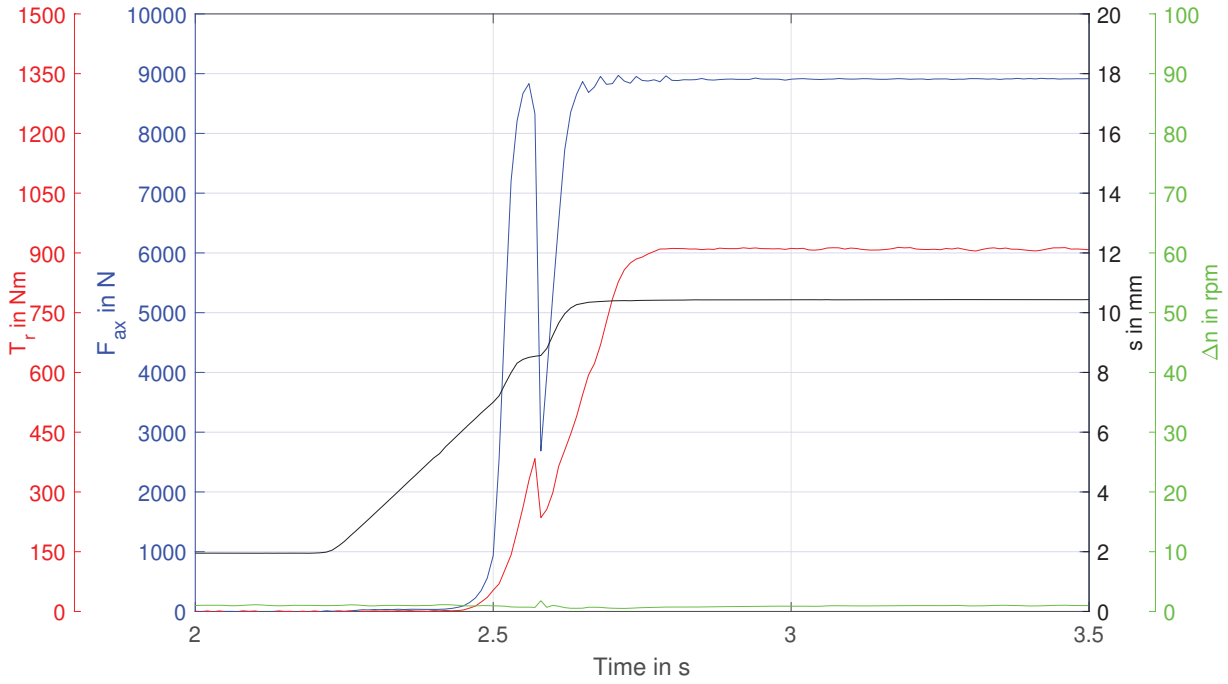

Figure A.35: Measured signal from test FFSK0191. Dog clutch variant V5, F_{ax} = 8500 N, Δn = 1 rpm, v_f = 5 mm/s

A.8.2 Delayed engagement / tooth rejection

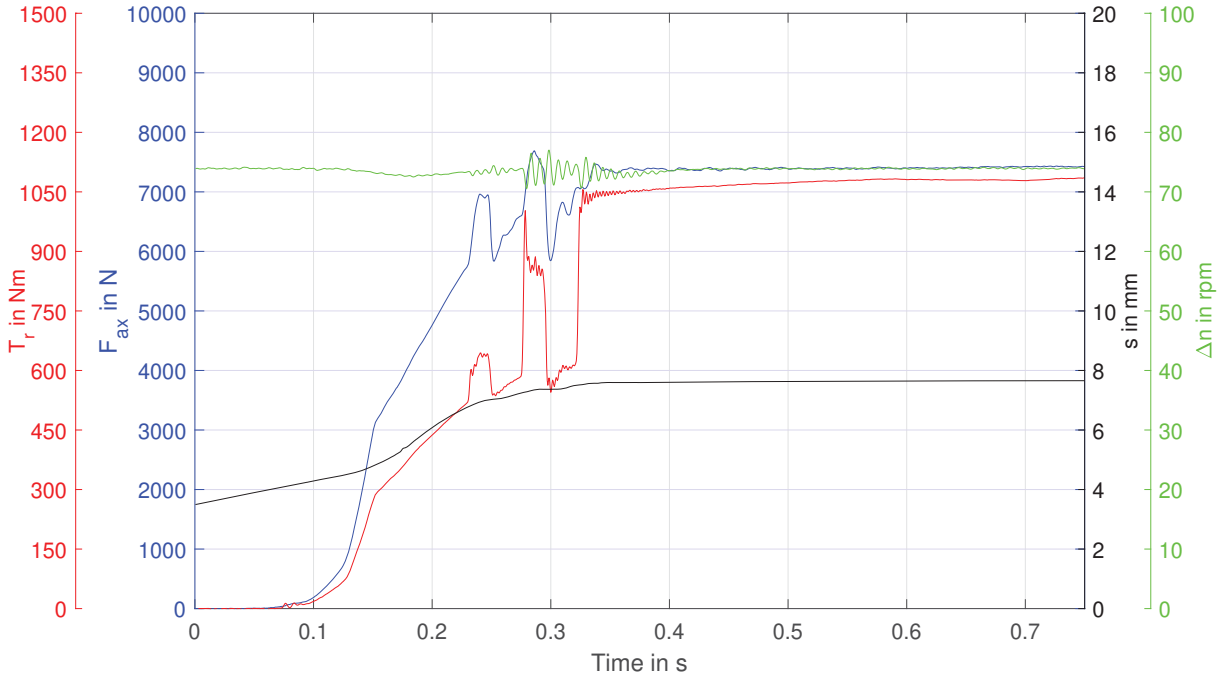

Figure A.36: Measured signal from test FFSK0209. Dog clutch variant V1, F_{ax} = 7500 N, Δn = 75 rpm, v_f = 5 mm/s

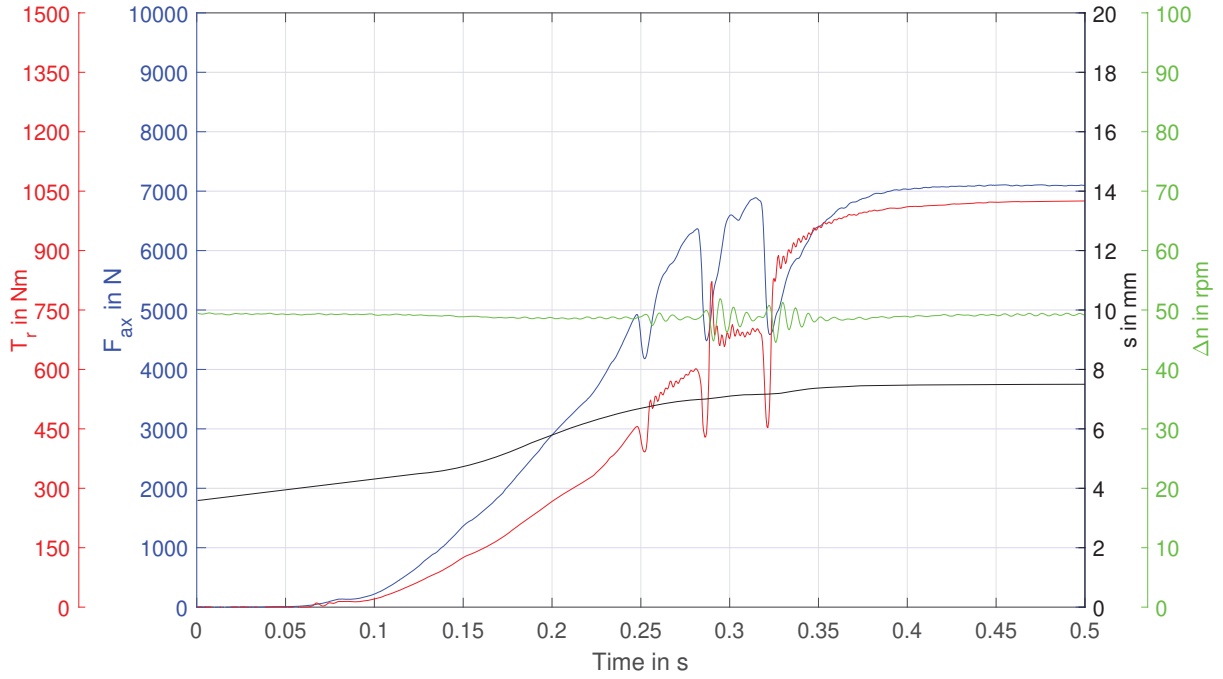

Figure A.37: Measured signal from test FFSK0223. Dog clutch variant V2, F_{ax} = 7500 N, Δn = 50 rpm, v_f = 5 mm/s

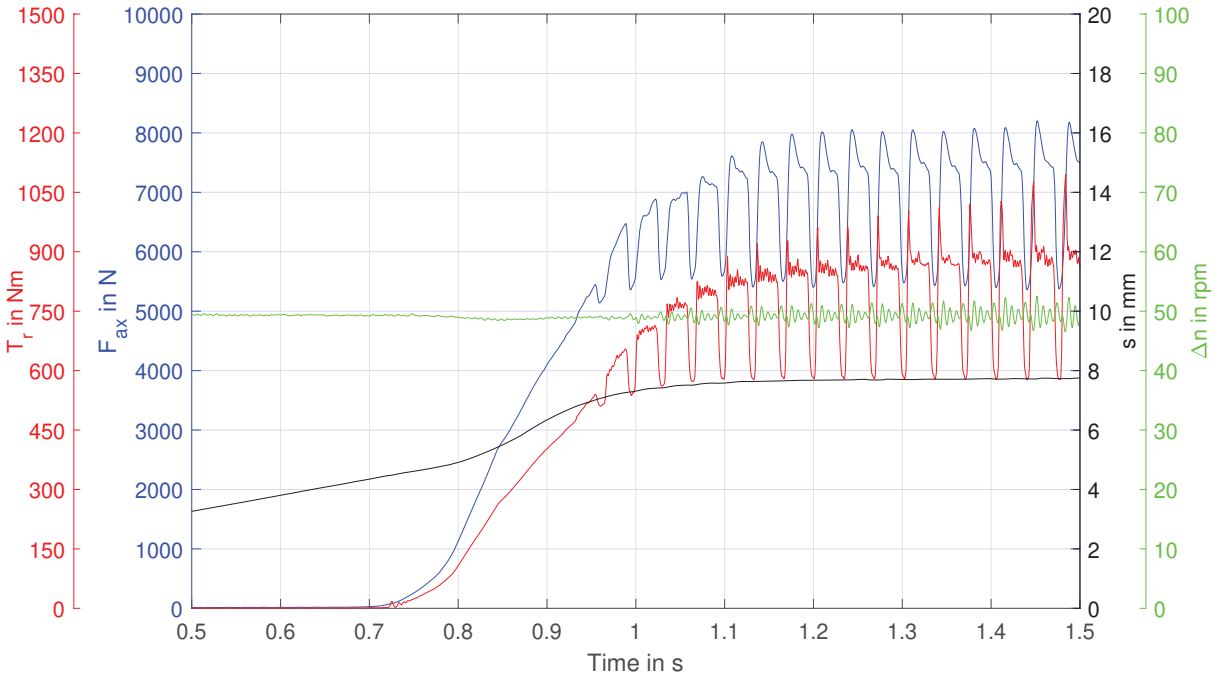

Figure A.38: Measured signal from test FFSK0243. Dog clutch variant V3, F_{ax} = 7500 N, Δn = 50 rpm, v_f = 5 mm/s

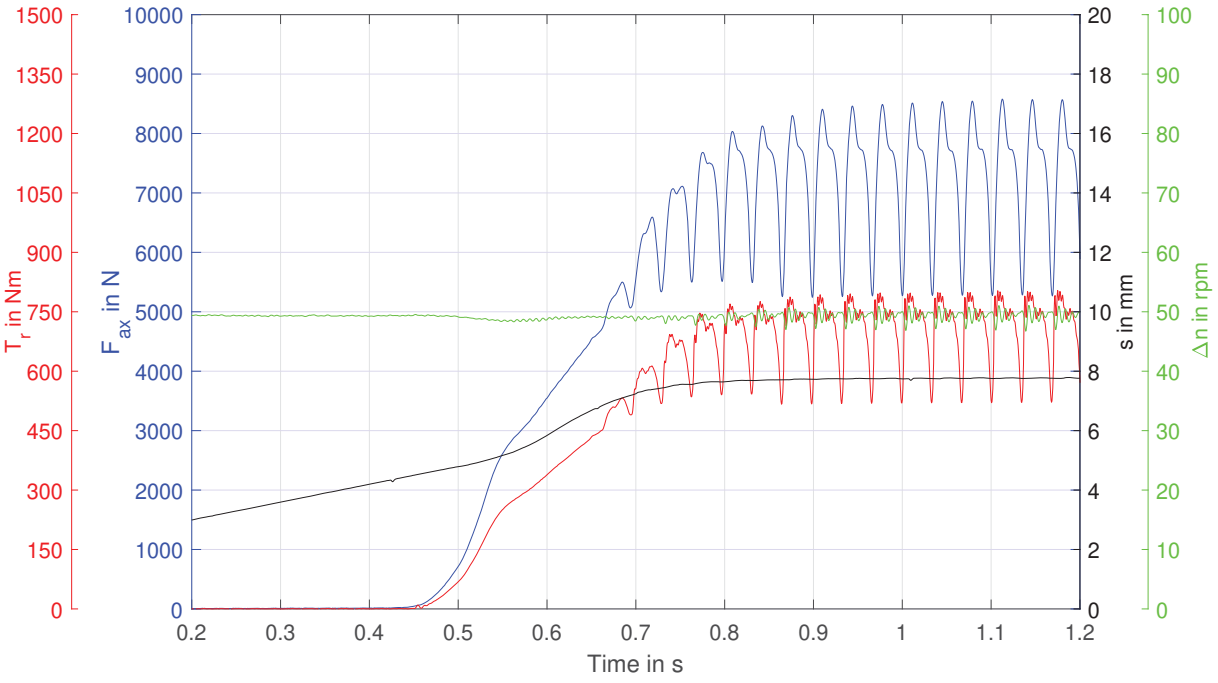

Figure A.39: Measured signal from test FFSK0263. Dog clutch variant V4, F_{ax} = 7500 N, Δn = 50 rpm, v_f = 5 mm/s

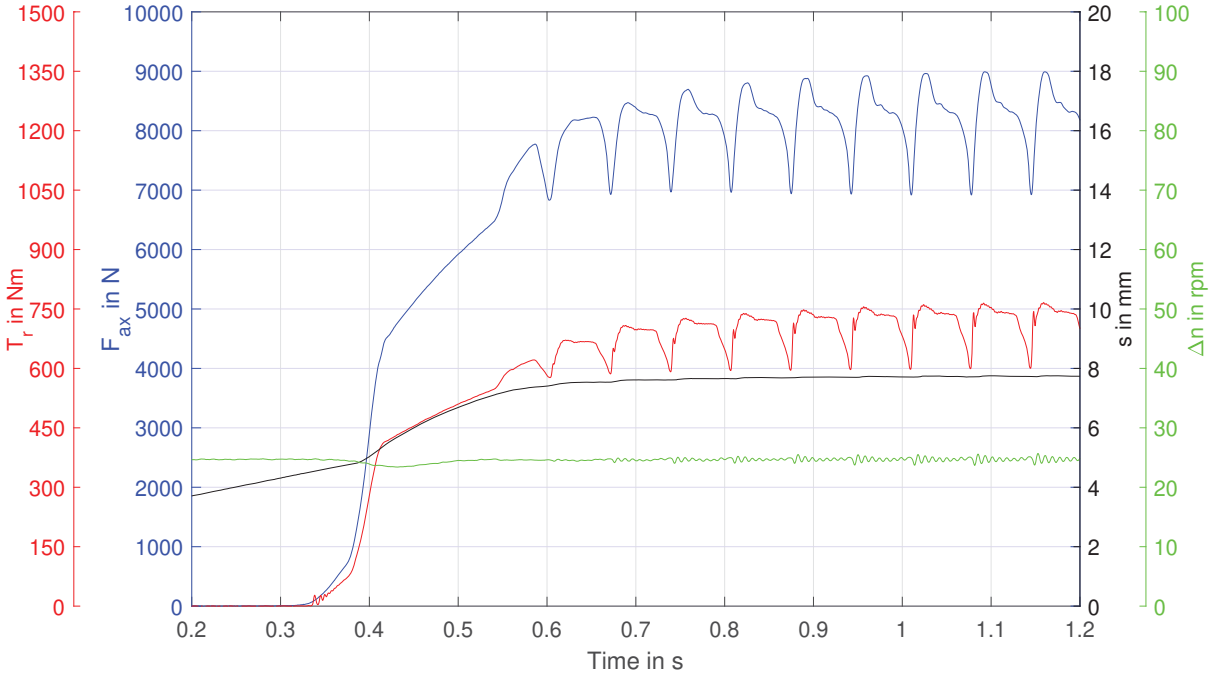

Figure A.40: Measured signal from test FFSK0482. Dog clutch variant V5, F_{ax} = 7500 N, Δn = 25 rpm, v_f = 5 mm/s

A.9 Dog clutch wear

Worn teeth of tested dog clutch variants after abuse tests are conducted. Variant V1 is omitted as it is shown in Figure 5.32.

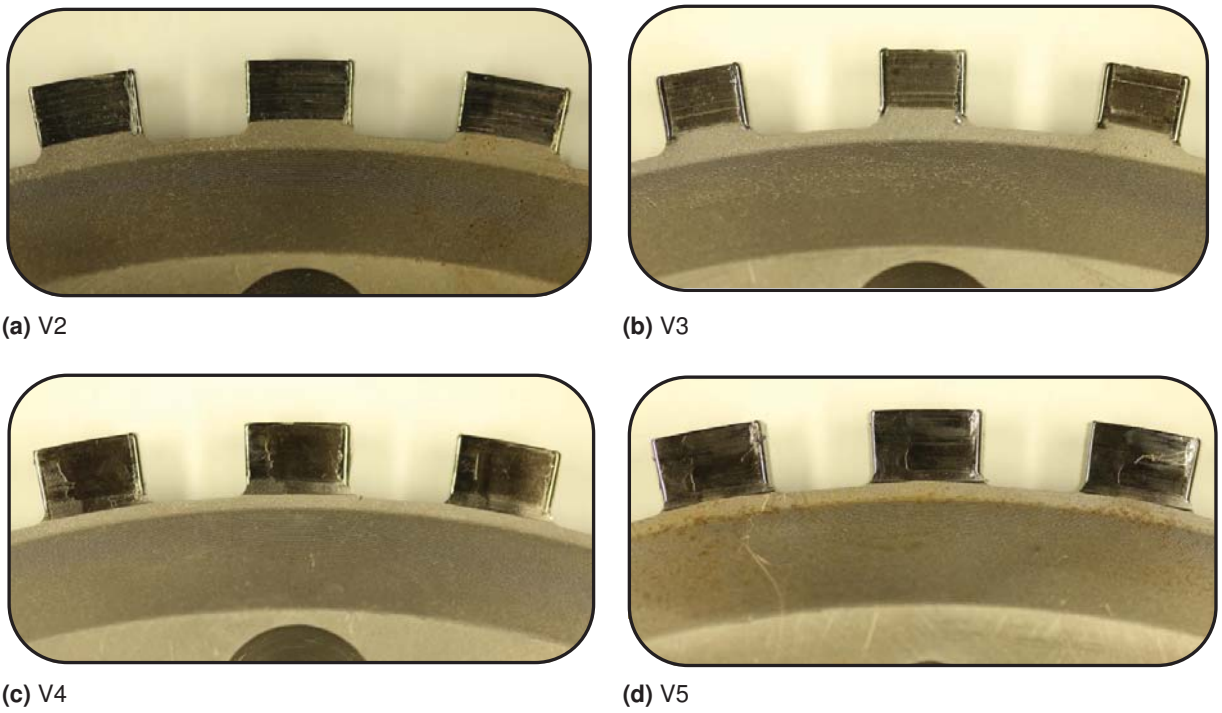

(a) V2 **(b)** V3

(c) V4 **(d)** V5

Figure A.41: Worn dog teeth of dog clutch inner ring of CCDC version 1

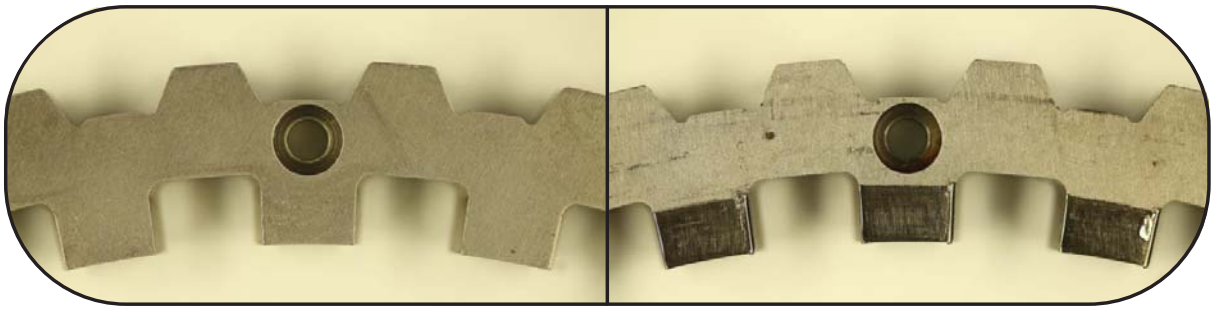

Figure A.42: New and worn teeth of outer ring of dog clutch utilised for zero play dog clutch V5

Dissertations at FZG

1.	PERRET, H.	Übertragung konstanter Leistung durch stufenlos mechanische Regeltriebe. TH Braunschweig (1935).
2.	BELLMANN, H.	Beiträge zur Prüfung von Bremsbelägen. TH Braunschweig (1939).
3.	HIERSIG, H.M.	Der Zusammenhang von Gestaltung und Beanspruchung bei Schneckengetrieben mit Evolventenverzahnung. TH Braunschweig (1943).
4.	HELBIG, F.	Walzenfestigkeit und Grübchenbildung von Zahnrad- und Wälzlagerwerkstoffen. TH Braunschweig (1943).
5.	ARF, D.	Pendelrollenlager mit symmetrischen und unsymmetrischen Rollen. TH Braunschweig (1944).
6.	OESMANN, W.	Entwicklung einer Stahlsand-Schalt- und Regelkupplung. TH Braunschweig (1945).
7.	RUBO, E.	Ermittlung der Achsfehler-Empfindlichkeit verschiedener Zylinder-Schneckengetriebe mit Hilfe des Einlauf-Abschliffvolumens. TH Braunschweig (1948).
8.	GLAUBNITZ, H.	Drehmomentmessungen zum Wendevorgang bei Raupenfahrwerken. TH Braunschweig (1948).
9.	TALKE, H.	Beiträge zur hydrodynamischen Schmiertheorie des ebenen Gleitschuhes auf ebener Fläche. TH Braunschweig (1948).
10.	CRAMER, H.	Über die Reibung und Schmierung feinmechanischer Geräte. TH Braunschweig (1949).
11.	THOMAS, W.	Reibscheiben-Regelgetriebe mit Linienberührung. TH Braunschweig (1949).
12.	MAUSHAKE, W.	Theoretische Untersuchung von Schneckengetrieben mit Globoidschnecke und Stirnrad. TH Braunschweig (1950).
13.	KRAUPNER, K.W.	Das plastische Verhalten umlaufender Stahlrollen bei Punktberührung. TH Braunschweig (1951).
14.	BANASCHEK, K.	Die Gleitreibung geschmierter Flächen kleiner Schmiegung. Einfluß von Werkstoffpaarung, Krümmung, Oberfläche und Schmierstoff. TH Braunschweig (1951).
15.	HEYER, E.	Versuche mit Zylinderschneckentrieben. Einfluß von Zahnform, Modul, Durchmesser und Schmierstoff auf Verlustleistung und Tragfähigkeit. TH München (1952).
16.	HENTSCHEL, G.	Der Hochleistungswälztrieb. Entwicklungsstand und Entwicklungsmöglichkeiten. TH München (1952).
17.	WINTER, H.	Tragfähigste Evolventengeradverzahnung. TH München (1954).

18. ROY, A.K. Spannungsoptische Untersuchung eines schrägverzahnten Stirnrades. TH München (1957).
19. RETTIG, H. Dynamische Zahnkraft. TH München (1957).
20. OHLENDORF, H. Verlustleistung und Erwärmung von Stirnrädern. TH München (1958).
21. UNTERBERGER, M. Geräuschuntersuchungen an geradverzahnten Zahnrädern. TH München (1958).
22. LOOMAN, J. Das Abrichten von profilierten Schleifscheiben zum Schleifen von schrägverzahnten Stirnrädern. TH München (1959).
23. JARCHOW, F. Versuche an Stirnrad-Globoidschneckentrieben. TH München (1960).
24. POPOVIC, L. Einfluß von Zahnform und Bearbeitung auf die Zahnfußfestigkeit. TH München (1960).
25. EHRLENSPIEL, K. Die Festkörperreibung von geschmierten und ungeschmierten Metallpaarungen mit Linienberührung. TH München (1962).
26. PITTROFF, H. Riffelbildung infolge Stillstandserschütterungen bei Wälzlagern. TH München (1962).
27. SCHREIBER, H. Zur Auswertung von Lebensdauerversuchen an Wälzlagern. TH München (1962).
28. ROTH, K. Untersuchungen über die Eignung der Evolventenzahnform für eine allgemein verwendbare feinwerktechnische Normverzahnung. TH München (1963).
29. NARUSE, Ch. Verschleiß, Tragfähigkeit und Verlustleistung bei Schraubenradgetrieben. TH München (1964).
30. GARTNER, F. Die Mischreibung bei Linienberührung. TH München (1964).
31. ASSMANN, H. Vergleichende Untersuchung von Getriebeölen im FZG-Stirnrad- und Esso-Hypoidprüfstand. TH München (1965).
32. REISTER, D. Einseitiges Breitentragen bei Stirnrädern. TH München (1965).
33. KORRENN, H. Gleitreibung in den Kontaktstellen zwischen den Wälzkörpern und den Laufbahnen der Ringe von Wälzlagern. TH München (1965).
34. HÖSEL, Th. Geräuschuntersuchungen an schrägverzahnten Stirnrädern mit Evolventenverzahnung. TH München (1965).
35. LANGENBECK, K. Die Verschleiß- und Freßgrenzlast der Hypoidgetriebe. TH München (1966).
36. MEMMEL, M. Untersuchungen über die Tragfähigkeit und Gebrauchsdauer von Gelenklagern. TH München (1966).

37. BÖTSCH, H. Der Einfluß der Oberflächenbearbeitung und -behandlung auf die Flankenfestigkeit von Stirnrädern aus Vergütungsstahl. TH München (1966).

38. LECHNER, G. Die Freßlastgrenze bei Stirnrädern aus Stahl. TH München (1966).

39. LANGE, S. Untersuchungen von Helicon- und Spiroidgetrieben mit abwickelbaren Schneckenflanken nach der hydrodynamischen und nach der Hertzschen Theorie. TH München (1967).

40. SCHWÄGERL, D. Untersuchung von Helicon- und Spiroidgetrieben mit trapezförmigem Schneckenprofil nach der Hertzschen und nach der hydrodynamischen Theorie. TH München (1967).

41. MICHELS, K. Schneckengetriebe mit Werkstoffpaarung Stahl/Grauguß. TH München (1968).

42. GACKSTETTER, G. Verlustarme Verzahnung. TH München (1968).

43. GEUPEL, H. Flüssigkeitsreibung bei Punktberührung. TH München (1969).

44. GREKOUSSIS, R. Vergleichende Untersuchungen zur Freßtragfähigkeit von Hypoid- und Stirnrädern. TH München (1969).

45. BAETHGE, J. Zahnfederhärte, Drehwegfehler und Geräusch bei Stirnrädern. TH München (1969).

46. SCHULZ, H.D. Untersuchung über Tragfähigkeiten und Verlustleistung von Schneckengetrieben mit trapezförmigem Schneckenprofil und kegeliger Schnecke. TH München (1969).

47. STÖLZLE, K. Leistungsübertragung in Planetengetrieben bei statischem und dynamischem Betrieb. Berechnung, Optimierung und Versuchsergebnisse. TH München (1970).

48. SEITZINGER, K. Die Erwärmung einsatzgehärteter Zahnräder als Kennwert für ihre Freßtragfähigkeit. TU München (1971).

49. STÖSSEL, K. Reibungszahlen unter elasto-hydrodynamischen Bedingungen. TU München (1971).

50. SCHMIDT, G. Berechnung der Wälzpressung schrägverzahnter Stirnräder unter Berücksichtigung der Lastverteilung. TU München (1972).

51. HIRT, M. Einfluß der Zahnfußausrundung auf Spannung und Festigkeit von Geradstirnrädern. TU München (1974).

52. WILKESMANN, H. Berechnung von Schneckengetrieben mit unterschiedlichen Zahnprofilformen (Tragfähigkeits- und Verlustleistung für Hohlkreis-, Evolventen- und Geradlinienprofil). TU München (1974).

53. RICHTER, M. Der Verzahnungswirkungsgrad und die Freßtragfähigkeit von Hypoid- und Schraubenradgetrieben - Versuchsergebnisse und Berechnungsmethoden. TU München (1976).

54. RÖSCH, H. Untersuchungen zur Wälzfestigkeit von Rollen - Einfluß von Werkstoff, Wärmebehandlung und Schlupf. TU München (1976).

55. GAGGERMEIER, H. Untersuchungen zur Reibkraftübertragung in Regel-Reibradgetrieben im Bereich elasto-hydrodynamischer Schmierung. TU München (1977).

56. KÄSER, W. Beitrag zur Grübchenbildung an gehärteten Zahnrädern. Einfluß von Härtetiefe und Schmierstoff auf die Flankentragfähigkeit. TU München (1977).

57. KNABEL, W. Geräusche und Schwingungen an Stirnradgetrieben. Untersuchungen geometrischer Einflüsse bei hohen Drehzahlen und Belastungen. TU München (1977).

58. WIRTH, X. Über den Einfluß von Schleifkerben auf die Zahnfußtragfähigkeit und das Schädigungsverhalten oberflächengehärteter Zahnräder. TU München (1977).

59. HUBER, G. Zylinderschneckengetriebe, ein Beitrag zur Berechnung von Grübchen- und Gleitverschleiß und Angaben zum Wirkungsgradverhalten aus Versuchen. TU München (1978).

60. BROSSMANN, U. Über den Einfluß der Zahnfußausrundung und des Schrägungswinkels auf Beanspruchung und Festigkeit schrägverzahnter Stirnräder. TU München (1979).

61. PLEWE, H.-J. Untersuchungen über den Abriebverschleiß von geschmierten, langsam laufenden Zahnrädern. TU München (1980).

62. FRESEN, G. Untersuchungen über die Tragfähigkeit von Hypoid- und Kegelradgetrieben (Grübchen, Ridging, Rippling, Graufleckigkeit und Zahnbruch). TU München (1981).

63. OSTER, P. Beanspruchung der Zahnflanken unter Bedingungen der Elastohydrodynamik. TU München (1982).

64. HORNUNG, K. Zahnräder aus Bainitischem Gusseisen mit Kugelgraphit. TU München (1983).

65. WEISS, T. Zum Festigkeits- und Verzugsverhalten von randschichtgehärteten Zahnrädern. TU München (1983).

66. VOJACEK, H. Das Reibungsverhalten von Fluiden unter elastohydrodynamischen Bedingungen. Einfluß der chem. Struktur des Fluides, der Werkstoffe und der Makro- und Mikrogeometrie der Gleit/Wälzkörper. TU München (1984).

67. SCHÖNNENBECK, G. Einfluß der Schmierstoffe auf die Zahnflankenermüdung (Graufleckigkeit und Grübchenbildung) hauptsächlich im Umfangsgeschwindigkeitsbereich 1...9 m/s. TU München (1984).

68. WIENER, H. Untersuchung der Rollenkinematik im Axial-Pendelrollenlager. TU München (1984).

69. MATHIAK, D. Untersuchungen über Flankentragfähigkeit, Zahnfußtragfähigkeit und Wirkungsgrad von Zylinderschneckengetrieben. TU München (1984).

70. STRASSER, H. Einflüsse von Verzahnungsgeometrie, Werkstoff und Wärmebehandlung auf die Zahnfußtragfähigkeit. TU München (1984).

71. JOACHIM, F.-J. Untersuchungen zur Grübchenbildung an vergüteten und normalisierten Zahnrädern (Einfluß von Werkstoffpaarung, Oberflächen- und Eigenspannungszustand). TU München (1984).

72. GERBER, H. Innere dynamische Zusatzkräfte bei Stirnradgetrieben - Modellbildung, innere Anregung und Dämpfung. TU München (1984).

73. SIMON, M. Messung von elasto-hydrodynamischen Parametern und ihre Auswirkung auf die Grübchentragfähigkeit vergüteter Scheiben und Zahnräder. TU München (1984).

74. SCHMIDT, W. Untersuchungen zur Grübchen- und zur Zahnfußtragfähigkeit geradverzahnter evolventischer Innenstirnräder. TU München (1984).

75. FUNCK, G. Wärmeabführung bei Getrieben unter quasistationären Betriebsbedingungen. TU München (1985).

76. PAUL, M. Einfluß von Balligkeit und Lageabweichungen auf die Zahnfußbeanspruchung spiralverzahnter Kegelräder. TU München (1986).

77. HOPPE, F. Das Abschalt- und Betriebsverhalten von mechanischen Sicherheitskupplungen. TU München (1986).

78. MICHAELIS, K. Die Integraltemperatur zur Beurteilung der Freßtragfähigkeit von Stirnradgetrieben. TU München (1987).

79. WECH, L. Untersuchungen zum Wirkungsgrad von Kegelrad- und Hypoidgetrieben. TU München (1987).

80. KNAUER, G. Zur Grübchentragfähigkeit einsatzgehärteter Zahnräder - Einfluß von Werkstoff, Schmierstoff und Betriebstemperatur. TU München (1988).

81. PLACZEK, T. Lastverteilung und Flankenkorrektur in gerad- und schrägverzahnten Stirnradstufen. TU München (1988).

82.	PFLAUM, H.	Das Reibungsverhalten ölgeschmierter Kegelreibkupplungen in Synchronisationseinrichtungen von Kraftfahrzeug-Schaltgetrieben. TU München (1988).
83.	BRINCK, P.	Zahnfußtragfähigkeit oberflächengehärteter Stirnräder bei Lastrichtungsumkehr. TU München (1989).
84.		(entfallen)
85.	NEUPERT, K.	Verschleißtragfähigkeit und Wirkungsgrad von Zylinder-Schneckengetrieben. TU München (1990).
86.	PREXLER, F.	Einfluß der Wälzflächenrauheit auf die Grübchenbildung vergüteter Scheiben im EHD-Kontakt. TU München (1990).
87.	SCHALLER, K.-V.	Betriebsfestigkeitsuntersuchungen zur Grübchenbildung an einsatzgehärteten Stirnradflanken. TU München (1990).
88.	COLLENBERG, H.-F.	Untersuchungen zur Freßtragfähigkeit schnellaufender Stirnradgetriebe. TU München (1991).
89.	MÜLLER, R.	Schwingungs- und Geräuschanregung bei Stirnradgetrieben. TU München (1991).
90.	ANZINGER, M.	Werkstoff- und Fertigungseinflüsse auf die Zahnfußtragfähigkeit, insbesondere im hohen Zeitfestigkeitsgebiet. TU München (1991).
91.	KAGERER, E.	Messung von elastohydrodynamischen Parametern im hochbelasteten Scheiben- und Zahnkontakt. TU München (1991).
92.	HASLINGER, K.	Untersuchungen zur Grübchentragfähigkeit profilkorrigierter Zahnräder. TU München (1991).
93.	VOLLHÜTER, F.	Einfluß der Achsversetzung auf die Grübchen- und Zahnfußtragfähigkeit von spiralverzahnten Kegelrädern. TU München (1992).
94.	PINNEKAMP, B.	Das Schaltverhalten von PKW-Getriebesynchronisierungen. TU München (1992).
95.	SCHUBERT, M.	Einfluß der Befestigungsart und Radkranzdicke auf die Zahntragfähigkeit von Innenstirnrädern. TU München (1993).
96.	STEINGRÖVER, K.	Untersuchung zu Verschleiß, Verlustgrad und Fressen bei Zylinder-Schneckengetrieben. TU München (1993).
97.	ELSTORPFF, M.-G.	Einflüsse auf die Grübchentragfähigkeit einsatzgehärteter Zahnräder bis in das höchste Zeitfestigkeitsgebiet. TU München (1993).
98.	EMMERT, S.	Untersuchungen zur Zahnflankenermüdung (Graufleckigkeit, Grübchenbildung) schnellaufender Stirnradgetriebe. TU München (1994).

99. SUCHANDT, Th. Betriebsfestigkeitsuntersuchungen zur Zahnfußtragfähigkeit einsatzgehärteter Zahnräder und zur Bruchfestigkeit vergüteter Laschenketten. TU München (1994).

100. HÄMMERL, B. Lebensdauer- und Temperaturverhalten ölgekühlter Lamellenkupplungen bei Lastkollektivbeanspruchung. TU München (1994).

101. WEISS, R. Einfluß der Ölalterung auf die Zahnflankentragfähigkeit. TU München (1994).

102. SCHLENK, L. Untersuchungen zur Freßtragfähigkeit von Großzahnrädern. TU München (1995).

103. MANN, U. Schmierfilmbildung in elastohydrodynamischen Kontakten, Einfluß verschiedener Grundöle und Viskositäts-Index-Verbesserer. TU München (1995).

104. RUDZEWSKI, S. Systemtechnische Verknüpfung eingeführter Getriebeberechnungsprogramme. TU München (1995).

105. RANK, R. Untersuchungen zur Lebensdauerprüfung von Synchronisierungen. TU München (1995).

106. EBERSPÄCHER, C. Reihenfolgeeffekte bei der Grübchen-Betriebsfestigkeit einsatzgehärteter Zahnräder. TU München (1995).

107. RANK, B. Untersuchungen zur Grübchenbildung bei Zylinder-Schneckengetrieben. TU München (1996).

108. SATTELBERGER, K. Schwingungs- und Geräuschanregung bei ein- und mehrstufigen Stirnradgetrieben. TU München (1997).

109. HIRSCHMANN, V. Tragfähigkeitsuntersuchungen an stufenlosen Umschlingungsgetrieben. TU München (1997).

110. THOMAS, J. Flankentragfähigkeit und Laufverhalten von hartfeinbearbeiteten Kegelrädern. TU München (1998).

111. WIKIDAL, F. Berechnung der Flankenpressung gerad- und schrägverzahnter Stirnräder für last- und fertigungsbedingte Abweichungen. TU München (1998).

112. PERPONCHER, V., CH. Einflüsse von Reibflächentopographie und Beanspruchungen auf das Reibungs- und Verschleißverhalten von Synchronisierungen. TU München (1998).

113. SCHEDL, U. Einfluß des Schmierstoffs auf die Grübchenlebensdauer einsatzgehärteter Zahnräder. TU München (1998).

114. VOLLMER, T. Methodik zur Entwicklung einer Fahrstrategie für Fahrzeuge, ausgeführt am Beispiel des Autarken Hybrids. TU München (1998).

115. HEITMANN, A. Entwicklung des i^2-Getriebes für den Autarken Hybrid-Antriebsstrang. TU München (1998).

116. PFLEGER, F. Schalt- und Lebensdauerverhalten von Lamellenkupplungen. TU München (1998).

117. KERSCHL, S. Der Autarke Hybrid - Optimierung des Antriebsstrangs hinsichtlich Energieverbrauch und Bestimmung des Einsparpotentials, TU München (1998).

118. DÖBEREINER, R. Tragfähigkeit von Hochverzahnungen geringer Schwingungsanregung, TU München (1998).

119. WEIGAND, U. Werkstoff- und Wärmebehandlungseinflüsse auf die Zahnfußtragfähigkeit, TU München (1999).

120. SCHRADE, U. Einfluß von Verzahnungsgeometrie und Betriebsbedingungen auf die Graufleckentragfähigkeit von Zahnradgetrieben, TU München (2000).

121. KÖLL, J. Konstruktion des Getriebes für ein Pkw-Hybridantriebssystem, TU München (2000).

122. FÖRSTER, W. Der Lastschaltvorgang beim stufenlosen i^2-Getriebe des Autarken Hybrid-Antriebsstrangs, TU München (1999).

123. LANGE, N. Hoch fresstragfähige Schneckengetriebe mit Rädern aus Sphaeroguß, TU München (2000).

124. LUTZ, M. Methoden zur rechnerischen Ermittlung und Optimierung von Tragbildern an Schneckengetrieben, TU München (2000).

125. KOPATSCH, F. Wirksamkeit von Viskositätsindex-Verbesserern im EHD-Zahnradkontakt, TU München (2000).

126. BAYERDÖRFER, I. Einfluß von betriebsbedingten Schmierstoffveränderungen auf die Flankentragfähigkeit einsatzgehärteter Stirnräder, TU München (2000).

127. TOBIE, T. Zur Grübchen- und Zahnfußtragfähigkeit einsatzgehärteter Zahnräder, TU München (2001).

128. STAHL, K. Grübchentragfähigkeit einsatzgehärteter Gerad- und Schrägverzahnungen unter besonderer Berücksichtigung der Pressungsverteilung, TU München (2001).

129. NEUMÜLLER, M. Einfluß der Ölalterung auf Reibungs- und Verschleißverhalten von Synchronisierungen, TU München (2001).

130. MOSBACH, C. Das Reibungs- und Reibschwing-Verhalten nasslaufender Lamellenkupplungen, TU München (2002).

131. DYLA, A. Modell einer durchgängig rechnerbasierten Produktentwicklung, TU München (2002).

132. GRASWALD, C. Reibung im elastohydrodynamischen Kontakt von Reibradgetrieben, TU München (2002).

133. GEISER, H.. Grundlagen zur Beurteilung des Schwingungsverhaltens von Stirnrädern, TU München (2002).

134. SCHINAGL, S. Zahnfußtragfähigkeit schrägverzahnter Stirnräder unter Berücksichtigung der Lastverteilung, TU München (2002).

135. DOLESCHEL, A. Wirkungsgradberechnung von Zahnradgetrieben in Abhängigkeit vom Schmierstoff, TU München (2003).

136. ANNAST, R. Kegelrad-Flankenbruch, TU München (2003)

137. SÜSSMUTH, J.-F. Eignungsbeurteilung von Schmierstoffen für stufenlose Umschlingungsgetriebe, TU München (2003).

138. MATTEN, D. Methode zur Entwicklung ingenieurwissenschaftlicher Berechnungsprogramme, TU München (2003).

139. GEIER, N. Untersuchung des Reibungs- und Verschleißverhaltens nasslaufender Kupplungen in Abhängigkeit ihrer Reibflächentopographie, TU München (2003)

140. HERTTER, T. Rechnerischer Festigkeitsnachweis der Ermüdungstragfähigkeit vergüteter und einsatzgehärteter Stirnräder, TU München (2003).

141. KRIEGER, H. Alterung von Schmierstoffen im Zahnradprüfstand und in Praxisgetrieben, TU München (2004).

142. STEUTZGER, M. Einfluß der Baugröße auf die Zahnfußtragfähigkeit einsatzgehärteter Stirnräder, TU München (2004).

143. SCHMIDBAUER, T. Aufbau und Erprobung des Autarken Hybrid-Antriebsstrangs im Versuchsfahrzeug. TU München (2004).

144. LIU, W. Einfluss verschiedener Fertigungsverfahren auf die Grauflecken-tragfähigkeit von Zahnradgetrieben. TU München (2004).

145. FEHLING, R. Höhere Tragfähigkeit bei Zahnradflanken durch eine nichtevolventische Profilmodifikation. TU München (2004).

146. GUTTENBERG, P. Der autarke Hybrid am Prüfstand - Funktion, Kraftstoffverbrauch und energetische Analyse. TU München (2004)

147. WIMMER, T. Einflüsse auf das Lastübernahmeverhalten von nasslaufenden Lamellenkupplungen. TU München (2004).

148. RADEV, T. Einfluss des Schmierstoffes auf die Grübchentragfähigkeit einsatzgehärteter Zahnräder - Entwicklung des Praxisnahen Pittingtests. TU München (2005)

149. KRASTEV, I. Optimierung des Lastschaltvorgangs im i^2-Getriebe. TU München (2005)

150. HEILEMANN, J. Tragfähigkeit und Wirkungsgrad bei unterschiedlichen Schnecken-Zahnflankenformen unter Berücksichtigung der Oberflächenhärte und Härtetiefe. TU München (2005).

151. HEIZENRÖTHER, M. Das Stirnraddifferenzial mit Innenverzahnung im Vergleich zum Kegelraddifferenzial inklusive einer Sperrwertanalyse. TU München (2005).

152. WIMMER, A. Lastverluste von Stirnradverzahnungen - Konstruktive Einflüsse, Wirkungsgradmaximierung, Tribologie. TU München (2006).

153. BRUCKMEIER, S. Flankenbruch bei Stirnradgetrieben. TU München (2006).

154. HAUSER, C. Einfluss der Ölalterung auf Reibcharakteristik und Reibschwingverhalten von Lamellenkupplungen. TU München (2007).

155. GROSSL, A. Einfluss von PVD-Beschichtungen auf die Flanken- und Fußtragfähigkeit einsatzgehärteter Stirnräder. TU München (2007).

156. STEINBERGER, G. Optimale Grübchentragfähigkeit von Schrägverzahnungen. TU München (2007).

157. JAROS, M. Integration des STEP-Produktmodells in den Getriebeentwicklungsprozess. TU München (2007).

158. RADEV, S. Einfluss von Flankenkorrekturen auf das Anregungsverhalten gerad- und schrägverzahnter Stirnradpaarungen. TU München (2007).

159. BRAYKOFF, C. Tragfähigkeit kleinmoduliger Zahnräder. TU München (2007).

160. STANGL, M. Methodik zur kinematischen und kinetischen Berechnung mehrwelliger Planeten-Koppelgetriebe. TU München (2007).

161. STENICO, A. Werkstoffmechanische Untersuchungen zur Zahnfußtragfähigkeit einsatzgehärteter Zahnräder. TU München (2007).

162. SCHWIENBACHER, S. Einfluss von Schleifbrand auf die Flankentragfähigkeit einsatzgehärteter Zahnräder. TU München (2008).

163. WINKLER, J. Tribologischer Schichtaufbau bei Synchronisierungen und sein Einfluss auf Reibung und Verschleiß. TU München (2008).

164. WIRTH, C. Zur Tragfähigkeit von Kegelrad- und Hypoidgetrieben. TU München (2008).

165. KREIL, O. Einfluss der Oberflächenstruktur auf Druckverteilung und Schmierfilmdicke im EHD-Kontakt. TU München (2009).

166. OTTO, H.-P. Flank load carrying capacity and power loss reduction by minimised lubrication. TU München (2009).

167. OTTO, M. Lastverteilung und Zahnradtragfähigkeit von schrägverzahnten Stirnrädern. TU München (2009).

168. TOMIC, D. Zum Verschleiß von Kegelreibkupplungen - Einflüsse von Belastung und Schmierstoff auf Reibschichteigenschaften. TU München (2009).

169. WEISEL, C. Schneckengetriebe mit lokal begrenztem Tragbild. TU München (2009).

170. WEITL, R. Zur Tragfähigkeitsberechnung von Wälzlagern und Stirnrädern. TU München (2010).

171. MULZER, F. Systematik hochübersetzender koaxialer Getriebe. TU München (2010).

172. SCHUDY, J. Untersuchungen zur Flankentragfähigkeit von Außen- und Innenverzahnungen. TU München (2010).

173. BRETL, N. Einflüsse auf die Zahnfußtragfähigkeit einsatzgehärteter Zahnräder im Bereich hoher Lastspielzahlen. TU München (2010).

174. GRIGGEL, T. Einfluss von Korrekturen und Fertigungsabweichungen auf die Schwingungsanregung von Stirnrädern. TU München (2010).

175. LAYHER, M. Einfluss der Schmierstoffadditivierung auf das Reibungsverhalten nasslaufender Reibschaltelemente. TU München (2011).

176. HOCHMANN, M. Zahnradtragfähigkeit bei Schmierung mit Getriebefließfetten. TU München (2011).

177. DETZEL, J. Tribologische Untersuchungen an Achsgetrieben zur Verbesserung des Wirkungsgrads. TU München (2011).

178. ZIEGLER, A. Zur verkürzten Systemlebensdauerprüfung von Zahnradgetrieben. TU München (2011).

179. THOMA, F. Lastübertragung im verformten System Lager-Welle-Zahnrad. TU München (2012).

180. FRÜHE, T. Berechnung und Minimierung der Zahnfußspannung von Standard- und LowLos-Verzahnungen. TU München (2012).

181. WITZIG, J. Flankenbruch - Eine Grenze der Zahnradtragfähigkeit in der Werkstofftiefe. TU München (2012).

182. KLEIN, M. Zur Fresstragfähigkeit von Kegelrad- und Hypoidgetrieben. TU München (2012).

183. KURTH, F. Efficiency Determination and Synthesis of Complex-Compound Planetary Gear Transmissions. TU München (2012).

184. WOHLLEBER, F. Thermischer Haushalt nasslaufender Lamellenkupplungen. TU München (2012).

185. HEIDER, M. Schwingungsverhalten von Zahnradgetrieben - Beurteilung und Optimierung des Schwingungsverhaltens von Stirnrad- und Planetengetrieben. TU München (2012).

186. MONZ, A. Tragfähigkeit und Wirkungsgrad von Schneckengetrieben bei Schmierung mit konsistenten Getriebefetten. TU München (2012).

187. WIRTH, M. Schleppmomente in Synchronisierungen von Fahrzeuggetrieben. TU München (2012).

188. BANSEMIR, G. Konstruktionsleitsystem für den durchgängig rechnerbasierten Zahnradgetriebeentwurf. TU München (2012).

189. HERGESELL, M. Grauflecken- und Grübchenbildung an einsatzgehärteten Zahnrädern mittlerer und kleiner Baugröße. TU München (2013).

190. KOLLER, P. Steigerung der Zahnflankentragfähigkeit durch Optimierung von Eigenspannungs- und Oberflächenzustand. TU München (2013).

191. SCHLEICH, T. Temperatur- und Verlustleistungsverhalten von Wälzlagern in Getrieben. TU München (2013).

192. STEMPLINGER, J.-P. Tragfähigkeit und Wirkungsgrad von Stirnradgetrieben bei Schmierung mit hochviskosen Fluiden und Fetten NLGI 0,1 und 2. TU München (2013).

193. FÜRSTENBERGER, M. Betriebsverhalten verlustoptimierter Kunststoffzahnräder. TU München (2013).

194. HOMBAUER, M. Grauflecken an Kegelrad- und Hypoidverzahnungen und deren Einfluss auf die Grübchentragfähigkeit. TU München (2013).

195. MAYER, J. Einfluss der Oberfläche und des Schmierstoffs auf das Reibungsverhalten im EHD-Kontakt. TU München (2013).

196. BAUHOFFER, H. Kontakt- und Laufverhalten von Kronenrädern unter Montageabweichungen. TU München (2014).

197. LECHNER, C. Energiebilanzierung des CVT-Hybrid. TU München (2014).

198. HINTERSTOISSER, M. Zur Optimierung des Wirkungsgrades von Stirnradgetrieben TU München (2014).

199. LOMBARDO, S. Einfluss von verschiedenen Carbonitrierverfahren auf die Zahnfuß- sowie Zahnflankentragfähigkeit von Stirnrädern. TU München (2014).

200. IDLER, S. Die Fresstragfähigkeit stufenloser Umschlingungsgetriebe. TU München (2014).

201. LANGHEINRICH, A. Geometrie, Beanspruchung und Verformung asymmetrischer Stirnradverzahnungen. TU München (2014).

202. MATT, P. Einfluss der Stirnkanten auf die Tragfähigkeit von Verzahnungen. TU München (2014).

203. HENSEL, M. Thermische Beanspruchbarkeit und Lebensdauerverhalten von nasslaufenden Lamellenkupplungen. TU München (2014).

204. GEIGER, J. Wirkungsgrad und Wärmehaushalt von Zahnradgetrieben bei instationären Betriebszuständen. TU München (2014).

205. SIGMUND, W. Untersuchung und Simulation des Verschleißverhaltens von Schneckengetrieben mit unvollständigem Tragbild. TU München (2015).

206. PARLOW, J. Entwicklung einer Methode zum anforderungsgerechten Entwurf von Stirnradgetrieben. TU München (2016).

207. NEUBAUER, B. Lastverteilung und Anregungsverhalten in Planetengetriebesystemen. TU München (2016).

208. NITSCH, Ch. Dynamisches Betriebsverhalten von Werkstoffverbundzahnrädern. TU München (2016).

209. BIHR, J. Untersuchung des Schwingungsverhaltens von mehrstufigen Stirnradgetrieben unter besonderer Berücksichtigung des Welle-Lager-Systems. TU München (2016).

210. SCHURER, S. Einfluss nichtmetallischer Einschlüsse in hochreinen Werkstoffen auf die Zahnfußtragfähigkeit. TU München (2016).

211. KADACH, D. Stillstandsmarkierungen an Zahnrädern und deren Auswirkungen auf die Flankentragfähigkeit. TU München (2016).

212. FELBERMAIER, M. Untersuchungen zur Graufleckenbildung und deren Einfluss auf die Grübchentragfähigkeit einsatzgehärteter Stirnräder. TU München (2016).

213. ACUNER, R. Synchronisierungen mit Carbon-Reibwerkstoffen unter hohen und extremen Beanspruchungen. TU München (2016).

214. LOHNER, T. Berechnung von TEHD Kontakten und Einlaufverhalten von Verzahnungen. TU München (2016).

215. ZIMMER, M. Berechnung und Optimierung von Geometrie und Eingriffsverhalten von Verzahnungen beliebiger Achslage. TU München (2017).

216. GWINNER, Ph. Auslegung schwingungsarmer Stirnradverzahnungen für den automobilen Einsatz in hochdrehenden, elektrisch angetriebenen Achsgetrieben. TU München (2017).

217. SCHULTHEISS, H. Zum Verschleißverhalten einsatzgehärteter Zahnradpaarungen in Abhängigkeit des Schmierungsmechanismus bei Fettschmierung. TU München (2017)

218. MOSER, K.	Methode zur Untersuchung des Betriebsverhaltens stufenloser Umschlingungsgetriebe. TU München (2017)
219. STREBEL, M.	Spontanschäden an nasslaufenden Lamellenkupplungen. TU München (2017)
220. BAAR, M.	Kennwerte zur Tragfäkigkeit kleinmoduliger Kronenradverzahnungen unterschiedlicher Werkstoffpaarung. TU München (2017)
221. WICKBORN, C.	Erweiterung der Flankentragfähigkeitsberechnung von Stirnrädern in der Werkstofftiefe. TU München (2017)
222. MEINGASSNER, G.	Methodik zur Untersuchung des Reibungsverhaltens nasslaufender Lamellenkupplungen bei Langsamlauf- und Mikroschlupf. TU München (2017)
223. ZORNEK, B.	Untersuchungen zur Flankentragfähigkeit vergüteter und nitrierter Innen- und Außenverzahnungen. TU München (2018)
224. DOBLER, F.	Einflüsse auf die Tragfähigkeit induktiv umlaufgehärteter Stirnräder. TU München (2018)
225. DAFFNER, M.	Validierung von Verformungsberechnungen im System Zahnrad-Welle-Lager-Gehäuse. TU München (2018)
226. HEIN, M.	Zur ganzheitlichen betriebsfesten Auslegung und Prüfung von Getriebezahnrädern. TU München (2018)
227. HASL, C.	Zur Zahnfußtragfähigkeit von Kunststoffstirnrädern. TU München (2018)
228. KOHN, B.	Topologische Flankenkorrektur zur Anregungsoptimierung von Stirnradgetrieben. TU München (2019)
229. BOIADJIEV, I.	Schadensentwicklung und Tragfähigkeit carbonitrierter Kegelradverzahnungen. TU München (2019)
230. MAUTNER, E.	Grübchentragfähigkeit von Schneckengetrieben großer Baugröße mit unvollständigem Tragbild. TU München (2019)
231. ENGELHARDT, C.	Einfluss von Wasser in Getriebeölen auf die Zahnflankentragfähigkeit einsatzgehärteter Stirnräder. TU München (2019)
232. VÖLKEL, K.	Charakterisierung des Einlaufverhaltens nasslaufender Lamellenkupplungen. TU München (2020)
233. BANSEMIR, S.	Bewertung von Berechnungstiefe und Aussagegüte bei der Stirnradgetriebeberechnung. TU München (2020)
234. UTAKAPAN, T.	Schwingungsverhalten mehrstufiger Getriebe. TU München (2020)
235. KÖNIG J.	Steigerung der Zahnflankentragfähigkeit durch optimierte Fertigung und Schmierung. TU München (2020).

236. JURKSCHAT T. Erweiterte Bestimmung lastabhängiger Verluste von Stirnradgetrieben. TU München (2020).

237. EBNER M. Selbstschmierung hochbelasteter Zahnradkontakte mit schmierstoffgetränkten porösen Eisenwerkstoffen. TU München (2021).

238. REIMANN T. Einfluss der Treibrichtung auf die Flankentragfähigkeit von Stirnrad-, Kegelrad- und Hypoidgetrieben. TU München (2021).

239. DOBLER A. Verschleiß als Lebensdauergrenze für Zahnräder. TU München (2021).

240. DAI R. Change-Management-fokussierte Einführung eines „Ganzheitlichen Produktionssystems“ in Klein- und Kleinstunternehmen. TU München (2021).

241. GÜNTNER C. Zum Einfluss der Härtbarkeit auf die Zahnfußtragfähigkeit einsatzgehärteter Stirnräder größerer Baugröße. TU München (2022).